Imperial College London
Department of Computing

Automatic MRI segmentation of the developing neonatal brain

Antonios Makropoulos

November 24, 2014

Supervised by Daniel Rueckert, Serena J. Counsell, A. David Edwards

Submitted in part fulfilment of the requirements for the degree of
Doctor of Philosophy
of
Imperial College London

To my amazing supervisors

Declaration of originality

I hereby declare that the work described in this thesis is my own, except where specifically acknowledged.

Antonios Makropoulos

Copyright declaration

Abstract

Detailed morphometric analysis of the neonatal brain is required to characterise normal brain development and investigate the neuroanatomical correlates of cognitive impairments. The segmentation of the brain in Magnetic Resonance Imaging (MRI) is a prerequisite to obtain quantitative measurements of regional brain structures. These measurements obtained at term-equivalent or early preterm age may lead to improved understanding of brain growth and may help evaluate long-term neurodevelopmental performance at an early stage.

This thesis focuses on the development of an accurate segmentation algorithm for the neonatal brain MR images and its application in large cohorts of subjects. Neonatal brain segmentation is challenging due to the large anatomical variability as a result of the rapid brain development in the neonatal period. The lack of training data in the neonatal period, encoded in brain atlases, further hinders the development of automatic segmentation tools.

A novel algorithm for the tissue segmentation of the neonatal brain is proposed. The algorithm is extended for the regional brain segmentation. This is the first segmentation method for the parcellation of the developing neonatal brain into multiple structures. A novel method is further proposed for the group-wise segmentation of the data that utilizes unlabelled data to complement the labelling information of brain atlases. Previous studies in the literature tended to overestimate the extent of the cortical region. A method based on the morphology of the cortex is introduced to correct for this over-segmentation.

The segmentation method is applied on an extensive database of neonatal MR images. Regional volumetric, surface and diffusion tensor imaging measurements are derived from the early preterm period to term-equivalent

age. These measurements allow characterisation of the regional brain development and the investigation of correlations with clinical factors. Finally, a spatio-temporal structural atlas is constructed for multiple regions of the neonatal brain.

Acknowledgements

I would first of all like to thank my supervisors, Daniel Rueckert, Serena Counsell and David Edwards, for all their help, inspiration and valuable advice and for giving me the freedom to explore different ideas throughout my PhD. I am also grateful to Paul Aljabar, Joseph Hajnal and Gareth Ball for being there to discuss and advise me on practical aspects of my work. Thanks to all my colleagues from the Imperial College London and King's College London for the great atmosphere and collaboration. It has really been a pleasure and honor to work with such enthusiastic people.

Many thanks to my parents, Ioannis and Dimitra, my brother, Vagelis, and Afroditi for their love and constant support. Thank you for giving me the strength to follow my dreams and believing in me. Many thanks to my friends from London, Edinburgh and Greece and especially George and Dimitra for all the off-work quality time.

Contents

List of Tables

List of Figures

List of Abbreviations

AAM	Active Appearance Model
AD	Axial Diffusivity
ADC	Apparent Diffusion Coefficient
ASM	Active Shape Model
BET	Brain Extraction Tool
BGT	Basal Ganglia and Thalami
CCS	Connected Components
CGM	Cortical Grey Matter
CNR	Contrast-to-Noise Ratio
CSF	Cerebrospinal Fluid
DGM	Deep Grey Matter
DTI	Diffusion Tensor Imaging
DWI	Diffusion Weighted Imaging
ECS	Extra-Cranial Space
EM	Expectation-Maximization
FA	Fractional Anisotropy
FC	Fractional Content
FCM	Fuzzy C-Means
fMRI	functional Magnetic Resonance Imaging
GA	Gestational Age
GM	Grey Matter
GMM	Gaussian Mixture Model
ICM	Iterated Conditional Modes
INU	Intensity Non-Uniformity
LW	Local Weighting
MAP	Maximum a Posteriori

MCD	Minimum Covariance Determinant
MR	Magnetic Resonance
MRF	Markov Random Field
MRI	Magnetic Resonance Imaging
MV	Majority Vote
NMI	Normalised Mutual Information
PMA	Post-Menstrual Age
PV	Partial Volume
RD	Radial Diffusivity
RF	Radio-Frequency
SA	Surface Area
SPM	Statistical Parametric Mapping
SSD	Sum of Squared Differences
SSIM	Structural Similarity Measure
TE	Echo-Time
TR	Repetition-Time
WM	White Matter

List of Publications

1. Makropoulos, A., Gousias, I. S., Ledig, C., Aljabar, P., Serag, A., Hajnal, J., Edwards, A. D., Counsell, S., and Rueckert, D. (2014). Automatic whole brain MRI segmentation of the developing neonatal brain. IEEE Transactions on Medical Imaging.

2. Ferrazzi, G., Kuklisova Murgasova, M., Arichi, T., Malamateniou, C., Fox, M. J., Makropoulos, A., Allsop, J., Rutherford, M., Malik, S., Aljabar, P., and Hajnal, J. V. (2014). Resting state fMRI in the moving fetus: a robust framework for motion, bias field and spin history correction. NeuroImage.

3. Ledig, C., Shi, W., Makropoulos, A., Koikkalainen, J., Heckemann, R. A., Hammers, A., Lötjönen, J. M., and Rueckert, D. (2014). Consistent and robust 4D whole-brain segmentation: application to traumatic brain injury. In IEEE International Symposium on Biomedical Imaging (ISBI).

4. Kersbergen, K. J., Makropoulos, A., Aljabar, P., Groenendaal, F., de Vries, L. S., Edwards, A. D., Counsell, S. J., and Benders, M. J. N. L. (2014). Serial volumetric measurements across 50 brain regions in a large cohort of very preterm infants. In Pediatric Academic Societies (PAS).

5. Tataranno, M. L., Kersbergen, K. J., Groenendaal, F., van Rooij, L. G., Toet, M. C., Buonocore, G., Counsell, S. J., Makropoulos, A., de Vries, L. S., and Benders, M. J. N. L. (2014). Early brain activity and brain growth in preterm infants. In Pediatric Academic Societies (PAS).

6. Makropoulos, A., Ball, G., Hajnal, J. V., Edwards, A. D., Rueckert, D., and Counsell, S. J. (2013). Assessing the impact of excluding a subset of the diffusion acquisition on the resultant fractional anisotropy values in the preterm brain. In International Society for Magnetic Resonance in Medicine (ISMRM).

7. Ball, G., Aljabar, P., Makropoulos, A., Arichi, T., Merchant, N., Edwards, A. D., and Counsell, S. J. (2013). Exploring the development of the human structural connectome in preterm neonates. In International Society for Magnetic Resonance in Medicine (ISMRM).

8. Hughes, E. J., Bond, J., Svrckova, P., Makropoulos, A., Ball, G., Sharp, D. J., Edwards, A. D., Hajnal, J. V., and Counsell, S. J. (2012). Regional changes in thalamic shape and volume with increasing age. NeuroImage.

9. Makropoulos, A., Ledig, C., Aljabar, P., Serag, A., Hajnal, J. V., Edwards, A. D., Counsell, S. J., and Rueckert, D. (2012b). Automatic tissue and structural segmentation of neonatal brain MRI using Expectation-Maximization. In MICCAI Grand Challenge on Neonatal Brain Segmentation 2012 (NeoBrainS12).

10. Makropoulos, A., Gousias, I., Ledig, C., Aljabar, P., Serag, A., Hajnal, J. V., Edwards, A. D., Counsell, S. J., and Rueckert, D. (2012a). Automatic multi-label segmentation of the preterm brain with the use of adaptive atlases. In International Society for Magnetic Resonance in Medicine (ISMRM).

11. Serag, A., Gousias, I., Makropoulos, A., Aljabar, P., Hajnal, J. V., Boardman, J., Counsell, S. J., and Rueckert, D. (2012). Unsupervised learning of shape complexity: Application to brain development. In MICCAI Workshop on Spatio-temporal Image Analysis for Longitudinal and Time-Series Image Data (STIA).

Submitted / In preparation

1. Išgum, I., Benders, M. J.N.L., Avants, B., Cardoso, M. J., Counsell, S. J., Gomez, E. F., Gui, L., Hüppi, P., Kersbergen, K. J., Makropoulos,

A., Melbourne, A., Moeskops, P., Mol, C. P., Kuklisova-Murgasova, M., Rueckert, D., Schnabel, J. A., Srhoj-Egekher, V., Wu, J., Wang, S., de Vries, L. S., and Viergever, M. A. Evaluation of automatic neonatal brain segmentation algorithms: the NeoBrainS12 challenge. Submitted in Medical Image Analysis.

2. Ledig, C., Heckemann, R. A., Hammers, A., Lopez, J. C., Makropoulos, A., Lötjönen, J., Menon, D., and Rueckert, D. Robust whole-brain segmentation: application to traumatic brain injury. Submitted in Medical Image Analysis.

3. Makropoulos, A., Aljabar, P., Hajnal, J. V., Edwards, A. D., Counsell, S. J., and Rueckert, D. Regional development in the neonatal population. In preparation.

4. Makropoulos, A., Aljabar, P., Ledig, C., Hajnal, J. V., Edwards, A. D., Counsell, S. J., and Rueckert, D. Label Propagation via Patch-Based Neighbors. In preparation.

Chapter 1

Introduction

1.1 Motivation

Studying the anatomy of the developing brain is essential to characterise normal development and investigate factors that affect brain growth. With improvements in neonatal intensive care, increasing numbers of infants who are born preterm now survive (Schwartz et al., 1994; Wilson-Costello et al., 2005). However, approximately 10% of infants who are born preterm will develop cerebral palsy (Hack and Fanaroff, 2000) and up to 50% will develop cognitive and/or behavioural problems in childhood (Marlow et al., 2005; Delobel-Ayoub et al., 2009). With advances in Magnetic Resonance Imaging (MRI), detailed images of the neonatal brain can be visualized non-invasively at a millimeter scale. Quantitative neuroimaging studies using MRI are increasingly being used to assess brain growth and development in this vulnerable population. These studies have identified disturbances in the growth of cortical grey matter (CGM) (Hüppi et al., 1998b; Peterson et al., 2000, 2003; Kapellou et al., 2006a; Thompson et al., 2007; Rathbone et al., 2011), white matter (WM) microstructure (Anjari et al., 2007; Ball et al., 2010; Boardman et al., 2010; van Kooij et al., 2012), regional brain growth and development of deep grey matter structures (Inder et al., 2005; Limperopoulos et al., 2005; Boardman et al., 2006; Mewes et al., 2006; Srinivasan et al., 2006, 2007; Thompson et al., 2007; Boardman et al., 2010; Ball et al., 2012; Gousias et al., 2012) compared to infants born at term. Quantitative MR measures, obtained at term equivalent age or older, are associated with neurodevelopmental performance (Peterson et al., 2000, 2003;

Woodward et al., 2005; Beauchamp et al., 2008; Counsell et al., 2008; Lodygensky et al., 2008; Thompson et al., 2008; Boardman et al., 2010; Lind et al., 2010, 2011; Rathbone et al., 2011; van Kooij et al., 2012).

Regional volumetric and shape measurements of the brain are derived on the basis of the segmented structures of the brain. Diffusion weighted imaging (DWI) and functional MRI (fMRI) further provide insights into the regional structural and functional connectivity of the brain at a macroscopic scale. Systematic assessment of these measurements in population studies is essential to identify regions of the brain that are affected by pathologies and provide information on the normal development of the brain. However, manual segmentation of MR images is extremely time consuming and thus an expensive process. Furthermore, manual labelling is subject to inter- and intra-observer variability, which limits its reproducibility. These limitations of manual approaches present an obstacle in labelling large cohorts of subjects that are required for population studies. There is therefore a need for an accurate automatic technique to parcellate the brain into multiple structures of interest. Automatic segmentation of the neonatal brain is considerably more challenging than the adult brain and hinders the development of image processing tools. MR images of the neonatal brain have a much lower contrast-to-noise ratio (CNR), frequently have lower signal-to-noise ratio due to the small size of the neonatal brain and vary enormously in terms of brain shape and appearance as a result of rapid brain development during this period.

The aim of the research in this thesis is to provide an accurate automatic method for regional segmentation of the neonatal brain. This allows for the first time regional quantitative measurements of the neonatal brain to be derived, from early preterm age to term-equivalent age. Regional brain measurements can lead to improved understanding of the development of the brain and will enable the impact of aberrant brain growth on subsequent neurodevelopment following preterm birth to be assessed.

1.2 Magnetic Resonance Imaging methods

Magnetic resonance imaging is increasingly being used for imaging the neonatal brain. MRI provides an excellent imaging technique to assess the brain development due to the high-resolution images it provides while being

non-invasive and non-ionizing. This section briefly overviews MR techniques used in structural imaging of the neonatal brain.

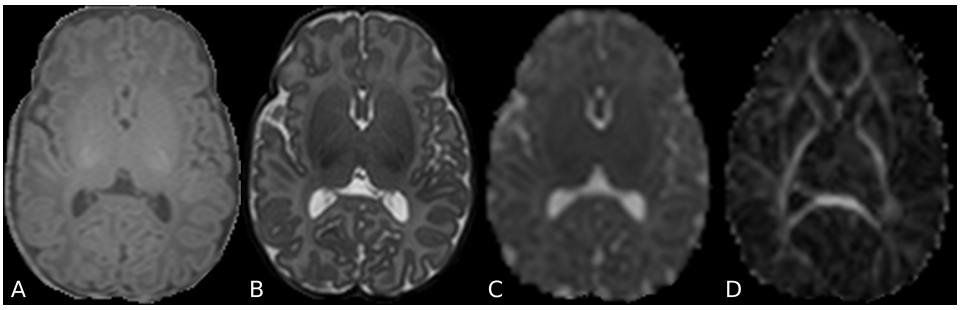

Figure 1.1: Structural imaging of the neonatal brain. T1-weighted image (A), T2-weighted image (B), ADC map (C) and FA map (D) of a neonatal brain (skull-stripped) acquired at 44 weeks post-menstrual age (PMA) are presented.

1.2.1 Magnetic Resonance Imaging

MRI is based on the quantum mechanical properties of the hydrogen protons in the body. Nuclei that have an odd number of protons and neutrons, like hydrogen, rotate/spin around their axis at random orientations. When placed in a magnetic field of strength B_0, the spin axis of the nuclei tends to align with the magnetic field in the parallel direction to the field. The nuclei reach an equilibrium with B_0 but their position is not fixed, they precess around their axis. If a pulse of radiofrequency (RF) is applied, the majority of the nuclei will align to the anti-parallel direction of the B_0, and start to precess in a phase coherent with each other. After the RF pulse, the nuclei lose their magnetization and recover to their equilibrium state as a result of two relaxation factors:

- T1 relaxation. The spin axis of the nuclei aligns back to the direction parallel to B_0.
- T2 relaxation. The spins of the nuclei lose their phase coherence.

The tissue contrast arises from the different concentration of hydrogen protons in the different tissues. This leads to different T1 and T2 relaxation rates among the tissues. The induced RF pulse can be manipulated in order to weight the acquired image according to the T1 relaxation factor

(T1-weighted images) or the T2 relaxation factor (T2-weighted images). Example T1-weighted and T2-weighted are presented in Figure 1.1.

1.2.2 Diffusion Weighted Imaging / Diffusion Tensor Imaging

Diffusion weighted imaging (DWI) is based on the application of diffusion gradients, that result in linearly-varying magnetic fields. Stejskal and Tanner (1965) introduced a commonly used method for a Diffusion Weighted Imaging (DWI) acquisition: Two gradient pulses with the same amplitude but opposite directions are applied. The static spins will result in the same MR signal as the two pulses will cancel each other. However, spins which have moved will result in a signal loss. This allows the macroscopic water displacement of water in each voxel of the image to be described. Applying different directions to the diffusion gradients allows to further compute the diffusion tensor, an estimate of the water diffusion direction in 3D. At least six different gradient directions are required to estimate the diffusion tensor.

Quantitative measures derived from DWI and DTI can be used to characterise the underlying tissue micro-structure. The motion of water molecules in the brain is restricted by structural barriers resulting in diffusion that is not equal in all directions. An example of such barriers are the WM tracts, axonal fibres in the WM that connect different parts of the brain. The water molecules' motion in the WM is preferential in the direction parallel to the WM tracts. Commonly used quantitative measures of the DWI/DTI include the apparent diffusion coefficient (ADC), axial diffusivity (AD), radial diffusivity (RD) and fractional anisotropy (FA). The ADC quantifies the overall diffusion of the water molecules. Diffusion anisotropy can be estimated from the eigenvalues of the diffusion tensor. AD is approximated with the eigenvalue of the principal eigenvector, while the RD is the average of the eigenvalues from the two minor eigenvectors. FA is computed from the three principal eigenvalues and quantifies the degree of anisotropy in the water diffusion. ADC and FA maps of a neonatal brain are shown in Figure 1.1.

1.3 Challenges of automatic segmentation in neonatal brain MRI

Automatic brain MRI segmentation is challenging due to several reasons:

- Intensity inhomogeneity/non-uniformity (INU). The intensity of a single tissue class is not uniform, rather changes gradually, over the image space. This inconsistency of the signal intensity is caused by non-uniform radio-frequency (RF) fields and reception sensitivity as well as electromagnetic interaction with the body (Belaroussi et al., 2006). Higher field strength scanners result in more significant intensity variability. Figure 1.2 shows the INU effect.

- Partial Volume (PV) effects. Partial Volume effect is the mixing of different tissue classes in a single voxel (Tofts, 2003). Since the image resolution is limited, voxels that contain more than one tissue result in an intensity intermediate of the composing tissues. The PV effect is evident in the tissue boundaries. Figure 1.3 presents the partial volume effect of the CGM and WM at the boundary between them.

- Noise in the image can be due to electromagnetic noise in the body and small anomalies in the reception electronics (Weishaupt et al., 2008).

Automatic segmentation of neonatal brain MRI is considerably more challenging than adult brain segmentation. The neonatal brain MR images further exhibit domain-specific challenges:

- Neonatal MRI data have a lower contrast-to-noise ratio (CNR) due to the small size of the neonatal brain and shorter scanning periods (Prastawa et al., 2005).

- Increased occurence of motion artifacts compared to the adults. Motion artifacts appear as mis-aligned image slices and ghosting effects along the direction of phase-encoding (Rutherford, 2002) (an example is presented in Figure 1.4).

- CSF-WM PV. The neonatal MR images exhibit a reverse WM/GM contrast compared to the adult data. The WM, which is predominantly unmyelinated in the neonatal brain, appears brighter than GM

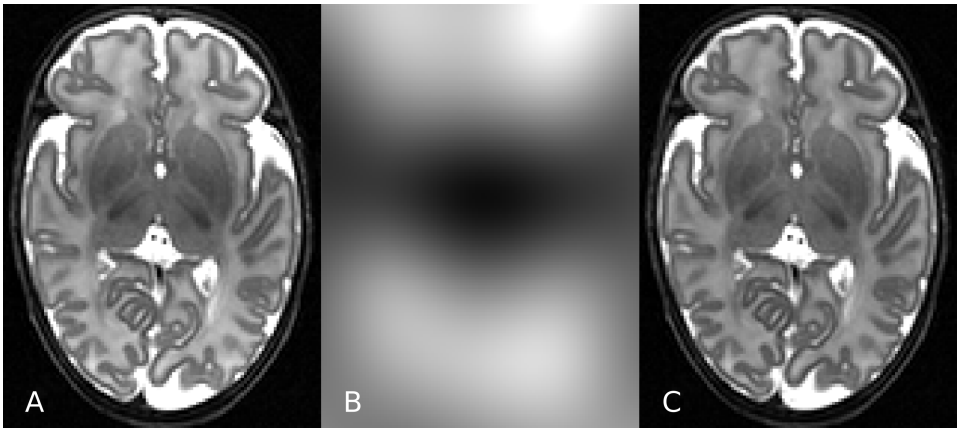

Figure 1.2: MRI intensity inhomogeneity exhibited on a neonatal T2 MR image acquired at 37 weeks PMA (A). Images (B) and (C) present the estimated bias field and bias-corrected image, respectively, using the N4 bias field correction (Tustison et al., 2010).

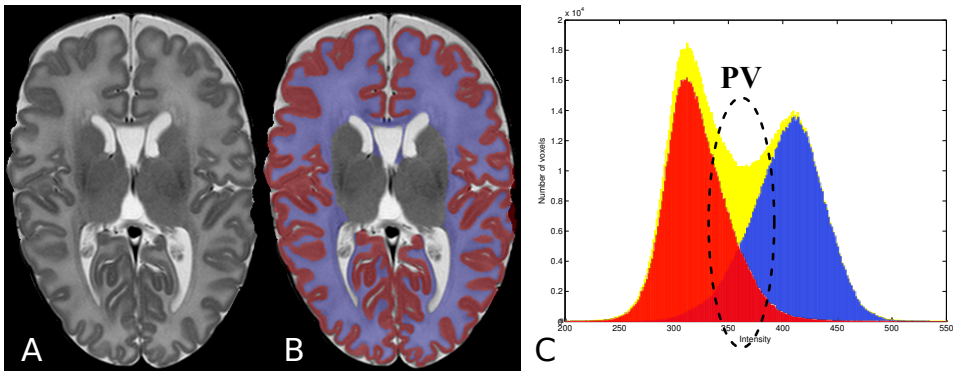

Figure 1.3: Partial volume effect in the CGM-WM interface. Image (A) presents a neonatal T2 MR image and image (B) the manually parcellated CGM (red) and WM (blue) (data obtained from http://neobrains12.isi.uu.nl). Image (C) displays the intensity histogram of the voxels belonging to the tissues (yellow color: combined CGM, WM histogram). The PV effect describes the intensity overlap (region of the histogram with dashed lines in image (C)) between the tissues at the boundary between them.

in the T2-weighted images while in the adult data GM has larger intensity values than WM. The mixing of CSF and GM in the CSF-CGM boundary leads to intensities similar to the intensity profile of the WM (see Figure 1.5). This PV effect leads to mislabelled PV voxels as WM in the CSF-CGM interface (Xue et al., 2007).

- Neonatal brains vary enormously in shape and appearance of structures due to the rapid brain development during this period (Figure 1.6 exhibits the changes occuring with increasing scan age). The neonatal cortex is rapidly folding and deep GM structures are formed. The precise registration of subjects of different scan ages is challenging due to these differences in anatomical characteristics.

- Lack of manually-labelled atlases across different scan ages. Manual delineation of detailed structures requires expert anatomical knowledge and is extremely time-consuming. Contrary to the atlas resources that exist for the adult brain, neonatal brain atlasing is very limited. The large variability in brain appearance in addition to the lack of atlases poses a challenge to segmentation techniques as the training data are limited.

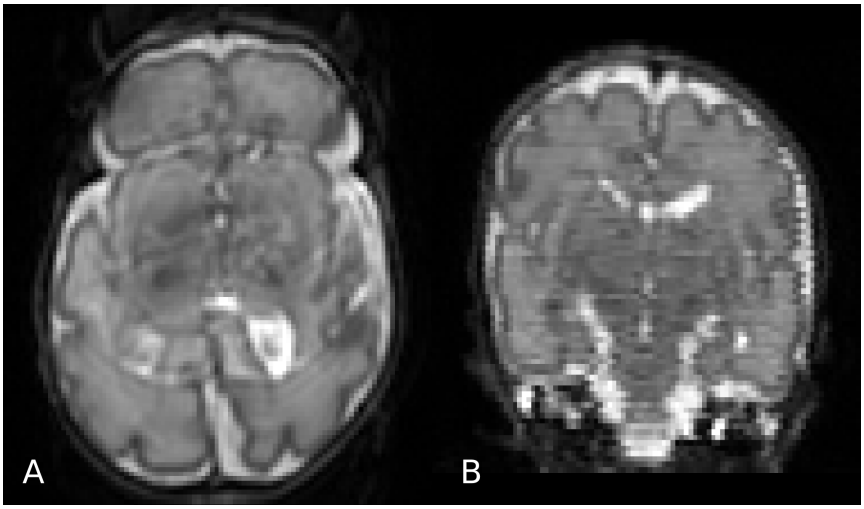

Figure 1.4: Motion artifacts on a neonatal T2 MR image acquired at 31 weeks PMA. Motion is evident with ghosting effects in the slices of the phase encoding direction (A) and mis-alignment of the slices along the direction (B).

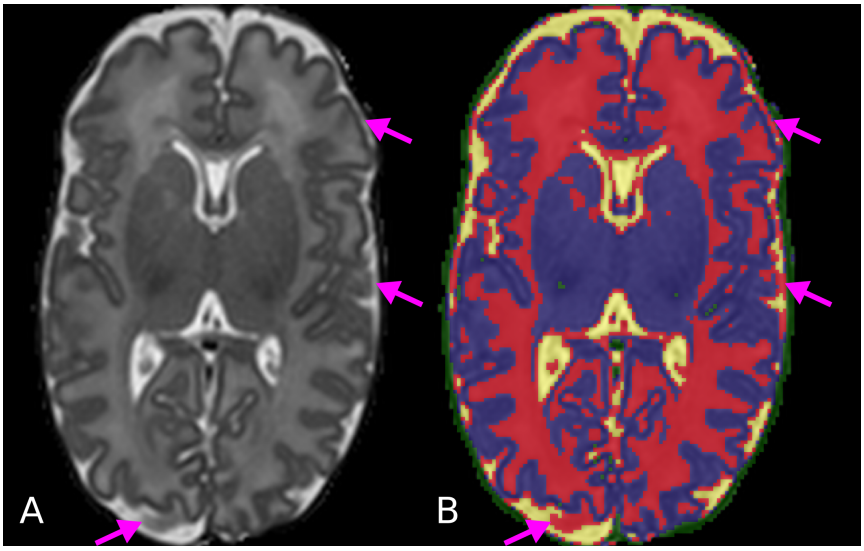

Figure 1.5: CSF-WM PV evident in the CSF-CGM boundary. A neonatal T2 MR image acquired at 36 weeks PMA (A) is split into tissues types (yellow:CSF, red:WM, blue:GM, green:background) with intensity clustering (B). The arrows point areas where the partial volume of CSF and CGM results in similar intensities to the WM.

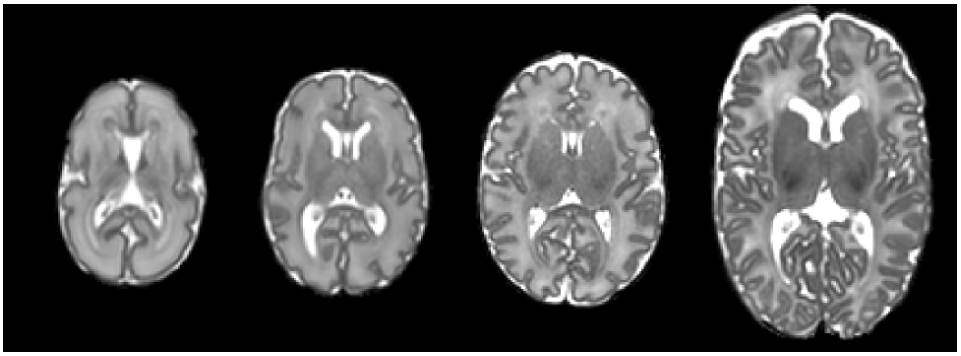

Figure 1.6: T2 MR images of the neonatal brain acquired at 28,32,36 and 44 weeks PMA (from left to right).

1.4 Thesis and contributions

This thesis aims to develop a robust and versatile segmentation framework for the regional parcellation of the developing neonatal brain. The main contributions are:

- An accurate tissue segmentation algorithm of the neonatal brain. The algorithm parcellates the neonatal brain into the different tissue types and the major subcortical structures, namely the brainstem, basal ganglia and thalami, cerebellum and ventricles. The presented framework is based on an Expectation-Maximization (EM) scheme (Van Leemput et al., 1999) for the segmentation of the brain. Spatial priors are propagated from a spatio-temporal atlas of the neonatal brain (Serag et al., 2012) and combined with subject-specific tissue priors. Since the developing brain encompasses large changes in shape and appearance, adaptivity is encouraged with a prior relaxation technique (Cardoso et al., 2011; Shiee et al., 2011; Cardoso et al., 2013). The spatial dependency of the labels in encoded with Markov Random Field (MRF) regularization (Van Leemput et al., 1999; Cardoso et al., 2011, 2013). The partial volume (PV) effect in the CSF-CGM interface is corrected as proposed in Xue et al. (2007). A recent neonatal brain segmentation challenge, NeoBrainS12 (2012), evaluated the performance of submitted tissue segmentation algorithms on a common reference. The proposed algorithm exhibited the most accurate results with respect to the manual reference.

- An accurate algorithm for the segmentation of the developing brain into 50 WM/CGM and subcortical structures (82 brain regions with the WM/CGM regions subdivided into WM and CGM). Previous approaches segment the brain into tissue types and major subcortical structures. This is the first detailed segmentation technique for the neonatal brain into a large number of regions. A detailed modelling of the brain allows the regional segmentation of the neonatal MRI from the early preterm period to term. "Superlabels", structures whose sub-regions share similar intensity characteristics, are introduced to prevent their sub-regions from competing in terms of intensity. In addition, a model averaging scheme tackles segmentation problems in

areas where there is not enough intensity information to differentiate between the structures. The CSF-WM PV correction is extended to multiple structures. The algorithm outperforms state-of-the-art techniques in the adult brain segmentation field in both accuracy and robustness in the challenging case of neonatal brains.

- A group-wise segmentation method that utilizes unlabelled images in addition to the labelled data to improve the segmentation performance. Similar patches across the unlabelled images in the database are encouraged to share the same labelling. This constraint is incorporated in the segmentation algorithm with a novel inter-image MRF energy that penalizes dissimilar label configurations across the unlabelled images. The proposed label propagation scheme provides a more accurate and consistent labelling than the individual segmentation of images.

- A method for the accurate delineation of the cortical ribbon. Improved delineation is achieved with a novel PV correction for the CGM-WM boundary and a cortical sulci correction method. Cortical sulci are hard to separate in the neonatal brain due to PV effects. The sulci are detected with the method presented in Han et al. (2004), and a sulci enhancement method is proposed based on the assumption that the cortical ribbon of a subject has similar thickness values regionally.

- Application of the segmentation algorithm for the parcellation of an extensive database of 420 neonatal brain MR images, from the early preterm period to term-equivalent age. Regional volumetric, surface and DTI measurements of the brain are derived from all the segmentations and used to investigate the brain growth and development in the neonatal period. The regional effect of prematurity is quantified in this population.

- A spatio-temporal structural atlas of 82 structures of the neonatal brain from 28 to 44 weeks scan age, publicly available for the neonatal research community[1]. The segmentations of the images in the database are propagated to the spatio-temporal atlas of Serag et al.

[1] http://brain-development.org/

(2012) and averaged with an age-weighted kernel to derive probabilistic spatial priors and average labelling of each structure at each scan age.

1.5 Thesis organisation

The thesis is organised as follows: The next chapter reviews the state-of-the-art segmentation techniques for the parcellation of brain MR images and methods applied in the neonatal segmentation field. Chapter 3 presents the contributions of this research for the segmentation of the neonatal brain MR images into tissue types. Chapter 4 introduces the automatic algorithm for the regional parcellation of the neonatal brain into a large number of brain structures. In Chapter 5 the algorithm is extended in order to incorporate unlabelled data, that are often readily available, to improve the segmentation accuracy and consistency. A novel method for the detailed delineation of the cortical ribbon and correction of the cortical sulci is presented in Chapter 6. Finally, Chapter 7 presents regional measurements of the brain in terms of volume, cortical surface and DTI measures and investigates their relations with clinical variables in an extensive database of neonatal brain MR images. The segmentations of the neonatal database are further used to build a spatio-temporal structural atlas of the brain for 82 structures that captures the brain development occuring from early preterm to term equivalent age. Chapter 8 concludes this research and describes future research directions.

Chapter 2

Background

Brain MR image segmentation is the process of partitioning an MR image of the brain into regions of interest according to intensity or anatomical characteristics. Different brain structures often share similar intensity characteristics. Therefore, a priori information is required to guide the segmentation on the expected anatomical location of the structures. This a priori information is provided with predefined rules or is encoded in the form of brain atlases.

The next section introduces the concept of brain atlases and presents existing neonatal atlases. Section 2.2 provides an overview of the main brain MR image segmentation approaches in the literature. Section 2.3 presents techniques that have been used for the segmentation of the neonatal brain into tissues. The NeoBrainS12 (2012) challenge evaluated different segmentation algorithms for the tissue parcellation. An overview of the submitted algorithms is presented in Section 2.4. Limited approaches have been proposed for the regional segmentation of the neonatal brain and are discussed in Section 2.5. Finally, the chapter presents techniques that have been used in the adult segmentation field that additionally utilize unlabelled data to aid the segmentation task.

2.1 Brain atlases

The term atlas is often used in an ambiguous fashion. In the context of this work we will use the term atlas to refer to a pair of images: One being the atlas template image (e.g. an MR image of the brain) and one being the atlas

label image. The atlas label image may contain either hard labels or soft labels (i.e. probabilities) indicating the presence of anatomical structures or tissues at every voxel. One of the first printed brain atlases in the literature was the Talairach atlas (Talairach et al., 1957; Talairach and Tournoux, 1988). The Talairach atlas provided a coordinate system to locate different brain regions based on a single subject. A drawback with a single-subject atlas is that it cannot accommodate the anatomical variability exhibited in the brain.

Probabilistic atlases were introduced to address this limitation based on multiple labelled subjects. Probabilistic atlases are composed of population-based templates and probability maps of brain structures. Population-based templates are mean MR images created by co-registering and averaging a large number of brain MR images, e.g. MNI-305 (Evans et al., 1993; Collins et al., 1994) was based on 305 images, ICBM152 (Mazziotta et al., 1995b,a) on 152 images. The corresponding segmentations of the images are averaged to construct the probability maps of the probabilistic atlases. An example probabilistic atlas is presented in Figure 2.1. The different probability maps can be further merged into a maximum probability map by assigning the structure with the highest probability to each voxel of the template. The atlases that are accompanied by the maximum probability map instead of multiple probability maps of brain structures are referred to as maximum probability atlases (e.g. Hammers et al. (2003)). Since the probabilistic and maximum probability atlases are typically based on a large number of subjects, manual delineation is extremely time-intensive. As an alternative, automatic segmentation of the subjects is often used for the labelling (e.g. Collins et al. (1995)), although some multi-subject atlases have been constructed based on manual delineations (e.g. Hammers et al. (2003); Shattuck et al. (2008)).

An alternative approach to account for the anatomical variability is the direct use of multiple single-subject atlases, where each one is manually segmented (such as the individual single-subject atlases of Hammers et al. (2003) or Shattuck et al. (2008)), instead of averaging them to a probabilistic atlas. These atlases can be used collectively as prior information of the anatomical location of each brain structure.

The availability of neonatal atlases is limited. Probabilistic atlases of tissues have been constructed based on automatically segmented data (Bhatia

et al., 2007; Shi et al., 2010; Kuklisova-Murgasova et al., 2011; Serag et al., 2012; Shi et al., 2014). The first manually delineated single-subject atlases of regional structures of the brain were introduced by Gousias et al. (2012). The following sections present the neonatal atlases utilized in this work.

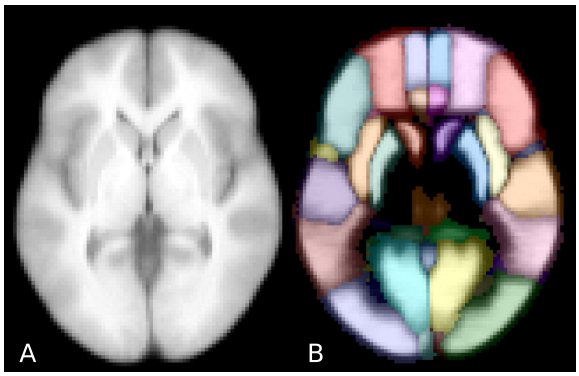

Figure 2.1: The Loni probabilistic brain atlas (LPBA40/SPM5) constructed by Shattuck et al. (2008) (image adapted from Shattuck et al. (2008)). (A) presents the population-based T1 template and (B) the probability maps of the different brain structures. The color at each voxel in (B) corresponds to the most probable structure, and the intensity indicates the probability of the respective structure.

2.1.1 Single-subject neonatal atlases

The structural atlases used in this work, ALBERTs (a label-based encephalic ROI template) (Gousias et al., 2012), were obtained by manual delination by an expert on MPRAGE MR brain images in 20 preterm infants. The atlases divide the brain into 50 regions, 32 WM/CGM regions and 18 subcortical regions. Table 2.1 presents the parcellated regions. The protocol followed for the delineation of the different structures is described in Gousias et al. (2012). The infants were born at a median (range) gestational age (GA) of 29^{+2} (26 - 38) and imaged at 40^{+6} (36^{+4} - 44^{+6}) weeks ($^{+days}$) post-menstrual age (PMA) at scan (GA plus number of weeks (days) after birth). MR imaging was performed on a Philips 3T system using an 8 channel head coil with the acquisition parameters in Table 2.2. The T2-weighted MRI of the atlases were co-registered to their corresponding T1 images (Gousias et al., 2012) to align the modalities in a common space. An example atlas can be seen in Figure 2.2.

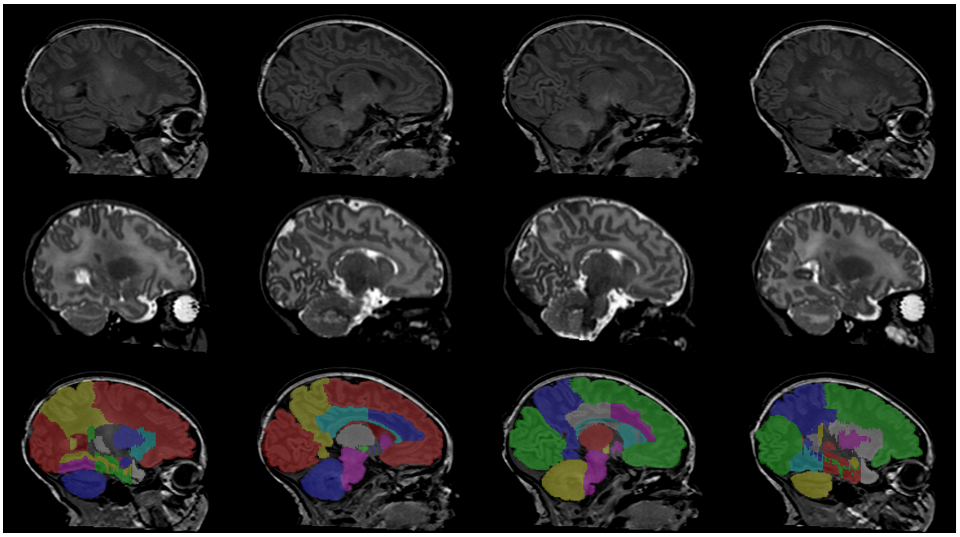

Figure 2.2: Different slices from one of the ALBERTs (Gousias et al., 2012) in the sagittal plane. The T1 image, T2 image and T1 image with the manually segmented labels overlaid are presented (from top to bottom row).

WM/CGM structures	
Frontal lobe (left/right)	
Parietal lobe (left/right)	
Occipital lobe (left/right)	**Subcortical Regions**
Anterior temporal lobe, medial part (left/right)	Hippocampus (left/right)
Anterior temporal lobe, lateral part (left/right)	Amygdala (left/right)
Gyri parahippocampalis et ambiens, anterior part (left/right)	Cerebellum (left/right)
Gyri parahippocampalis et ambiens, posterior part (left/right)	Brainstem
Superior temporal gyrus, middle part (left/right)	Caudate nucleus (left/right)
Superior temporal gyrus, posterior part (left/right)	Thalamus (left/right)
Medial and inferior temporal gyrus, anterior part (left/right)	Sub-thalamic nucleus (left/right)
Medial and inferior temporal gyrus, posterior part (left/right)	Lentiform nucleus (left/right)
Fusiform gyrus, anterior part (left/right)	Corpus callosum
Fusiform gyrus, posterior part (left/right)	Lateral ventricles (left/right)
Insula (left/right)	
Cingulate gyrus, anterior part (left/right)	
Cingulate gyrus, posterior part (left/right)	

Table 2.1: Manually segmented regions defined in the ALBERTs (Gousias et al., 2012).

2.1.2 Probabilistic neonatal atlas

Kuklisova-Murgasova et al. (2011) used non-parametric kernel regression to construct age-dependent anatomical templates for the ages at scan of 28 to 44 weeks. The template was based on 142 images that were affinely registered to a common space. Each age of the template is accompanied with tissue probability maps obtained by averaging tissue segmentations of

	T1	T2
TR (ms)	17	8670
TE (ms)	4.6	160
flip angle (∘)	13	90
FOV	210×210	220×220
matrix	256×256	256×256
thickness (mm)	0.8	1
resolution (mm×mm)	0.82×0.82	0.86×0.86

Table 2.2: MR Acquisition parameters of the ALBERTs (Gousias et al., 2012)

the subjects (automatically segmented). Serag et al. (2012) used a similar approach to develop a "high-definition" atlas, that was based on non-linear pairwise registration of 204 subjects, instead of affine used in Kuklisova-Murgasova et al. (2011). Similarly to Kuklisova-Murgasova et al. (2011), Serag et al. (2012) additionally constructed age-dependent tissue probability maps. In this work, the atlas of Serag et al. (2012) was selected due to the superior level of regional detail of the template. The spatio-temporal probabilistic atlas of (Serag et al., 2012) is presented in Figure 2.3.

2.2 Automatic brain MRI segmentation

The segmentation techniques applied to brain MRI can be categorized into:

- Supervised and unsupervised classification techniques
- Atlas-based approaches
- Deformable models

2.2.1 Supervised classification techniques

Classification techniques address the problem of dividing the data into distinct categories. In the MR image segmentation field the voxels of the image are divided/segmented into a number of labels. The classification methods are categorised into supervised and unsupervised techniques. Supervised classification techniques learn a model for the categorisation based on training data. Unsupervised methods do not require training data. Supervised methods further fall into two categories: parametric and non-parametric techniques.

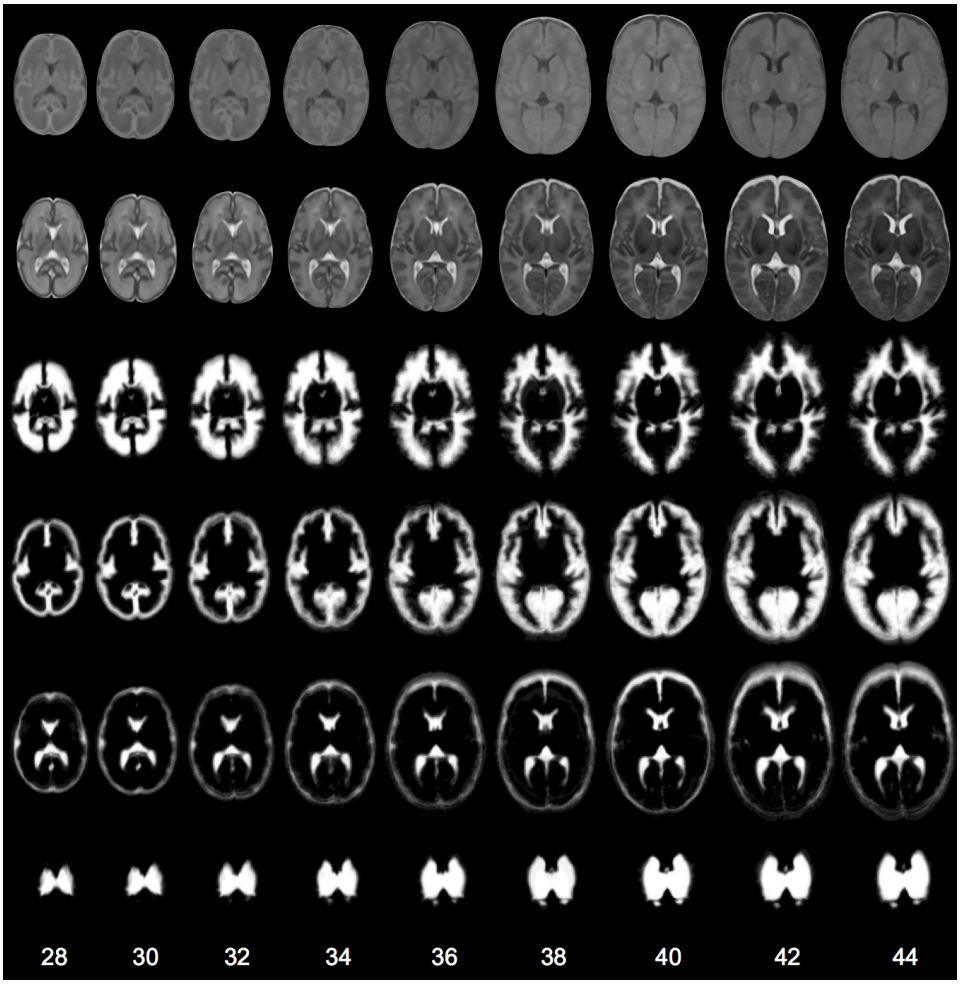

Figure 2.3: Different ages of the probabilistic neonatal atlas developed by Serag et al. (2012) (image from http://www.brain-development.org). The T1 image, T2 image and the probability maps of WM, GM, CSF and deep grey matter (DGM) are depicted (from top to bottom row)

Parametric techniques

Parametric models solve the segmentation problem by fitting a model (e.g. a statistical model) to the data. The (posterior) voxel probabilities are derived as a composition of a spatial prior term and an intensity term:

$$p_{ik} = \frac{P(y_i \mid z_i = e_k, \Phi_y)P(z_i = e_k)}{\sum_{j=1}^{K} P(y_i \mid z_i = e_j, \Phi_y)P(z_i = e_j)}$$
$$\propto P(y_i \mid z_i = e_k, \Phi_y)P(z_i = e_k) \tag{2.1}$$

The posterior probability p_{ik} of voxel i belonging to structure k is obtained based on the spatial prior distribution of k, $P(z_i = e_k)$, and the intensity likelihood of the structure, $P(y_i \mid z_i = e_k, \Phi_y)$ (where y_i the intensity of the voxel and Φ_y the model parameters). The product of the spatial prior and intensity likelihood of structure k is normalised by the products (of the spatial prior and intensity likelihood) of all the K structures. The spatial prior distribution essentially encodes the spatial location of each structure and is usually derived based on probabilistic or single-subject atlases. A typical choice of parametric distribution for the intensity model is the Gaussian mixture model (GMM), where the intensity likelihood of each brain structure ($P(y_i \mid z_i = e_k, \Phi_y)$) is modelled with a Gaussian distribution. The model is then normally fitted to the data with the use of Expectation-Maximization (EM), Iterated Conditional Modes (ICM) or graph cuts.

The EM-GMM algorithm for tissue segmentation was introduced by Wells et al. (1996). The EM algorithm alternates between a Expectation and a Maximization step until convergence (see Figure 2.4). The Expectation step estimates the posterior probability for each structure (according to the spatial priors and the intensity model). The parameters of the intensity model are then re-estimated at the Maximization step. Each voxel is finally labelled according to the structure with the highest posterior probability. Van Leemput et al. (1999) incorporated an atlas-based spatial prior term to constrain the spatial location of the structures. Van Leemput et al. (1999) further introduced a MRF regularization term to model the spatial interaction of structures and approximated the intensity inhomogeneity with polynomial basis functions. In their later work (Van Leemput et al., 2003), they further model the PV effect with a mixed distribution. Van Leemput et al. (2009) and Lötjönen et al. (2010) utilized the algorithm for the purpose of structural segmentation. Shiee et al. (2011) proposed a prior relaxation that adapts the spatial priors according to the posteriors in order to accomodate

mis-registrations and pathologies. Fischl et al. (2002) developed FreeSurfer (http://freesurfer.net), a segmentation software extensively used in the literature. A novelty of the work is the introduction of a non-stationary MRF learned from the manually labelled atlases. Ashburner and Friston (2005) proposed a model that combines the tissue segmentation, bias correction and non-linear registration and is optimised with ICM. They proposed the use of multiple Gaussians per structure to account for the PV effect. Their model has been implemented as part of the Statistical Parametric Mapping (SPM) software (http://www.fil.ion.ucl.ac.uk/spm). Song et al. (2006) and van der Lijn et al. (2008) introduced the use of graph cuts to fit the parametric model.

Non-parametric techniques

Non-parametric methods do not assume a parameterization of the data in the target image. A classifier is directly trained on the atlases to learn the label assignment based on image-derived features, such as the intensity of single or multiple modalities and spatial features. Estimated labels from other segmentation techniques can be further incorporated as features to learn and correct for the segmentation bias of the techniques (Wang et al., 2010). Afterwards, the classifier labels the voxels in the subject image on the basis of the learned model. Example non-parametric techniques in the literature have employed k-NN (Srhoj-Egekher et al., 2012; Chiţă et al., 2013), naive Bayes (Srhoj-Egekher et al., 2012), decision forests (Criminisi et al., 2012; Pereira et al., 2013) and Adaboost classifiers (Wang et al., 2010).

2.2.2 Unsupervised classification techniques

The unsupervised techniques classify the data according to some measure of inherent similarity and do not require training data. Unsupervised techniques in the segmentation domain incorporate methods that exploit image-derived features to split the brain into intensity-distinct regions. Example techniques that can be classified in this category are: thresholding (Al-Attas and El-Zaart, 2007), region growing (Adams and Bischof, 1994; Justice and Stokely, 1996), morphological operations (Mangin et al., 1995), watershed segmentation (Sijbers et al., 1997), edge detection (Yu-qian et al., 2005) and

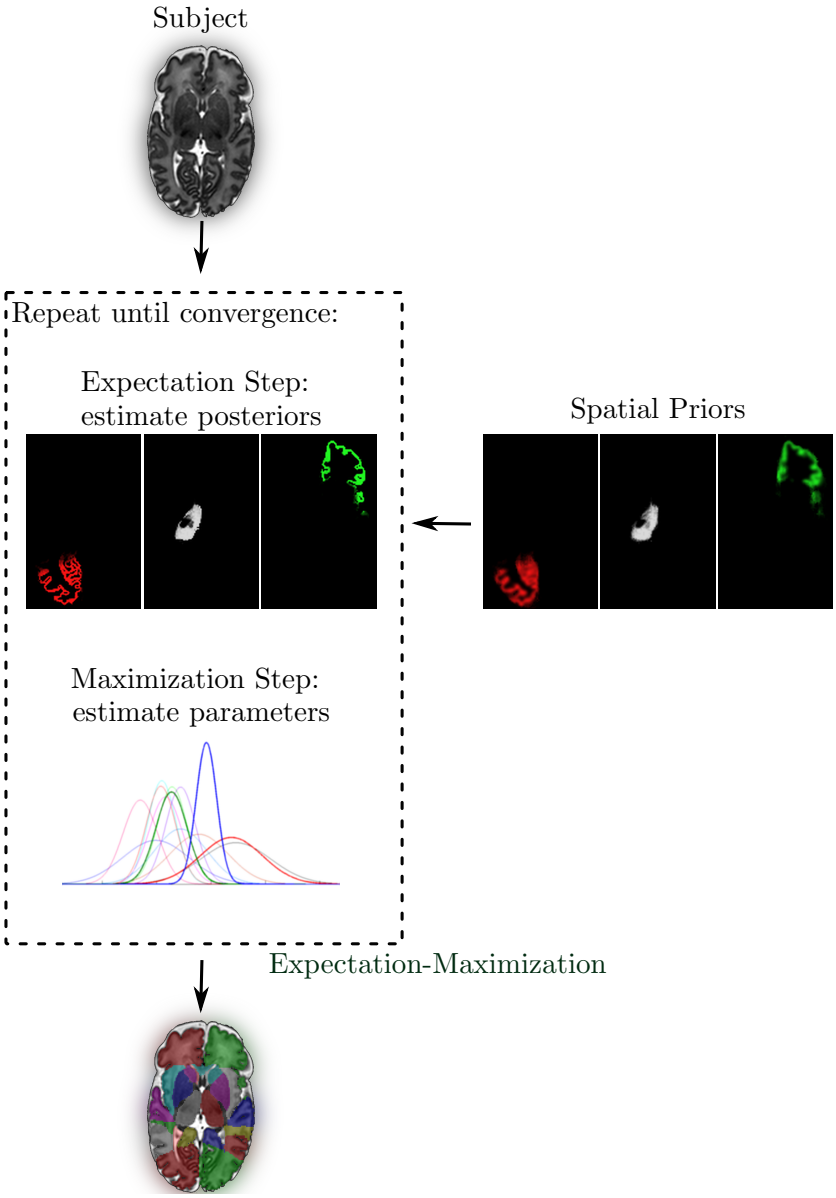

Figure 2.4: Expectation-Maximization. The Expectation step estimates the posteriors based on the spatial priors and the intensity model. The Maximization step re-estimates the parameters of the intensity model. The Expectation and Maximization step are computed iteratively until convergence. The resulting posteriors are then used to derive the segmentation of the brain.

clustering (Pham and Prince, 1999).

Thresholding techniques use a pre-defined or automatically defined thresh-

old to split the image into distinct regions. Region growing methods start by a seed voxel or set of voxels in the image and iteratively add adjacent voxels if they satisfy a certain criterion. Morphological operations are used to isolate or fill an image region and are composed of simple erosion and dilation steps. Watershed segmentation is a method for splitting an image into "basins", low intensity set of points that share a boundary with other "basins". Connected component labelling can be used to identify different components of the image according to a specified connectivity. Edge detection methods split the image into regions according to edges where the intensity signal has discontinuities. Further details on the aforementioned techniques can be found in textbooks on image processing, e.g. Pitas (2000); Pratt (2007); Bankman (2008).

Clustering techniques aim to group data points, in this case voxels, into a number of classes such that the points belonging to each class are similar to each other and dissimilar to points of other classes. Clustering algorithms can be classified into hard and soft or fuzzy clustering according to the assignment of points to classes. Hard clustering assigns each point to a single class, while soft clustering assigns the points to multiple classes with a membership level that reflects the probability of each class. k-means (Macqueen, 1967) and fuzzy c-means (FCM) (Bezdek, 1981) are popular algorithms for hard and soft clustering respectively, that assign the points to a predefined k number of classes. k-means and FCM operate in a similar way: Initially, the points are randomly assigned to a class. The algorithm then iteratively computes the centroid of each cluster and estimates the membership (soft or hard) of the points to the classes according to the distance to the centroids. k-means and FCM minimize the intra-cluster variance but they converge to a local minimum that depends on the initial random assignment. A simple stability solution is to re-run the algorithm multiple times and select the solution with the best fit to the data.

Unsupervised techniques are highly susceptible to noise, intensity inhomogeneity and partial volume averaging. They are usually employed in the literature to refine the segmentation, e.g. to exclude mislabelled small WM components with connected component labelling (Xue et al., 2007; Weisenfeld and Warfield, 2009; Wang et al., 2011). Clustering techniques have been used in the literature for tissue segmentation. For example, k-means has been used to initialize the intensity distributions of the data in

an Expectation-Maximization framework (Xue et al., 2007), a supervised classification technique. Pham and Prince (Pham and Prince, 1999; Pham, 2002) proposed an FCM model for tissue segmentation that estimates the INU bias field and penalizes assignment of different class to neighboring voxels to account for noise. A combination of unsupervised methods has been also used in limited studies (Tang et al., 2000; Gui et al., 2012b).

2.2.3 Atlas-based approaches

Atlas-based approaches are methods that segment the image based on the labels of aligned atlases. The images of the atlases are initially registered to the target image. Image registration is the process of spatially aligning a pair of images into the same coordinate system. The registration estimates a transformation, a mapping, between the images that maximises the similarity between the source and the target image. The registration can be global or local and estimates a linear or non-linear transformation, respectively, of the source to the target image. The global registration accounts for rigid or affine motion. The local registration deforms the source image locally in order to align it to the target image, e.g. by moving a set of control points. By registering an atlas MR image to the subject image, the estimated transformation can be used to transform/warp the atlas image and labels to the subject space. The propagated labels can then be considered as an estimate of the spatial location of the structures in the subject space.

Early atlas-based approaches segmented the target image by propagating the labels of a single atlas (Christensen et al., 1994; Collins et al., 1995). However, by using a single atlas, the segmentation is limited to the accurate registration of a single pair of brains. This is a non-trivial problem due to differences in the anatomy of the subjects. The mapping between different brains will fail in areas where the brain appearance is different in the pair of images. To resolve this issue and increase the robustness of the segmentation, Rohlfing et al. (2004), proposed the multi-atlas segmentation. Multiple atlases are registered to the target image and the transformed labels are combined/fused to provide the segmentation result (Rohlfing et al., 2004; Heckemann et al., 2006) (see Figure 2.5).

Label fusion techniques are amongst the most accurate techniques for

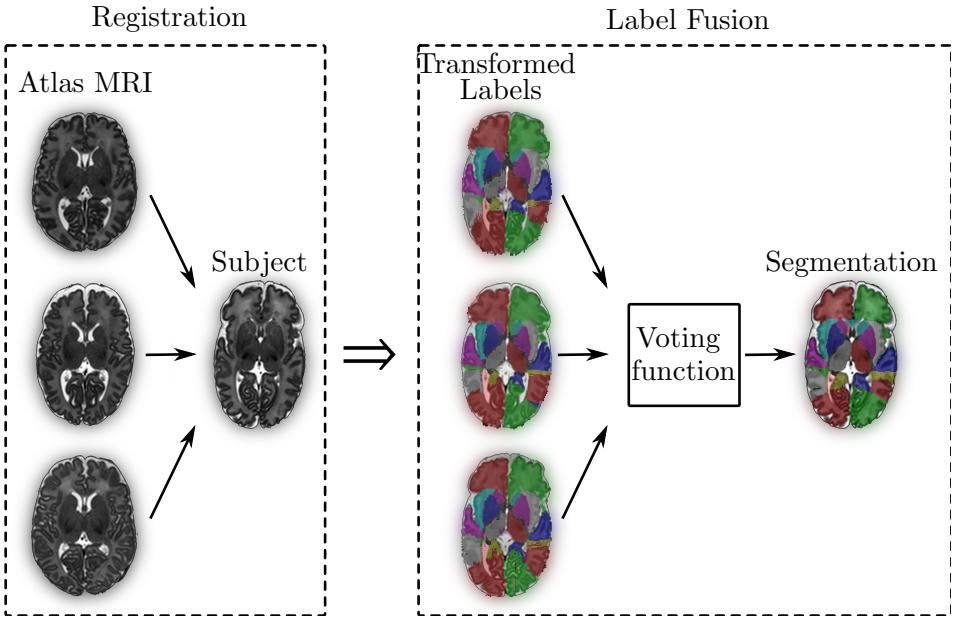

Figure 2.5: Label fusion. The atlases' MR images are registered to the subject image and their labels are propagated to the target. The segmentation is obtained by fusing the propagated labels according to a voting function on the atlases.

brain segmentation. Every atlas provides a vote to the estimated segmentation:

$$p_{ik} = \frac{\sum_{a=1}^{A} w_{ia}\gamma_{ik}^{a}}{\sum_{j=1}^{K}\sum_{a=1}^{A} w_{ia}\gamma_{ij}^{a}}$$

where $a = \{1, .., A\}$ denotes the atlases and γ_{ik}^{a} is the vote for structure k produced by atlas a calculated as

$$\gamma_{ik}^{a} = \begin{cases} 1, & \text{if voxel } i \text{ belongs to structure } k \text{ in atlas } a \\ 0, & \text{else} \end{cases}$$

Majority voting label fusion (Heckemann et al., 2006) assumes an equal weight for the atlases and labels each voxel of the image according to the structure that is favoured by most of the atlases. More sophisticated voting schemes weight the vote of each atlas according to the similarity of the atlas MR image to the unseen image, either globally or locally. Artaechevarria et al. (2009) provide a comparison of different voting schemes in label fusion, where locally-weighting schemes are shown to result in better accuracy. The

accuracy of label fusion techniques increases with an increase in the number of manually labelled atlases provided (Heckemann et al., 2006; Aljabar et al., 2009). However, atlas selection (Aljabar et al., 2009) has been also used to discard atlases that degrade the result, e.g. due to registration errors.

Patch-based techniques (Coupé et al., 2011; Rousseau et al., 2011) provide a non-local alternative to the label fusion techniques. In patch-based methods the most similar patches in the atlases are located for each voxel of the image at the neighborhood of the voxel. After a patch preselection, e.g. using the structural similarity measure (SSIM) (Wang et al., 2004), the labels of the patches are fused with a weight defined by the similarity of the atlas patch to the image patch around the voxel. The weighting can be further refined in order to reduce the joint atlas errors between different atlases as shown in Wang et al. (2012a); Wang and Yushkevich (2013).

Another family of atlas-based techniques, STAPLE (Simultaneous Truth and Performance Level Estimation), was proposed by Warfield et al. (2004). STAPLE computes an estimate of the true segmentation and weights the atlases according to their performance to the estimated segmentation. The procedure is repeated until convergence in an Expectation-Maximization framework.

Atlas-based techniques are limited by the anatomical variability exhibited in the available atlases as they do not explicitly model the intensity of the unseen image. This is problematic in the presence of pathological cases or large changes in anatomy, such as the changes occuring in the anatomy of the developing brain.

2.2.4 Deformable models

Deformable models are physics-based models that segment an object by deforming a closed surface. The surface is iteratively expanded or contracted under the influence of an external and an internal energy. The external energy is usually an image-driven data fitting term that moves the surface to the desired object boundary. The internal energy ensures the smoothness of the propagating surface and constrains the evolution driven by the external energy. The internal energy may further incorporate prior knowledge about the object of interest. Deformable models are classified into two categories: the parametric and geometric models.

Parametric models (Kass et al., 1988; Terzopoulos and Fleischer, 1988) provide an explicit parameterization of the surface. The main advantage of this family of deformable models is their fast convergence to the optimal solution. A limitation is that it is difficult to incorporate topological adaptation, such as splitting or merging parts of the surface, in the surface propagation. Furthermore, these models are limited to the segmentation of a single object - the desired ROI and the background. An example method using parametetric deformable models is the widely used algorithm for brain extraction proposed by Smith (2002) (the algorithm is implemented as part of the FSL software, http://fsl.fmrib.ox.ac.uk). It evolves a tesselated surface with an intensity-driven external force until it reaches the low intensity area of CSF or skull. The internal force is implemented as a constraint in the curvature of the vertices and enforces smoothness of the propagating surface.

Geometric models (Osher and Sethian, 1988; Malladi et al., 1995), also referred to as level set deformable models, represent the surface implicitly as the zero level-set of a higher-dimensional function. A level-set is essentially a set of points that have the same function value. The surface in these models is evolved implicitly by updating the level-set function. The surface parameterization is computed after the convergence of the model and therefore allows topological adaptivity. An example geometric model has been used for cortical surface reconstruction by Han et al. (2004). In this work, the level-set function is updated based on an external force described by tissue class probabilities and an internal force computed based on the surface curvature. Multi-object segmentation in the level-set framework can be implemented with coupling-surfaces regularizers, refered to as coupled level-sets. The regularization is introduced with an additional energy that retains the distance between objects within a predefined range. Zeng et al. (1999) introduced the coupling-surfaces regularizer to constrain the distance between the exterior cortical surface (CSF-GM boundary) and the interior cortical surface (GM-WM boundary).

Prior information in the deformable models can be incorporated with statistical models of shape or intensity. Cootes et al. proposed the Active Shape Models (ASM) (Cootes et al., 1995) and the Active Appearance Models (AAM) (Cootes et al., 1998) to constrain the shape/appearance of the surface according to the variability exhibited in training data. A large

number of variations to these models have been proposed in the literature (e.g. Van Ginneken et al. (2002); Jiao et al. (2003); Matthews and Baker (2004); Donner et al. (2006); Langs et al. (2006)). An example application of these models for the brain segmentation into different structures is the method of Patenaude et al. (2011) (the algorithm is implemented as part of the FSL software, http://fsl.fmrib.ox.ac.uk). The segmentation problem is formulated within a Bayesian framework that allows relationships between shape and intensity of different structures to be integrated in the model.

2.3 Neonatal brain MRI tissue segmentation

Studies in the neonatal segmentation field are mostly focused to tissue segmentation of the brain MR images (CSF, GM, un-myelinated WM, myelinated WM, subcortical GM, brainstem, cerebellum). An example parcellation into different tissue types is presented in Figure 2.6. This section presents methods used in the literature for the tissue segmentation of the neonatal brain.

2.3.1 Supervised classification techniques

Parametric techniques

Prastawa et al. (2005) developed a method for tissue segmentation based on the Expectation-Maximization algorithm of Van Leemput et al. (1999). Novelties of the work include the differentiation between the myelinated and unmyelinated WM class according to a graph based clustering technique (minimum spanning tree) and removal of outliers with the use of the Minimum Covariance Determinant (MCD) estimator. Spatial tissue priors of CSF,GM and WM were propagated with affine warping of a probabilistic atlas. Sample locations of high atlas probability were used to estimate the initial intensity estimates with the MCD estimator. The segmentation was carried out with the EM algorithm proposed in Van Leemput et al. (1999) with inhomogeneity correction. The segmentation was consequently refined with the use of non-parametric kernel density estimates. A drawback of the technique is that the atlas was created by averaging semi-automatic segmentations from three subjects and therefore can not capture the large differences undergoing in the neonatal population.

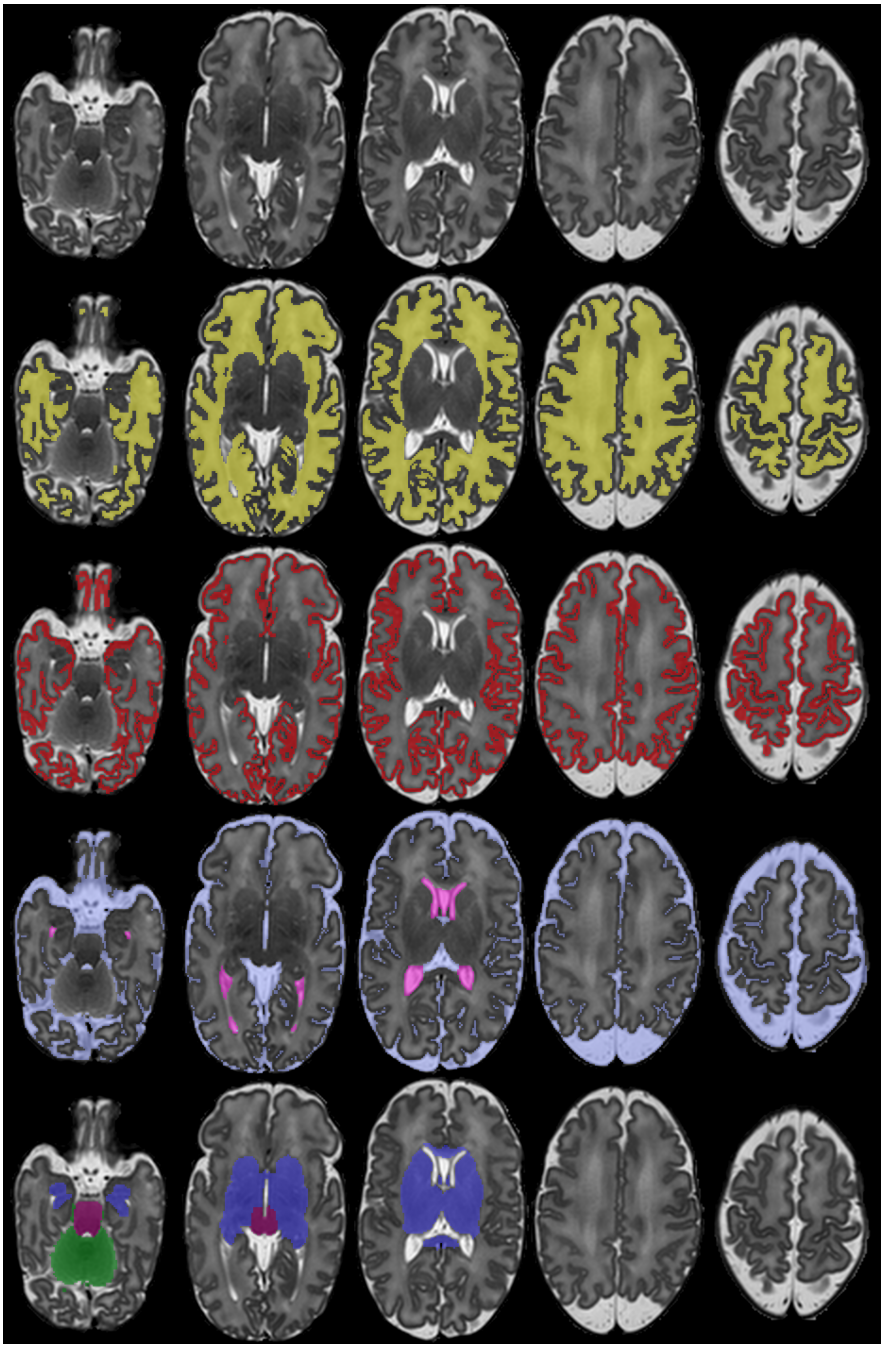

Figure 2.6: Example tissue segmentation of a neonatal MRI acquired at 36 weeks PMA with the method proposed in this thesis (second row: WM label, third row: GM label, fourth row: CSF labels, fifth row: subcortical GM labels).

Xue et al. (2007) implemented an EM scheme with a MRF regularization term similar to Van Leemput et al. (1999) to enforce a smooth labelling. In their work, subject-specific tissue priors were estimated with k-means clustering, eliminating the use of an atlas for the spatial priors. Further, Xue et al. addressed the CSF-WM partial volume problem with a knowledge-based method implemented with connected component labelling. The spatial priors of misclassified partial volume voxels were adjusted to correct for the CSF-WM PV effect. Instead of using global statistics in the intensity distributions, the authors introduce a local splitting of the brain into different regions and estimate the Gaussian parameters in a more localised fashion.

Song et al. (2007) proposed a neonatal brain MRI segmentation technique based on graph-cuts, which were used to minimise a Gibbs energy composed of four terms: likelihood, intensity-based prior, probabilistic atlas prior and MRF. The likelihood term is estimated with the use of non-parametric Parzen-window estimators and the intensity-based prior is learned with fuzzy nonlinear SVMs. They further adopted an extensive preprocessing of the images with edge-preserving anisotropic smoothing, inhomogeneity correction and adaptive histogram equalization. Song et al. only segmented the GM,WM having excluded the skull and CSF with manual delineation.

Cardoso et al. (2011, 2013) proposed an EM-MRF scheme that adapts the atlas priors similar to Shiee et al. (2011). The atlas priors provided by atlases were modelled as samples drawn from a Dirichlet distribution (in essence a hyperprior) and were adapted according to the posteriors of each EM iteration. The CSF-WM PV was modelled as mixed distributions among the different tissues. Moreover, they deviated from the classic Gaussian modelling by introducing a semi-conjugate Gaussian prior over the tissue Gaussian means initialised by sampling manually selected patches. Cardoso et al. in their work avoid the dependence on the atlas alignment with the prior relaxation scheme. However, when segmenting structures with very similar intensity profiles it is unclear how the relaxation scheme will adapt the propagated priors, for example in deep grey matter structures.

Shi et al. (2010) presented a framework for neonatal tissue segmentation taking advantage of a subject-specific probabilistic atlas that is generated from longitudinal data acquired at a later time. The atlas is built with AFCM, a fuzzy clustering technique. Afterwards, the atlas is used in a joint registration-segmentation framework that performs atlas registration, bias

field correction, and atlas-based tissue segmentation iteratively in a modified EM algorithm. In their later work (Shi et al., 2011), the segmentations of neonatal brains computed from Shi et al. (2010) were used to build a neonatal atlas of the brain. Instead of averaging the images for the atlas construction, Shi et al. construct a subject specific atlas by weighting the images according to their similarity to the underlying subject. The similarity is measured across a cortical GM confidence map of the subject generated with the use of a Hessian filter. The constructed subject-specific atlas is used for the segmentation of the images in a joint registration-segmentation fashion as in Shi et al. (2010).

Non-parametric techniques

Anbeek et al. (2008) proposed a tissue segmentation method based on k-NN classification. They construct a multidimensional feature space based on intensity and spatial features of training images. The segmentation is estimated from the affinity of the k closest neighbors in the multidimensional space for each voxel of the unseen image.

Chiţă et al. (2013) presented a supervised classification technique for the neonatal image segmentation. Voxel classification was performed in three stages: The feature space of the algorithm was composed of spatial, intensity features and the current probabilistic output. Intensity features were obtained from both T1 and T2 images. The first and second stage perform independent 2-class k-NN classification for each tissue separately and the third stage uses a 4-class k-NN for all the classes. The best features of each stage were selected using a forward feature selection scheme.

2.3.2 Unsupervised classification techniques

Gui et al. (2012b) derived a segmentation method that is based on prior knowledge about brain morphology and avoids the use of any atlases. In their work, Gui et al. use both the T1 and T2 modalities and segment the brain tissues with application of the watershed segmentation, region growing, active contour segmentation and morphological operations.

2.3.3 Atlas-based techniques

Weisenfeld and Warfield (2009) used an iterative sample editing process for segmentation of the brain tissues. Initially, the labels of the atlases were fused into the subject space to result in an initial estimate of the segmentation. Afterwards, they iteratively refine each atlas' samples with the use of the segmentation, and reestimate the segmentation with the STAPLE algorithm. Weisenfeld et al. further perform CSF-WM PV correction with a method similar to Xue et al. (2007), model spatial homogeneity with a MRF term and correct for noise with anisotropic diffusion. The tissue segmentation of Weisenfeld et al. heavily depends on the initial alignment of atlases, which is a non-trivial problem due to the large changes with increasing scan age of the neonates.

2.3.4 Deformable models

Wang et al. (2011) proposed a segmentation algorithm based on coupled level sets with a local intensity information term, atlas tissue priors and a cortical thickness constraint. Local intensity information was modelled with Gaussian distributions with spatially varying mean and variance. The cortical thickness constraint is used to retain the CSF/GM and GM/WM surface distance within a predefined extent. CSF-WM PV correction is incorporated in the model with a method similar to Xue et al. (2007). They later (Wang et al., 2012b) extended their method in a multi-modal and longitudinal framework. The segmentation utilized a multi-modality data fitting term using both T1, T2 and FA images. Additionally, images obtained at different timepoints were incorporated in a longitudinally guided level-set segmentation. The different timepoints were iteratively co-registered with a 4D registration method and segmented in a longitudinal fashion with constraints from neighboring timepoints.

2.4 NeoBrainS12 challenge

A recent neonatal brain segmentation challenge, NeoBrainS12 (2012), was held and aimed to evaluate the performance of submitted tissue segmentation algorithms on a common reference. This section presents the automatic techniques that participated in the challenge. Example parcellations with

different techniques submitted to the challenge are presented in Figure 2.7.

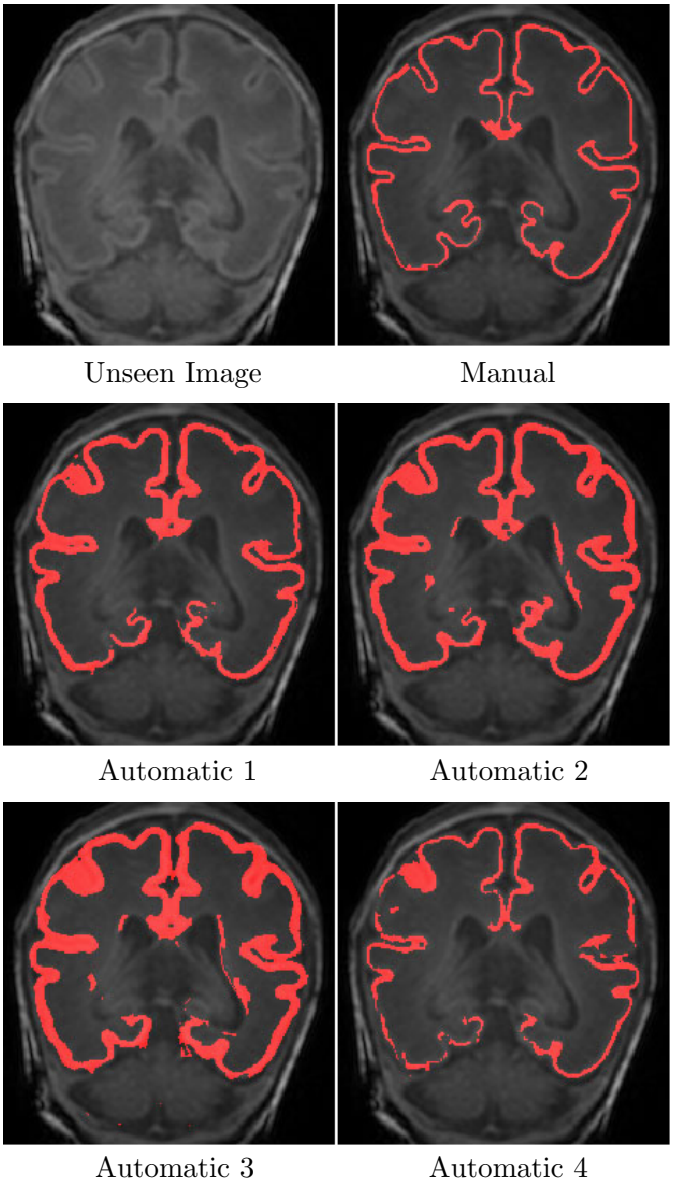

Figure 2.7: Example GM segmentations from the NeoBrainS12 (2012) challenge of a neonatal MRI acquired at 30 weeks PMA (data from http://neobrains12.isi.uu.nl). The T2 image and the corresponding manual segmentation can be observed in the top row. The second and third row display the GM segmentation produced by four different automatic techniques.

2.4.1 Supervised classification techniques

Parametric techniques

In Makropoulos et al. (2012b) we proposed a state-of-the-art tissue segmentation method for the neonatal brain. The algorithm was based on an EM-MRF scheme with prior adaptation as in Cardoso et al. (2011, 2013). Partial volume correction for the CSF-WM intensity overlap was implemented as in Xue et al. (2007). A second partial volume correction step was added for the correction of the WM-GM boundary, which enabled a more detailed delineation of the cortical ribbon. Structure priors were obtained as a combination of atlas priors and subject-specific priors derived from intensity clustering with k-means. Chapter 3 provides the details of the method.

Wang et al. (2012c) participated with a method based on the Statistical Parametric Mapping (SPM) Segment software (www.fil.ion.ucl.ac.uk/spm). The SPM segmentation algorithm iteratively refines the tissue segmentation, bias correction and non-linear registration of a probabilistic atlas. The tissue segmentation method was based on an EM scheme and the joint cost function was optimised with ICM. After convergence, partial volume correction was performed with the use of connected component labelling.

Melbourne et al. (2012) used the technique developed by Cardoso et al. (2011, 2013) to segment the neonatal challenge data. The algorithm was extended to perform outlier rejection of intensity clusters that have a large Mahalanobis distance from the estimated model in order to reduce their influence in the parameter estimation. The prior adaptation was excluded from the original model.

Wu and Avants (2012) presented a technique based on the Atropos tool (Avants et al., 2011). An EM-MRF technique was used with ICM parameter optimisation. Both T1 and T2 images were used in a multivariate data-term. Clusters of misclassified voxels were corrected based on the atlas-based prior probabilities.

Non-parametric techniques

Srhoj-Egekher et al. (2012) proposed a method based on label fusion and supervised classification. The priors of an initial label fusion step are com-

bined with the probabilities from an independent 2-class k-NN classification for each tissue. The k-NN classification is performed on intensity features derived from both T1 and T2 modalities. A final step is using a naive Bayes classifier in a reduced dimensional space obtained with Principal Component Analysis to classify voxels assigned to more than one tissue classes.

Anbeek et al. and Chiţă et al. applied the segmentation techniques described in Anbeek et al. (2008) and Chiţă et al. (2013) respectively in the neonatal challenge (described in Section 2.3.1).

2.4.2 Unsupervised classification techniques

Gui et al. used the technique proposed in Gui et al. (2012b) for the segmentation of the challenge data (described in Section 2.3.1).

2.5 Neonatal brain MRI structural segmentation

Delineation of more localised structures of the brain is limited. Due to the lack of manually segmented atlases, previous automatic methods (Peterson et al., 2003; Mewes et al., 2006; Gilmore et al., 2007; Thompson et al., 2007) did not segment deep grey matter structures and parcellated CGM and WM regions according to arbitrary linear parcellations which did not reflect regional anatomy. The first regional atlases of the brain were manually delineated by Gousias et al. (2012) that define 50 brain regions in 20 term-equivalent neonatal brains. In Makropoulos et al. (2012a) we presented the first study to automatically segment the neonatal brain from early preterm to term-equivalent age, into 50 structures with the use of these atlases. The method was extended and presented in detail in Makropoulos et al. (2014) (an example parcellation is presented in Figure 2.8). We discuss the proposed structural segmentation method in Chapter 4. Gousias et al. (2013) investigated the segmentation of term-equivalent brains based on label fusion of the atlases or alignment of a maximum probability atlas.

2.6 Label propagation for brain MRI segmentation

Previous studies in the literature have demonstrated the increase in segmentation accuracy with the introduction of more labelled datasets (Heckemann

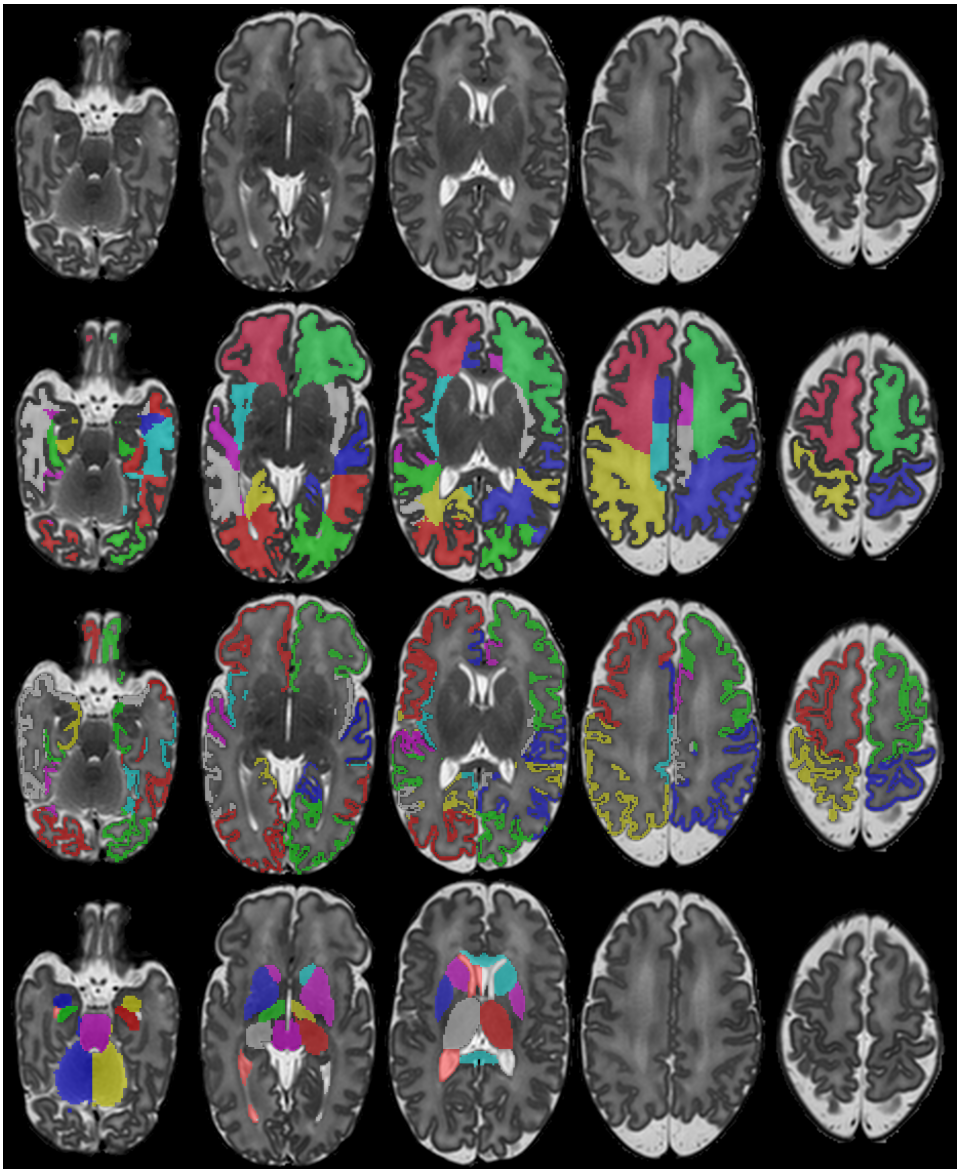

Figure 2.8: Example structural segmentation of a neonatal MRI acquired at 36 weeks PMA with the method proposed in this thesis (second row: WM labels, third row: CGM labels, fourth row: subcortical GM labels and ventricles).

et al., 2006; Aljabar et al., 2009). Since manual segmentation of magnetic resonance (MR) images is an extremely time consuming and expensive process, the number of atlases available for a specific application may be limited. However, large numbers of unlabeled images are often available at a low cost. There is an increasing interest in the segmentation field for the potential use of unlabelled images to improve the automatic methods in terms of consistency and accuracy.

Recent studies focus on ways to extract additional information from the unlabeled images to complement the prior information (e.g. in form of atlases). Wolz et al. (2010) proposed LEAP, a stepwise propagation approach. The manually labeled atlases are propagated to unlabeled images which are then in turn used as atlases for the segmentation of other images in the dataset. The atlases are initially propagated to N unlabeled images that are the most similar to the atlases. Afterwards, the segmented images are added to the pool of labelled images as atlases. In the next iteration the new atlases (the manually labelled atlases and the segmented images) are used in turn for the segmentation of the remaining N most similar images in the dataset. The closest M atlases to the subject to be labelled are selected to drive the segmentation. The algorithm stops once all the unlabelled images in the database have been segmented. An illustration of the label propagation in Wolz et al. (2010) is presented in Figure 2.9. In Wolz et al. (2010) the similarity of images for the label propagation is estimated according to the distance of the images in a manifold. The images are transformed to a common space defined by a template. The manifold is then built using Laplacian eigenmaps and Normalised Mutual Information (NMI) (Studholme et al., 1999) of images in a mask around the region of the interest (Wolz et al., 2010). The segmentation of the images is refined with graph-cuts.

Similarly, Jia et al. (2012) presented a technique for group-wise registration and segmentation, where the segmented images are iteratively updated based on the labels of the remaining images in the database. A tree-based group-wise registration is proposed for the registration of an image to the database. A tree of atlases is built where the nodes represent the atlases and the edges the deformation required to align the pair of images at the edges. A new (target) image is linked to the tree by locating the most similar image in the tree and registering the target image to it. The deformation

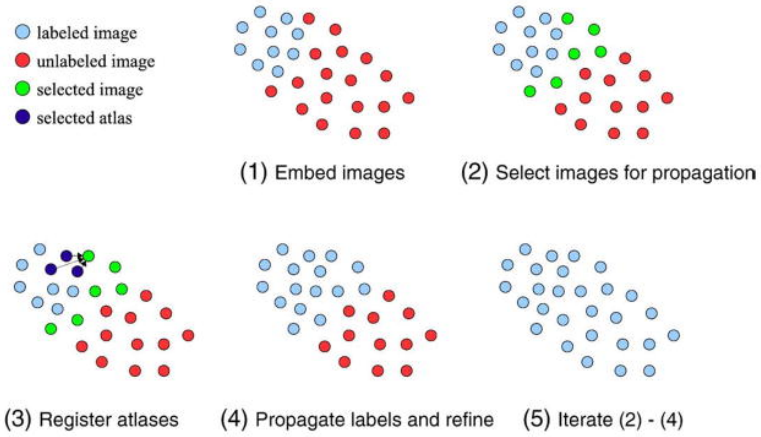

Figure 2.9: Label propagation in LEAP (Wolz et al., 2010). The images are initially embedded in the manifold (1). The N most similar images to the atlases are selected for the label propagation (2). Each image is segmented according to the M most similar atlases and is included in the database as an atlas (3-4). The process is repeated until all the images have been labelled (5). Image from Wolz et al. (2010).

of the target image to any other image in the tree can be then obtained by following the path in the tree that connects the two images and concatenating the deformations along the path. The main idea behind the proposed registration technique is that the registration between images with large shape differences can be difficult. By locating the most similar image in the tree, the target image can be reliably registered to the database. Having estimated the deformation of the target image to all the atlases, the image is segmented with locally-weighted label fusion. All the unlabelled images in the database are initally segmented in this manner. Afterwards, the segmented images are considered as atlases and all the images are re-segmented with the use of all the atlases (manually and automatically segmented). The process is repeated until convergence.

Bhatia et al. (2007) proposed a method for group-wise segmentation and registration to improve both the alignment and the segmentation of images in their average space. The segmentation is performed with a standard EM segmentation algorithm (Van Leemput et al., 1999). A single EM step is initially performed for all the subjects using the MNI 305 priors (Evans et al., 1993) as the spatial priors. The posteriors of the subjects are averaged to obtain the new spatial priors for the next segmentation step. The images

are then re-aligned according to their posteriors to the group average using the KLM divergence (Kullback and Leibler, 1951) as the registration metric. After the alignment the next segmentation step is run using the new spatial posteriors. The interleaved segmentation-registration is iterated until convergence.

Riklin-Raviv et al. (2010) and Dittrich et al. (2011) presented a level-set group-wise segmentation technique where a latent atlas is inferred from the images of the database, which in turn constrains the individual segmentations. Riklin-Raviv et al. (2010) model the segmentation with a probabilistic formulation of level-sets that incorporates an image likelihood term, a spatial prior term and a smoothness constraint. The parameters of each term are minimized in an interleaved manner. The parameters of the image likelihood term are modelled with a GMM that is optimised with the EM algorithm for each image. The spatial term parameters are estimated as a probabilistic average of all the individual segmentations and can be thought as a 'latent atlas'. All the images are aligned before the segmentation with a group-wise registration technique. The segmentation is performed for a single structure and is based on a single manually segmented atlas. Dittrich et al. (2011) extend the model of Riklin-Raviv et al. (2010) with an age-dependent latent atlas. A spatio-temporal latent atlas is derived as the age-weighted average of the segmentations at different ages.

Cardoso et al. (2012) propose the label propagation through a spatially variant graph. They construct a graph at each voxel based on morphological and intensity similarities of each image with the rest of the images in the database. Instead of retaining the complete graph for all the voxels and all the pairwise combinations of images, they reduce the graph to a local embedding. Afterwards, the labelling is obtained as a locally-weighted label fusion at each voxel with the weights defined from the graph. At each iteration all the labelled voxels act as atlases, with the manually labelled ones having a larger influence. The segmentation proceeds until the voxels of all the images have been labelled.

In Chapter 5 we propose a novel multi-atlas group-wise segmentation technique that is based on the assumption that similar patterns across images should exhibit similar labelling. A graph of local correspondences among the images in the database is constructed at each voxel in a patch-based fashion. These correspondences are used to propagate the labelling from

the database to each image with an inter-image MRF energy similar to Sotiras et al. (2009); Rubinstein et al. (2012).

2.7 Discussion and conclusions

This chapter overviewed techniques used in the literature for the segmentation of brain MR images. Segmentation techniques can be categorised into: classification techniques, atlas-based approaches and deformable models. Training data used as input to brain segmentation techniques are typically encoded in atlases. Numerous segmentation techniques have been proposed for the delineation of tissues in the neonatal brain. However, methods for the regional segmentation of the neonatal MR images are lacking. This is due to the limited atlases available for the newborn brain. The first detailed atlases of the neonatal brain were introduced by Gousias et al. (2012). This chapter further presented techniques that improve the segmentation performance by incorporating unlabelled data (in addition to atlases) as training data. The following chapters accordingly propose algorithms for the segmentation of the neonatal brain into: different tissue types (Chapter 3), detailed structures of the brain (Chapter 4), and the use of unlabelled data as additional information to the atlases (Chapter 5).

Chapter 3

Neonatal tissue segmentation

This chapter is based on:
Makropoulos, A., Gousias, I. S., Ledig, C., Aljabar, P., Serag, A., Hajnal, J., Edwards, A. D., Counsell, S., and Rueckert, D. (2014). Automatic whole brain MRI segmentation of the developing neonatal brain. IEEE Transactions on Medical Imaging.

Makropoulos, A., Ledig, C., Aljabar, P., Serag, A., Hajnal, J. V., Edwards, A. D., Counsell, S. J., and Rueckert, D. (2012b). Automatic tissue and structural segmentation of neonatal brain MRI using Expectation-Maximization. In MICCAI Grand Challenge on Neonatal Brain Segmentation 2012 (NeoBrainS12).

Išgum, I., Benders, M. J.N.L., Avants, B., Cardoso, M. J., Counsell, S. J., Gomez, E. F., Gui, L., Hüppi, P., Kersbergen, K. J., Makropoulos, A., Melbourne, A., Moeskops, P., Mol, C. P., Kuklisova-Murgasova, M., Rueckert, D., Schnabel, J. A., Srhoj-Egekher, V., Wu, J., Wang, S., de Vries, L. S., and Viergever, M. A. Evaluation of automatic neonatal brain segmentation algorithms: the NeoBrainS12 challenge. Submitted in Medical Image Analysis.

3.1 Introduction

Segmentation of neonatal brain MR images is considerably more challenging than adult brain segmentation. The CSF-WM PV effect, the lower

contrast-to-noise ratio compared to the adult brain, and the large changes in appearance of the brain occuring from the early preterm period to term-equivalent age present obstacles for the segmentation techniques.

A number of algorithms have been proposed in the literature for the neonatal tissue segmentation (Prastawa et al., 2005; Song et al., 2007; Xue et al., 2007; Anbeek et al., 2008; Weisenfeld and Warfield, 2009; Shi et al., 2010; Cardoso et al., 2011, 2013; Wang et al., 2011; Gui et al., 2012b; Chiţă et al., 2013). Direct comparison of these techniques is not easily feasible due to different data acquisition parameters, different manual reference segmentations as well as different definition of structures and number of structures segmented. To address this problem, a recent neonatal segmentation challenge, NeoBrainS12 (2012), compared submitted algorithms on a common reference. Evaluation was performed on three different image sets of preterm infants with eight manually segmented structures. In Makropoulos et al. (2012b) we proposed a neonatal tissue segmentation method that achieved the highest accuracy in NeoBrainS12 (2012) with respect to the manual reference. This chapter presents details of the submitted algorithm (Makropoulos et al., 2012b).

3.2 Data acquisition

Three different sets of T1 and T2 images were provided as part of the NeoBrainS12 challenge:

- Axial scans acquired at 40 weeks corrected age (Set 1),
- Coronal scans acquired at 30 weeks corrected age (Set 2) and
- Coronal scans acquired 40 weeks corrected age (Set 3).

The scan acquisition parameters for the three sets are summarized in Table 3.1. Imaging data of seven infants were included from Set 1 and Set 2 and five infants from Set 3. The brain MR images were manually parcellated in eight regions: cortical grey matter (CGM), unmyelinated white matter (WM), myelinated white matter (MWM), brainstem, basal ganglia and thalami (BGT), cerebellum, CSF and ventricles. The segmentation protocol is described in the webpage of the challenge, http://neobrains12.isi.uu.nl. The challenge consisted of two stages: a part prior to the challenge and an

on-site part. Datasets of three infants per set were provided as test data in the part prior to the challenge and two infants per set at the on-site part, without the manual segmentations. The algorithms were evaluated on these datasets. The teams could select which datasets and tissue types to segment. A two hours timeframe was set for the on-site part. The remaining datasets of two infants per Set 1 and Set 2 were provided as training data accompanied by the manual segmentations.

	Axial (40 weeks)		Coronal (30 weeks)		Coronal (40 weeks)	
	T1	T2	T1	T2	T1	T2
TR (ms)	9.4	6293	9.4	10085	9.5	4847
TE (ms)	4.6	120	4.6	120	4.6	150
time (min)	3.44	5.4	4.44	6.23	7.02	5.05
FOV	180×180	180×180	130×104	130×104	200×200	180×180
matrix	512×512	512×512	384×384	384×384	256×256	512×512
thickness (mm)	2	2	2	2	1.2	1.2
nr. sections	50	50	50	50	110	110
resolution (mm×mm)	0.35×0.35	0.35×0.35	0.34×0.34	0.34×0.34	0.78×0.78	0.35×0.35

Table 3.1: Acquisition parameters of the MR images in NeoBrainS12 (2012) (data from http://neobrains12.isi.uu.nl)

3.3 Methods

We propose a Expectation-Maximization (EM) framework for the segmentation of the neonatal brain into seven regions: CSF, CGM, unmyelinated WM, ventricles, brainstem, cerebellum and BGT. The myelinated WM could not be consistently segmented and was excluded from the model.

The EM algorithm of Van Leemput et al. (1999) is extended with a number of modifications for the case of neonatal segmentation: The spatial proximity of structures is modelled with a Markov Random Field (MRF) regularization term (Section 3.3.5). A prior relaxation scheme is introduced to account for the large anatomical variability in the neonatal brain (Section 3.3.6). Mislabelled WM voxels in the CSF-CGM interface (CSF-WM PV) are corrected with connected component labelling and knowledge-based rules (Section 3.3.7). A novel PV correction is further implemented for the accurate delineation of the CGM-WM boundary. The CGM-WM PV correction is outlined in Chapter 6. These modifications are implemented in the Correction step of the proposed EM algorithm.

The next section presents the proposed segmentation pipeline and Sections 3.3.2-3.3.7 describe the different components of the pipeline. Section 3.3.8 summarizes the modified EM algorithm for the tissue segmentation.

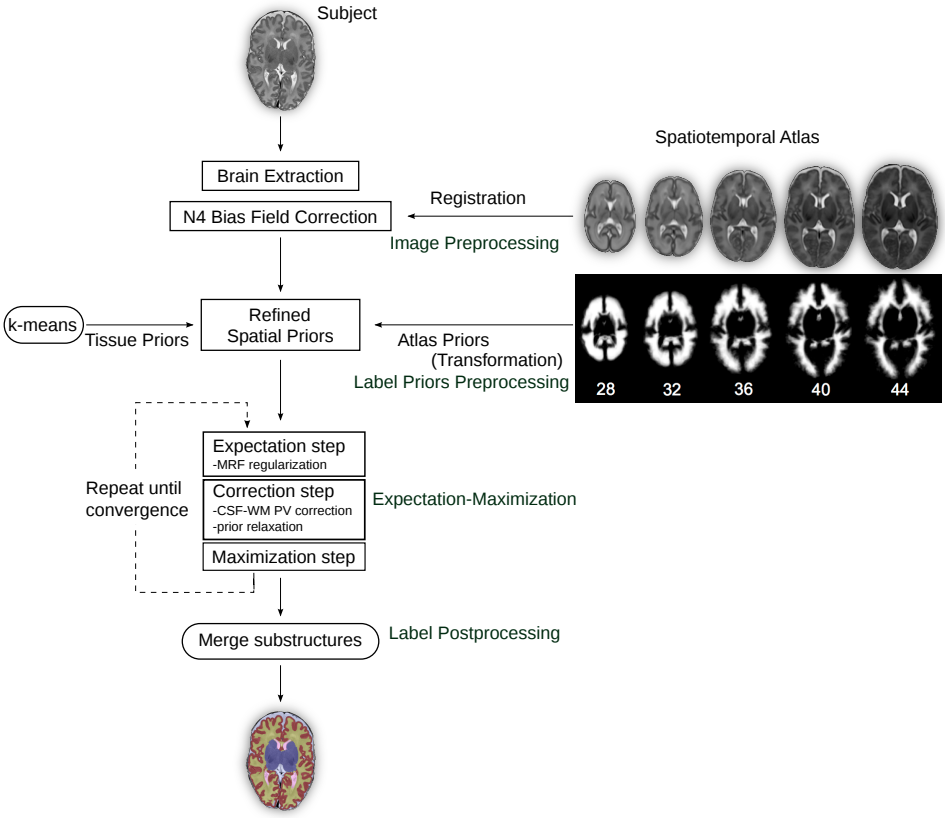

Figure 3.1: Tissue segmentation pipeline. The subject's MR image is brain-extracted and bias field corrected. Atlas priors are propagated from the spatio-temporal atlas of Serag et al. (2012) and combined with subject-specific tissue priors. The proposed EM algorithm is initialised with the combined tissue priors and results in the final labelling (after a postprocessing of the labels). The algorithm incorporates MRF regularisation, CSF-WM PV correction and prior relaxation.

3.3.1 Segmentation pipeline

Figure 3.1 presents an overview of the tissue segmentation pipeline. The target image is initially skull-stripped with the Brain Extraction Tool (BET) (Smith, 2002) and corrected for the intensity inhomogeneity with the N4 algorithm (Tustison et al., 2010). The spatio-temporal neonatal atlas of Serag et al. (2012) is then registered to the image and the tissue probabilities of the atlas are propagated to the subject space. The atlas priors are combined with subject-specific tissue priors obtained with k-means to provide a robust initialization of the EM algorithm. Finally, the proposed EM

algorithm results in the parcellation of the brain into tissues (after a post-processing step). The segmentations were performed in the T2 images of the subjects due to their superior contrast over T1 for tissue differentiation in the neonatal population.

3.3.2 Atlas priors

The spatio-temporal atlas of Serag et al. (2012) was used to propagate spatial priors for the target image. Since the atlas has different structure definitions from the delineations provided in NeoBrainS12, the tissue probability maps of the atlas were manually modified to comply with the protocol of the challenge. The CSF prior was divided into left and right ventricle and extra-cerebral CSF. Parts of the BGT were removed and merged with the CGM map and the brainstem mask was modified to have a better agreement with the NeoBrainS12 definitions.

For each subject the corresponding age template of the atlas was rigidly, affinely and non-rigidly registered to the subject space. The non-rigid registration was carried out using free-form deformations with control point grid spacings of 20mm, 10mm, 5mm and 2.5mm and normalized mutual information (NMI) as the similarity measure (Rueckert et al., 1999). The tissue probability maps were then warped to the native space of the subject using the estimated transformation.

3.3.3 Subject-specific tissue priors

Subject-specific priors that reflect the tissue proportions of the target image were obtained with k-means (Macqueen, 1967). The image intensities were clustered into four classes that represent the three tissue memberships (CSF, GM, WM) and the background. The CSF class from k-means was re-clustered into two parts, a low intensity and a high intensity part, with a second k-means clustering. The low intensity part is mainly attributed to the low CSF intensities of the brain and some high WM intensities observed in the frontal and occipital lobe. The high intensity part corresponds to the 'pure' CSF intensities of the brain. Subject-specific tissue priors were then modelled with a Gaussian distribution initialized with each of the five resulting k-means classes' centroids and variances (extra-cranial space, GM, WM, high intensity WM/low intensity CSF, CSF) and blurred with a Gaussian

kernel with standard deviation $\sigma_C = 1$. To avoid local minima of k-means, the clustering was repeated multiple times using random initialisation and the solution with the best fit to the data was retained.

The atlas priors were then refined by multiplying them with the appropriate subject-specific tissue priors for each region (e.g. the CGM atlas prior was multiplied with the GM tissue prior to result in the refined CGM prior, the CSF atlas prior was divided into a low intensity CSF and a CSF prior by multiplying it with the low intensity CSF and the CSF tissue prior respectively). The refined priors were used to initialise the spatial prior term, $P(z_i = e_k)$, of the EM algorithm, providing a better initialization than the atlas priors alone. The structures introduced into the EM model were: CSF, low intensity CSF, CGM, high intensity WM, WM, BGT, brainstem, cerebellum, left ventricle, right ventricle and extra-cranial space (ECS).

3.3.4 Expectation-Maximization formulation

This section presents the standard EM algorithm with a notation similar to Van Leemput et al. (1999). The image intensity likelihood is approximated by a Gaussian Mixture Model of the K structures (here $K = 11$). The label of each voxel i is denoted by a 1-of-K indicator variable z_i. The prior distribution of z_i's is denoted with the $K \times 1$ vector parameter π_i, i.e.

$$P(z_i = e_k) = \pi_{ik} \quad . \tag{3.1}$$

π_{ik} is the (spatial) prior probability of observing structure k in voxel i.

Assuming the observed intensities y_i are independent, the problem can be formalised as a Maximum a Posteriori (MAP) estimation of the means μ_k and standard deviations σ_k of the structures' Gaussian distributions $G(. \mid \mu_k, \sigma_k)$ (Van Leemput et al., 1999). The parameters $\Phi_y = \{\mu_1, .., \mu_k, \sigma_1, ..., \sigma_k\}$ are estimated with the EM algorithm (Dempster et al., 1977), at each iteration m:

Expectation step:

$$\begin{aligned} p_{ik}^{[m+1]} &= P(z_i = e_k \mid y_i, \Phi_y) \\ &= \frac{P(y_i \mid z_i = e_k, \Phi_y^{[m]}) P(z_i = e_k)}{\sum_{j=1}^{K} P(y_i \mid z_i = e_j, \Phi_y^{[m]}) P(z_i = e_j)} \end{aligned} \tag{3.2}$$

$$\text{where } P(y_i \mid z_i = e_k, \Phi_y^{[m]}) = G(y_i \mid \mu_k, \sigma_k) \quad . \tag{3.3}$$

Maximization step:

$$\mu_k^{[m+1]} = \frac{\sum_{i=1}^{N} p_{ik}^{[m+1]} y_i}{\sum_{i=1}^{N} p_{ik}^{[m+1]}} \tag{3.4}$$

$$(\sigma_k^{[m+1]})^2 = \frac{\sum_{i=1}^{N} p_{ik}^{[m+1]} (y_i - \mu_k^{[m+1]})^2}{\sum_{i=1}^{N} p_{ik}^{[m+1]}} \quad . \tag{3.5}$$

3.3.5 Markov Random Field regularization

In practice, the label of a voxel is dependent on the label assignment of its surrounding voxels. To account for this, we introduce a spatial regularisation term to enforce a smooth labelling among neighbouring voxels (Van Leemput et al., 1999). The Markov Random Field (MRF) implementation in the present work follows the work of Cardoso et al. (2011) adopting the mean field approximation, where the regularisation term is expressed with a multiclass extension of the Potts model:

$$P(z_i = e_k) = \frac{\pi_{ik} e^{-\beta \; U_{MRF}(e_k|N_i)}}{\sum_{j=1}^{K} \pi_{ij} e^{-\beta \; U_{MRF}(e_j|N_i)}} \quad . \tag{3.6}$$

Here N_i are the first-order neighbours of voxel i and β the overall MRF strength. The energy function U_{MRF} is defined as:

$$U_{MRF}(e_k \mid N_i) = \sum_{j=1}^{K} A_{kj} \Big(\sum_{l \in N_i^x} s_x p_{lj} + \sum_{l \in N_i^y} s_y p_{lj} + \sum_{l \in N_i^z} s_z p_{lj} \Big) \tag{3.7}$$

where the variable $s = \{s_x, s_y, s_z\}$, models the anisotropic voxel spacing (Cardoso et al., 2011). A_{kj} is an a-priori defined connectivity strength matrix that penalises the interaction of structures according to their spatial proximity. A_{kj} is defined as:

$$A_{kj} = \begin{cases} 0, & \text{if structure } k \text{ is the same as } j \\ b, & \text{if structure } k \text{ is neighbouring } j, \\ c, & \text{if structure } k \text{ is distant from } j \end{cases}$$

with $b < c$. Larger values attribute a stronger effect of the neighboring voxels resulting in a smoother labelling. The connectivity strength parameters were empirically set to $b = 1$, $c = 5$ and the overall MRF strength to $\beta = 0.33$.

3.3.6 Prior relaxation

Since the neonatal brain presents a large anatomical variability, the spatio-temporal atlas may not be registered accurately to parts of the target image. Adaptivity of the spatial priors in this work is introduced as in Shiee et al. (2011); Cardoso et al. (2011, 2013) to correct for such misalignments. The π_{ik} are modelled as the posteriors of a Dirichlet distribution (the Dirichlet distribution is in essence a hyperprior of the model). The π_{ik}'s are updated by

$$\pi_{ik} = (1 - \alpha)\pi_{ik} + \alpha(C * p_{ik}) \tag{3.8}$$

where C is a Gaussian kernel and $*$ denotes the convolution operation. The spatial priors of the model are adapted according to the EM posteriors. The amount of adaptivity allowed for the spatial priors is determined with the parameter α, $0 \leq \alpha \leq 1$. Here the relaxation factor was set to $\alpha = 0.5$ similarly to Shiee et al. (2011).

3.3.7 CSF-WM Partial Volume correction

The spatial regularisation introduced by the MRF allows the removal of isolated voxels that may be mislabelled due to partial volume signal averaging and noise in the image. However, there is a large number of adjacent voxels that can be misclassified when labelled based on the intensity in the neonatal brain. Since most of these voxels are neighboring each other, they favor their neighbors through the MRF energy formulation. As a result, the MRF alone is not sufficient to remove them. A way to overcome this problem as shown in Xue et al. (2007) is to introduce a knowledge-based approach designed specifically to lower the probability of partial volume (PV) in misclassified regions.

Table 3.2 summarizes the knowledge-based rules defined here to detect partial volume voxels and the tissues they should belong to instead. Isolated partial volume regions are detected with connected component labelling.

Knowledge-based rules	Misclassified tissue	Appropriate tissues
WM ccs,voxels in CSF-ECS boundary	WM	CSF
WM voxels in GM - CSF, GM-ECS boundaries	WM	CSF, GM
CSF ccs mainly surrounded by WM	CSF	WM
GM voxels in CSF-ECS boundary	GM	CSF, ECS

Table 3.2: Knowledge-based rules for detecting misclassified voxels and their appropriate tissues according to the connected components (ccs) of the tissues.

The partial volume correction in (Xue et al., 2007) is performed by reducing the prior probability of the misclassified tissue in favor of the appropriate tissue(s). Let r represent the misclassified tissue class and c_j the appropriate tissue classes. The prior probabilities of the detected voxels are adjusted as follows:

$$\pi'_{ic_j} = \pi_{ic_j} + (1-\lambda) w_{ic_j} \pi_{ir}$$

$$\pi'_{ir} = \lambda \pi_{ir} \quad .$$

Here

$$w_{ic_j} = \frac{\pi_{ic_j}}{\sum_n \pi_{ic_n}}$$

and λ is set to 0.5 in our experiments. Essentially, the PV correction redistributes the misclassified tissue probability mass to the appropriate tissue(s) after each EM iteration.

3.3.8 Summary

Algorithm 1 presents the proposed EM algorithm for the segmentation of the neonatal brain into tissues. The EM steps (Expectation, Correction, Maximization) are repeated until convergence.

3.4 Evaluation

The segmentation accuracy was assessed with the manual reference data of the NeoBrainS12 challenge in the on-site part and the part prior to the challenge. Tables 3.3 and 3.4 present the overlap, measured with the Dice coefficient, between the submitted automatic techniques and the manual segmentations. The Dice coefficient (Dice, 1945) between the sets of corresponding voxels S_a and S_m of two segmentations of the same object, is

Algorithm 1 The proposed EM algorithm for tissue segmentation.

Repeat

Expectation step

$$p_{ik} = \frac{\pi_{ik} e^{-\beta\ U_{MRF}(e_k|N_i)} G(y_i \mid \mu_k, \sigma_k)}{\sum_{j=1}^{K} \pi_{ij} e^{-\beta\ U_{MRF}(e_j|N_i)} G(y_i \mid \mu_j, \sigma_j)}$$

Correction step

$$\pi_{ik} = (1-\alpha)\pi_{ik} + \alpha(C * p_{ik})$$

Detect partial volume voxels i and $c_j, r \in [CGM, WM, CSF, ECS]$ with connected component labelling and update:

$$\pi_{ic_j} = \pi_{ic_j} + (1-\lambda)\frac{\pi_{ic_j}}{\sum_n \pi_{ic_n}}\pi_{ir}$$

$$\pi_{ir} = \lambda \pi_{ir}$$

Maximization step

Calculate parameters Φ_y:

$$\mu_k = \frac{\sum_{i=1}^{N} p_{ik} y_i}{\sum_{i=1}^{N} p_{ik}}$$

$$\sigma_k^2 = \frac{\sum_{i=1}^{N} p_{ik}(y_i - \mu_k)^2}{\sum_{i=1}^{N} p_{ik}}$$

Until convergence

defined as

$$Dice = \frac{2|S_a \cap S_m|}{|S_a| + |S_m|} \tag{3.9}$$

where $|S_a|$, $|S_m|$ is the number of voxels of the segmented object in S_a and S_m respectively and $|S_a \cap S_m|$ the number of common voxels between the two segmentations. The measure takes a value of 1 in the case of perfect match amongst the two segmentations and 0 when there is no overlap.

The following methods were submitted to the challenge: Makropoulos et al. (2012b), Wang et al. (2012c), Melbourne et al. (2012), Wu and Avants (2012), Gui et al. (2012a), Srhoj-Egekher et al. (2012), Anbeek et al. (2008), Chiţă et al. (2013). The last three methods (Srhoj-Egekher et al. (2012), Anbeek et al. (2008), Chiţă et al. (2013)) had the manual reference data of the test set available during the method construction. These methods were not considered in the method ranking in NeoBrainS12, however they are included here as a benchmark. The methods by Makropoulos et al. (2012b), Wang et al. (2012c), Melbourne et al. (2012), Wu and Avants (2012) segmented all the sets of images. In Makropoulos et al. (2012b) we did not specifically delineate the MWM tissue because it could not be consistently segmented in initial experiments. The performance of the submitted methods in the MWM segmentation (ranging from 0.07 to 0.69) further demonstrated this effect. The method developed by Gui et al. (2012a) segmented the CSF and ventricles as a single class. Chiţă et al. (2013) delineated only the WM, CGM and CSF tissues. The rest methods (Wang et al. (2012c), Melbourne et al. (2012), Wu and Avants (2012), Srhoj-Egekher et al. (2012), Anbeek et al. (2008)) segmented all the tissue types of the challenge.

Example segmentations of the proposed technique are shown in Figure 3.2. The average runtime of the segmentation was less than 30 minutes per subject. The whole pipeline requires around 95 minutes per subject and was amongst the most demanding methods in terms of execution time submitted in the challenge (reported times in minutes ($'$) were: $7'$ for Wang et al. (2012c), $15'$ for Melbourne et al. (2012), $80'$-$100'$ for Wu and Avants (2012), $120'$ for Gui et al. (2012a), $60'$ for Srhoj-Egekher et al. (2012), $15'$ for Anbeek et al. (2008) and $15'$ for Chiţă et al. (2013)). The proposed algorithm achieved high Dice overlaps in all the segmented regions, with an average Dice of 0.83 in the different parts of the challenge. Equal or better results to the other techniques were obtained in the majority of the regions

and the method was ranked first in NeoBrainS12 (2012) for the segmentation accuracy. A notable exception is the area of the ventricles which presents worse results than the other techniques. Due to the similar intensity of the ventricles and CSF, the prior relaxation described in Section 3.3.6 often resulted in "leakage" of the ventricles in the CSF tissue. An example can be seen in Figure 3.2.B, where the ventricles are oversegmented in the middle part of the brain. It should be noted here that the differences in the results between the methods were small in most of the cases. Furthermore, since evaluation was performed on a limited number of images (two images per set on the on-site and three per set in the part prior to the challenge), significance of the results was not assessed in NeoBrainS12 (2012).

3.5 Discussion and conclusions

This chapter presents an algorithm for the segmentation of neonatal T2 images into 7 tissue types: CSF, CGM, unmyelinated WM, brainstem, cerebellum, basal ganglia and thalami and ventricles. The algorithm is based on an EM scheme similar to Van Leemput et al. (1999) with a spatial prior term and an intensity model of the image. Spatial priors of the structures are propagated from a spatio-temporal probabilistic atlas and are refined with subject-specific tissue priors obtained with k-means. The intensity of the image is modelled with a GMM. Spatial regularization is enforced with an MRF term and spatial adaptivity with a prior relaxation term as in Cardoso et al. (2011). The proposed technique further incorporates bias field and partial volume correction. The next chapter builds upon the proposed EM scheme for the structural segmentation of the neonatal brain.

Evaluation of the proposed algorithm was performed on manually segmented data from the NeoBrainS12 challenge. The method achieved state-of-the-art results and outperformed submitted techniques in the majority of regions. The challenge evaluated the performance of the algorithms on limited datasets. A larger-scale evaluation would allow further exploration of the strengths and weaknesses of different automatic segmentation techniques for the neonatal brain.

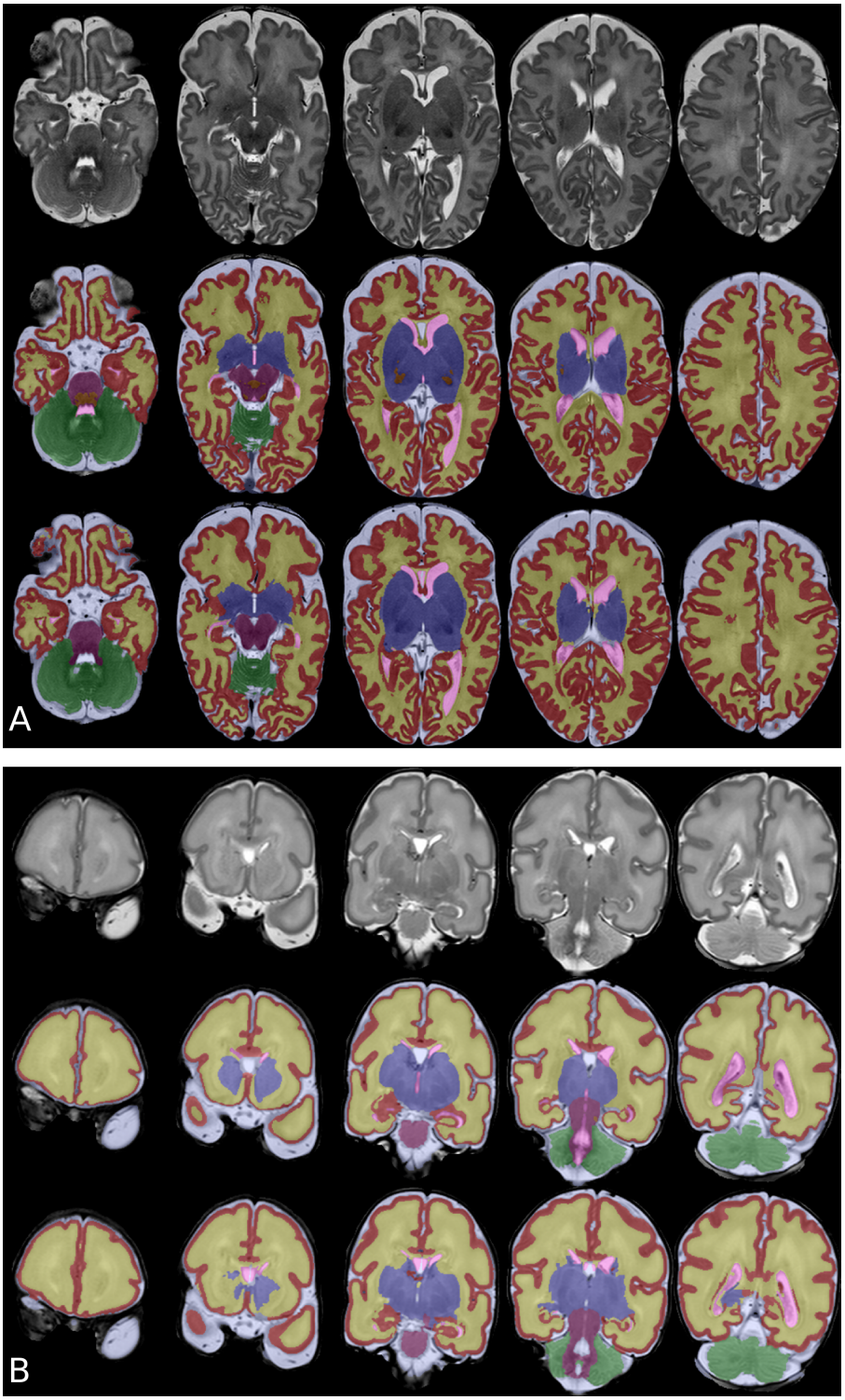

Figure 3.2: Example tissue segmentation of a neonatal MRI from Set 1 (A) and Set 2 (B) of the NeoBrainS12 challenge (second row: manual segmentation, third row: automatic segmentation).

	CGM			WM			MWM			WM+MWM			CSF		
	Set 1	Set 2	Set 3	Set 1	Set 2	Set 3	Set 1	Set 2	Set 3	Set 1	Set 2	Set 3	Set 1	Set 2	Set 3
Makropoulos et al. (2012b)	**0.84**	0.70	0.75	**0.89**	**0.91**	0.86	-	-	-	-	-	-	**0.76**	**0.84**	**0.75**
Wang et al. (2012c)	0.83	0.60	0.72	0.88	0.86	0.84	**0.43**	0.29	**0.52**	**0.88**	0.86	**0.84**	0.72	0.75	0.71
Melbourne et al. (2012)	0.83	**0.71**	0.73	0.87	0.90	0.84	0.22	0.16	0.08	0.87	**0.90**	0.83	0.71	0.76	0.58
Wu and Avants (2012)	0.80	0.60	0.69	0.85	0.87	0.83	0.32	**0.69**	0.07	0.84	0.87	0.82	0.61	0.63	0.71
Gui et al. (2012a)	-	-	**0.76**	-	-	**0.89**	-	-	-	-	-	-	-	-	
Srhoj-Egekher et al. (2012)	0.85	-	-	0.91	-	-	0.55	-	-	0.91	-	-	0.77	-	-
Anbeek et al. (2008)	0.82	-	-	0.87	-	-	0.46	-	-	0.87	-	-	0.72	-	-
Chiţă et al. (2013)	-	0.70	-	-	0.94	-	-	-	-	-	-	-	-	0.85	-

	ventricles			CSF+ventricles			brainstem			cerebellum			BGT		
	Set 1	Set 2	Set 3	Set 1	Set 2	Set 3	Set 1	Set 2	Set 3	Set 1	Set 2	Set 3	Set 1	Set 2	Set 3
Makropoulos et al. (2012b)	0.80	0.86	0.82	**0.77**	**0.85**	**0.77**	**0.84**	**0.75**	**0.73**	0.91	**0.87**	**0.92**	**0.91**	0.82	0.86
Wang et al. (2012c)	0.85	**0.88**	0.83	0.74	0.78	0.72	0.80	0.69	0.71	**0.92**	**0.87**	0.90	0.87	0.82	**0.88**
Melbourne et al. (2012)	0.81	0.86	0.70	0.73	0.78	0.61	0.82	0.73	**0.73**	0.90	**0.87**	**0.92**	0.89	**0.84**	0.85
Wu and Avants (2012)	**0.86**	0.87	**0.84**	0.64	0.66	0.72	0.74	0.65	0.36	0.91	0.85	0.91	0.80	0.74	0.79
Gui et al. (2012a)	-	-	-	-	-	0.71	-	-	0.71	-	-	0.89	-	-	0.85
Srhoj-Egekher et al. (2012)	0.83	-	-	0.78	-	-	0.87	-	-	0.93	-	-	0.93	-	-
Anbeek et al. (2008)	0.81	-	-	0.73	-	-	0.85	-	-	0.93	-	-	0.92	-	-
Chiţă et al. (2013)	-	-	-	-	-	-	-	-	-	-	-	-	-	-	-

Table 3.3: Results of the part prior to the NeoBrainS12 challenge (data from http://neobrains12.isi.uu.nl). The submitted algorithms are compared in terms of the Dice coefficient with the manual reference. The methods submitted by Srhoj-Egekher et al. (2012),Anbeek et al. (2008),Chiţă et al. (2013) had the manual reference data of the test set available during the method construction and were not considered in the method ranking in NeoBrainS12. The best result from the rest methods is noted with bold font.

	CGM			WM			MWM			WM+MWM			CSF		
	Set 1	Set 2	Set 3	Set 1	Set 2	Set 3	Set 1	Set 2	Set 3	Set 1	Set 2	Set 3	Set 1	Set 2	Set 3
Makropoulos et al. (2012b)	**0.88**	**0.67**	0.74	**0.91**	**0.91**	0.86	-	-	-	-	-	-	**0.82**	**0.82**	**0.81**
Wang et al. (2012c)	0.86	0.54	0.71	0.89	0.85	0.85	**0.55**	**0.21**	**0.42**	**0.89**	**0.71**	**0.84**	0.81	0.72	0.78
Melbourne et al. (2012)	-	-	-	-	-	-	-	-	-	-	-	-	-	-	-
Wu and Avants (2012)	-	-	-	-	-	-	-	-	-	-	-	-	-	-	-
Gui et al. (2012a)	-	-	**0.76**	-	-	**0.89**	-	-	-	-	-	-	-	-	-
Srhoj-Egekher et al. (2012)	0.88	-	-	0.92	-	-	0.68	-	-	0.92	-	-	0.85	-	-
Anbeek et al. (2008)	0.86	-	-	0.88	-	-	0.62	-	-	0.88	-	-	0.81	-	-
Chiţă et al. (2013)	-	0.73	-	-	0.94	-	-	-	-	-	-	-	-	0.87	-

	ventricles			CSF+ventricles			brainstem			cerebellum			BGT		
	Set 1	Set 2	Set 3	Set 1	Set 2	Set 3	Set 1	Set 2	Set 3	Set 1	Set 2	Set 3	Set 1	Set 2	Set 3
Makropoulos et al. (2012b)	0.84	0.80	0.80	**0.83**	**0.83**	**0.82**	**0.82**	**0.78**	**0.77**	**0.93**	0.88	0.90	**0.90**	0.82	0.88
Wang et al. (2012c)	**0.86**	**0.88**	**0.85**	0.82	0.75	0.79	0.76	0.73	0.72	**0.93**	**0.89**	0.89	**0.90**	**0.83**	**0.89**
Melbourne et al. (2012)	-	-	-	-	-	-	-	-	-	-	-	-	-	-	-
Wu and Avants (2012)	-	-	-	-	-	-	-	-	-	-	-	-	-	-	-
Gui et al. (2012a)	-	-	-	-	-	**0.82**	-	-	0.72	-	-	**0.93**	-	-	0.87
Srhoj-Egekher et al. (2012)	0.89	-	-	0.85	-	-	0.87	-	-	0.95	-	-	0.92	-	-
Anbeek et al. (2008)	0.84	-	-	0.82	-	-	0.86	-	-	0.94	-	-	0.91	-	-
Chiţă et al. (2013)	-	-	-	-	-	-	-	-	-	-	-	-	-	-	-

Table 3.4: Results of the on-site part of the NeoBrainS12 challenge (data from http://neobrains12.isi.uu.nl). The submitted algorithms are compared in terms of the Dice coefficient with the manual reference. The methods submitted by Srhoj-Egekher et al. (2012),Anbeek et al. (2008),Chiţă et al. (2013) had the manual reference data of the test set available during the method construction and were not considered in the method ranking in NeoBrainS12. The best result from the rest methods is noted with bold font.

Chapter 4

Neonatal structural segmentation

This chapter is based on:
Makropoulos, A., Gousias, I. S., Ledig, C., Aljabar, P., Serag, A., Hajnal, J., Edwards, A. D., Counsell, S., and Rueckert, D. (2014). Automatic whole brain MRI segmentation of the developing neonatal brain. IEEE Transactions on Medical Imaging.

4.1 Introduction

Due to the lack of detailed atlases of the neonatal brain, previous neonatal segmentation techniques focused on the parcellation of brain tissues. In order to assess regional brain development, detailed segmentations of a large number of brain regions are required. In Makropoulos et al. (2012a, 2014), we presented the first study to automatically segment the developing neonatal brain, from the early preterm period to term-equivalent age, into 50 structures (82 when the WM/CGM regions are subdivided into WM, CGM).

The contributions of this work are three-fold:

- A novel multi-structural segmentation algorithm is presented for the parcellation of the developing brain into 50 regions.
- The proposed segmentation outperforms current state-of-the-art techniques used in the segmentation field. The model is compared with standard label fusion techniques which are amongst the most accurate techniques for the structural segmentation of the brain (Babalola et al., 2009).

- The presented algorithm allows for the first time accurate detailed segmentation of the neonatal brain from 24 weeks gestational age to term-equivalent age. The algorithm was successfully applied to 234 T2-weighted images of different gestational ages.

This chapter presents the multi-structural segmentation technique outlined in Makropoulos et al. (2014).

4.2 Data acquisition

T2-weighted MR images were acquired for 198 premature infants and 36 term controls. The cohort characteristics for the T2 scans are presented in Table 4.1. Ear protection was provided for each infant with earplugs moulded from a silicone-based putty (President Putty, Coltene Whaledent, Mahwah, NJ) and neonatal ear protectors (MiniMuffs, Natus Medical, San Carlos, CA). All examinations were supervised by a pediatrician experienced in MRI procedures and pulse oximetry, temperature and electrocardiography data were monitored throughout the procedure. The T2-weighted MR images were acquired using the parameters in Table 2.2.

T2	preterm infants	term controls
number of images	198	36
age at birth (weeks)	29^{+2} (24^{+3} - 35^{+2})	39^{+2} (36 - 41^{+5})
age at scan (weeks)	39^{+1} (26^{+5} - 44^{+2})	40^{+6} (36^{+3} - 44^{+4})
weight at birth (kg)	1.18 (0.6 - 3.7)	3.3 (2.2 - 4.3)
weight at scan (kg)	2.3 (0.75 - 5.5)	3.44 (2.18 - 4.71)
head circumference at birth (cm)	27.15 (22 - 36.8)	34 (23 - 39.6)
head circumference at scan (cm)	33.3 (23.1 - 39.6)	35.5 (32 - 38.7)

Table 4.1: Cohort characteristics for the T2 images. Median (range) age, weight and head circumference at the time of birth and scan are presented.

4.3 Methods

We propose a novel multi-structure EM-based segmentation technique for the subdivision of the whole brain. Structural information is provided from multiple single-subject atlases (described in Section 2.1.1). In atlas-based segmentation methods, the MR images of manually segmented atlases are registered to the subject's MR image and their labels are propagated to

it, based on the calculated transformations (Heckemann et al., 2006). The propagated labels of multiple atlases can then be fused to yield probabilistic spatial priors or to provide the final segmentation result. In the proposed framework spatial priors are combined with an intensity model to segment the structures in a fashion similar to Lötjönen et al. (2010); Ledig et al. (2012).

A number of improvements to the standard EM algorithm employed for brain segmentation (Van Leemput et al. (1999); Ledig et al. (2012); Lötjönen et al. (2010)) are proposed here for the accurate segmentation of the neonatal brain:

- The manual protocol of the atlases (Gousias et al., 2012) subdivides the combined WM and CGM space into 32 structures. Each one of the 32 structures contains both the WM and CGM part of the respective region of the brain (see Figures 2.2, 4.1 for an example of this manual parcellation). The boundaries between the WM/CGM structures are based on the morphology of the cortex and are not separated according to image intensity. A hierarchy within anatomical structures is introduced here to overcome this issue. The whole CGM and WM tissues are modelled as 'superlabels' (aggregations) of their subdivisions. This hierarchical modelling allows the accurate sampling of the tissues' intensities. Furthermore, the boundaries between the WM/CGM structures are defined according to the spatial priors and are not modified according to the intensity. In contrast to this, the boundaries of the WM/CGM structures to the other structures (e.g. CSF, subcortical GM) are adapted with the EM segmentation.

- Segmentation of the subcortical grey matter into different regions based on the intensity is difficult for some parts of the brain. Subcortical GM structures have very similar intensity profiles and parts of their boundaries are often hard to distinguish. This challenge is addressed in the present work by defining the predictive (posterior) distribution as a model averaging of label fusion and the Gaussian Mixture Model (GMM). The segmentation decision in homogeneous regions in the deep grey matter is primarily based on label fusion rather than the GMM since the intensity is less reliable in these areas.

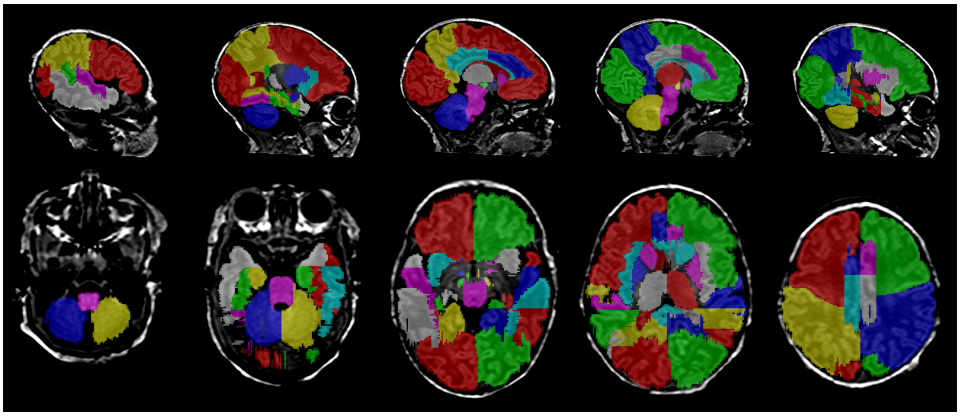

Figure 4.1: *Different slices from one of the manually segmented atlases used in this work (Gousias et al., 2012), in the sagittal and axial plane (top and bottom row respectively) with the manually defined labels overlaid.*

The proposed technique further incorporates bias field correction (Tustison et al., 2010), spatial regularization (Cardoso et al., 2011) and partial volume correction (Xue et al., 2007), similarly to the previous chapter. The prior relaxation discussed in Section 3.3.6 for the purpose of tissue segmentation is explictly not incorporated in the structural segmentation of the brain. The prior relaxation adapts the priors according to the posteriors and helps when segmenting between the brain tissues that have large differences in intensity. In the structural segmentation, there are a large number of structures, for example the subcortical GM structures, that exhibit very similar intensity profiles. Since the intensity likelihood of these structures is similar, adaptation of the priors according to the posteriors will introduce errors in the segmentation.

Section 4.3.1 presents the segmentation pipeline. Sections 4.3.2 and 4.3.3 describe the atlas propagation and the probabilistic modelling of the whole brain. The EM algorithm presented in the previous chapter is extended for the regional segmentation of the brain. Sections 4.3.4 to 4.3.7 present the new components of the EM framework for the purpose of structural segmentation. Section 3.3.8 concludes the methodology with the modified EM algorithm for the structural segmentation.

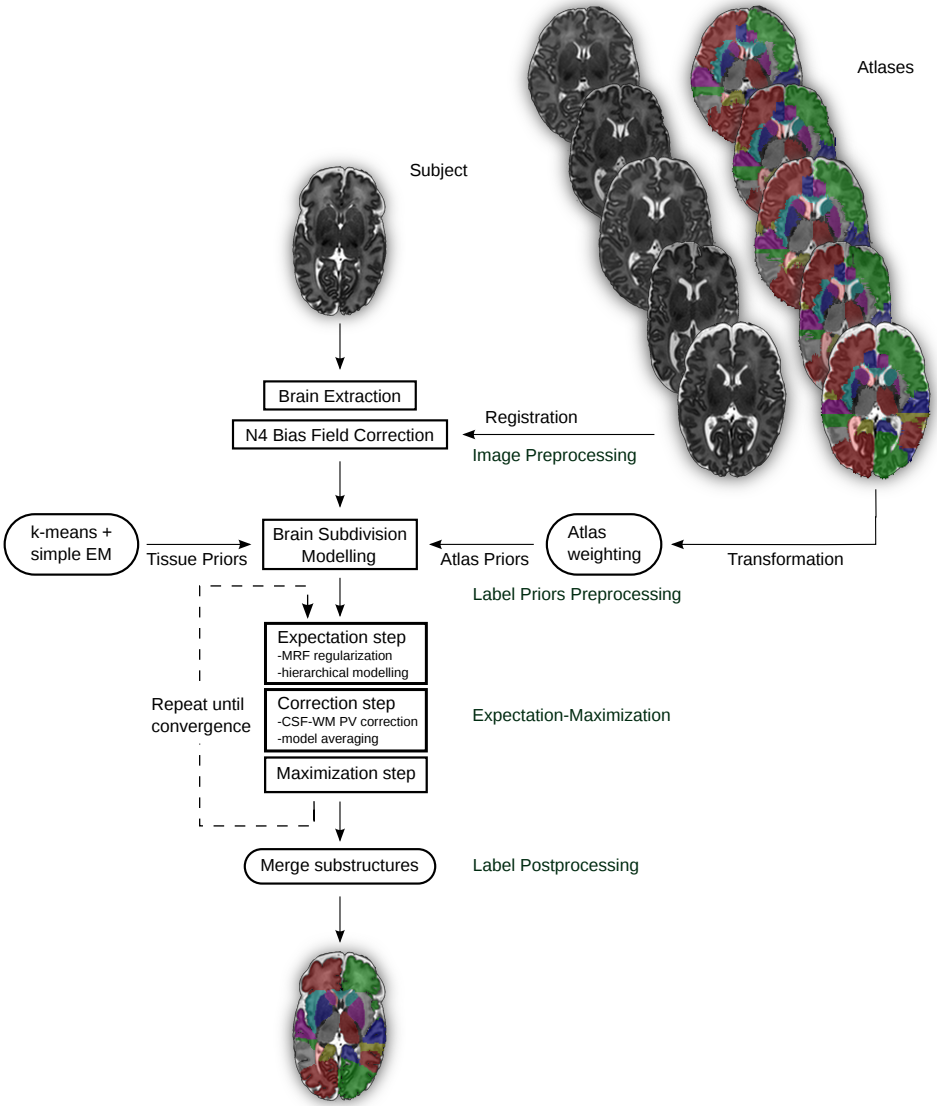

Figure 4.2: Structural segmentation pipeline. After the preprocessing of the subject's MR image, the atlases' MR images are registered to it and the atlas labels are propagated to the image. The atlas priors are combined with subject-specific tissue priors. The resulting spatial priors of the structures are introduced to the proposed EM algorithm that provides the final segmentation, after a label postprocessing step. The algorithm extends the MRF regularisation and CSF-WM PV correction of Chapter 3 and introduces a hierarchical modelling of the structures and a model averaging correction.

4.3.1 Segmentation pipeline

Figure 4.2 presents an overview of the proposed segmentation pipeline. The unlabelled MRI is initially brain-extracted with the Brain Extraction Tool (Smith, 2002) and bias field corrected with the N4 algorithm (Tustison et al., 2010). Afterwards, the atlases' MR images are registered to the target image and the atlas labels are propagated to the image. The propagated labels are averaged in a locally-weighted scheme and subdivided with the use of subject-specific tissue priors obtained with k-means clustering. The proposed EM scheme is used for the estimation of the resulting labelling. Finally, a postprocessing step results in a labelling similar to that of the atlases.

4.3.2 Atlas priors

The atlases' MR images are rigidly, affinely and non-rigidly registered to each subject's image in the T2 space. The non-rigid registration is based on free-form deformations with control point grid spacings of 20mm, 10mm, 5mm and 2.5mm and normalized mutual information (NMI) as the similarity measure (Rueckert et al., 1999). The atlas labels are then propagated to the image space and are averaged to form a probabilistic spatial prior for each structure (for each voxel i):

$$\pi_{ik} = \frac{\sum_{a=1}^{A} w_{ia}\gamma_{ik}^{a}}{\sum_{j=1}^{K}\sum_{a=1}^{A} w_{ia}\gamma_{ij}^{a}}$$

where $a = \{1, .., A\}$ denotes the transformed labels of each atlas and $k \in [1..K]$ denotes the different structures, γ_{ik}^{a} is the vote for structure k produced by atlas a calculated as

$$\gamma_{ik}^{a} = \begin{cases} 1, & \text{if voxel } i \text{ belongs to structure } k \text{ in atlas } a \\ 0, & \text{else} \end{cases}$$

and w_{ia} denotes the weight of each atlas. w_{ia} may be set to a uniform value of 1 globally for all voxels or may be spatially varying in a local weighting scheme. In this work both cases are examined. The local weighting is based on the sum of squared differences (SSD) of the intensity-normalized images of the atlas and the unseen image (Artaechevarria et al., 2009), in the local

neighbourhood of each voxel (in patches of $3 \times 3 \times 3$ size). Notice that π_{ik} is the segmentation estimate of label fusion, as described in Section 2.2.3.

4.3.3 Brain subdivision modelling

EM segmentation involves the accurate modelling of the intensities of the whole space covered by the different regions of the brain. In the standard EM segmentation, every region is assumed to follow a Gaussian distribution over the intensities of the voxels. This section describes the subdivision of regions that need to be described with more than one Gaussian distribution. The subdivision is performed in the space of the image to be segmented by splitting the spatial priors propagated from the atlases.

As the manual segmentation protocol (Gousias et al., 2012) did not divide the WM/CGM structures of the brain into CGM and WM, these regions contain both tissues. Therefore, in order to describe each structure with a single Gaussian intensity model, each WM/CGM structure was divided into its corresponding tissue parts (WM, CGM) using a soft segmentation. The prior probability of each WM/CGM structure in the individual subject space is multiplied with a WM and a CGM probability map to define the corresponding WM and CGM parts. The required subject-specific tissue probabilities are obtained as the posteriors of a simple EM scheme with 4 classes (CSF, GM, WM and extra-cranial space) in the intensity domain. In this EM scheme, the means and standard deviations are initialised using k-means clustering (Macqueen, 1967). The k-means clustering is performed in the intensity space with k=4 clusters. An alternative approach would be to segment the WM/CGM structures of the atlases into WM and CGM and use the modified atlases for the propagation of the CGM,WM components of these structures. However, the registration between different neonatal brains does not align accurately the cortical ribbon (Figure 4.11.A. demonstrates this effect). The term-equivalent atlases have very different cortical complexity from early neonatal brains and the registration can not capture the large deformations occuring as a result of the rapid development. Therefore, we have chosen to differentiate between the tissue types in the space of the target image with intensity clustering.

The background of the manual segmentations contains the extra-cranial space, CSF, as well as parts of the subcortical GM space as can be seen

in Figure 4.1. The background prior probability is subdivided accordingly into three parts. The CSF and extra-cranial space are defined from the tissue probability maps. The ventricles were further excluded as separate regions from the CSF. The subcortical background mainly represents the internal capsule and is segmented by masking the background with a deep grey matter binary map (obtained by transforming and thresholding the subcortical GM map of Serag et al. (2012)).

The ventrolateral nuclei of the thalamus deviates significantly in terms of intensity from the rest of the thalamus (Counsell and Rutherford, 2002). To account for this, the right and left thalamus were subdivided into the low intensity (in T2 space, inversely for the T1 space) part of the thalamus that represents the ventrolateral nuclei and the rest of the thalamus, with another simple EM scheme initialised with a 2 cluster k-means technique.

The remaining subcortical structures retain their propagated definitions from the atlases. It should be noted that the subcortical GM background and the thalamus parts are segmented using a hard segmentation in the atlas space and then propagated to the subject image, as these regions are difficult to differentiate in early preterm brains. The initial labels and the ones resulting from the subdivision are presented in Figure 4.3. The 50 atlas labels are subdivided into 87 labels. Once the EM estimation has converged, the subdivided parts of the structures are merged.

4.3.4 Markov Random Field regularization

MRF regularization is modelled as in the previous chapter (Equation 3.6). The spatial proximity is automatically defined from the atlases. A pair of structures is defined as "neighboring" if the structures have neighboring voxels in at least one set of atlas labels. Since the atlases did not differentiate the WM/CGM structures into WM, CGM, these parts were automatically subdivided prior to the definition of the neighboring structures.

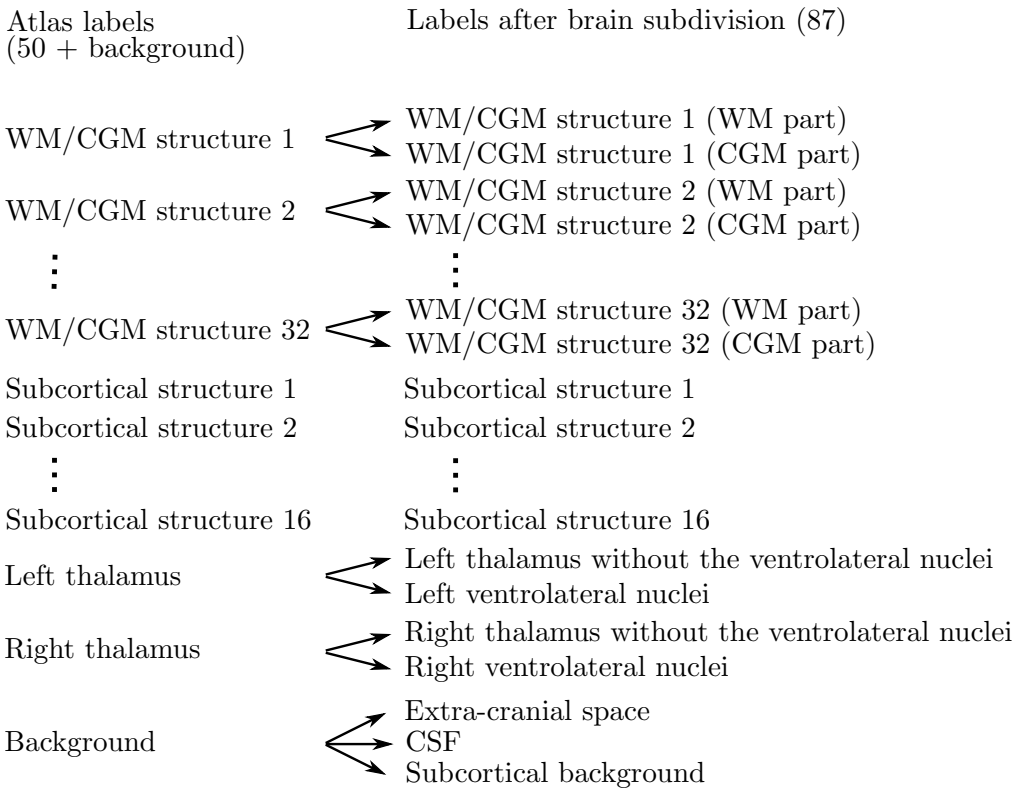

Figure 4.3: Initial labels of the atlases and labels after the subdivision.

Here A_{kj} is defined as:

$$A_{kj} = \begin{cases} 0, & \text{if structure } k \text{ is the same as } j \\ a, & \text{if structure } k \text{ is neighbouring } j, \\ & \quad \text{and both } k \text{ and } j \text{ belong to WM/CGM} \\ b, & \text{if structure } k \text{ is neighbouring } j, \\ & \quad \text{and either } k \text{ or } j \text{ do not belong to WM/CGM} \\ c, & \text{if structure } k \text{ is distant from } j \end{cases}$$

with $a < b < c$. To preserve the propagated anatomical information at the boundaries between the WM/CGM structures while removing isolated voxels, a weak smoothing is allowed here to alter the boundaries between these structures. The connectivity strength parameters were empirically set to $a = 1$, $b = 3$, $c = 5$.

4.3.5 Superlabels

The WM/CGM structures on the atlases were parcellated according to the position of the sulci and gyri. Therefore, the boundaries between these regions are determined by anatomical landmarks and not according to intensity. In the standard EM formulation, the different structures that belong to the same tissue (WM, CGM) compete with each other based on their prior and intensity likelihoods. As a result, the WM part of a WM/CGM structure can expand into the space of neighboring WM parts (and the CGM part of a WM/CGM structure can expand into the space of neighboring CGM parts) driven by its intensity likelihood. To prevent this from happening, we constrain the expansion amongst structures of the same tissue using only the prior probability, by defining a single intensity likelihood for all the divisions of the same tissue.

We define superlabels for the WM and CGM, as aggregations of their subdivisions. Figure 4.4 presents the implemented hierarchical tree of the structures and Figure 4.5 an example of segmented superlabels.

Let the WM regions belong to the WM superclass S_{WM} and the CGM regions to the CGM superclass S_{CGM}. The WM and CGM prior and posterior probabilities are defined as the summation of the prior and posterior probabilities of their subdivisions (at the Expectation step (Equation 3.2)):

$$\pi_{iCGM} = \sum_{k \in S_{CGM}} \pi_{ik}^{[m+1]}, \;\; p_{iCGM} = \sum_{k \in S_{CGM}} p_{ik}^{[m+1]}$$

$$\pi_{iWM} = \sum_{k \in S_{WM}} \pi_{ik}^{[m+1]}, \;\; p_{iWM} = \sum_{k \in S_{WM}} p_{ik}^{[m+1]}$$

The intensity of each superlabel is described with a single Gaussian (G_{CGM}, G_{WM}) which is updated in the standard Maximization step in equations 3.4-3.5 as an additional class. The superlabel's Gaussian distribution is thus sampled from the whole space of its subdivisions. This allows for a more accurate estimation of the tissue parameters. In order to consider only the prior probabilities for the separation of the WM subdivisions and the CGM subdivisions, the same intensity likelihood is defined for all the subdivisions

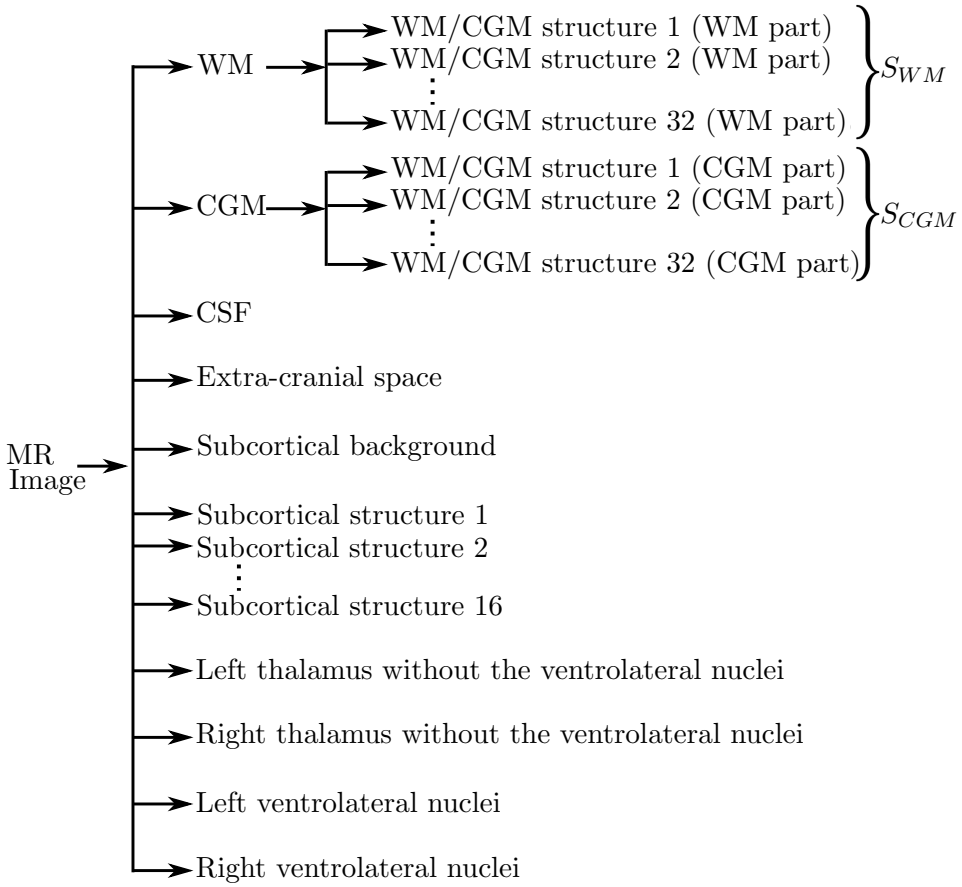

Figure 4.4: Label hierarchy.

of each superlabel as:

$$k \in S_{CGM}:$$
$$P(y_i \mid z_i = e_k, \Phi_y^{[m]}) = P(y_i \mid z_i = e_{CGM}, \Phi_y^{[m]})$$

$$k \in S_{WM}:$$
$$P(y_i \mid z_i = e_k, \Phi_y^{[m]}) = P(y_i \mid z_i = e_{WM}, \Phi_y^{[m]})$$

The segmentation problem is thus reduced to the estimation of $\Phi_h = \{\mu_{H(1)}, .., \mu_{H(k)}, \sigma_{H(1)}, ..., \sigma_{H(k)}\}$, where $|\Phi_h| < |\Phi_y|$. H is a hierarchy function similar to Van Leemput et al. (2009) and indicates the parent of the

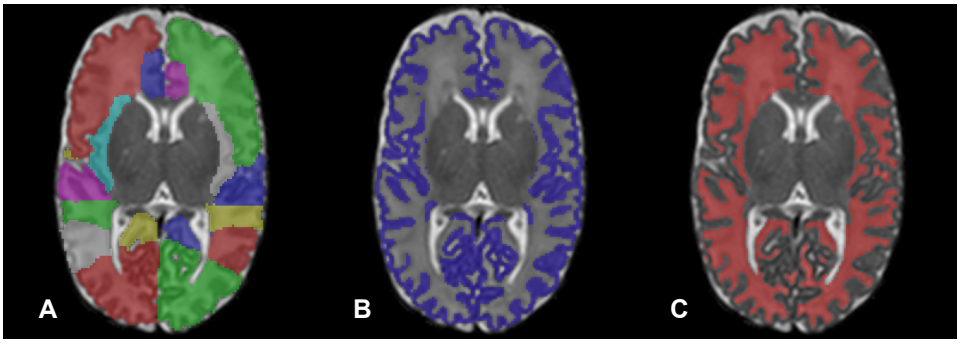

Figure 4.5: Example of segmented WM/CGM structures (A) and the corresponding superlabels for CGM (B) and WM (C) in the axial plane of a T2-weighted MRI.

label in the hierarchical tree of the structures:

$$H(k) = \begin{cases} CGM, & \text{if } k \in S_{CGM} \\ WM, & \text{if } k \in S_{WM} \\ k, & \text{else} \end{cases}$$

The estimation of the Gaussian parameters in the proposed hierarchical framework is similar to the hippocampal subfield segmentation in Van Leemput et al. (2009). Van Leemput et al. (2009) define a global WM, CGM and CSF tissue type with a shared mean and variance over the tissue subparts as proposed here. In the present work the hierarchical model is defined for the whole brain instead of a region of interest (Van Leemput et al., 2009). The proposed hierarchical modelling is further similar to Pohl et al. (2004) where a whole-brain hierarchical model is defined. In Pohl et al. (2004), the Gaussian parameters are estimated for all the substructures. Then the intensity distribution for structures with children is defined as the weighted sum of the intensity distribution of its sub-structures, where the weight is equal to the atlas prior. The hierearchical framework described in this section deviates from the hierarchical modelling in Pohl et al. (2004) in the sense that the Gaussian parameters are estimated from top to bottom in the hierarchy, starting from the superlabels, rather than starting from the substructures.

As shown in Van Leemput et al. (2009), the EM update equations still

hold by setting:

$$P(y_i \mid z_i = e_k, \Phi_y^{[m]}) = P(y_i \mid z_i = e_{H(k)}, \Phi_y^{[m]}) \tag{4.1}$$

4.3.6 CSF-WM Partial Volume correction

The CSF-WM PV correction is performed as described in Section 3.3.7, however is implemented to follow the top to bottom hierarchy described in the previous section. The correction for labels that have subdivisions is initially estimated for the (tissue) superlabels and then passed to their subdivisions with respect to their prior probability:

$$t \in [GM, WM], k \in S_t : \pi'_{ik} = \frac{\pi_{ik}}{\sum_{j \in S_t} \pi_{ij}} \pi'_{it}$$

4.3.7 Model averaging

A challenge in the GMM modelling for multi-class whole brain labelling arises when segmenting the deep grey matter into subcortical structures. These structures are very similar in terms of intensity and the differentiation between them is very difficult. The Gaussian distributions of deep grey matter structures overlap significantly (see Figure 4.7). The problem becomes more significant for images of early preterm infants where the contrast is limited.

To account for this, we model the predictive distribution of the data as model averaging of an ensemble of two models, label fusion and GMM. A weighting scheme reduces the update based on the GMM model in voxels belonging to homogeneous regions (with low gradient with respect to their neighborhood) of the deep GM. In these regions the segmentation is primarily based on label fusion of the atlases. This modelling prevents the expansion of structures in homogeneous areas due to intensity and favors the anatomical definition based on the a-priori information of the propagated labels of the atlases.

The predictive (posterior) distribution p_{ik}^C of the ensemble of models,

indexed by M, with overall parameters $\Phi = \{\Phi_M\}$ can be written as

$$\begin{aligned} p_{ik}^C = P(z_i = e_k \mid y_i, \Phi) &= \sum_M P(M) P(z_i = e_k \mid y_i, M, \Phi_M) \\ &= P(M_{GMM}) P(z_i = e_k \mid y_i, M_{GMM}, \Phi_{M_{GMM}}) + \\ &\quad [1 - P(M_{GMM})] P(z_i = e_k \mid y_i, M_{fus}, \Phi_{M_{fus}}) \end{aligned}$$

where M_{GMM} denotes the GMM model with parameters $\Phi_{M_{GMM}}$ and M_{fus} denotes the fusion model with parameters $\Phi_{M_{fus}}$.

The predictive distribution of label fusion is independent of the intensity modelling of the image. It is effectively equal to the spatial prior formed as the averaged propagated label sets from the atlases:

$$P(z_i = e_k \mid y_i, M_{fus}, \Phi_{M_{fus}}) = \pi_{ik}$$

The weighting of the GMM is spatially defined as $P(M_{GMM}) = \tau_i$. τ_i is set to 1 to allow for the standard EM update with the GMM, except for the subcortical regions where τ is defined as

$$\tau = 1 - (1 + L(\nabla I, \sigma_e))^{-1} \tag{4.2}$$

where ∇I is the gradient magnitude of the image. The L-function represents the robust Lorentzian error norm in Black et al. (1998) with σ_e being a spatially-variant scale calculated in the local neighborhood of the voxels (an example of the weighting factor can be seen in Figure 4.6).

Modelling the segmentation as averaging of label fusion and GMM alters the predictive distribution of the original EM model as

$$p_{ik} = p_{ik}^C = (1 - \tau_i)\pi_{ik} + \tau_i p_{ik} \tag{4.3}$$

The posteriors with the new modelling are updated at each iteration of the modified EM algorithm in the Correction step.

4.3.8 Summary

The proposed EM algorithm for the structural segmentation is outlined in Algorithm 2.

Algorithm 2 The proposed EM algorithm for structural segmentation.

Repeat

Expectation step

$$p_{ik} = \frac{\pi_{ik} e^{-\beta\ U_{MRF}(e_k|N_i)} G(y_i \mid \mu_{H(k)}, \sigma_{H(k)})}{\sum_{j=1}^{K} \pi_{ij} e^{-\beta\ U_{MRF}(e_j|N_i)} G(y_i \mid \mu_{H(j)}, \sigma_{H(j)})}$$

$$t \in [CGM, WM] : p_{it} = \sum_{k \in S_t} p_{ik}$$

Correction step

$$p_{ik} = (1 - \tau_i)\pi_{ik} + \tau_i p_{ik}$$

Detect partial volume voxels i and $c_j, r \in [CGM, WM, CSF, ECS]$ with connected component labelling and update:

$$\pi_{ic_j} = \pi_{ic_j} + (1 - \lambda)\frac{\pi_{ic_j}}{\sum_n \pi_{ic_n}}\pi_{ir}$$

$$\pi_{ir} = \lambda \pi_{ir}$$

$$t \in [CGM, WM], k \in S_t : \pi_{ik} = \frac{\pi_{ik}}{\sum_{j \in S_t} \pi_{ij}}\pi_{it}$$

Maximization step

Calculate parameters Φ_h:

$$\mu_{H(k)} = \frac{\sum_{i=1}^{N} p_{iH(k)} y_i}{\sum_{i=1}^{N} p_{iH(k)}}$$

$$\sigma^2_{H(k)} = \frac{\sum_{i=1}^{N} p_{iH(k)} (y_i - \mu_{H(k)})^2}{\sum_{i=1}^{N} p_{iH(k)}}$$

Until convergence

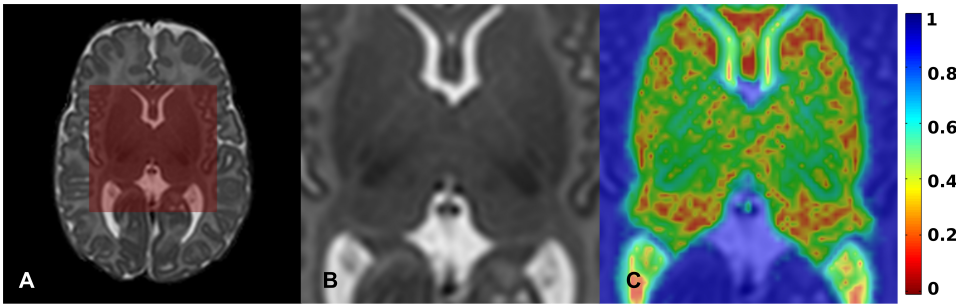

Figure 4.6: Axial slice of a T2-weighted MRI (A), magnified region of the deep grey matter (B) and the weighting of EM in the model ensemble (C). In red areas the segmentation decision is primarily based on label fusion while in blue areas the result is dominated by the GMM model.

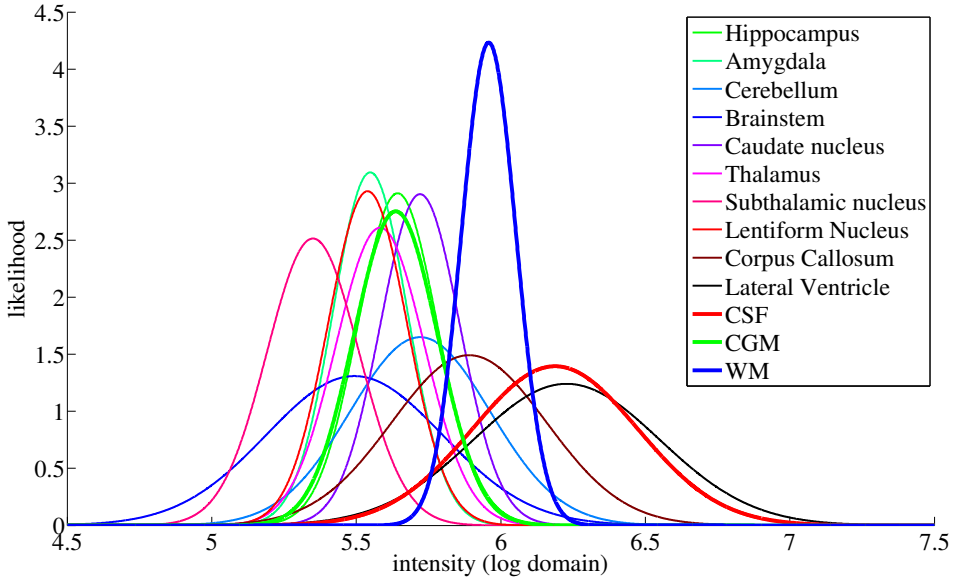

Figure 4.7: Gaussian intensity likelihood of the subcortical structures and the tissues in the log domain (in the T2 space)

4.4 Evaluation

Leave one out cross-validation using the atlases by Gousias et al. (2012) was carried out by specifying in turn one of the atlases as the target and using the remaining atlases to segment it. The atlases were segmented using the proposed EM algorithm and label fusion with both atlas weighting schemes (global and local). The atlas segmentations were carried out on the T1 images as the manual delineations of the atlases are defined in the T1 space

(Gousias et al., 2012). The T2-weighted MR images present a different intensity contrast from the T1-weighted images in the tissue boundaries. Therefore, performing the segmentations in the T1-weighted images allows a more accurate comparison to the gold standard which follows the T1 intensity profile for the structure delineation.

The methods were evaluated with the Dice coefficient to compare overlaps of the automatically computed labels with the manually parcellated gold standard. A primary analysis explores the segmentation accuracy of the two techniques in labelling the whole brain, obtained as the union of the segmented areas with each method. Further exploratory analysis assesses the improvement in regional accuracy of the proposed technique over label fusion. Regional Dice scores are presented in Section 4.4.1.

The atlases are derived from subjects scanned at term and registrations between pairs of atlas images are more likely to succeed given that the morphology of the subjects corresponds to very similar stages of development. However, early preterm brains vary largely in the cortical appearance and subcortical structures compared to the term-equivalent brains. To test performance of the methods across a range of gestational ages, the proposed segmentation scheme was applied to 198 preterm subjects with age ranging from 24^{+3} to 35^{+2} weeks GA and 36 term controls with GA ranging from 36 - 41^{+5}. The segmentations were performed in the T2 images since the T2 intensity profile provides more contrast for the neonatal images between the subcortical GM, unmyelinated WM and cortical GM. The T2 images allow a better intensity characterization and therefore more reliable intensity segmentation. All the 234 segmentations were rated by an observer blinded to the processing method with a scale from 1 to 5 (1=segmentation failure, 2=extensive region inaccuracies/alignment problems, 3=moderate region inaccuracies/alignment problems, 4=regional boundaries inaccuracies, 5=accurate segmentation) with both label fusion and the proposed EM algorithm in the locally-weighted scheme based on 7 equally spaced axial slices. Example segmentations rated with the different scores are presented in Figure 4.8. The rating performance of the 2 techniques is presented in Section 4.4.2.

15 cases were further selected to qualitatively evaluate the method at different scan ages (26^{+5}, 27^{+6}, 28^{+2}, 29, 30, 31^{+1}, 32, 33, 34, 35^{+2}, 36, 37^{+2}, 39^{+6}, 42, 44^{+2} weeks) in all the structures and all the image slices. The

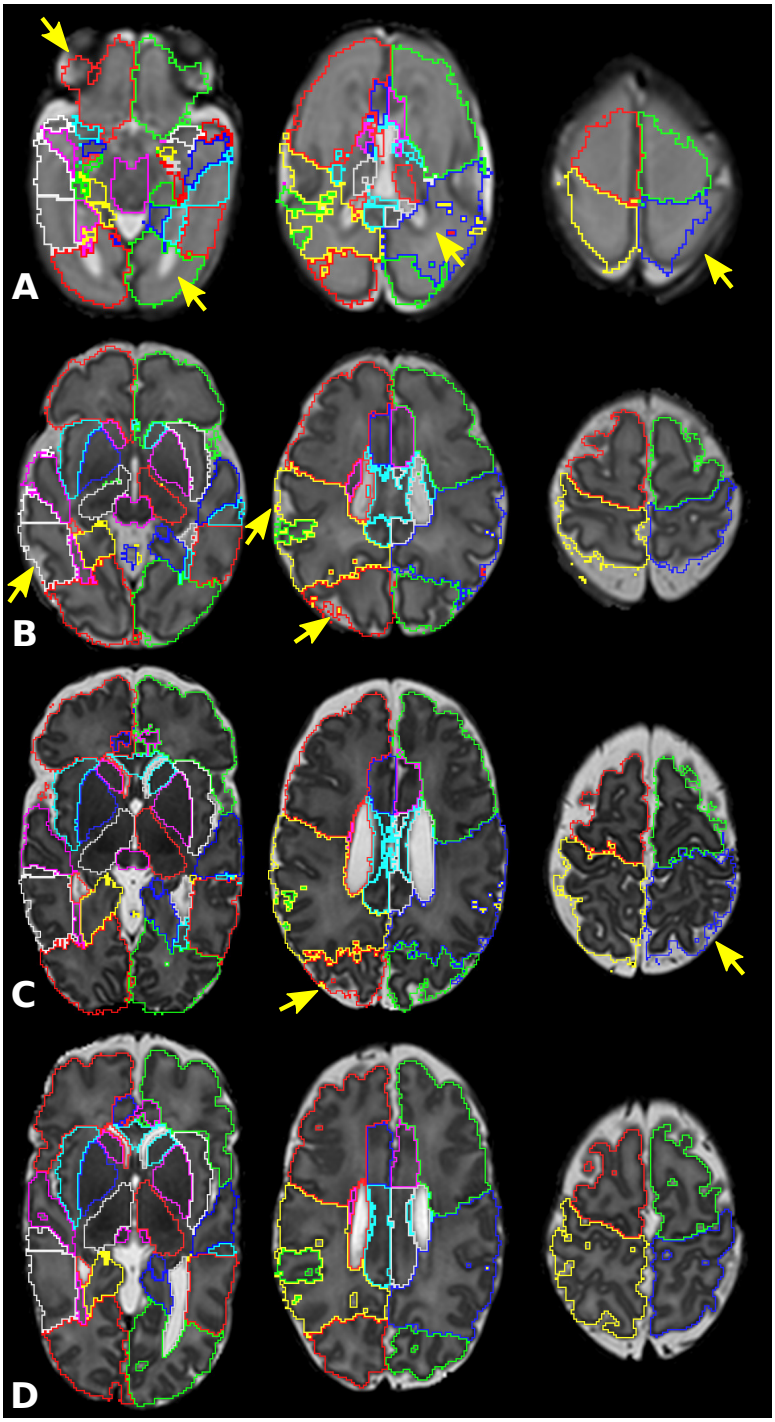

Figure 4.8: Example segmentations rated with the different scores (image A: 2=extensive region inaccuracies/alignment problems, image B: 3=moderate region inaccuracies/alignment problems, image C: 4=regional boundaries inaccuracies, image D: 5=accurate segmentation) All the images in the database could be segmented (no images were rated with 1=segmentation failure). The arrows indicate problematic areas in the segmentations.

qualitative evaluation was based on the region definitions in the protocol used for the manual delineation of the atlases (Gousias et al., 2012). In order to evaluate quantitatively the performance of the proposed algorithm at different gestational ages, the ventricles, frontal and occipital lobe were manually segmented for each of the 15 selected cases. An initial version of the labels was semi-automatically obtained with label fusion and automatic tissue segmentation (Xue et al., 2007). These labels were then refined with manual editing to result in the final labels. The manually segmented cases were compared against label fusion and EM with both weighting schemes. Section 4.4.3 presents the qualitative and quantitative evaluation of the 15 cases. The rater that performed the qualitative assessment and manual segmentations of the data was different from the expert who performed the manual segmentation of the atlases.

Comparison between techniques is performed with two-sided paired t-tests. The results are conservatively adjusted for multiple comparisons using Bonferroni's correction where stated.

4.4.1 Atlas cross-validation

EM significantly ($p < 10^{-4}$) improves the whole-brain segmentation accuracy with a mean Dice score of 0.961 compared to 0.957 obtained with label fusion in the local weighting of the atlases (0.958 over 0.949 with majority vote weighting, $p < 10^{-5}$). The results of the leave-one-out cross-validation of the atlases for all 50 structures are shown in Table 4.4 with both weighting schemes. To allow for an easier comparison, the averaged results of the major WM/CGM and subcortical regions over the two hemispheres are presented in Table 4.2.

Local weighting of the atlases performs significantly better in both label fusion and EM. LW-EM performs equally or better in all structures, with significantly better results ($p < 0.05$) for 36 out of 50 structures with majority vote weighting (24 after Bonferroni correction), and 39 out of 50 structures with locally-weighted voting (25 after Bonferroni correction). The structures with stronger intensity differentiation from their surrounding regions benefit most by using the EM technique, such as the lateral ventricles, hippocampus and corpus callosum and the WM/CGM structures. The boundaries of these structures can be more clearly separated in terms of intensity

Structure	MV-Fusion	MV-EM	LW-Fusion	LW-EM
hippocampus	0.758	**0.772**	0.780	**0.790**
amygdala	0.818	**0.822**	0.820	**0.826**
cerebellum	0.922	**0.925**	0.925	**0.929**
brainstem	0.920	0.922	0.917	**0.922**
caudate nucleus	0.840	0.844	0.843	0.846
thalamus	0.902	0.900	0.901	0.901
subthalamic nucleus	0.741	0.743	0.741	0.744
lentiform nucleus	0.872	**0.874**	0.873	**0.876**
corpus callosum	0.706	0.710	0.717	**0.727**
lateral ventricle	0.790	**0.829**	0.813	**0.838**
frontal lobe	0.918	**0.927**	0.927	**0.932**
occipital lobe	0.850	**0.860**	0.857	**0.860**
WM/CGM structures	0.790	**0.801**	0.802	**0.808**
subcortical structures	0.828	**0.836**	0.835	**0.842**
overall	0.804	**0.814**	0.814	**0.820**

Table 4.2: Dice coefficient of leave one out cross-validation with the atlases. The atlas segmentations are carried out in the T1-weighted images. Fusion and EM are compared with both majority vote (MV) and local weighting (LW) of the training atlases (bold = significantly better at $p < 0.05$).

and are improved with the presented EM technique through the GMM modelling. Label fusion relies on accurate registration of the atlases and does not model the intensity of the structures. However, accurate registration of neonatal brain images is challenging, even in areas of large intensity contrast, due to the large developmental changes. As a result, label fusion is sensitive to misalignments as it cannot remove the intensity outliers in the boundaries of the structures. Segmentation results in areas that boundaries are difficult to identify such as the thalamus, caudate nucleus and subthalamic nucleus are not significantly different to label fusion. In these areas the weighting of label fusion in the model ensemble is increased through the Lorentzian error norm. This avoids expansion of structures into areas without sufficient intensity differentiation. The overall significance of improvement was assessed comparing the average Dice scores of each structure obtained with EM against label fusion. EM is significantly better than label fusion with $p < 10^{-8}$ for global and $p < 10^{-10}$ for local weighting of the atlases.

Another experiment was performed to compare the modelling of the predictive distribution as a model averaging as opposed to the Gaussian Mixture Model formulation alone (essentially the effect of Equation (4.3)). The

results are summarized in Table 4.5. The proposed modelling with the model ensemble results in significantly better overlap for 31 out of 50 structures and worse for one structure with majority vote weighting (better for 22 structures after Bonferroni correction), and significantly better score in 20 out of 50 structures with locally-weighted voting (10 after Bonferroni correction). All of the subcortical structures except for the hippocampus and corpus callosum have significantly better ($p < 0.05$) overlap with respect to the gold standard. Figure 4.9 allows a visual comparison of the results of the atlas cross-validation presented in this section.

4.4.2 Evaluation across the subject cohort

Results of the blinded rating (1-5) of all 234 segmentations of locally-weighted label fusion and the proposed technique are presented in Figure 4.10. The segmentations produced with the presented method are greatly improved with a mean rating of 4.9 across ages compared to 3.8 judged for label fusion. The majority of the segmentations with the proposed EM implementation are rated with 5 (accurate segmentation) at all scan ages (92% of the cases), in contrast to label fusion mostly voted with 4 (regional boundaries inaccuracies) for brains around term (81.9% of the cases) and declines to 3 (moderate region inaccuracies/alignment problems) for early preterm brains (16% of the cases). The increase is consistent and significant ($p < 0.05$) for all the ages with a minimum increase in the rating of 0.9 (for the age of 40 weeks) up to 1.8 (for the age of 30 weeks).

Example segmentations of neonates at 28 weeks, 31 weeks and 32 weeks GA with the two techniques are shown in Figure 4.11. Registration between term-equivalent brains to early preterm brains is challenging, especially in the cortical areas due to different degree of cortical complexity. Utilizing the intensity information, the tissue boundaries are refined (see Figure 4.11.A).

4.4.3 Manually segmented cases

Label fusion and EM were compared in the 15 subjects selected at different scan ages. The method produced segmentations that were judged more accurate than locally-weighted label fusion in an average of 21 out of 26 structures (structures that are defined separately for each hemisphere were merged) in the 15 cases, and equally accurate in the rest of the structures.

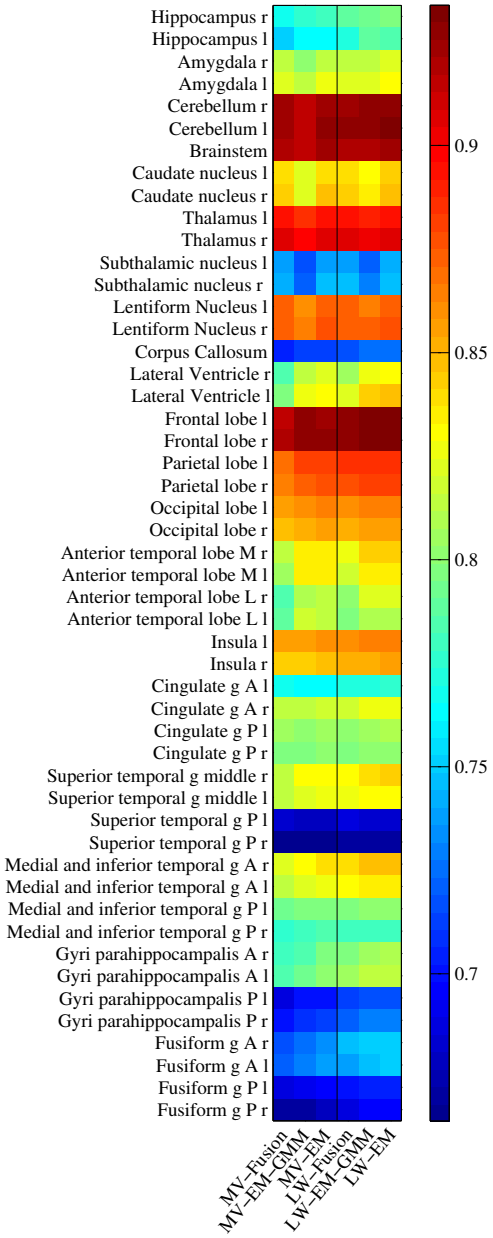

Figure 4.9: Dice coefficient of leave one out cross-validation with the atlases. Fusion, EM with the GMM modelling and the proposed EM (as model averaging) are compared with both majority vote (MV) and local weighting (LW) of the training atlases. The Dice coefficient of each method (columns of the table) for each structure (rows of the table) is represented according to the color scale displayed on the right of the table.

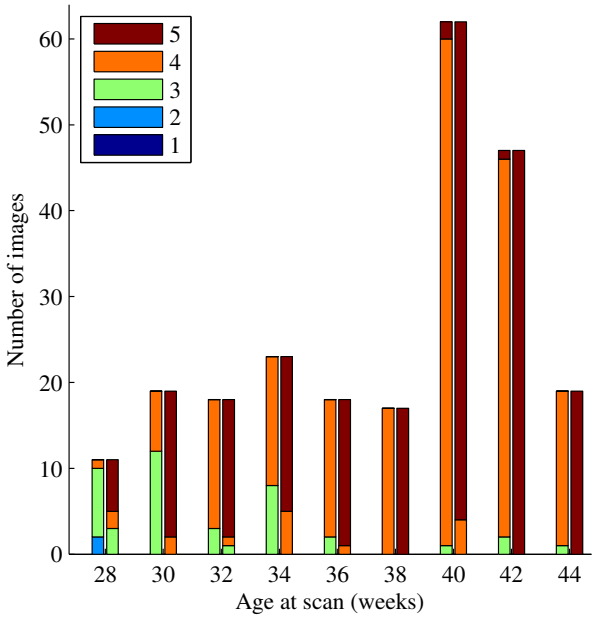

Figure 4.10: Rating (5=best) of label fusion (left columns) and the proposed EM segmentation method (right columns) with local weighting across the scan ages of the cohort. Each age at the horizontal axis covers the span $[age - 1\ week, age + 1\ week)$.

Structure	MV-Fusion	MV-EM	LW-Fusion	LW-EM
lateral ventricle	0.690	**0.821**	0.712	**0.806**
frontal lobe	0.905	**0.952**	0.934	**0.963**
occipital lobe	0.805	**0.870**	0.903	**0.945**

Table 4.3: Dice coefficient of the ventricles, frontal and occipital lobe in the 15 manually segmented cases. Fusion and EM are compared with both majority vote (MV) and local weighting (LW) of the training atlases (bold = significantly better at $p < 0.05$).

Table 4.6 summarizes the qualitative results. The volumetric comparison in terms of the Dice score of the manually segmented cases against label fusion and EM is presented in Table 4.3. The proposed technique significantly outperforms label fusion in the manually segmented regions in both employed weighting schemes.

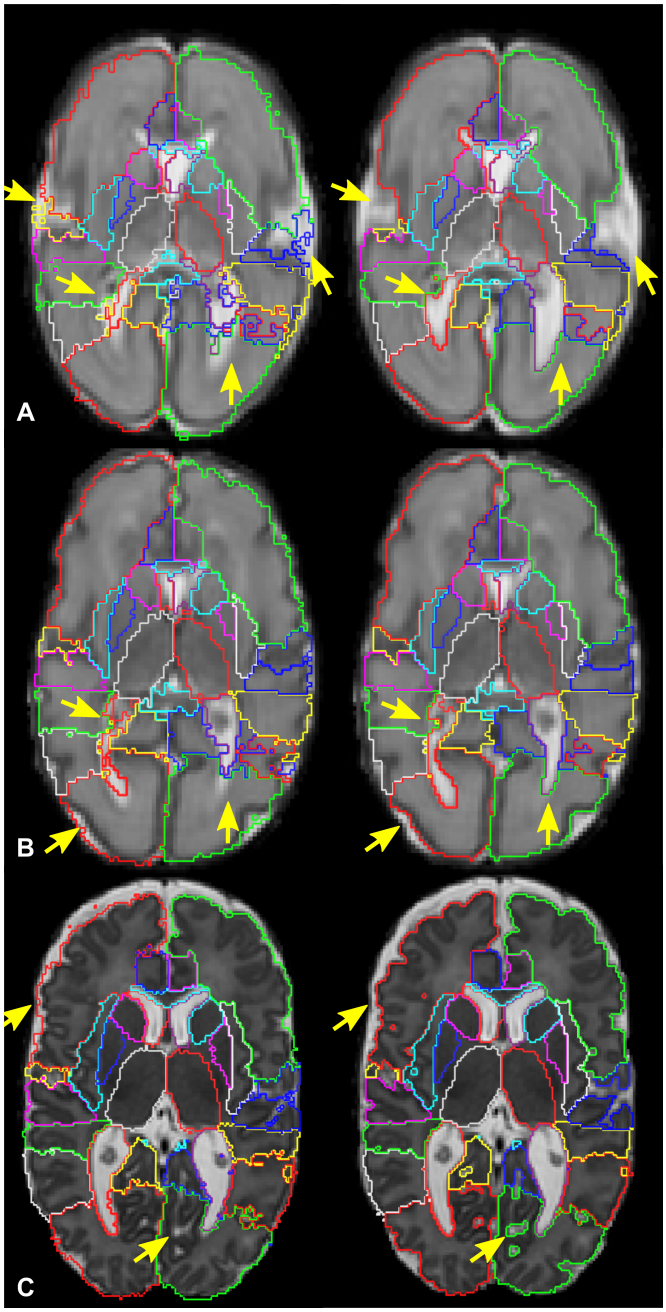

Figure 4.11: Axial slices of T2 weighted MRIs of 28(A), 31(B) and 32(C) weeks GA brains at different scan ages (28, 31, 42 weeks) with labels overlaid. The labels are estimated with label fusion (left images) and the proposed EM scheme (right images). The arrows show areas of improvement with the proposed technique.

4.5 Discussion and conclusions

This chapter presented an automatic segmentation algorithm that allows for the first time detailed parcellation of the neonatal brain from the early preterm period to term equivalent age. In contrast to existing methods for neonatal MR image segmentation, the algorithm performs whole brain intensity-based segmentation into 50 structures, enabling the detailed assessment of regional brain growth and development in these infants.

An EM scheme is adapted to segment a large number of structures simultaneously for the neonatal brain. The proposed method improves the segmentation utilizing the image intensity and provides more accurate results than state of the art techniques used in the segmentation field (majority-vote, local-weighted fusion). The novelties of the EM implementation compared to previous approaches (Van Leemput et al. (1999); Ledig et al. (2012); Lötjönen et al. (2010)) include the hierarchical intensity modelling of the whole brain and constraints allowing for the restriction of the EM update to regions that are difficult to be differentiated from the signal intensity.

A careful modelling was adopted to subdivide the subject's brain MRI into distinct intensity regions that allowed each structure to be modelled with a single Gaussian distribution. Furthermore, a hierarchical approach is introduced to model the WM subdivisions and CGM subdivisions to avoid competition between them in terms of the intensity likelihood. This hierarchical modelling is essential for the segmentation of different structures that belong to the same tissue. Modelling the predictive distribution as a model averaging between label fusion and the GMM prevents subcortical labels from expanding in homogeneous regions. This is essential as in homogeneous areas the intensity distributions of the subcortical structures overlap significantly and this would introduce errors in the segmentations. The model averaging is necessary due to the low contrast in the subcortical space in the neonatal brains, especially in early preterm MR images.

The proposed technique was compared with label fusion, one of the most commonly used techniques, using leave-one-out cross-validation in a global and local weighting of the atlases. A qualitative and quantitative evaluation is further performed in a wide range of gestational ages, from early preterm to term-equivalent, as the atlases cover a spectrum of ages around term equivalent age. The segmentation results are clearly improved over the label

fusion labelling in terms of intensity and regions problematic for registration.

In summary, the proposed framework allows the segmentation of neonatal MR brain images with gestational ages ranging from the early preterm period to term-equivalent age, a time when the developing brain is changing considerably in terms of brain volume, cortical folding and signal intensity on MR images. The EM scheme described in the previous chapter was extended for the segmentation of tissues in order to divide the brain into multiple brain structures. The proposed algorithm outperforms current approaches. This improvement becomes even more significant in the brain of early preterm infants that vary considerably from the brain at term-equivalent age. The next chapter presents a group-wise extension of the algorithm to further encourage a consistent labelling across different images of a database.

Region	MV-Fusion	MV-EM	LW-Fusion	LW-EM
Hippocampus right	0.767	**0.781**	0.788	**0.797**
Hippocampus left	0.749	**0.764**	0.772	**0.783**
Amygdala right	0.813	0.817	0.816	**0.821**
Amygdala left	0.822	**0.828**	0.824	**0.831**
Cerebellum right	0.921	**0.925**	0.924	**0.929***
Cerebellum left	0.922	0.925	0.926	**0.930***
Brainstem, spans the midline	0.920	0.922	0.917	**0.922***
Caudate nucleus right	0.843	0.846	0.844	0.848
Caudate nucleus left	0.837	0.842	0.841	0.845
Thalamus right	0.908	0.907	0.907	0.908
Thalamus left	0.895	0.894	0.895	0.895
Subthalamic nucleus right	0.744	0.746	0.746	0.748
Subthalamic nucleus left	0.738	0.740	0.737	0.740
Lentiform Nucleus right	0.873	**0.876**	0.874	**0.877**
Lentiform Nucleus left	0.871	**0.873**	0.872	**0.874**
Corpus Callosum	0.706	0.710	0.717	**0.727***
Lateral Ventricle right	0.785	**0.822***	0.803	**0.829***
Lateral Ventricle left	0.795	**0.836***	0.822	**0.846***
Frontal lobe right	0.918	**0.929***	0.928	**0.934***
Frontal lobe left	0.917	**0.925***	0.926	**0.930***
Parietal lobe right	0.866	**0.877***	0.876	**0.881**
Parietal lobe left	0.870	**0.883**	0.884	0.887
Occipital lobe right	0.846	**0.856***	0.852	**0.856***
Occipital lobe left	0.854	**0.864***	0.862	**0.865**
Anterior temporal lobe, medial part right	0.815	**0.837***	0.826	**0.842***
Anterior temporal lobe, medial part left	0.806	**0.836***	0.819	**0.834**
Anterior temporal lobe, lateral part right	0.783	**0.814***	0.802	**0.821***
Anterior temporal lobe, lateral part left	0.788	**0.815***	0.797	**0.811***
Insula right	0.843	**0.848***	0.852	**0.856***
Insula left	0.856	**0.860**	0.862	**0.866***
Cingulate gyrus, anterior part right	0.816	**0.819**	0.820	**0.826***
Cingulate gyrus, anterior part left	0.766	0.765	0.770	**0.774**
Cingulate gyrus, posterior part right	0.799	**0.802**	0.798	**0.803***
Cingulate gyrus, posterior part left	0.804	0.806	0.803	**0.808***
Superior temporal gyrus, middle part right	0.816	**0.831***	0.833	**0.841***
Superior temporal gyrus, middle part left	0.816	**0.825***	0.828	**0.832**
Superior temporal gyrus, posterior part right	0.667	0.667	0.671	0.671
Superior temporal gyrus, posterior part left	0.682	0.681	0.686	0.685
Medial and inferior temporal gyri anterior part right	0.821	**0.838***	0.840	**0.847***
Medial and inferior temporal gyri anterior part left	0.814	**0.827***	0.830	**0.836**
Medial and inferior temporal gyri posterior part right	0.777	**0.784***	0.778	0.781
Medial and inferior temporal gyri posterior part left	0.795	**0.799**	0.799	0.800
Gyri parahippocampalis et ambiens anterior part right	0.782	**0.796***	0.797	**0.810***
Gyri parahippocampalis et ambiens anterior part left	0.786	**0.801***	0.805	**0.814***
Gyri parahippocampalis et ambiens posterior part right	0.701	**0.714***	0.721	**0.729***
Gyri parahippocampalis et ambiens posterior part left	0.689	**0.702***	0.712	**0.718**
Fusiform gyrus anterior part right	0.718	**0.734***	0.745	**0.752***
Fusiform gyrus anterior part left	0.721	**0.739***	0.740	**0.749***
Fusiform gyrus posterior part right	0.672	**0.679**	0.688	**0.695***
Fusiform gyrus posterior part left	0.686	**0.696***	0.702	**0.705**

Table 4.4: Dice coefficient of leave one out cross-validation with the atlases. Fusion and EM are compared with both majority vote (MV) and local weighting (LW) of the training atlases (bold = significantly better at $p < 0.05$, *= significantly better after Bonferroni correction).

Region	MV-EM-GMM	MV-EM	LW-EM-GMM	LW-EM
Hippocampus right	0.776	0.781	0.794	0.797
Hippocampus left	0.763	0.764	0.788	0.783
Amygdala right	0.800	**0.817***	0.814	**0.821**
Amygdala left	0.812	**0.828***	0.823	**0.831**
Cerebellum right	0.916	**0.925***	0.927	**0.929**
Cerebellum left	0.915	**0.925***	0.929	0.930
Brainstem, spans the midline	0.914	**0.922***	0.919	**0.922**
Caudate nucleus right	0.824	**0.846***	0.834	**0.848***
Caudate nucleus left	0.822	**0.842***	0.832	**0.845***
Thalamus right	0.900	**0.907***	0.901	**0.908***
Thalamus left	0.886	**0.894***	0.890	**0.895***
Subthalamic nucleus right	0.723	**0.746***	0.729	**0.748***
Subthalamic nucleus left	0.715	**0.740***	0.720	**0.740***
Lentiform Nucleus right	0.865	**0.876***	0.871	**0.877***
Lentiform Nucleus left	0.859	**0.873***	0.866	**0.874***
Corpus Callosum	0.711	0.710	0.727	0.727
Lateral Ventricle right	0.815	**0.822***	0.826	**0.829**
Lateral Ventricle left	0.828	**0.836***	0.844	**0.846**
Frontal lobe right	0.929	0.929	0.934	0.934
Frontal lobe left	0.926	0.925	0.930	0.930
Parietal lobe right	0.874	**0.877***	0.881	0.881
Parietal lobe left	0.881	**0.883**	0.887	0.887
Occipital lobe right	0.853	**0.856**	0.856	0.856
Occipital lobe left	0.862	0.864	0.864	0.865
Anterior temporal lobe, medial part right	0.835	0.837	0.842	0.842
Anterior temporal lobe, medial part left	0.836	0.836	0.833	0.834
Anterior temporal lobe, lateral part right	0.810	0.814	0.821	0.821
Anterior temporal lobe, lateral part left	**0.819**	0.815	0.811	0.811
Insula right	0.844	**0.848***	0.852	**0.856***
Insula left	0.855	**0.860***	0.864	**0.866***
Cingulate gyrus, anterior part right	0.815	**0.819**	0.825	**0.826**
Cingulate gyrus, anterior part left	0.764	0.765	0.773	**0.774**
Cingulate gyrus, posterior part right	0.799	**0.802**	0.803	0.803
Cingulate gyrus, posterior part left	0.803	**0.806**	0.807	0.808
Superior temporal gyrus, middle part right	0.829	0.831	0.841	0.841
Superior temporal gyrus, middle part left	0.824	0.825	0.832	0.832
Superior temporal gyrus, posterior part right	0.664	0.667	0.670	0.671
Superior temporal gyrus, posterior part left	0.681	0.681	0.684	0.685
Medial and inferior temporal gyri anterior part right	0.831	**0.838***	0.847	0.847
Medial and inferior temporal gyri anterior part left	0.824	0.827	0.836	0.836
Medial and inferior temporal gyri posterior part right	0.782	0.784	0.781	0.781
Medial and inferior temporal gyri posterior part left	0.797	0.799	0.799	0.800
Gyri parahippocampalis et ambiens anterior part right	0.783	**0.796***	0.807	**0.810**
Gyri parahippocampalis et ambiens anterior part left	0.791	**0.801**	0.813	0.814
Gyri parahippocampalis et ambiens posterior part right	0.709	**0.714**	0.728	0.729
Gyri parahippocampalis et ambiens posterior part left	0.699	0.702	0.717	0.718
Fusiform gyrus anterior part right	0.726	**0.734***	0.751	**0.752**
Fusiform gyrus anterior part left	0.732	**0.739**	0.749	0.749
Fusiform gyrus posterior part right	0.672	**0.679***	0.694	0.695
Fusiform gyrus posterior part left	0.690	**0.696**	0.705	0.705

Table 4.5: Dice coefficient of leave one out cross-validation with the atlases. The proposed EM as an ensemble of models is compared with the EM with GMM modelling alone with both majority vote (MV) and local weighting (LW) of the training atlases (bold = significantly better at $p < 0.05$, *= significantly better after Bonferroni correction).

Region	26+5	27+6	28+2	29	30	31+1	32	33	34	35+2	36	37+2	39+6	42	44+2
Hippocampus	o	EM	EM	EM	o	o	EM	EM	o	o	EM	o	o	EM	o
Amygdala	EM	o	EM	EM	EM	o	EM	o	o	o	EM	o	o	EM	o
Cerebellum	EM	EM	EM	EM	EM	EM	EM	EM	EM	EM	EM	EM	EM	EM	EM
Brainstem, spans the midline	EM	EM	EM	EM	EM	EM	EM	EM	EM	EM	EM	EM	EM	EM	EM
Caudate nucleus	EM	EM	o	o	EM	EM	EM	EM	EM	o	o	EM	o	EM	o
Thalamus	EM	EM	o	o	EM	EM	EM	o	EM	o	EM	o	EM	EM	o
Subthalamic nucleus	o	o	EM	o	EM	o	o	o	o	o	o	o	o	o	o
Lentiform Nucleus	o	EM	EM	EM	EM	EM	EM	o	EM	o	EM	EM	o	EM	EM
Corpus Callosum	o	EM	EM	EM	EM	EM	EM	o	EM	o	EM	EM	o	EM	o
Lateral Ventricle	EM	EM	EM	EM	EM	EM	EM	EM	EM	EM	EM	EM	EM	EM	EM
Frontal lobe	EM	EM	EM	EM	EM	EM	EM	EM	EM	EM	EM	EM	EM	EM	EM
Parietal lobe	EM	EM	EM	EM	EM	EM	EM	EM	EM	EM	EM	EM	EM	EM	EM
Occipital lobe	EM	EM	EM	EM	EM	EM	EM	EM	EM	EM	EM	EM	EM	EM	EM
Insula	EM	o	EM	EM	EM	o	EM	o	EM	EM	EM	EM	EM	EM	EM
Medial and inferior temporal gyri, anterior part	EM	EM	EM	EM	EM	EM	EM	EM	EM	EM	EM	EM	EM	EM	o
Medial and inferior temporal gyri posterior part	EM	EM	EM	EM	EM	EM	EM	EM	EM	EM	EM	EM	EM	EM	o
Cingulate gyrus, anterior part	o	EM	o	o	EM	EM	EM	o	EM	EM	EM	EM	EM	EM	EM
Cingulate gyrus, posterior part	EM	EM	EM	o	EM	EM	EM	o	EM	EM	EM	EM	EM	EM	EM
Gyri parahippocampalis et ambiens anterior part	EM	EM	o	EM	EM	EM	EM	o	EM	EM	EM	o	o	EM	EM
Gyri parahippocampalis et ambiens posterior part	o	EM	EM	EM	EM	EM	EM	EM	EM	EM	EM	o	o	EM	EM
Fusiform gyrus anterior part	EM	EM	EM	EM	EM	EM	EM	EM	EM	EM	EM	o	EM	EM	EM
Fusiform gyrus posterior part	EM	EM	o	EM	EM	EM	EM	EM	EM	EM	EM	EM	EM	EM	EM
Superior temporal gyrus, middle part	EM	EM	EM	EM	EM	EM	EM	EM	EM	EM	EM	EM	EM	EM	EM
Superior temporal gyrus, posterior part	EM	EM	EM	EM	EM	EM	EM	EM	EM	EM	EM	EM	EM	EM	EM
Anterior temporal lobe, medial part	EM	EM	EM	EM	EM	EM	EM	EM	EM	EM	EM	EM	EM	EM	EM
Anterior temporal lobe, lateral part	EM	EM	EM	EM	EM	EM	EM	EM	EM	EM	EM	EM	EM	EM	EM

Table 4.6: Qualititative comparison of fusion and EM with local weighting of the training atlases. The best segmentation result for each label is presented according to the observer. Labels where the two segmentation techniques are equally accurate are denoted with 'o'.

Chapter 5

Label propagation via Patch-Based Neighbors for neonatal segmentation

5.1 Introduction

Previous studies have demonstrated the increase in segmentation accuracy with the introduction of more labelled datasets (Heckemann et al., 2006; Aljabar et al., 2009). Since manual segmentation of magnetic resonance (MR) images is an extremely time-consuming and expensive process, the number of atlases available for a specific application may be limited. However, large numbers of unlabeled images are often available at a low cost that can be employed to improve the automatic methods. Recent studies focus on ways to extract additional information from the unlabeled images to complement the prior information (e.g. in form of atlases) (Bhatia et al., 2007; Riklin-Raviv et al., 2010; Wolz et al., 2010; Dittrich et al., 2011; Cardoso et al., 2012; Jia et al., 2012).

This chapter proposes a group-wise segmentation technique that is based on the assumption that similar patterns across images should exhibit similar labelling. This assumption is incorporated as a constraint into the EM algorithm presented in the previous chapter. Implicit information of the image appearance in the image ensemble which is not provided by the atlases is derived from the image ensemble, which is utilised to improve the segmentation technique. The proposed technique is tested on a large database of preterm infants, with 420 MR images, with a broad range of scan ages, from 27 to 45 weeks. The group-wise method outperforms the individual segmen-

tation of images both in terms of accuracy when compared to the manual ground truth, and consistency across the database. Due to the very limited number of labeled atlases that exist for the neonatal period and the vast variability in appearance with increasing scan age, additional information to the labelled atlases can be used to improve the automatic segmentation techniques.

5.2 Data acquisition

420 T2-weighted MR images were acquired for 312 infants born at a median (range) GA of 30 (23^{+2} - 42) weeks at birth and imaged at 39^{+1} (27^{+1} - 44^{+6}) weeks PMA at scan. None of the infants had evidence of focal abnormalities on MRI. The median (range) weight at birth of the subjects was 1.23 (0.54 - 4.3) kg and at scan was 2.3 (0.54 - 5.7) kg. The head circumference of the infants at birth was 27 (20 - 38) cm and at scan was 33 (20.5 - 39.6) cm. Ear protection was provided for each infant with earplugs molded from a silicone-based putty (President Putty, Coltene Whaledent, Mahwah, NJ) and neonatal ear protectors (MiniMuffs, Natus Medical, San Carlos, CA). All examinations were supervised by a pediatrician experienced in MRI procedures and pulse oximetry, temperature and electrocardiography data were monitored throughout the procedure. The T2-weighted MR images were acquired using the parameters in Table 2.2.

5.3 Methods

Labelling information is propagated through similar patches of different images. The proposed method in this chapter exploits local image correspondences among a large database of unlabeled images to build a graph for the information propagation. In contrast to previous group-wise segmentation techniques (Wolz et al., 2010; Jia et al., 2012; Bhatia et al., 2007; Riklin-Raviv et al., 2010; Dittrich et al., 2011; Cardoso et al., 2012), the local image correspondences are computed in a patch-based fashion rather than relying on the global alignment accuracy of the images. With this localization, the method is better able to adapt to large variations in images.

The labelling information is then propagated through the graph of images at each iteration of the EM algorithm. The information propagation is

integrated into the EM model presented in the previous chapters with the addition of an inter-image Markov Random Field (MRF) energy, similarly to Sotiras et al. (2009); Rubinstein et al. (2012).

The following sections (5.3.1-5.3.3) present the group-wise segmentation technique in three parts:

- The information propagation through the images in the database.
- The graph construction using global and local image correspondences.
- The group-wise implementation of the information propagation.

5.3.1 Information propagation

The label of each voxel i is dependent on the label assignment of its neighboring voxels $N_{intra}(i)$ in the 3D lattice of the image (here the 6 first-order neighbors). As shown in Chapter 3, the spatial dependency can be introduced into the model with an (intra-image) MRF energy. The proposed group-wise model is based on the assumption that similar patches across images in the database should additionally have a similar labelling. This constraint is implemented with an inter-image MRF energy that regularizes the labelling of the center voxel of the patch to be similar to that of the center voxels $N_{inter}(i)$ of its closest patches, in terms of the patch similarity, in the graph (see Figure 5.1). The prior probability of each structure k with the new MRF energy can be written as :

$$P(z_i = e_k) = \frac{\pi_{ik}\Psi_{intra,ik}\Psi_{inter,ik}}{\sum_{j=1}^{K}\pi_{ij}\Psi_{intra,jk}\Psi_{inter,jk}} \quad .$$

Here $\Psi_{intra,ik}$ and $\Psi_{inter,ik}$ are the intra-image and inter-image MRF energies respectively :

$$\begin{aligned}\Psi_{intra,ik} &= e^{-\beta_{intra}\ U_{MRF}(e_k|N_{intra}(i))} \\ \Psi_{inter,ik} &= e^{-\beta_{inter}\ U_{MRF}(e_k|N_{inter}(i))} \quad .\end{aligned}$$

β_{intra}, β_{inter} are the energy weightings set to $\beta_{intra} = \beta_{inter} = 0.33$ in the experiments. U_{MRF} is defined similarly to Equation 3.7 based on the

neighbors $N(i)$ and the a-priori defined interaction matrix A_{kj}:

$$U_{MRF}(e_k \mid N(i)) = \sum_{j=1}^{K} A_{kj} \sum_{l \in N_{(i)}} p_{lj} \quad .$$

For the sake of simplicity, the neighbor weighting according to the anisotropic voxel spacing is omitted from the notation.

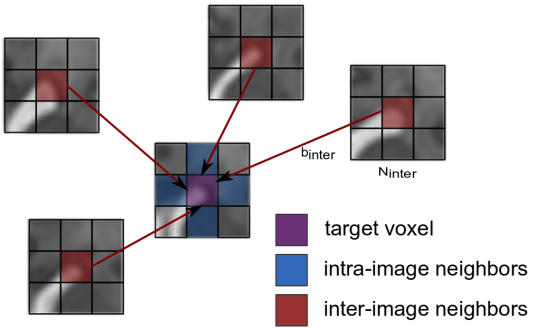

Figure 5.1: Information propagation from the intra-image and inter-image neighbors

5.3.2 Graph construction

The graph for the propagation of information among corresponding patches of the images in the database is constructed in two stages :

- **Coarse Image Correspondence.** The images are initially aligned non-rigidly to the same space, defined by the mid-template (36 weeks) of the spatio-temporal template by Serag et al. (2012) (presented in Section 2.1.2). The nearest neighbors I_{NN} of image $I \in [I_1..I_{N_d}]$ in the database are defined as the most similar in terms of the Normalized Mutual Information (NMI) (Studholme et al., 1999). Since the brain morphology encompasses large changes in terms of shape and appearance with increasing age, the neighbors of the target image were further constrained to be similar in terms of age by limiting the difference in age of the neighbours to a maximum of two weeks.

- **Local Image Correspondence.** Local image correspondences are

computed at the voxel level (after the initial image alignment). For each image I_{NN} the patches for which the center is in the 5×5×5 neighborhood of the center voxel of the target patch are added to the graph. The edge weight of two connected patches in the graph is defined as in Coupé et al. (2011); Rousseau et al. (2011):

$$w_{I,I_{NN}}(i,j) = e^{-\frac{\|P_I(i)-P_{I_{NN}}(j)\|_2^2}{h}} \tag{5.1}$$

where $\| P_I(i) - P_{I_{NN}}(j) \|_2^2$ is the sum of squared intensity differences (SSD) between the patch $P_I(i)$ surrounding voxel i in the target image and the patch $P_{I_{NN}}(j)$ centered at voxel j in image I_{NN}. The locally varying decay parameter h is estimated as proposed in Coupé et al. (2011). The patch size to 5×5×5 in the experiments.

The most similar N_{inter} patches at each voxel were used for the propagation of label information among the images in the database. In order to enforce wide propagation, each of the N_{inter} patches used for a specific voxel was constrained to originate from a different I_{NN} image. In the experiments, the 20 closest I_{NN} images to image I were selected for the label propagation, and consequently the 20 closest N_{inter} patches were selected for each voxel of I (one patch per selected image I_{NN}).

5.3.3 Group-wise implementation

In most multi-atlas segmentation techniques the labelling is estimated independently for each image. Alternative methods interleave the segmentation of the images and the group-wise correction between the images (Bhatia et al., 2007; Wolz et al., 2010; Riklin-Raviv et al., 2010; Jia et al., 2012). Here, the message passing among the images of the database is implemented directly into the segmentation algorithm as in Rubinstein et al. (2012). The group-wise segmentation alternates between the estimation of the intensity model for all the images (in the M-step) and the message passing (in the E-step), where the labelling information (EM posteriors) obtained at the current iteration is propagated to the neighboring patches in the graph. The segmentation of the image ensemble is assumed to have converged once convergence is met for the segmentation of all of the images.

5.3.4 Summary

The proposed EM algorithm for the group-wise structural segmentation is outlined in Algorithm 3.

Algorithm 3 The proposed EM algorithm for group-wise structural segmentation.

Construct the graph for the information propagation.
Repeat

For each image in the collection:

Expectation step

$$p_{ik} = \frac{\pi_{ik}\ e^{-\beta_{intra}U_{MRF}(e_k|N_{intra}(i))}\ e^{-\beta_{inter}U_{MRF}(e_k|N_{inter}(i))}\ G(y_i \mid \mu_{H(k)}, \sigma_{H(k)})}{\sum_{j=1}^{K}\pi_{ij}\ e^{-\beta_{intra}U_{MRF}(e_j|N_{intra}(i))}\ e^{-\beta_{inter}U_{MRF}(e_j|N_{inter}(i))}\ G(y_i \mid \mu_{H(j)}, \sigma_{H(j)})}$$

$$t \in [CGM, WM] : p_{it} = \sum_{k \in S_t} p_{ik}$$

Correction step

$$p_{ik} = (1-\tau_i)\pi_{ik} + \tau_i p_{ik}$$

Detect partial volume voxels i and $c_j, r \in [CGM, WM, CSF, ECS]$ with connected component labelling and update:

$$\pi_{ic_j} = \pi_{ic_j} + (1-\lambda)\frac{\pi_{ic_j}}{\sum_n \pi_{ic_n}}\pi_{ir}$$

$$\pi_{ir} = \lambda\pi_{ir}$$

$$t \in [CGM, WM], k \in S_t : \pi_{ik} = \frac{\pi_{ik}}{\sum_{j \in S_t}\pi_{ij}}\pi_{it}$$

Maximization step

Calculate parameters Φ_h:

$$\mu_{H(k)} = \frac{\sum_{i=1}^{N} p_{iH(k)} y_i}{\sum_{i=1}^{N} p_{iH(k)}}$$

$$\sigma^2_{H(k)} = \frac{\sum_{i=1}^{N} p_{iH(k)} (y_i - \mu_{H(k)})^2}{\sum_{i=1}^{N} p_{iH(k)}}$$

Until convergence

5.4 Results

The proposed method was evaluated on the ALBERTs in terms of segmentation accuracy and in all 420 images in the database for the segmentation consistency. Individual segmentation of the images (without the label propagation) is compared with the group-wise method. This is equivalent to removing the influence of the inter-image MRF term, and reduces to the segmentation of individual images separately as presented in the previous

chapter, i.e. without feedback from the rest of the images in the database. Example segmentations with the group-wise segmentation technique are presented in Figure 5.2.

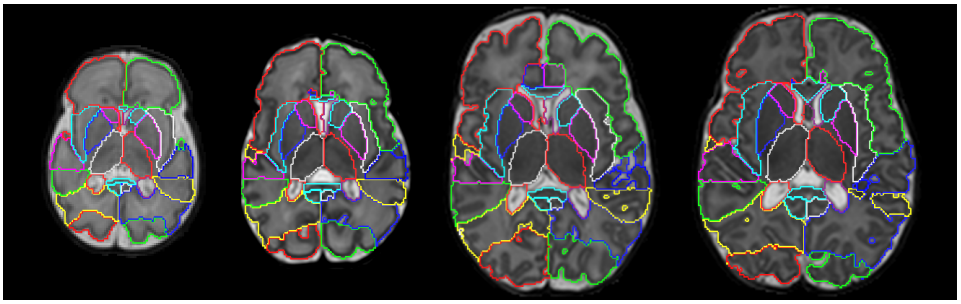

Figure 5.2: Example segmentations with the proposed group-wise segmentation technique at different ages at scan (29, 33, 39 and 44 weeks).

5.4.1 Segmentation accuracy

To assess the segmentation accuracy, the manually labelled atlases were segmented with both methods in a leave one out fashion. The accuracy was measured with the average Dice coefficient of the 50 structures. The proposed group-wise segmentation resulted in an average Dice coefficient of 0.815 which was significantly ($p < 10^{-12}$) higher than the individual segmentation of images (0.807). The results for all structures are presented in Table 5.1. Note that differences in the results of individual segmentation in this chapter to the results of the previous chapter are due to the use of the T2 instead of the T1 space in the segmentation of the ALBERTs. The segmentation with the label propagation resulted in a significantly ($p < 0.05$) better overlap in 36 out of 50 structures (better for 24 structures after Bonferroni correction).

A second experiment was performed to demonstrate the advantage of utilising unlabelled data when the available atlases are limited. The 10 oldest atlases were defined as the training set and used to segment the 10 youngest atlases (test set). The resulting Dice coefficient with the group-wise segmentation (0.805) outperformed significantly ($p < 10^{-7}$) the individual segmentation (0.800). By using all 19 remaining atlases, the accuracy of the individual segmentation increased to 0.803 in the test set. The accuracy was worse than the group-wise method that used only the 10 atlases

as the training data. The proposed method outperforms the individual segmentation of images, as it utilises information from the unlabelled images in the dataset.

5.4.2 Segmentation consistency

To compare the segmentation consistency, the labels of each of the 420 subjects, obtained with the two segmentation techniques, were propagated to the 36 weeks' template of the spatio-temporal atlas (Serag et al., 2012). The mean overall overlap of the labels of an individual subject to all the other subjects in the database is used as a measure of the segmentation consistency. The results of the two methods across different scan ages are presented in Figures 5.3, 5.4. The segmentation consistency across the database increases significantly ($p < 10^{-193}$) from an average Dice of 0.823 to 0.840 with the label propagation. The increase in consistency varies from 0.023 in the early preterm ages (scan age < 32 weeks) to 0.013 in the late term-equivalent period (scan age > 40 weeks).

It should be noted that the consistency of both methods decreases as the subjects' ages deviate from the 36-44 weeks range. This is expected as this is the range of ages for which the 20 manually labelled atlases are available.

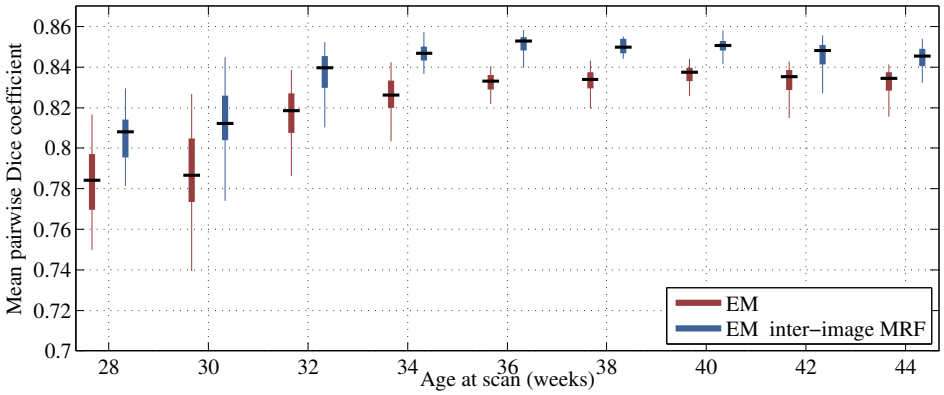

Figure 5.3: Segmentation consistency in different ages with and without the introduction of the inter-image MRF term presented with boxplots.

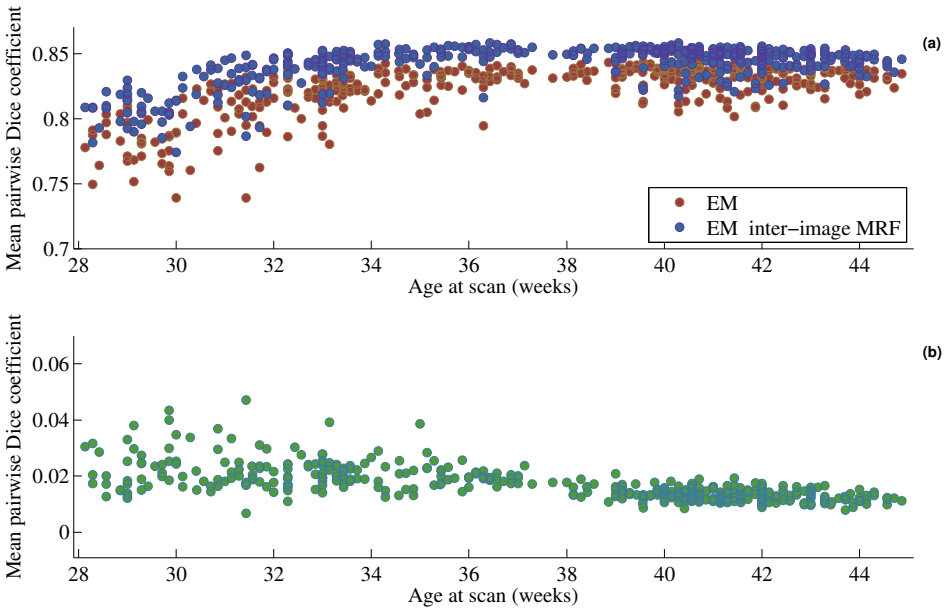

Figure 5.4: Segmentation consistency in different ages with and without the introduction of the inter-image MRF term (a). The increase in consistency with the proposed group-wise technique is depicted in (b).

5.4.3 Computational requirements

The group-wise segmentation has increased computational requirements over the individual segmentation of images. Each image of the database needs to be embedded in the graph which takes approximately 100 minutes. Computation of the inter-MRF term for the different structures takes around one minute (run in parallel) at each E-step. This increases the overall segmentation time from less than 30 minutes for the individual segmentation to around 2 hours for the group-wise segmentation. The execution time is reported here for $N_{inter} = 20$. Increase in the number of N_{inter} neighbors will result in (linear) increase in the computation time. The inter-MRF term further requires additional memory over the individual segmentation and needs to store in memory one image per structure.

5.5 Discussion and conclusions

This chapter presented a method that improves the segmentation by incorporating additional information from unlabeled images available at a

Region	EM	EM inter-image MRF
Hippocampus right	0.770	**0.780**
Hippocampus left	0.787	**0.794**
Amygdala right	0.833	0.831
Amygdala left	0.822	0.825
Cerebellum right	0.903	**0.911**
Cerebellum left	0.906	**0.912***
Brainstem, spans the midline	0.899	**0.901**
Caudate nucleus right	0.844	0.845
Caudate nucleus left	0.844	0.844
Thalamus right	0.893	0.893
Thalamus left	0.905	0.905
Subthalamic nucleus right	0.741	0.735
Subthalamic nucleus left	0.744	0.748
Lentiform Nucleus right	0.876	**0.879**
Lentiform Nucleus left	0.878	**0.881**
Corpus Callosum	0.697	0.698
Lateral Ventricle right	0.834	0.832
Lateral Ventricle left	0.821	0.819
Frontal lobe right	0.907	**0.920***
Frontal lobe left	0.912	**0.925***
Parietal lobe right	0.861	**0.876***
Parietal lobe left	0.857	**0.871***
Occipital lobe right	0.846	**0.856***
Occipital lobe left	0.840	**0.852***
Anterior temporal lobe, medial part right	0.825	0.829
Anterior temporal lobe, medial part left	0.817	**0.827**
Anterior temporal lobe, lateral part right	0.778	**0.788**
Anterior temporal lobe, lateral part left	0.791	**0.804**
Insula right	0.854	**0.869***
Insula left	0.847	**0.861***
Cingulate gyrus, anterior part right	0.755	**0.767**
Cingulate gyrus, anterior part left	0.805	0.810
Cingulate gyrus, posterior part right	0.793	**0.807***
Cingulate gyrus, posterior part left	0.784	**0.798***
Superior temporal gyrus, middle part right	0.816	**0.829***
Superior temporal gyrus, middle part left	0.825	**0.834**
Superior temporal gyrus, posterior part right	0.675	**0.691***
Superior temporal gyrus, posterior part left	0.662	0.665
Medial and inferior temporal gyri anterior part right	0.824	**0.833***
Medial and inferior temporal gyri anterior part left	0.835	**0.842***
Medial and inferior temporal gyri posterior part right	0.789	**0.798***
Medial and inferior temporal gyri posterior part left	0.775	**0.785***
Gyri parahippocampalis et ambiens anterior part right	0.801	**0.816***
Gyri parahippocampalis et ambiens anterior part left	0.788	**0.801***
Gyri parahippocampalis et ambiens posterior part right	0.705	**0.725***
Gyri parahippocampalis et ambiens posterior part left	0.715	**0.732***
Fusiform gyrus anterior part right	0.743	**0.759***
Fusiform gyrus anterior part left	0.738	**0.749***
Fusiform gyrus posterior part right	0.699	**0.710**
Fusiform gyrus posterior part left	0.683	**0.696***

Table 5.1: Dice coefficient of leave one out cross-validation of the ALBERTs with and without the introduction of the inter-image MRF term (bold = significantly better at $p < 0.05$, *= significantly better after Bonferroni correction).

low cost to complement the labelling information provided by expert human raters. Local correspondences are computed among the images in a patch-based fashion which are then used to build a graph that allows the propagation of information across images. The labelling information at each voxel is propagated to similar patches in the graph across different images with the introduction of an inter-image MRF energy.

The proposed group-wise segmentation technique was evaluated with atlas cross-validation and significantly improves the segmentation accuracy over the individual segmenatation of the atlases. This improvement persists even when only half of the atlases are used as training data. The group-wise segmentation technique was further tested on a large neonatal database and increases the segmentation consistency throughout the different images. However, the segmentation of the images individually requires less memory and execution time.

Chapter 6

Accurate delineation of the cortex in neonates

6.1 Introduction

Accurate delineation of the cortex in the neonatal brain is challenging due to partial volume effects and limits in the MRI resolution. A partial volume correction technique for the CSF-WM PV effect was presented in Chapters 3 and 4. Partial volume effects are also evident at the CGM-WM boundary. The interior cortical boundary is difficult to delineate as the CGM-WM PV can lead to overestimation of the segmented CGM. Furthermore, accurate delineation of the exterior cortical boundary is challenging. The complexity of the cortical surface in conjuction with limits in the MRI resolution render the sulci delineation in neonatal MRI problematic. Especially in areas where cortical gyri "touch" each other there is often very little evidence, in terms of intensity, of the CSF inside the sulcus (see Figure 6.1). Surface measurements are affected from undetected sulci, e.g. such as increased cortical thickness estimates. Only a few segmentation approaches focus on delineating the cortical ribbon in terms of morphology in the neonatal population (Xue et al., 2007; Wang et al., 2011, 2012b, 2013). Xue et al. (2007) employ an implicit surface evolution technique to reconstruct the cortical surface in neonates. Wang et al. (2011) define a coupling function of the inner and outer cortical surface that maintains the distance, in essence thickness, within a predefined range. Wang et al. (2012b, 2013) extend this approach with the introduction of a longitudinal cortical constraint term to

drive a consistent cortical segmentation throughout the age of the subject. However, to the best of our knowledge, there are not any approaches that attempt to specifically detect and delineate the cortical sulci in the neonatal population.

This chapter presents:

- A CGM-WM PV correction that reduces the CGM overestimation, and improves the interior cortical boundary. The CGM-WM PV correction is described in Section 6.2.1.
- A novel approach for cortical sulci correction in voxel-based segmentation methods, that improves the exterior cortical boundary. The sulci correction is based on the assumption that the thickness of the cortical ribbon is locally consistent. The thickness estimation is outlined in Section 6.2.2 and the sulci detection and enhancement in Section 6.2.3.

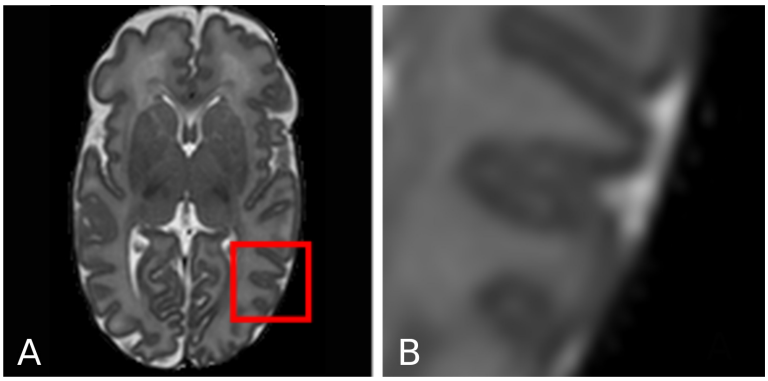

Figure 6.1: Axial slice of a T2-weighted MRI (A) and magnified region of the cortex (B). Due to PV effects, the CSF inside the cortical sulci is often hard to discriminate, and consequently delineate with intensity-based segmentation techniques.

6.2 Methods

6.2.1 CGM-WM Partial Volume correction

Due to the partial volume between WM and CGM in the interface between the two tissues, automatic techniques tend to overestimate the CGM volume. Figure 6.2 depicts this effect. The voxels between WM and CGM have

an intermediate intensity and it is difficult to attribute them to either tissue. A Gaussian Mixture Model (GMM) that assumes one class for WM and one class for CGM tends to overestimate the CGM extent. To account for this effect in Makropoulos et al. (2012b) we implemented a partial volume correction for the CGM-WM boundary.

An additional class is added to the GMM as a partial volume class between CGM and WM. The PV class is approximated with a mixed class similar to Cardoso et al. (2013, 2011). The Gaussian parameters $\mu_{\text{CGM/WM}}, \sigma_{\text{CGM/WM}}$ of the mixed class distribution are initialised as:

$$\mu_{\text{CGM/WM}} = \Gamma_{\text{CGM/WM}}\ \mu_{\text{CGM}} + (1 - \Gamma_{\text{CGM/WM}})\mu_{\text{WM}}$$
$$(\sigma_{\text{CGM/WM}})^2 = \Gamma^2_{\text{CGM/WM}}\ \sigma^2_{\text{CGM}} + (1 - \Gamma_{\text{CGM/WM}})^2\sigma^2_{\text{WM}}$$

where $\Gamma_{\text{CGM/WM}}$ is the average of the fractional content (FC) of the voxels. The FC of a voxel i, $\Gamma_{\text{CGM/WM},i}$, is defined as:

$$\Gamma_{\text{CGM/WM},i} = (\mu_{\text{CGM}} - y_i)/(\mu_{\text{CGM}} - \mu_{\text{WM}})$$

where y_i is the voxel intensity. The average FC value, $\Gamma_{\text{CGM/WM}}$, is calculated over the voxels with $\Gamma_{\text{CGM/WM},i} \in [0, 1]$. The spatial prior $\pi_{i,\text{CGM/WM}}$ of the mixed class is defined as the normalised geometric mean of the CGM and WM posteriors ($p_{i,\text{CGM}},\ p_{i,\text{WM}}$):

$$\pi_{i,\text{CGM/WM}} = \frac{\sqrt{p_{i,\text{CGM}}\ p_{i,\text{WM}}}}{0.5}$$

Once the Expectation-Maximization scheme has converged, the PV class is merged with the WM class to reduce the CGM overestimation and enhance the WM tissue estimate.

6.2.2 Cortical thickness estimation using Laplace's equation

Voxelwise cortical thickness is estimated as described in Jones et al. (2000). In this approach, a potential field from the CGM-WM interface to the CGM-CSF interface is determined by solving the Laplace's equation:

$$\nabla^2\psi = \frac{\delta^2\psi}{\delta x^2} + \frac{\delta^2\psi}{\delta y^2} + \frac{\delta^2\psi}{\delta z^2} = 0 \tag{6.1}$$

where $\psi = \psi_1$ in voxels labelled as CSF and $\psi = \psi_2$ in the WM voxels.

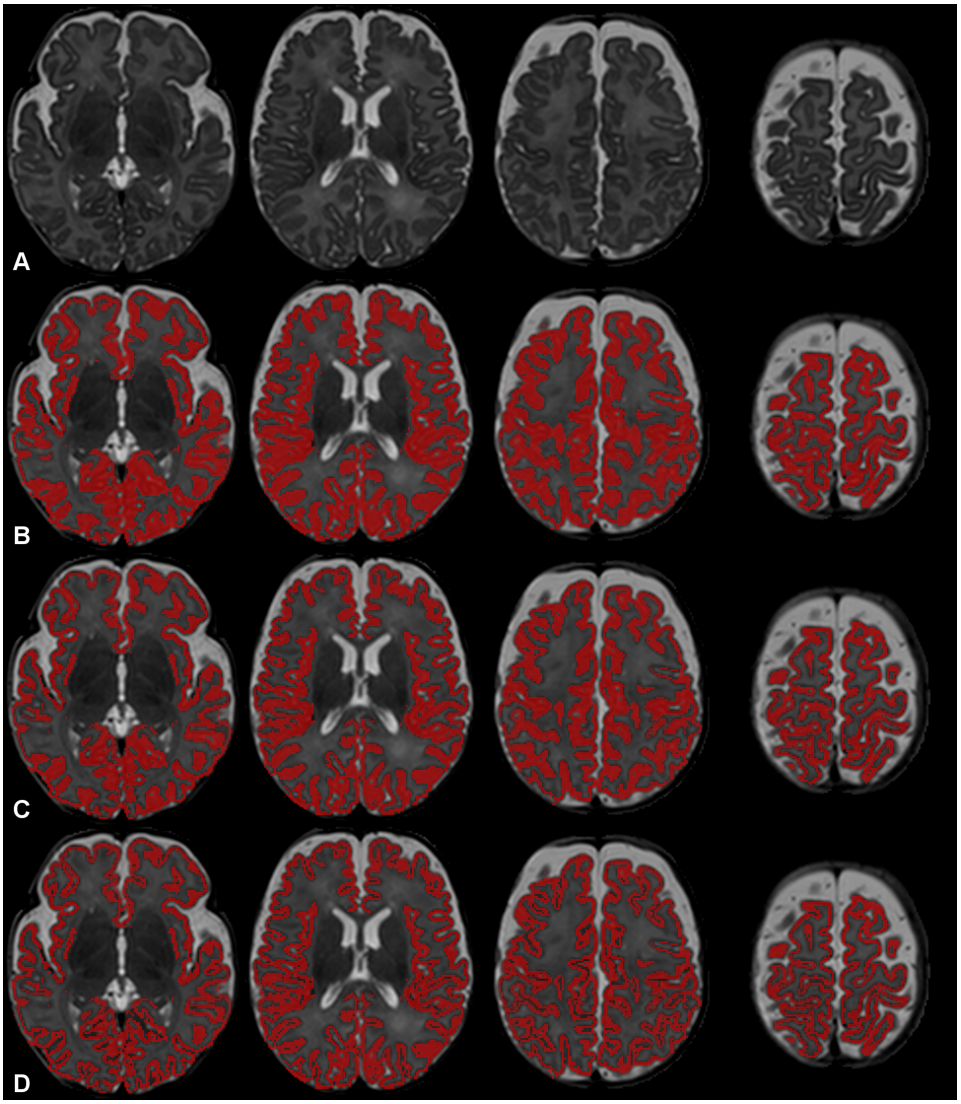

Figure 6.2: Example segmentations of a neonatal MRI acquired at 44 weeks (A). B presents the original segmentation with the standard Gaussian Mixture Model. C is obtained with the CGM-WM Partial Volume correction, reducing the CGM oversegmentation. D illustrates the final segmentation after the sulci delineation.

The potential field defines nonintersecting intermediate lines, or isopotentials, between the inner and outer cortical surface, essentially dividing the cortical ribbon into layers. Streamlines are calculated for the CGM voxels starting from each voxel on the cortical ribbon and following the direction perpendicular to the isopotentials, $E = -\nabla\psi$ (see Figure 6.3). The distance

of a voxel i to WM, $D_{WM,i}$, is defined as the length of the streamline that starts at the voxel location and ends at the CGM-WM interface. Accordingly, the distance of a voxel to CSF, $D_{CSF,i}$, is defined as the length of the streamline that starts at the voxel location and ends at the outer cortical boundary. Voxelwise thickness is then estimated at each voxel as the sum of the voxel's distance to WM and the voxel's distance to CSF. Example streamlines are displayed in Figure 6.4.

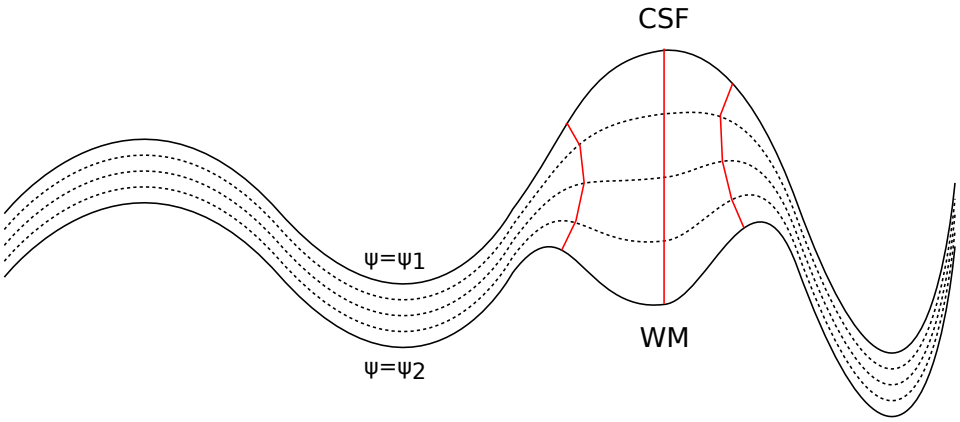

Figure 6.3: Schematic of the cortical thickness estimation using Laplace's equation (Jones et al., 2000) in 2-D. Isopotentials (dashed lines) between the inner and outer cortical surface (normal lines) are determined by solving the Laplace's equation. The cortical thickness at a CGM voxel can then be estimated from the streamline (red lines) that starts from the voxel and follows the direction perpendicular to the isopotentials. The points along the same streamline share the same thickness.

Due to the limited resolution, the cortical ribbon in the two hemispheres may be connected in different parts of the midsection of the brain (an example can be seen in Fig.6.5.A). In order to avoid an artificial increase in the thickness estimation as a result of streamlines crossing the two hemispheres, the voxelwise cortical thickness is estimated separately for each hemisphere. The median cortical thickness of a subject can finally be estimated as the median value of thickness across the central line of the cortex, in essence the intermediate isopotential with $\psi = (\psi_1 + \psi_2)/2$.

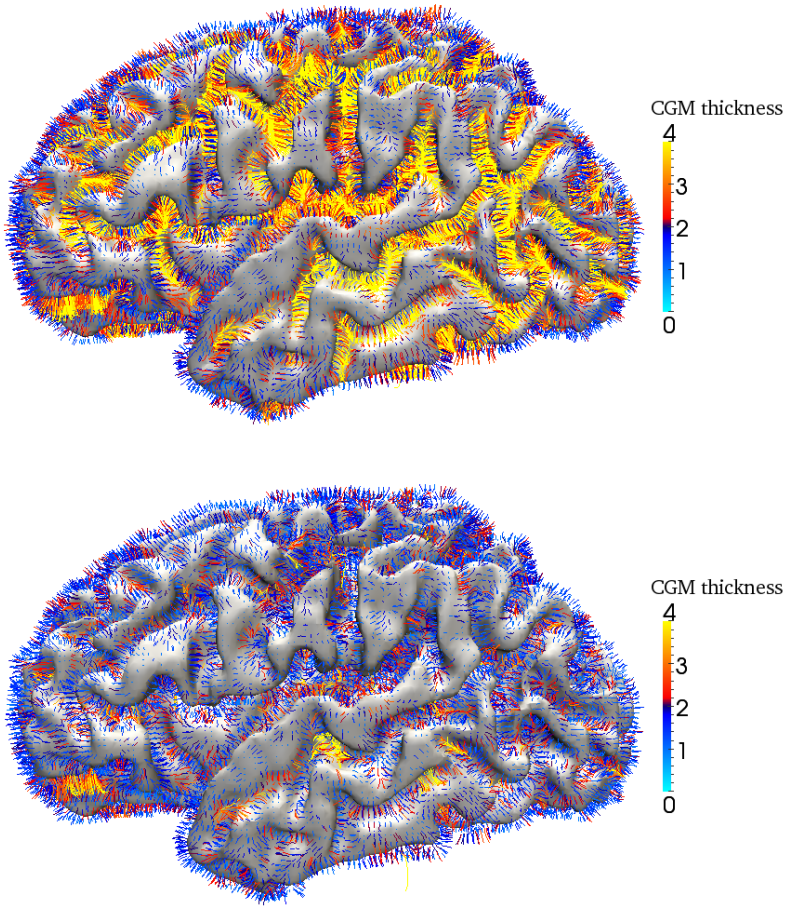

Figure 6.4: Example streamlines starting from the CGM-WM surface and ending at the CGM-CSF boundary. The color of the streamlines represents the length of the streamline (estimated cortical thickness). Notice the difference prior to the corrections (top image) and after the corrections proposed in this chapter (bottom image).

6.2.3 Sulci detection and enhancement

Delineation of the sulci in the neonatal cortex is difficult due to the limited resolution that leads to partial volume effects. This section presents a novel approach for sulci enhancement for the neonatal images, based on the assumption that cortical sulci ought to have similar cortical thickness to neigboring parts of the cortical ribbon.

Sulci detection is performed in a way similar to Han et al. (2004). The

CGM-WM interface (interior cortical surface) is iteratively propagated with the fast marching method with speed defined from the CSF posterior obtained with EM. The distance D_{FMM} to the CGM-WM interface is defined by solving the following Eikonal equation:

$$F(i)\|\nabla D_{FMM}(i)\| = 1$$

where $D_{FMM}(i) = 0$ for voxels in the CGM-WM interface and $F(i) = 1 - 0.9\ p_{i,CSF}$ according to the CSF posterior p_{CSF} of the EM algorithm. The gradient ∇D_{FMM} can subsequently be used to identify "shock" points, points where the spatial derivative is not well defined:

$$S = \{i|\ F(i)\|\nabla D_{FMM}(i)\| <= T\} \quad .$$

Here T is set to 0.8 as in Han et al. (2004). At these points two sulcal banks will merge in the propagated surface and ∇D_{FMM} will be small. A second type of "shock" points is further added here for CGM voxels from different hemispheres that are neighboring each other in the midsection of the brain. As described in the previous section, due to the low CNR, gyri of the two hemispheres appear to be connected in the midsection.

Having detected these points, Han et al. (2004) perform morphological thinning to create a thin layer, one voxel thick, of CSF that splits the two sulcal banks apart. However, defining the CSF inside the sulcus to be one voxel wide might induce an artificial cortical thickness to the points belonging to the sulcal banks. As can be seen in Figure 6.5.B, since the cortical thickness is estimated from the CGM-WM interface to the CGM-CSF interface, the width of the layer of the "shock" points will have a direct effect to the cortical thickness measured in the sulcal regions.

In this work the "shock" voxels are attributed to CSF only if their distance $D_{WM,i}$ to the CGM-WM interface is equal or larger than the cortical thickness of neighboring parts of the cortical ribbon. $D_{WM,i}$ is measured voxelwise as described in the previous section. A distance $D_{allowed,i}$ is then measured for each "shock" voxel as the mean, locally weighted, cortical thickness measured on other points of the cortical ribbon. $D_{allowed,i}$ is only averaged over points that their streamlines do not cross a "shock" point, in essence points that are not inside a cortical sulcus. Connected components of "shock" points, points that belong to the same sulcus, are identified with

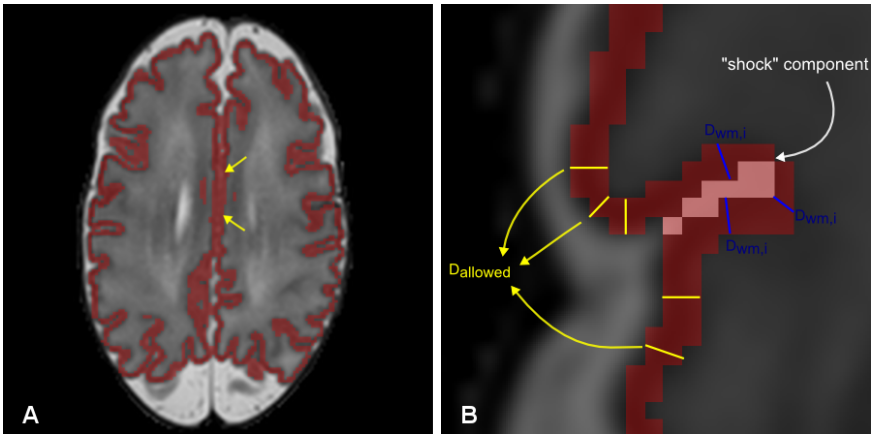

Figure 6.5: A: T2 with the cortical segmentation overlaid. The arrows show parts of the cortical ribbon connected across the two hemispheres in the midsection of the brain. B: Example "shock" points (in pink) detected for the cortical segmentation (in red). "Shock" voxels are labelled as CSF if their distance $D_{WM,i}$ to the WM is equal or larger to $D_{allowed,component}$. $D_{allowed,component}$ is estimated from neighboring parts of the cortical ribbon that their streamlines do not cross "shock" points (yellow lines).

connected component labelling. Points that belong to the same sulcus are then defined to have the same $D_{allowed,component}$, which is the mean $D_{allowed,i}$ of the "shock" points in the component. Finally, "shock" points are labelled as CSF only if their distance to the CGM-WM interface $D_{WM,i}$ is equal or larger than $D_{allowed,component}$. The sulcal points are thus prevented from having an incosistent thickness to the rest of the cortex, since their cortical thickness is approximated based on the thickness of close parts in the cortical ribbon.

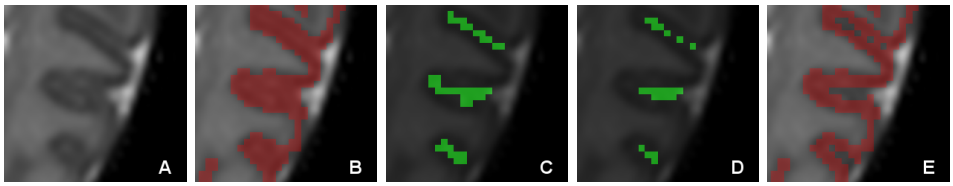

Figure 6.6: Sulci detection and enhancement. The cortical segmentation of the MRI in A is presented in B and E before and after the sulci delineation. "Shock" voxels detected are illustrated in C. The voxels that are finally labelled as CSF (sulci enhancement) are presented in D.

6.3 Results

The method was applied in 420 neonatal T2-weighted scans in a large range of scan ages (27^{+1} - 44^{+6} weeks) and ages at birth (23^{+2} - 42 weeks). The data acquisition details were already presented in Chapter 5. Volumetric and surface analysis of the data is described in detail in the next chapter. The CGM oversegmentation caused by a Gaussian Mixture Model that assumes one class for WM and one class for CGM can be observed in Fig. 6.7. Without the introduction of the CGM-WM partial volume correction, the segmentation tends to attribute a larger proportion of the brain to the CGM.

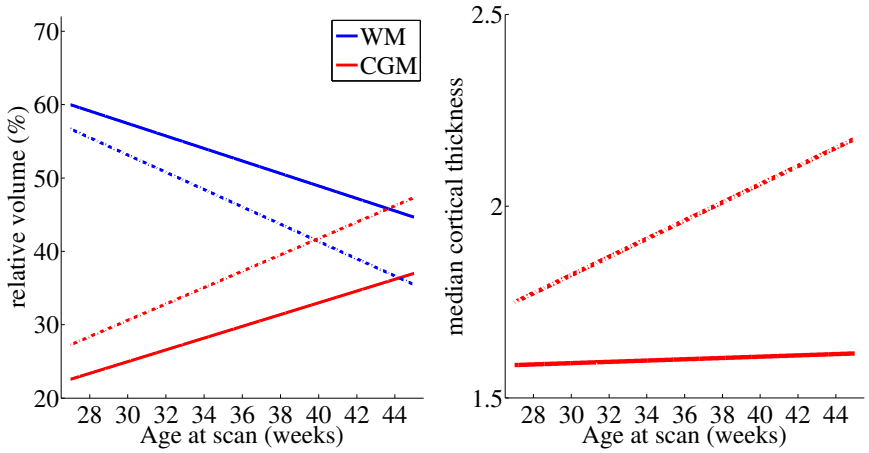

Figure 6.7: Relative WM and CGM volumes (left plot) and cortical thickness (right plot) with increasing age at scan. Dotted lines present the results obtained by a Gaussian Mixture Model that assumes one class for WM and one class for CGM. Solid lines present the results including the proposed CGM-WM partial volume correction and sulci correction .

The tissue volumes obtained after the proposed corrections are similar to volumes in the literature evaluated using manual segmentation approaches. Anbeek et al. (2008) provide average tissue volumes (mL) of 13 subjects around term who were born over a wide age range of gestations (gestational age 25.9 - 42.9 weeks, corrected age at test -3.6 - 5.1 weeks): CSF 51.4, CGM 101.2, WM 146.4, BGT 20, Brain 319. Corresponding CGM and WM volumes are obtained here over the scan ages of 36-40 weeks (see Table 7.13 of the next chapter). The CGM in Anbeek et al. (2008) represents about 32% of the brain volume and the WM around 46% of the brain

volume. The relative volumes obtained here are 34% for the CGM and 48% for the WM around term (see Table 6.1). It should be noted that the relative volumes prior to correction for the CGM-WM partial volume and sulci correction were 43% and 40% for the CGM and WM respectively. This overestimation of CGM obtained prior to the corrections is consistent with previous automatic segmentation studies (see Table 6.2). Similar volumes to manual results are further obtained for the early preterm period after the proposed corrections (see Table 6.1). Moeskops et al. (2013) present a relative CGM volume of 18% and relative WM volume of 70% for 10 neonates scanned at 30.8 ± 0.7 weeks age at scan. The relative volumes in our study are 25% for the CGM and 57% for the WM around 30 weeks age at scan (prior to the corrections the relative CGM and WM were 31% and 52% respectively).

	early preterm period	term period
manual	CGM:18%, WM:70%	CGM:32%, WM:46%
proposed, prior to corrections	CGM:31%, WM:52%	CGM:43%, WM:40%
proposed	CGM:25%, WM:57%	CGM:34%, WM:48%

Table 6.1: Relative CGM and WM volumes in the early preterm and term period reported using manual segmentation (Moeskops et al. (2013) for the early preterm and Anbeek et al. (2008) for the term period) and the proposed technique with and without correction for the CGM-WM partial volume and sulci correction.

	preterm infants	term controls
Inder et al. (2005)	178 ± 41	227 ± 26
Thompson et al. (2007)	159 ± 41	173 ± 32
Cardoso et al. (2013)	centiles: 120-200	
proposed, prior to corrections	164 ± 42, centiles: 139-184	176 ± 41, centiles: 144-193
proposed	126 ± 31, centiles: 108-140	130 ± 30, centiles: 107-144

Table 6.2: CGM volumes (mL) around term-equivalent age reported with different automatic segmentation techniques (mean ± standard deviation, centiles: 25%-75%).

Median thickness across the subjects in the cohort is presented in Fig.6.7. The cortical thickness estimated using the segmentations without the sulci correction produces an increasing thickness with age at scan. The thickness of the uncorrected segmentations correlates significantly with the age at scan ($p < 10^{-36}$). However, with the introduction of the sulci correction,

the cortical thickness measured over the subjects remains unaffected by the age at scan ($p = 0.07$) of the neonate. The cortical thickness estimated from the segmentations has a median value of 1.59 ± 0.09 mm across the database (the 25th and 75th percentiles are 1.54 and 1.65 mm respectively). Cortical thickness in the neonatal population has been previously presented in Xue et al. (2007); Moeskops et al. (2013) for limited datasets. Moeskops et al. (2013) obtain a median cortical thickness of around 1-1.2 mm for the early preterm brains and Xue et al. (2007) around 1.2-1.4 mm for the neonatal brain. The cortical thickness estimated here remains constant in the neonatal brain, similarly to Xue et al. (2007), with a value around 1.6 mm, from the early preterm period to term-equivalent age. Differences in thickness values can be attributed to the different in-plane resolution of the MRI (Moeskops et al. (2013) have a highly anisotropic resolution, 2 x 0.34 x 0.34mm, while the analysed data have a resolution of 0.86 x 0.86 x 1mm), and different thickness measurement methods (Xue et al. (2007)).

6.4 Discussion and conclusions

Two novel corrections were presented for the detailed delineation of the cortical ribbon in the neonatal brain. The first correction estimates a partial volume class between the CGM and WM which is consequently relabelled as WM in order to limit the over-inclusion of voxels in the CGM tissue. The second correction detects and delineates the cortical sulci that are hard to segment with intensity-based segmentation techniques. The cortical sulci are detected from the expansion of the interior cortical surface as areas of the surface that collapse to each other. The thickness of the detected sulcal areas is then approximated from neighboring parts of the cortical ribbon where the thickness can be accurately measured. Derived volumetric and thickness measures after the application of the method presented in this chapter are similar to measurements obtained from manually segmented data.

Chapter 7

Applications

7.1 Introduction

Volumetric, surface and DTI measurements of the brain provide important information on normal development and have the potential to predict long-term neurodevelopmental performance (Peterson et al., 2003; Inder et al., 2005; Anjari et al., 2007; Counsell et al., 2008; Thompson et al., 2008; Rathbone et al., 2011; Boardman et al., 2010).

Quantitative measurements of the neonatal brain are not yet well characterised. Brain tissue volumes and volumes of large subcortical structures have been reported in the literature (Hüppi et al., 1998b; Murphy et al., 2001; Peterson et al., 2003; Inder et al., 2005; Prastawa et al., 2005; Mewes et al., 2006; Nishida et al., 2006; Zacharia et al., 2006; Gilmore et al., 2007; Song et al., 2007; Thompson et al., 2007; Xue et al., 2007; Anbeek et al., 2008; Dubois et al., 2008b,a; Pienaar et al., 2008; Rodriguez-Carranza et al., 2008; Yu et al., 2010; Cardoso et al., 2013; Wang et al., 2012b; Moeskops et al., 2013). However, most of the studies present results on limited datasets and narrow range of ages at scan (see Table 7.1). Furthermore, tissue volumes are often reported with inclusion of the basal ganglia and thalami, cerebellum or brainstem. Volumetric studies of more detailed brain structures are lacking. Cortical surface measurements in the neonatal population have been presented in a few studies (Kapellou et al., 2006b; Xue et al., 2007; Dubois et al., 2008b,a; Pienaar et al., 2008; Rodriguez-Carranza et al., 2008; Rathbone et al., 2011; Moeskops et al., 2013). Cortical surface area has been reported in Kapellou et al. (2006b); Xue et al. (2007); Dubois

et al. (2008b,a); Pienaar et al. (2008); Rodriguez-Carranza et al. (2008); Rathbone et al. (2011) and curvature measurements in Xue et al. (2007); Pienaar et al. (2008); Rodriguez-Carranza et al. (2008); Moeskops et al. (2013).

Preterm birth is associated with widespread alterations in the neonatal brain. Previous studies have demonstrated reduction in brain volume of preterm infants (Peterson et al., 2003; Inder et al., 2005; Thompson et al., 2007; Ball et al., 2012) and decreased cortical surface area (Ajayi-Obe et al., 2000; Kapellou et al., 2006b). Prematurity has been further associated with diffuse WM micro-structural disturbances, reductions in the WM fractional anisotropy and increases in diffusivity (Hüppi et al., 1998a; Miller et al., 2002; Partridge et al., 2004; Counsell et al., 2006; Anjari et al., 2007; Cheong et al., 2009; Ball et al., 2010, 2012). Similar alterations of DTI measures have been described in animal models of dysmyelination and white matter injury (Song et al., 2002; Wang et al., 2009).

The previous chapters presented an accurate segmentation technique for the regional parcellation of the neonatal brain. This chapter aims to:

- analyse regional brain growth of the developing preterm brain. The segmentation method is applied to an extensive database of 380 T2 images of prematurely born infants at a wide range of ages at scan, from 27 to 45 weeks, and 82 regions of the brain are delineated: 18 subcortical regions, 32 WM and 32 CGM structures. Regional volumetric and cortical surface measurements are derived for the cohort of subjects. Centiles and correlations of the measurements with increasing age at scan are reported.

- investigate the effect of prematurity on volumes and morphology of the cortical ribbon. A group of healthy term-born infants are compared with age-matched preterm infants to evaluate alterations associated with preterm birth. Increasing prematurity is further explored based on all the preterm subjects.

- characterise alterations of the underlying tissue micro-structure as a result of brain maturation and prematurity. DTI data are aligned with the corresponding T2 images of the infants. The segmentation labels are transformed to the DTI space and are used to obtain regional quantitative measures of DTI (FA,ADC,AD,RD). Associations

of these measures with age at birth and age at scan of the subjects are presented.

- construct a spatio-temporal structural atlas with 82 structures of the neonatal brain. Segmentations of 420 neonatal images are propagated to the spatio-temporal template of Serag et al. (2012) to define the average labelling from 28 to 44 weeks age at scan

The data acquisition is decribed in Section 7.2. The data analysis and the derived measurements of the brain are presented in Sections 7.3.1 and 7.3.2 respectively. Section 7.4 presents the results of the analysis with respect to brain development and prematurity. Finally, Section 7.5 outlines the construction of the spatio-temporal structural atlas of the neonatal brain.

Author	N cases (MRI)	Age at birth (GA)	Age at scan	Method	V	SA	C	Notes
Prastawa et al. (2005)	4 (4)			A	✓			CB,BS not sep
Pienaar et al. (2008)	9 (9)	corrected GA: 30-40w		S	✓	✓	✓	BGT not sep
Song et al. (2007)	10 (10)	TEA	TEA	A	✓			BGT,CB,BS not sep
Moeskops et al. (2013)	10 (10)	27±1w	31±1w	M	✓		✓	
Nishida et al. (2006)	12 (12)	31-43w		S	✓			
Anbeek et al. (2008)	13 (13)	26-43w	GA+2w	M,A	✓			
Rodriguez-Carranza et al. (2008)	15 (15)	24-31w	28-37w	S	✓	✓	✓	BGT not sep
Peterson et al. (2003)	24 (24)		35±1, 41w	S	✓			
Xue et al. (2007)	25 (25)	24-40w	27-44w	A	✓	✓	✓	
Dubois et al. (2008b)	25 (25)	26-36w	27-36w	S	✓	✓		CB,BS not sep
Wang et al. (2012b)	28 (28)		TEA	A	✓			BGT,CB,BS not sep
Yu et al. (2010)	30 (30)	23-29w	TEA	S	✓			
Murphy et al. (2001)	25 (25)	23-31w, TEA	TEA	S	✓			CB,BS not sep
Zacharia et al. (2006)	25 (37)	32±1w, TEA	GA, TEA	S	✓			CB,BS not sep
Dubois et al. (2008a)	34 (68)	26-36w	GA, TEA	S	✓	✓		CB,BS not sep
Mewes et al. (2006)	28 (61)	28-33w, TEA	33±2, TEA	S	✓			
Gilmore et al. (2007)	74 (74)	39-48	40±1w	A	✓			
Hüppi et al. (1998b)	78 (78)	28-40w	29-41w	S	✓			CB,BS not sep
Cardoso et al. (2013)	80 (80)	23-32w	TEA	A	✓			
Inder et al. (2005)	140 (140)	32w, TEA	TEA	S	✓			CB,BS not sep
Rathbone et al. (2011)	82 (217)	<30w	24-44w	S		✓		
Thompson et al. (2007)	238 (238)	<30w, TEA	TEA	S	✓			CB,BS not sep
Kapellou et al. (2006b)	113 (274)	22-29w	23-48w	S		✓		

Table 7.1: Tissue volumes and surface measurements of the neonatal brain in the literature.
abbreviations: N cases (MRI)=number of normal neonates (MRI), TEA=term equivalent age, GA=gestational age, M=manual segmentation, S=semi-automatic segmentation, A=automatic segmentation, V=tissue volumes, SA=surface area, C=curvature, w=weeks, BGT=basal ganglia and thalami, CB=cerebellum, BS=brainstem, not sep=not separated from tissues.

7.2 Data acquisition

MRI data of 312 infants were used for the analysis in this chapter. The same cohort of subjects was described in Chapter 5. Inclusion criterion for the infants in this cohort was the absence of focal abnormalities on MRI.

The following MRI data were acquired for the subjects:

- 380 T2-weighted MR images of preterm subjects and 40 of term controls (acquisition parameters are described in Table 2.2). The cohort characteristics for the T2 scans are presented in Table 7.2.
- 210 DTI data of preterm infants and 21 of term controls. Single shot echo planar DTI was acquired in 32 non-collinear directions with the following parameters: TR 8000ms, TE 49ms, slice thickness 2mm, field of view 224mm, voxel size $2\times2\times2mm^3$, b value 750 s/mm^2, SENSE factor 2. The cohort characteristics for the DTI data are presented in Table 7.3.

T2	preterm infants	term controls
number of images	380	40
age at birth (weeks)	29^{+3} (23^{+2} - 36)	39^{+2} (36^{+1} - 42)
age at scan (weeks)	37^{+6} (27^{+1} - 44^{+6})	40^{+6} (37 - 44^{+4})
weight at birth (kg)	1.17 (0.54 - 3.71)	3.42 (1.93 - 4.34)
weight at scan (kg)	2.19 (0.64 - 5.5)	3.48 (1.93 - 4.71)
head circumference at birth (cm)	27 (20 - 38.5)	34.3 (30.2 - 38.7)
head circumference at scan (cm)	31.6 (22 - 39.6)	35.4 (30.2 - 38)

Table 7.2: Cohort characteristics for the T2 images. Median (range) age, weight and head circumference at the time of birth and scan are presented.

DTI	preterm infants	term controls
number of images	210	21
age at birth (weeks)	29^{+5} (23^{+2} - 35^{+4})	39^{+1} (36^{+1} - 42)
age at scan (weeks)	39^{+2} (26 - 45^{+1})	40^{+1} (37 - 44^{+4})
weight at birth (kg)	1.17 (0.56 - 3.71)	3.45 (1.93 - 4.34)
weight at scan (kg)	2.2 (0.68 - 5.67)	3.48 (1.93 - 4.71)
head circumference at birth (cm)	27 (20.5 - 37.5)	34.1 (30.2 - 38.7)
head circumference at scan (cm)	32.25 (20.5 - 39.3)	35.8 (30.2 - 38)

Table 7.3: Cohort characteristics for the DTI data. Median (range) age, weight and head circumference at the time of birth and scan are presented.

7.3 Methods

7.3.1 Data analysis

Image segmentation

The T2 images were segmented with the pipeline presented in Chapter 4 that was extensively validated for different ages of the neonatal brain. The segmentation incorporated the CGM-WM PV correction and cortical sulci detection and enhancement outlined in Chapter 6. Example segmentations of the proposed segmentation technique in an early and term-equivalent brain can be seen in Figures 7.1, 7.2 respectively.

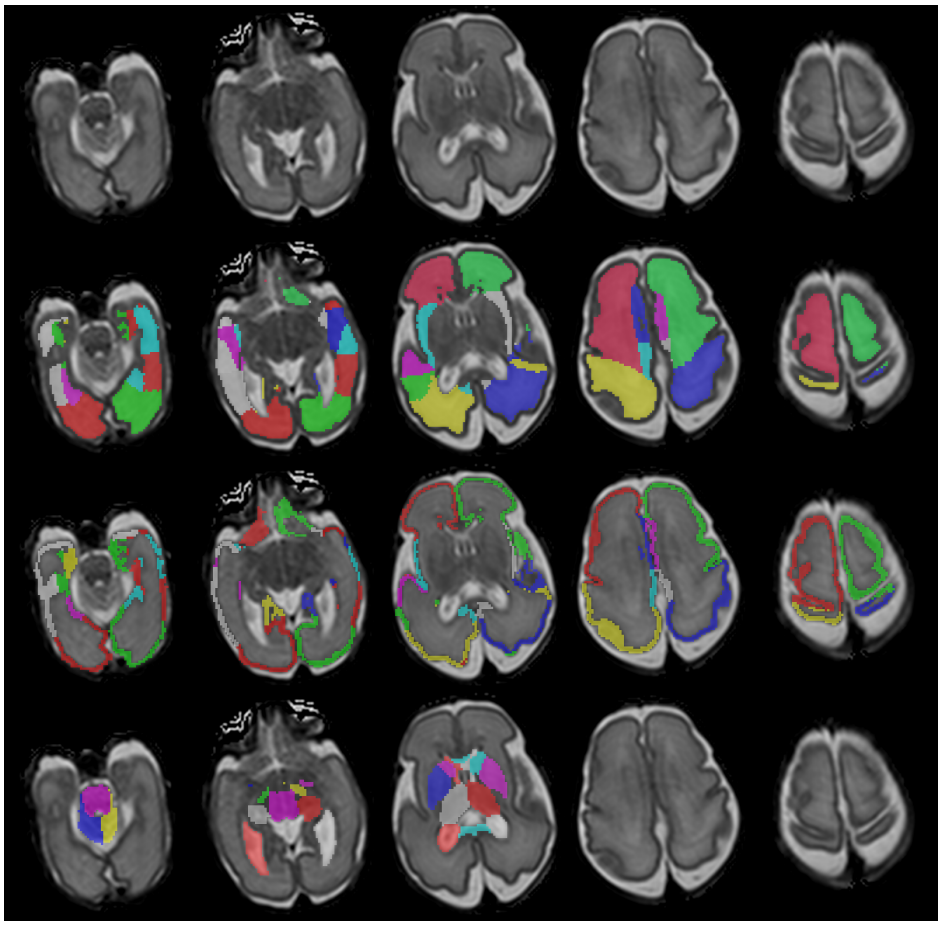

Figure 7.1: Example segmentation of a neonatal MRI acquired at 28 weeks age at scan with the 82 labels overlaid (second row: WM labels, third row: CGM labels, fourth row: subcortical GM labels and ventricles).

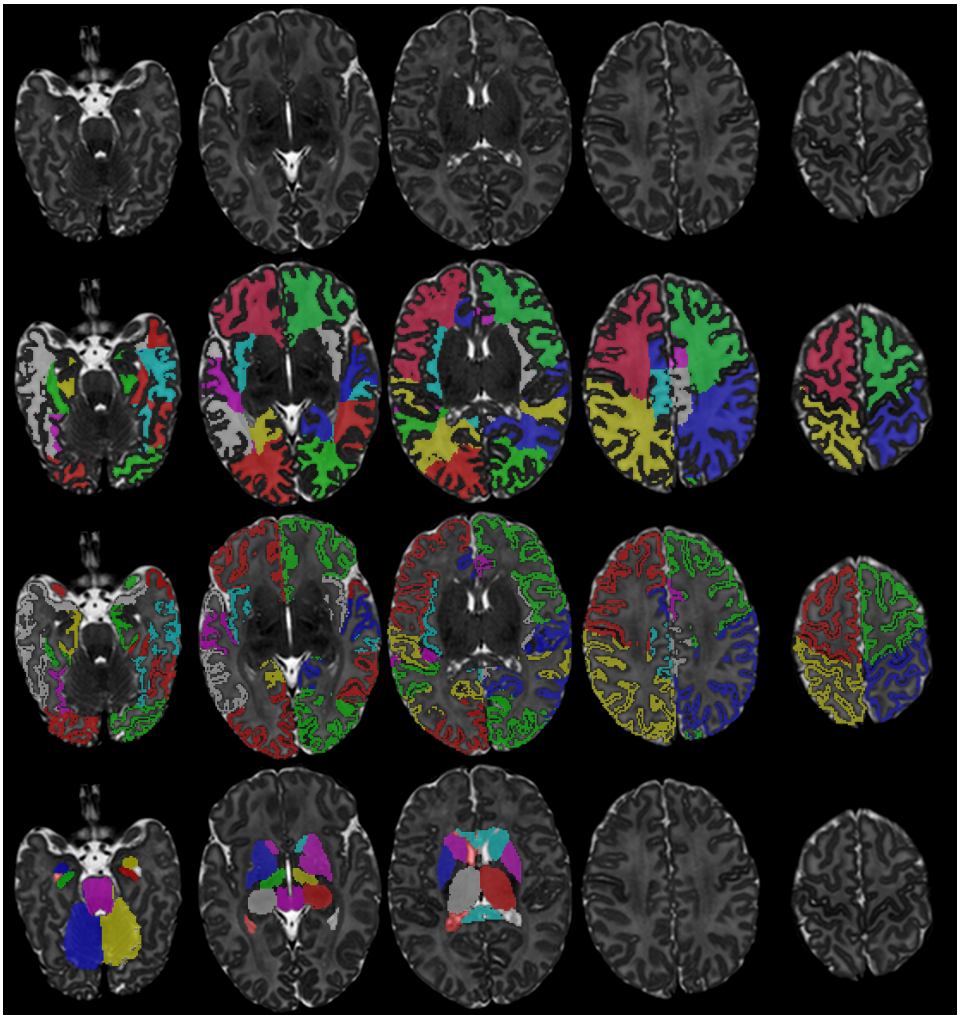

Figure 7.2: Example segmentation of a neonatal MRI acquired at 44 weeks age at scan with the 82 labels overlaid (second row: WM labels, third row: CGM labels, fourth row: subcortical GM labels and ventricles).

Cortical surface reconstruction

Cortical surface meshes were obtained by triangulation of the CGM-WM isosurface with the marching cubes algorithm (Lorensen and Cline, 1987). The surfaces were slightly smoothed with Laplacian smoothing (Herrmann, 1976) to improve the mesh quality. Laplacian smoothing re-estimates the position of each mesh vertex according to its neighboring vertices and distributes the mesh vertices more evenly. The surface region that belongs to the boundary between WM and deep GM was excluded from the cortical surface (see Figure 7.3). Example cortical surfaces are presented in Figure 7.4.

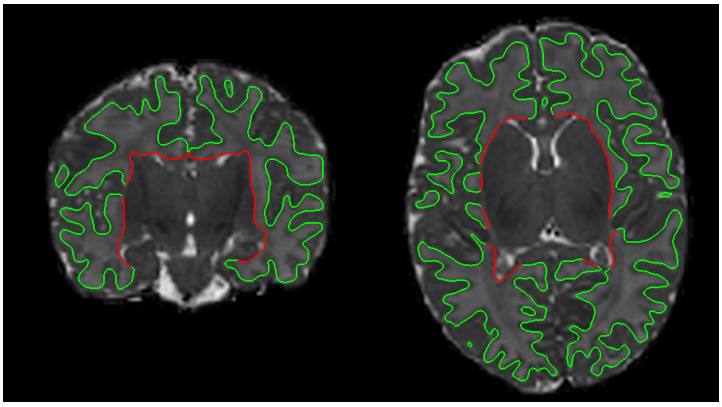

Figure 7.3: Example cortical surface of a neonate at 44 weeks age at scan. The red part of the surface that corresponds to the WM - deep GM boundary is excluded from the cortical surface measurements.

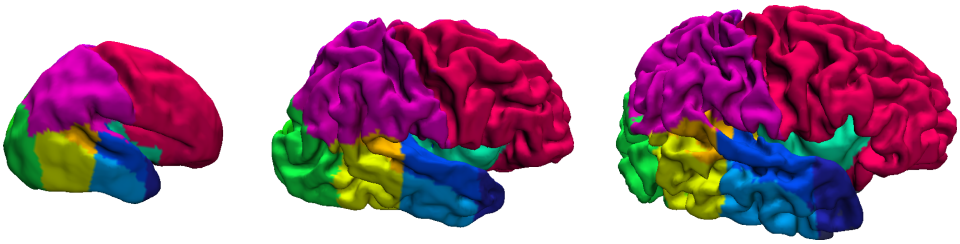

Figure 7.4: Example cortical surfaces for neonates at 28, 36 and 44 weeks age at scan with the labels overlaid.

DTI analysis

Fractional anisotropy (FA), apparent diffusion coefficient (ADC), axial diffusivity (AD), and radial diffusivity (RD) maps were calculated from the DTI datasets with the FSL software (http://fsl.fmrib.ox.ac.uk). The DTI space was aligned to the T2 native space with registration of the RD maps to the T2 images. Echo planar DTI is often degraded from geometric distortions caused by field imperfections due to eddy currents and static magnetic field inhomogeneities (Jezzard and Balaban, 1995; Jezzard et al., 1998). To deal with geometric distortions, the 2 spaces were registered non-rigidly, in order to align the distorted brain regions of the DTI (an example is presented in Figure 7.5). The estimated transformation was used to propagate the segmentation labels from the T2 space to the DTI space.

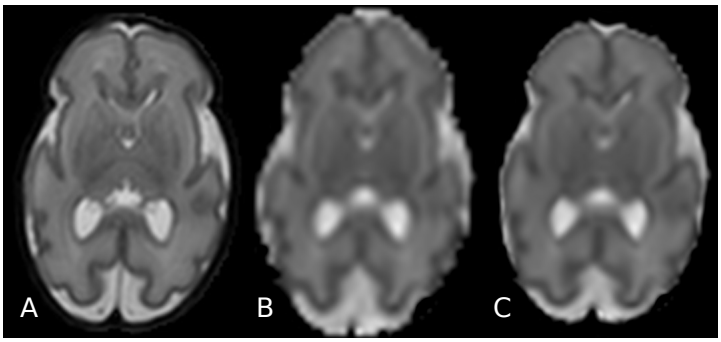

Figure 7.5: Geometric distortions exhibited on the ADC map of a neonatal brain acquired at 29 weeks age at scan. The ADC map that is rigidly registered (B) to the T2 image (A) presents an example of these distortions (evident in the anterior part of the brain). Non-rigid registration of the ADC map (C) improves the alignment to the T2 space.

7.3.2 Measurements of the brain

Volumetric measurements

Absolute and relative volumes of the tissues and 82 structures of the brain were measured directly from the segmentations. Relative volume was determined as the ratio of the structure volume to the total brain volume (excluding the CSF and ventricles).

Cortical surface measurements

Surface area and curvature measures of the cortex were computed from the cortical surface meshes. A number of area-independent curvature measures from Rodriguez-Carranza et al. (2008) were adopted with T-normalization that are not sensitive to the surface area of the brain. This allows comparison of brains with different sizes, as is the case with the developing neonatal brain. The curvature measures included in this study are: global curvedness, mean curvature L^2 norm and Gaussian curvature L^2 norm. Their formulation is presented in Table 7.4.

Regional cortical surface measurements were measured based on the segmented CGM structures. The segmentations were propagated to the surface meshes. Each vertex of the mesh was labelled with the closest CGM structure in the 3-dimensional space.

Global curvedness	$GC_T = \frac{T}{A} \sum_A c$
mean curvature L^2 norm	$MLN_T = \frac{T^2}{A} \sum_A H^2$
Gaussian curvature L^2 norm	$GLN_T = T \sqrt[4]{\frac{1}{A} \sum_A K^2}$

Table 7.4: Area-independent curvature measures.
Notation: H=mean curvature, K=Gaussian curvature, c=curvedness, A=surface area, T=3*volume/A.

DTI measurements

The T2 segmentations were transformed in the DTI space. This allowed measurement of FA, ADC, AD, and RD values regionally. Since the resolution of the DTI is limited, approximately half of the T2 images, small structures were merged into larger regions to obtain more reliable regional estimates. Different structures across the two hemispheres were further merged into a single structure. The insula were excluded from the DTI analysis as the CGM part in early brains is constituted of a small number of voxels (in the diffusion space). DTI measurements were obtained on the structures presented in Table 7.5.

DTI structures	T2 structures
WM/CGM structures	
Frontal lobe	Frontal lobe (left/right)
Parietal lobe	Parietal lobe (left/right)
Occipital lobe	Occipital lobe (left/right)
Temporal lobe	Anterior temporal lobe, medial part (left/right) Anterior temporal lobe, lateral part (left/right) Medial and inferior temporal gyrus, anterior part (left/right) Medial and inferior temporal gyrus, posterior part (left/right) Superior temporal gyrus, middle part (left/right) Superior temporal gyrus, posterior part (left/right)
Fusiform gyrus	Fusiform gyrus, anterior part (left/right) Fusiform gyrus, posterior part (left/right) Gyri parahippocampalis et ambiens, anterior part (left/right) Gyri parahippocampalis et ambiens, posterior part (left/right)
Cingulate gyrus	Cingulate gyrus, anterior part (left/right) Cingulate gyrus, posterior part (left/right)
Subcortical Regions	
Hippocampus	Hippocampus (left/right)
Amygdala	Amygdala (left/right)
Cerebellum	Cerebellum (left/right)
Brainstem	Brainstem
Caudate nucleus	Caudate nucleus (left/right)
Thalamus	Thalamus (left/right)
Sub-thalamic nucleus	Sub-thalamic nucleus (left/right)
Lentiform nucleus	Lentiform nucleus (left/right)
Corpus callosum	Corpus callosum

Table 7.5: Correspondence between the structures defined in the DTI and the T2 space.

7.4 Results

Volumetric, cortical surface and DTI measurements are analysed in this section:

- Centiles of the measurements and correlations with the age at scan were determined for the preterm datasets to investigate the premature brain development (with increasing age at scan).
- The effect of preterm birth was assessed comparing the group of term controls versus an equal-sized group of early preterm subjects born at less than 30 weeks with equivalent ages at scan. Group comparison was performed with two-sided paired t-tests.
- The incidence of increasing prematurity was further explored for all

the preterm subjects with correlations of the measurements with the age at birth (correcting for the age at scan).

Multiple measurements in all cases were adjusted with Bonferroni correction. Significance is assumed with $p < 0.05$.

7.4.1 Volumetric measurements

Absolute and relative volumes of the brain tissues with increasing age at scan are illustrated in Figures 7.6, 7.7 and centiles are reported in Tables 7.13, 7.14 respectively. Tissue volumes estimated with the proposed automatic segmentation method are similar to volumetric results of manually segmented data in early preterm subjects (Moeskops et al., 2013) and term-equivalent brain (Anbeek et al., 2008) in the literature (as discussed in Section 6.3). Absolute volumes for all the 82 structures are presented in Table 7.15.

Correlations with age at scan are displayed in Tables 7.7 and 7.8. Significant correlation of the absolute and relative volume with age at scan is observed for all the tissues. With the exception of the ventricles, all the tissue volumes have a prominent linear correlation to age at scan with a correlation coefficient larger than 0.8. A negative trend between the relative volume and age at scan is observed for the WM, ventricles, basal ganglia and thalami and brainstem. Absolute volume of all the 82 regional structures is significantly correlated with increasing age at scan. After Bonferroni correction most of the structures have a significant linear correlation of their relative volumes to age at scan with the exception of: anterior temporal lobe medial right WM, anterior temporal lobe lateral left WM, cingulate gyrus anterior right WM, cingulate gyrus anterior left GM, cingulate gyrus posterior GM, fusiform gyrus anterior right WM, gyri parahippocampalis anterior GM (left/right) and gyri parahippocampalis posterior WM (left/right).

Volumetric differences between the groups (of term controls and the preterm subjects) are presented in Tables 7.9 and 7.10. Tables 7.11 and 7.12 demonstrate the correlations with age at birth (correcting for the age at scan). Total brain volume of the preterm group was significantly smaller than the term controls and this reduction is significantly associated with increasing prematurity. This adverse effect has been consistently reported in the literature (Peterson et al., 2003; Inder et al., 2005; Thompson et al., 2007; Ball

et al., 2012). The preterm infants had significantly reduced WM volume and more specifically in the parietal lobe, anterior temporal lobe, medial and inferior temporal gyrus and the left hemispheric parts of the insula, cingulate gyrus posterior,superior temporal gyrus middle and gyri parahippocampalis anterior. The degree of prematurity was associated with a decline in total and regional WM volume in all the WM parts except for the fusiform gyrus anterior and the gyri parahippocampalis anterior right. The CGM was less affected overall with significant group differences localised in the anterior temporal lobe and the fusiform gyrus anterior. Decreasing age at birth was significantly associated with reduced volume in these regions and was further negatively correlated in the frontal lobe left, cingulate gyrus anterior left, superior temporal gyrus middle and the anterior parts of the medial and inferior temporal gyrus, gyri parahippocampalis and fusiform gyrus. Regional decreases in the WM have been previously described in Mewes et al. (2006); Thompson et al. (2007). These studies presented both reductions and increases in the regional CGM volumes. The volume of subcortical GM structures is significantly affected by prematurity. The preterm subjects indicated reduced volume in the areas of the amygdala, caudate nucleus, thalamus right, subthalamic nucleus and corpus callosum. Volumes of all the subcortical GM structures were significantly reduced with increasing prematurity. Similar volumetric associations in the subcortical GM and more specifically in the amygdala, thalamus, hippocampus and lentiform nucleus have been reported in Peterson et al. (2000); Srinivasan et al. (2007); Ball et al. (2012). Larger volumes of CSF and ventricles in the preterm subjects have been found in previous studies (Peterson et al., 2000; Mewes et al., 2006; Thompson et al., 2007). In this study, the relative volume of CSF and ventricles was significantly increased for the preterm subjects and this increase is correlated with increasing prematurity. Prematurity was further associated with widespread regional volume changes in the brain (see Table 7.10 and 7.12).

7.4.2 Cortical surface measurements

The different surface measures of the cortex with respect to age at scan are illustrated in Figure 7.8 and correlations in Tables 7.6 and 7.16,7.17 for the whole cortex and the different cortical areas respectively. Regional cen-

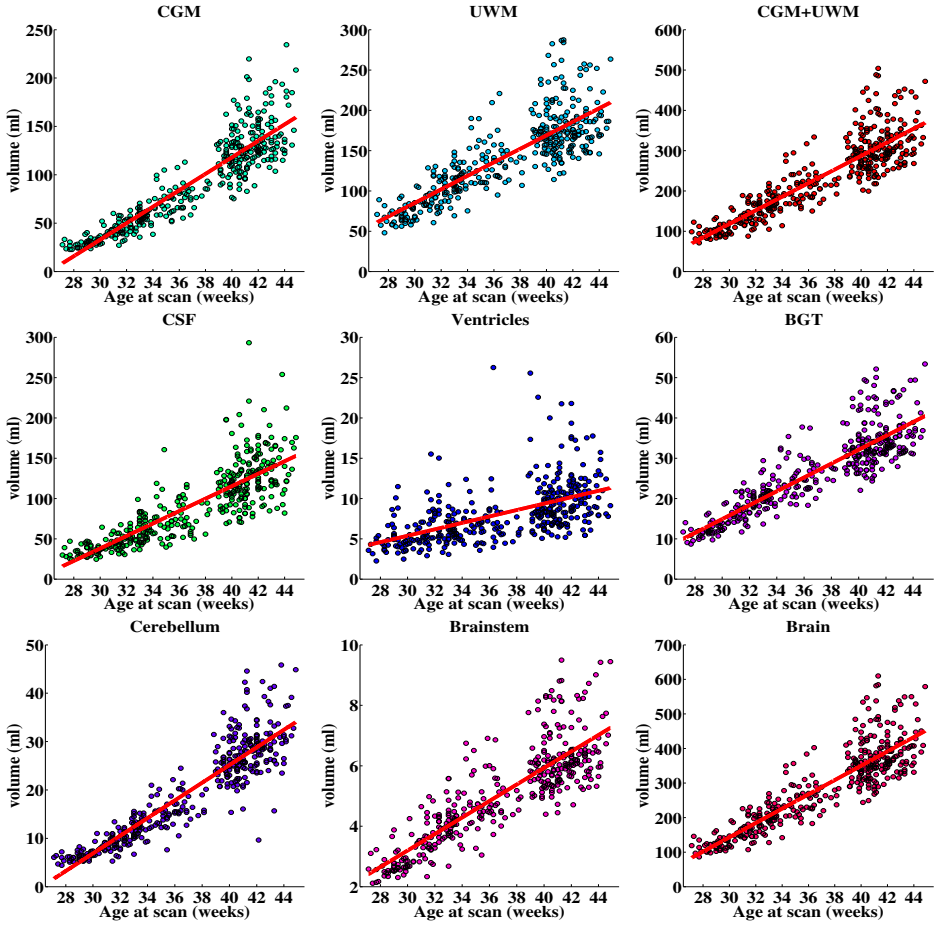

Figure 7.6: Change in tissue volumes with increasing age at scan.

	SA	MLN_T	GLN_T	GC_T
age at scan	**0.921**	**0.880**	**0.894**	**0.909**
age at birth | age at scan	**0.244**	-0.039	-0.017	0.089

Table 7.6: Correlations of surface measures with age at scan and age at birth correcting for the age at scan (bold=significant at $p < 0.05$).

tiles of the cortical surface area are reported in Table 7.22. The curvature measures and surface area are positively related to the age at scan for the whole cortex and for almost all the cortical regions after Bonferroni correction (exceptions are the mean curvature L^2 norm and global curvedness of the gyri parahippocampalis anterior left). The relative surface area presents both regional increases and decreases with increasing age at scan that are significantly associated in the majority of cortical regions. Cortical surface

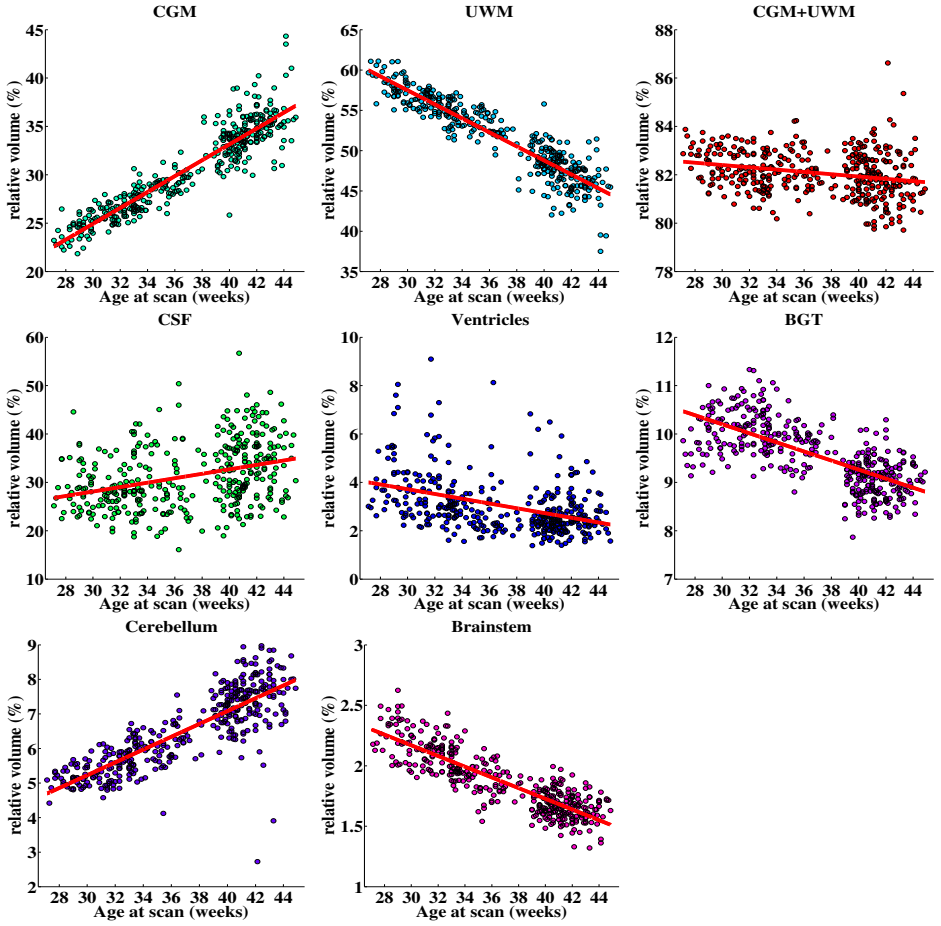

Figure 7.7: Relative tissue volumes with increasing age at scan (% of the total brain volume).

area measurements have been previously presented for the neonatal brain with a range of 150-1500 cm^2 between 27 and 44 weeks post-mentrual age at scan (Kapellou et al., 2006b; Xue et al., 2007; Dubois et al., 2008b; Pienaar et al., 2008; Rodriguez-Carranza et al., 2008; Moeskops et al., 2013). The surface area of the cortex in this study was around 120-1100 cm^2 in the corresponding ages at scan. Curvature measurements have been reported in a limited number of studies (Xue et al., 2007; Pienaar et al., 2008; Rodriguez-Carranza et al., 2008; Moeskops et al., 2013) which used different definitions of curvature measures and included only small numbers of subjects. Here, the curvature measures from Rodriguez-Carranza et al. (2008) were adopted that are invariant to the surface area. Similar positive correlations

of cortical curvature with age at scan to Rodriguez-Carranza et al. (2008) are derived in this analysis. Xue et al. (2007) and Dubois et al. (2008b) likewise presented increasing mean curvature and gyrification, respectively, with increasing age at scan.

Ajayi-Obe et al. (2000) presented reduced cortical surface area in preterm infants compared to term controls. Kapellou et al. (2006b) further demonstrated a decreasing surface area in the cortex with increasing prematurity. Similarly to these studies, the cortical surface area was found to be significantly reduced in the preterm subjects and more specifically in the frontal lobe, anterior temporal lobe lateral and the left hemispheric parts of the parietal lobe, anterior temporal lobe medial, insula and gyri parahippocampalis anterior (see Table 7.18). Increasing prematurity was further associated with descreasing surface area in the whole cortex and most of the regions (see Tables 7.6, 7.20). Ajayi-Obe et al. (2000) additionally reported reduced cortical folding in the preterm population. The curvature measurements in the present analysis were not associated with age at birth in the whole cortex and the majority of cortical regions (see Tables 7.6 and 7.21). A notable exception is the anterior part of the temporal lobe that consistently presented a positive correlation with increasing prematurity in all of the curvature measures. Kesler et al. (2006) demonstrated similar results in prematurily-born children, where the temporal lobe was shown to be specifically disrupted by preterm delivery with increased gyrification in the preterm population. Kesler et al. (2006) suggested that increased gyrification may be due to abnormal growth of the inner cortical layers. The preterm infants demonstrated increased curvature measurements compared to the term controls (see Table 7.19). Since cortical curvature is largely not affected by the age at birth of the infants, the increased curvature may reflect the prolonged extra-uterine growth of the preterm infants versus the term control group.

7.4.3 DTI measurements

Correlations of the DTI measurements with age at scan are presented in Table 7.23. FA was positively related to age at scan in the WM and deep GM structures with the exception of the hippocampus and cingulate gyrus WM. All the CGM structures had a significant negative correlation of FA to

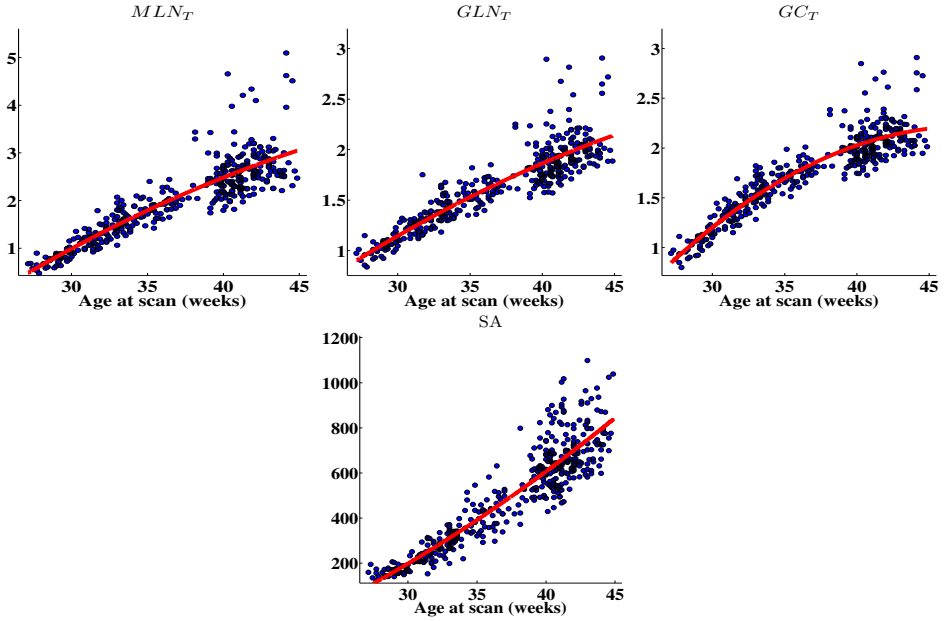

Figure 7.8: Cortical surface measures with increasing age at scan.

the age at scan of the preterm subjects. ADC, AD and RD had a significant negative correlation in all the structures except for the cingulate gyrus GM RD.

The preterm group demonstrated significant differences in the corpus callosum with reduced FA and increased RD and ADC values (see Table 7.24). Reduced FA values were also present in the thalamus of the preterm infants. The corpus callosal and thalamic alterations were further significantly associated with increasing prematurity (see Table 7.25). Similar alterations in the preterm population have been described in (Anjari et al., 2007) for the corpus callosum and the posterior limb of the internal capsule. Differences between the groups were also detected in the cingulate gyrus GM with increased AD. Decreases in fractional anisotropy and increases in diffusivity may indicate dysmyelination as shown in experimental models (Song et al., 2002; Wang et al., 2009). Increasing prematurity was further accompanied by increased FA in the caudate nucleus and frontal lobe GM and decreased AD in the fusiform gyrus WM. Increased FA may be related to increasing maturation of WM fibre tracts associated with the exposure to the extrauterine environment (Giménez et al., 2008).

7.4.4 Tables with volumetric results

Tissues	
CGM	**0.909***
UWM	**0.825***
CGM+UWM	**0.878***
CSF	**0.829***
Ventricles	**0.543***
BGT	**0.875***
Cerebellum	**0.911***
Brainstem	**0.847***
Brain	**0.884***

Subcortical structures	
Hippocampus r	**0.841***
Hippocampus l	**0.831***
Amygdala r	**0.844***
Amygdala l	**0.841***
Cerebellum r	**0.913***
Cerebellum l	**0.908***
Brainstem	**0.847***
Caudate nucleus r	**0.846***
Caudate nucleus l	**0.857***
Thalamus r	**0.878***
Thalamus l	**0.880***
Subthalamic nucleus r	**0.814***
Subthalamic nucleus l	**0.803***
Lentiform Nucleus r	**0.868***
Lentiform Nucleus l	**0.862***
Corpus Callosum	**0.888***
Lateral Ventricle r	**0.550***
Lateral Ventricle l	**0.485***

WM structures		CGM structures	
Frontal lobe r wm	**0.797***	**Frontal lobe r gm**	**0.903***
Frontal lobe l wm	**0.806***	**Frontal lobe l gm**	**0.904***
Parietal lobe r wm	**0.833***	**Parietal lobe r gm**	**0.913***
Parietal lobe l wm	**0.822***	**Parietal lobe l gm**	**0.911***
Occipital lobe r wm	**0.800***	**Occipital lobe r gm**	**0.909***
Occipital lobe l wm	**0.790***	**Occipital lobe l gm**	**0.912***
Anterior temporal lobe M r wm	**0.778***	**Anterior temporal lobe M r gm**	**0.872***
Anterior temporal lobe M l wm	**0.821***	**Anterior temporal lobe M l gm**	**0.860***
Anterior temporal lobe L r wm	**0.693***	**Anterior temporal lobe L r gm**	**0.844***
Anterior temporal lobe L l wm	**0.768***	**Anterior temporal lobe L l gm**	**0.862***
Insula r wm	**0.683***	**Insula r gm**	**0.887***
Insula l wm	**0.668***	**Insula l gm**	**0.881***
Cingulate g A r wm	**0.814***	**Cingulate g A r gm**	**0.845***
Cingulate g A l wm	**0.813***	**Cingulate g A l gm**	**0.838***
Cingulate g P r wm	**0.871***	**Cingulate g P r gm**	**0.845***
Cingulate g P l wm	**0.868***	**Cingulate g P l gm**	**0.843***
Superior temporal g middle r wm	**0.795***	**Superior temporal g middle r gm**	**0.890***
Superior temporal g middle l wm	**0.788***	**Superior temporal g middle l gm**	**0.902***
Superior temporal g P r wm	**0.753***	**Superior temporal g P r gm**	**0.903***
Superior temporal g P l wm	**0.728***	**Superior temporal g P l gm**	**0.882***
Medial & inferior temporal g A r wm	**0.816***	**Medial & inferior temporal g A r gm**	**0.857***
Medial & inferior temporal g A l wm	**0.798***	**Medial & inferior temporal g A l gm**	**0.863***
Medial and inferior temporal g P r wm	**0.819***	**Medial and inferior temporal g P r gm**	**0.913***
Medial and inferior temporal g P l wm	**0.821***	**Medial and inferior temporal g P l gm**	**0.918***
Gyri parahippocampalis A r wm	**0.710***	**Gyri parahippocampalis A r gm**	**0.834***
Gyri parahippocampalis A l wm	**0.659***	**Gyri parahippocampalis A l gm**	**0.824***
Gyri parahippocampalis P r wm	**0.790***	**Gyri parahippocampalis P r gm**	**0.878***
Gyri parahippocampalis P l wm	**0.799***	**Gyri parahippocampalis P l gm**	**0.883***
Fusiform g A r wm	**0.835***	**Fusiform g A r gm**	**0.828***
Fusiform g A l wm	**0.865***	**Fusiform g A l gm**	**0.840***
Fusiform g P r wm	**0.868***	**Fusiform g P r gm**	**0.865***
Fusiform g P l wm	**0.863***	**Fusiform g P l gm**	**0.873***

Table 7.7: Correlations of absolute volumes with age at scan (bold=significant at $p < 0.05$, *=significant after Bonferroni correction).

Tissues	
CGM	**0.923***
UWM	**-0.920***
CGM+UWM	**-0.249***
CSF	**0.339***
Ventricles	**-0.408***
BGT	**-0.699***
Cerebellum	**0.825***
Brainstem	**-0.858***

Subcortical structures	
Hippocampus r	**-0.428***
Hippocampus l	**-0.655***
Amygdala r	**-0.458***
Amygdala l	**-0.574***
Cerebellum r	**0.827***
Cerebellum l	**0.812***
Brainstem	**-0.858***
Caudate nucleus r	**-0.284***
Caudate nucleus l	**-0.217***
Thalamus r	**-0.608***
Thalamus l	**-0.630***
Subthalamic nucleus r	**-0.781***
Subthalamic nucleus l	**-0.814***
Lentiform Nucleus r	**-0.556***
Lentiform Nucleus l	**-0.676***
Corpus Callosum	**0.414***
Lateral Ventricle r	**-0.376***
Lateral Ventricle l	**-0.382***

WM structures	
Frontal lobe r wm	**-0.917***
Frontal lobe l wm	**-0.913***
Parietal lobe r wm	**-0.793***
Parietal lobe l wm	**-0.828***
Occipital lobe r wm	**-0.676***
Occipital lobe l wm	**-0.688***
Anterior temporal lobe M r wm	**0.172**
Anterior temporal lobe M l wm	**0.384***
Anterior temporal lobe L r wm	**-0.269***
Anterior temporal lobe L l wm	-0.017
Insula r wm	**-0.810***
Insula l wm	**-0.767***
Cingulate g A r wm	**-0.131**
Cingulate g A l wm	**0.239***
Cingulate g P r wm	**0.237***
Cingulate g P l wm	**0.450***
Superior temporal g middle r wm	**-0.764***
Superior temporal g middle l wm	**-0.806***
Superior temporal g P r wm	**-0.662***
Superior temporal g P l wm	**-0.735***
Medial & inferior temporal g A r wm	**-0.641***
Medial & inferior temporal g A l wm	**-0.724***
Medial and inferior temporal g P r wm	**-0.695***
Medial and inferior temporal g P l wm	**-0.754***
Gyri parahippocampalis A r wm	**-0.201***
Gyri parahippocampalis A l wm	**-0.217***
Gyri parahippocampalis P r wm	**-0.191***
Gyri parahippocampalis P l wm	-0.042
Fusiform g A r wm	-0.081
Fusiform g A l wm	**0.478***
Fusiform g P r wm	**0.510***
Fusiform g P l wm	**0.580***

CGM structures	
Frontal lobe r gm	**0.905***
Frontal lobe l gm	**0.898***
Parietal lobe r gm	**0.901***
Parietal lobe l gm	**0.891***
Occipital lobe r gm	**0.865***
Occipital lobe l gm	**0.876***
Anterior temporal lobe M r gm	**0.628***
Anterior temporal lobe M l gm	**0.546***
Anterior temporal lobe L r gm	**0.494***
Anterior temporal lobe L l gm	**0.549***
Insula r gm	**0.855***
Insula l gm	**0.854***
Cingulate g A r gm	**0.393***
Cingulate g A l gm	0.039
Cingulate g P r gm	**0.145**
Cingulate g P l gm	-0.065
Superior temporal g middle r gm	**0.846***
Superior temporal g middle l gm	**0.883***
Superior temporal g P r gm	**0.777***
Superior temporal g P l gm	**0.763***
Medial & inferior temporal g A r gm	**0.313***
Medial & inferior temporal g A l gm	**0.498***
Medial and inferior temporal g P r gm	**0.858***
Medial and inferior temporal g P l gm	**0.908***
Gyri parahippocampalis A r gm	**0.124**
Gyri parahippocampalis A l gm	0.041
Gyri parahippocampalis P r gm	**0.623***
Gyri parahippocampalis P l gm	**0.654***
Fusiform g A r gm	**0.390***
Fusiform g A l gm	**0.455***
Fusiform g P r gm	**0.567***
Fusiform g P l gm	**0.566***

Table 7.8: Correlations of relative volumes with age at scan (bold=significant at $p < 0.05$, *=significant after Bonferroni correction).

Tissues	
CGM	$\downarrow$
UWM	$\downarrow^{*}$
CGM+UWM	$\downarrow^{*}$
CSF	$\uparrow$
Ventricles	$\uparrow^{*}$
BGT	$\downarrow^{*}$
Cerebellum	$\downarrow$
Brainstem	$\downarrow^{*}$
Brain	$\downarrow^{*}$

Subcortical structures	
Hippocampus r	$\downarrow$
Hippocampus l	$\downarrow$
Amygdala r	$\downarrow^{*}$
Amygdala l	$\downarrow^{*}$
Cerebellum r	$\downarrow$
Cerebellum l	$\downarrow$
Brainstem	$\downarrow$
Caudate nucleus r	$\downarrow^{*}$
Caudate nucleus l	$\downarrow^{*}$
Thalamus r	$\downarrow^{*}$
Thalamus l	$\downarrow$
Subthalamic nucleus r	$\downarrow^{*}$
Subthalamic nucleus l	$\downarrow^{*}$
Lentiform Nucleus r	$\downarrow$
Lentiform Nucleus l	$\downarrow$
Corpus Callosum	$\downarrow^{*}$
Lateral Ventricle r	$\uparrow$
Lateral Ventricle l	$\uparrow^{*}$

WM structures		CGM structures	
Frontal lobe r wm	$\downarrow$	**Frontal lobe r gm**	$\downarrow$
Frontal lobe l wm	$\downarrow$	**Frontal lobe l gm**	$\downarrow$
Parietal lobe r wm	$\downarrow^{*}$	**Parietal lobe r gm**	
Parietal lobe l wm	$\downarrow^{*}$	**Parietal lobe l gm**	$\downarrow$
Occipital lobe r wm	$\downarrow$	**Occipital lobe r gm**	
Occipital lobe l wm	$\downarrow$	**Occipital lobe l gm**	
Anterior temporal lobe M r wm	$\downarrow$	**Anterior temporal lobe M r gm**	$\downarrow$
Anterior temporal lobe M l wm	$\downarrow^{*}$	**Anterior temporal lobe M l gm**	$\downarrow^{*}$
Anterior temporal lobe L r wm	$\downarrow^{*}$	**Anterior temporal lobe L r gm**	$\downarrow^{*}$
Anterior temporal lobe L l wm	$\downarrow^{*}$	**Anterior temporal lobe L l gm**	$\downarrow^{*}$
Insula r wm	$\downarrow$	**Insula r gm**	
Insula l wm	$\downarrow^{*}$	**Insula l gm**	
Cingulate g A r wm	$\downarrow$	**Cingulate g A r gm**	
Cingulate g A l wm		**Cingulate g A l gm**	
Cingulate g P r wm	$\downarrow$	**Cingulate g P r gm**	
Cingulate g P l wm	$\downarrow^{*}$	**Cingulate g P l gm**	
Superior temporal g middle r wm	$\downarrow$	**Superior temporal g middle r gm**	$\downarrow$
Superior temporal g middle l wm	$\downarrow^{*}$	**Superior temporal g middle l gm**	$\downarrow$
Superior temporal g P r wm		**Superior temporal g P r gm**	
Superior temporal g P l wm	$\downarrow$	**Superior temporal g P l gm**	
Medial & inferior temporal g A r wm	$\downarrow^{*}$	**Medial & inferior temporal g A r gm**	$\downarrow$
Medial & inferior temporal g A l wm	$\downarrow^{*}$	**Medial & inferior temporal g A l gm**	$\downarrow$
Medial and inferior temporal g P r wm		**Medial and inferior temporal g P r gm**	
Medial and inferior temporal g P l wm	$\downarrow$	**Medial and inferior temporal g P l gm**	
Gyri parahippocampalis A r wm	$\downarrow$	**Gyri parahippocampalis A r gm**	
Gyri parahippocampalis A l wm	$\downarrow^{*}$	**Gyri parahippocampalis A l gm**	
Gyri parahippocampalis P r wm	$\downarrow$	**Gyri parahippocampalis P r gm**	
Gyri parahippocampalis P l wm	$\downarrow$	**Gyri parahippocampalis P l gm**	
Fusiform g A r wm		**Fusiform g A r gm**	$\downarrow$
Fusiform g A l wm		**Fusiform g A l gm**	$\downarrow^{*}$
Fusiform g P r wm		**Fusiform g P r gm**	
Fusiform g P l wm	$\downarrow$	**Fusiform g P l gm**	

Table 7.9: Comparison of absolute volumes between the group of early preterm infants and the term controls. Significant ($p < 0.05$) volumetric increases/decreases of the volumes in the preterm subjects are annotated with $\uparrow/\downarrow$ (*=significantly different after Bonferroni correction).

Tissues	
CGM	$\uparrow^{*}$
UWM	$\downarrow^{*}$
CGM+UWM	
CSF	$\uparrow^{*}$
Ventricles	$\uparrow^{*}$
BGT	
Cerebellum	
Brainstem	

Subcortical structures	
Hippocampus r	
Hippocampus l	
Amygdala r	
Amygdala l	$\downarrow$
Cerebellum r	
Cerebellum l	
Brainstem	
Caudate nucleus r	$\downarrow$
Caudate nucleus l	
Thalamus r	
Thalamus l	
Subthalamic nucleus r	$\downarrow$
Subthalamic nucleus l	
Lentiform Nucleus r	
Lentiform Nucleus l	
Corpus Callosum	$\downarrow^{*}$
Lateral Ventricle r	$\uparrow^{*}$
Lateral Ventricle l	$\uparrow^{*}$

WM structures	
Frontal lobe r wm	$\downarrow$
Frontal lobe l wm	$\downarrow$
Parietal lobe r wm	$\downarrow$
Parietal lobe l wm	$\downarrow^{*}$
Occipital lobe r wm	
Occipital lobe l wm	
Anterior temporal lobe M r wm	
Anterior temporal lobe M l wm	$\downarrow$
Anterior temporal lobe L r wm	$\downarrow^{*}$
Anterior temporal lobe L l wm	$\downarrow^{*}$
Insula r wm	
Insula l wm	$\downarrow$
Cingulate g A r wm	
Cingulate g A l wm	
Cingulate g P r wm	
Cingulate g P l wm	$\downarrow^{*}$
Superior temporal g middle r wm	
Superior temporal g middle l wm	$\downarrow$
Superior temporal g P r wm	
Superior temporal g P l wm	
Medial & inferior temporal g A r wm	$\downarrow^{*}$
Medial & inferior temporal g A l wm	$\downarrow^{*}$
Medial and inferior temporal g P r wm	$\uparrow$
Medial and inferior temporal g P l wm	
Gyri parahippocampalis A r wm	
Gyri parahippocampalis A l wm	$\downarrow^{*}$
Gyri parahippocampalis P r wm	
Gyri parahippocampalis P l wm	
Fusiform g A r wm	$\uparrow$
Fusiform g A l wm	$\uparrow$
Fusiform g P r wm	$\uparrow$
Fusiform g P l wm	

CGM structures	
Frontal lobe r gm	
Frontal lobe l gm	
Parietal lobe r gm	$\uparrow^{*}$
Parietal lobe l gm	$\uparrow$
Occipital lobe r gm	$\uparrow^{*}$
Occipital lobe l gm	$\uparrow^{*}$
Anterior temporal lobe M r gm	
Anterior temporal lobe M l gm	$\downarrow$
Anterior temporal lobe L r gm	$\downarrow^{*}$
Anterior temporal lobe L l gm	$\downarrow^{*}$
Insula r gm	
Insula l gm	
Cingulate g A r gm	$\uparrow^{*}$
Cingulate g A l gm	$\uparrow$
Cingulate g P r gm	$\uparrow^{*}$
Cingulate g P l gm	$\uparrow^{*}$
Superior temporal g middle r gm	
Superior temporal g middle l gm	
Superior temporal g P r gm	$\uparrow^{*}$
Superior temporal g P l gm	$\uparrow^{*}$
Medial & inferior temporal g A r gm	
Medial & inferior temporal g A l gm	
Medial and inferior temporal g P r gm	$\uparrow^{*}$
Medial and inferior temporal g P l gm	$\uparrow^{*}$
Gyri parahippocampalis A r gm	
Gyri parahippocampalis A l gm	$\uparrow$
Gyri parahippocampalis P r gm	$\uparrow^{*}$
Gyri parahippocampalis P l gm	$\uparrow$
Fusiform g A r gm	
Fusiform g A l gm	
Fusiform g P r gm	
Fusiform g P l gm	$\uparrow$

Table 7.10: Comparison of relative volumes between the group of early preterm infants and the term controls. Significant ($p < 0.05$) volumetric increases/decreases of the volumes in the preterm subjects are annotated with $\uparrow/\downarrow$ (*=significantly different after Bonferroni correction).

Tissues	
CGM	**0.152***
UWM	**0.342***
CGM+UWM	**0.278***
CSF	-0.089
Ventricles	-0.093
BGT	**0.313***
Cerebellum	**0.193***
Brainstem	**0.341***
Brain	**0.281***

Subcortical structures	
Hippocampus r	**0.315***
Hippocampus l	**0.311***
Amygdala r	**0.318***
Amygdala l	**0.356***
Cerebellum r	**0.194***
Cerebellum l	**0.190***
Brainstem	**0.341***
Caudate nucleus r	**0.379***
Caudate nucleus l	**0.340***
Thalamus r	**0.284***
Thalamus l	**0.264***
Subthalamic nucleus r	**0.303***
Subthalamic nucleus l	**0.324***
Lentiform Nucleus r	**0.289***
Lentiform Nucleus l	**0.300***
Corpus Callosum	**0.288***
Lateral Ventricle r	-0.062
Lateral Ventricle l	**-0.105**

WM structures	
Frontal lobe r wm	**0.374***
Frontal lobe l wm	**0.363***
Parietal lobe r wm	**0.315***
Parietal lobe l wm	**0.328***
Occipital lobe r wm	**0.224***
Occipital lobe l wm	**0.226***
Anterior temporal lobe M r wm	**0.275***
Anterior temporal lobe M l wm	**0.216***
Anterior temporal lobe L r wm	**0.427***
Anterior temporal lobe L l wm	**0.368***
Insula r wm	**0.376***
Insula l wm	**0.371***
Cingulate g A r wm	**0.369***
Cingulate g A l wm	**0.313***
Cingulate g P r wm	**0.281***
Cingulate g P l wm	**0.304***
Superior temporal g middle r wm	**0.312***
Superior temporal g middle l wm	**0.341***
Superior temporal g P r wm	**0.265***
Superior temporal g P l wm	**0.277***
Medial & inferior temporal g A r wm	**0.407***
Medial & inferior temporal g A l wm	**0.391***
Medial and inferior temporal g P r wm	**0.187***
Medial and inferior temporal g P l wm	**0.228***
Gyri parahippocampalis A r wm	**0.175**
Gyri parahippocampalis A l wm	**0.251***
Gyri parahippocampalis P r wm	**0.247***
Gyri parahippocampalis P l wm	**0.262***
Fusiform g A r wm	**0.141**
Fusiform g A l wm	0.082
Fusiform g P r wm	**0.210***
Fusiform g P l wm	**0.224***

CGM structures	
Frontal lobe r gm	**0.153**
Frontal lobe l gm	**0.178***
Parietal lobe r gm	**0.117**
Parietal lobe l gm	**0.161**
Occipital lobe r gm	0.069
Occipital lobe l gm	0.099
Anterior temporal lobe M r gm	**0.247***
Anterior temporal lobe M l gm	**0.283***
Anterior temporal lobe L r gm	**0.306***
Anterior temporal lobe L l gm	**0.290***
Insula r gm	0.071
Insula l gm	0.055
Cingulate g A r gm	0.085
Cingulate g A l gm	**0.175***
Cingulate g P r gm	0.067
Cingulate g P l gm	**0.116**
Superior temporal g middle r gm	**0.231***
Superior temporal g middle l gm	**0.154**
Superior temporal g P r gm	0.037
Superior temporal g P l gm	0.060
Medial & inferior temporal g A r gm	**0.179***
Medial & inferior temporal g A l gm	**0.236***
Medial and inferior temporal g P r gm	0.046
Medial and inferior temporal g P l gm	0.084
Gyri parahippocampalis A r gm	**0.272***
Gyri parahippocampalis A l gm	**0.286***
Gyri parahippocampalis P r gm	0.092
Gyri parahippocampalis P l gm	**0.106**
Fusiform g A r gm	**0.273***
Fusiform g A l gm	**0.336***
Fusiform g P r gm	**0.129**
Fusiform g P l gm	**0.109**

Table 7.11: Partial correlations of absolute volumes with age at birth correcting for the age at scan (bold=significant at $p < 0.05$, *=significant after Bonferroni correction).

Tissues	
CGM	**-0.153***
UWM	**0.148***
CGM+UWM	0.012
CSF	**-0.344***
Ventricles	**-0.296***
BGT	0.002
Cerebellum	0.004
Brainstem	**-0.113**

Subcortical structures	
Hippocampus r	0.097
Hippocampus l	-0.015
Amygdala r	0.083
Amygdala l	**0.142**
Cerebellum r	0.011
Cerebellum l	-0.004
Brainstem	**-0.113**
Caudate nucleus r	**0.314***
Caudate nucleus l	**0.224***
Thalamus r	-0.076
Thalamus l	**-0.145**
Subthalamic nucleus r	-0.083
Subthalamic nucleus l	-0.071
Lentiform Nucleus r	-0.017
Lentiform Nucleus l	-0.022
Corpus Callosum	**0.110**
Lateral Ventricle r	**-0.264***
Lateral Ventricle l	**-0.278***

WM structures		CGM structures	
Frontal lobe r wm	**0.285***	**Frontal lobe r gm**	-0.063
Frontal lobe l wm	**0.248***	**Frontal lobe l gm**	-0.032
Parietal lobe r wm	0.020	**Parietal lobe r gm**	**-0.191***
Parietal lobe l wm	0.024	**Parietal lobe l gm**	**-0.105**
Occipital lobe r wm	**-0.159**	**Occipital lobe r gm**	**-0.370***
Occipital lobe l wm	**-0.135**	**Occipital lobe l gm**	**-0.277***
Anterior temporal lobe M r wm	**0.123**	**Anterior temporal lobe M r gm**	**0.119**
Anterior temporal lobe M l wm	0.052	**Anterior temporal lobe M l gm**	**0.154**
Anterior temporal lobe L r wm	**0.303***	**Anterior temporal lobe L r gm**	**0.237***
Anterior temporal lobe L l wm	**0.248***	**Anterior temporal lobe L l gm**	**0.182***
Insula r wm	**0.167**	**Insula r gm**	-0.006
Insula l wm	**0.207***	**Insula l gm**	-0.025
Cingulate g A r wm	**0.176***	**Cingulate g A r gm**	**-0.191***
Cingulate g A l wm	**0.179***	**Cingulate g A l gm**	-0.069
Cingulate g P r wm	0.097	**Cingulate g P r gm**	**-0.325***
Cingulate g P l wm	**0.173**	**Cingulate g P l gm**	**-0.285***
Superior temporal g middle r wm	-0.004	**Superior temporal g middle r gm**	**0.189***
Superior temporal g middle l wm	0.028	**Superior temporal g middle l gm**	-0.014
Superior temporal g P r wm	-0.007	**Superior temporal g P r gm**	**-0.200***
Superior temporal g P l wm	-0.028	**Superior temporal g P l gm**	**-0.183***
Medial & inferior temporal g A r wm	**0.278***	**Medial & inferior temporal g A r gm**	**-0.119**
Medial & inferior temporal g A l wm	**0.188***	**Medial & inferior temporal g A l gm**	-0.003
Medial and inferior temporal g P r wm	**-0.282***	**Medial and inferior temporal g P r gm**	**-0.313***
Medial and inferior temporal g P l wm	**-0.224***	**Medial and inferior temporal g P l gm**	**-0.243***
Gyri parahippocampalis A r wm	-0.030	**Gyri parahippocampalis A r gm**	**0.126**
Gyri parahippocampalis A l wm	0.058	**Gyri parahippocampalis A l gm**	**0.132**
Gyri parahippocampalis P r wm	0.027	**Gyri parahippocampalis P r gm**	-0.066
Gyri parahippocampalis P l wm	0.063	**Gyri parahippocampalis P l gm**	-0.054
Fusiform g A r wm	**-0.187***	**Fusiform g A r gm**	**0.201***
Fusiform g A l wm	**-0.186***	**Fusiform g A l gm**	**0.316***
Fusiform g P r wm	0.056	**Fusiform g P r gm**	-0.018
Fusiform g P l wm	0.100	**Fusiform g P l gm**	-0.074

Table 7.12: Partial correlations of relative volumes with age at birth correcting for the age at scan (bold=significant at $p < 0.05$, *=significant after Bonferroni correction).

Scan age(weeks)	CGM			UWM			CGM+UWM		
28	24.40	27.36 ± 4.41	30.40	58.62	67.18 ± 11.44	72.66	83.03	95.54 ± 15.36	103.20
30	30.06	32.83 ± 8.04	39.60	67.09	79.32 ± 14.59	85.52	96.85	111.45 ± 22.22	123.74
32	41.57	48.53 ± 9.68	54.47	87.65	101.55 ± 19.39	116.11	129.93	151.28 ± 28.67	169.17
34	55.57	59.92 ± 14.01	66.59	109.39	116.65 ± 25.01	127.93	166.98	176.57 ± 38.62	192.85
36	65.81	76.37 ± 13.45	82.77	117.89	137.25 ± 26.52	148.69	184.62	215.89 ± 39.46	227.81
38	78.09	90.79 ± 23.46	111.40	122.44	140.67 ± 31.40	166.43	213.85	227.51 ± 54.75	277.82
40	102.90	118.77 ± 21.22	130.08	152.03	169.47 ± 33.14	190.03	255.86	285.80 ± 52.76	322.04
42	121.98	133.18 ± 26.60	154.96	163.61	176.16 ± 37.59	194.99	282.87	308.98 ± 62.97	348.12
44	126.30	136.65 ± 35.51	180.27	166.78	185.78 ± 31.96	198.37	292.86	330.79 ± 59.20	365.62

Scan age(weeks)	CSF			Ventricles			BGT		
28	27.97	31.08 ± 7.79	39.36	3.69	4.88 ± 1.48	5.42	10.43	11.69 ± 1.77	12.02
30	33.63	37.67 ± 8.71	42.15	3.88	4.56 ± 1.97	5.50	12.19	13.80 ± 2.53	15.55
32	42.98	49.78 ± 14.84	60.41	5.0	5.99 ± 2.71	8.06	16.55	18.46 ± 3.51	20.79
34	51.43	63.40 ± 23.87	76.59	5.45	6.15 ± 1.76	7.35	19.70	21.60 ± 4.49	23.33
36	58.87	71.71 ± 19.24	82.57	5.59	6.85 ± 3.77	7.85	22.38	24.59 ± 4.42	26.85
38	71.71	94.25 ± 24.66	102.25	5.47	7.00 ± 7.00	12.81	24.78	27.37 ± 4.54	27.75
40	92.67	111.94 ± 29.12	128.20	7.04	8.36 ± 2.92	10.23	28.62	31.59 ± 5.82	34.49
42	117.87	133.83 ± 33.64	155.35	7.86	10.10 ± 3.60	11.77	31.69	34.17 ± 5.83	37.55
44	117.64	136.32 ± 37.98	164.65	8.08	10.08 ± 3.20	12.86	32.04	35.76 ± 6.42	38.83

Scan age(weeks)	Cerebellum			Brainstem			Brain		
28	5.34	5.98 ± 0.86	6.31	2.45	2.55 ± 0.44	2.77	102.02	115.76 ± 18.21	124.30
30	6.48	6.93 ± 1.46	7.91	2.65	2.84 ± 0.53	3.31	118.14	133.98 ± 26.71	149.13
32	8.67	9.98 ± 2.26	11.49	3.40	3.77 ± 0.68	4.29	158.75	184.10 ± 34.76	205.93
34	11.73	12.70 ± 2.80	14.67	3.92	4.18 ± 0.85	4.70	201.28	215.92 ± 46.21	234.04
36	14.34	15.48 ± 3.34	17.12	4.39	4.65 ± 0.82	5.14	227.18	260.75 ± 47.34	277.84
38	15.31	18.97 ± 5.88	23.84	4.54	5.02 ± 0.99	5.48	257.70	279.41 ± 65.35	334.75
40	22.67	25.33 ± 4.14	27.73	5.36	5.87 ± 0.95	6.30	313.34	349.98 ± 62.76	387.78
42	26.08	29.11 ± 5.59	31.31	5.90	6.26 ± 0.99	6.55	351.69	377.99 ± 73.94	419.84
44	26.47	30.89 ± 6.58	33.67	5.83	6.42 ± 1.24	7.01	357.95	401.25 ± 72.21	447.58

Table 7.13: Volume(mL) centiles of tissues with increasing scan age. The left column for each region represents the 25% centile over the subjects in the database, the middle column the median value ± the standard deviation, and the right column the 75% centile.

Scan age(weeks)	CGM			UWM			CGM+UWM		
28	23.00	24.34 ± 1.25	24.85	57.25	58.46 ± 1.65	59.65	82.26	82.79 ± 0.70	83.02
30	24.43	25.43 ± 1.20	26.23	55.91	56.83 ± 1.56	58.31	81.87	82.28 ± 0.77	83.15
32	25.66	26.42 ± 1.18	27.10	54.77	55.65 ± 1.39	56.66	81.54	81.99 ± 0.72	82.76
34	26.60	27.90 ± 1.15	28.80	53.13	53.95 ± 1.49	55.05	81.54	82.18 ± 0.76	82.75
36	28.31	29.15 ± 1.23	29.74	52.13	52.83 ± 1.53	54.27	81.55	82.14 ± 0.87	82.79
38	30.30	31.99 ± 2.30	33.28	47.07	49.72 ± 2.38	50.83	81.42	81.67 ± 0.83	82.37
40	32.13	33.55 ± 1.99	34.19	47.65	48.65 ± 2.16	49.99	81.39	82.01 ± 0.83	82.62
42	33.93	34.94 ± 1.79	35.91	45.44	46.99 ± 1.89	47.83	80.91	81.66 ± 1.22	82.54
44	34.90	35.58 ± 3.33	36.70	45.08	45.97 ± 3.18	46.92	81.05	81.42 ± 1.17	82.39

Scan age(weeks)	CSF			Ventricles			BGT		
28	24.85	27.92 ± 5.84	34.49	3.26	4.04 ± 1.10	5.18	9.58	9.82 ± 0.46	10.20
30	25.16	27.41 ± 4.14	31.11	2.72	3.29 ± 1.45	4.28	9.71	10.20 ± 0.46	10.52
32	26.06	28.08 ± 5.12	31.01	2.65	3.30 ± 1.50	4.16	10.00	10.28 ± 0.47	10.62
34	24.09	28.36 ± 6.93	35.91	2.56	2.97 ± 0.59	3.22	9.64	9.91 ± 0.42	10.17
36	23.82	27.38 ± 7.28	32.03	2.09	2.37 ± 1.31	3.16	9.45	9.83 ± 0.37	9.94
38	26.45	30.24 ± 5.28	33.79	2.08	2.66 ± 1.54	3.12	8.54	9.62 ± 0.74	10.04
40	27.31	32.06 ± 6.84	37.13	2.11	2.39 ± 0.84	2.70	8.82	9.14 ± 0.38	9.33
42	29.78	34.80 ± 6.45	38.61	2.12	2.47 ± 0.88	2.93	8.67	9.07 ± 0.43	9.28
44	28.26	34.77 ± 6.19	39.56	2.16	2.38 ± 0.83	2.84	8.81	9.04 ± 0.35	9.38

Scan age(weeks)	Cerebellum			Brainstem		
28	4.89	5.13 ± 0.27	5.30	2.13	2.28 ± 0.17	2.39
30	5.02	5.17 ± 0.32	5.45	2.03	2.18 ± 0.15	2.25
32	5.11	5.59 ± 0.44	5.85	2.0	2.13 ± 0.12	2.17
34	5.55	6.02 ± 0.45	6.27	1.88	1.95 ± 0.13	1.99
36	5.77	6.16 ± 0.60	6.52	1.79	1.83 ± 0.15	1.96
38	6.23	6.68 ± 0.60	7.09	1.64	1.85 ± 0.16	1.89
40	6.83	7.24 ± 0.54	7.62	1.62	1.69 ± 0.10	1.78
42	7.11	7.64 ± 0.91	8.14	1.56	1.63 ± 0.12	1.72
44	7.12	7.72 ± 0.94	8.01	1.58	1.64 ± 0.13	1.71

Table 7.14: Relative volume (ratio of structure's volume to the total brain volume) centiles of tissues with increasing scan age. The left column for each region represents the 25% centile over the subjects in the database, the middle column the median value ± the standard deviation, and the right column the 75% centile.

Scan age(weeks)	Hippocampus r			Hippocampus l			Amygdala r			Amygdala l			Cerebellum r			Cerebellum l		
28	0.25	0.26 ± 0.05	0.28	0.25	0.26 ± 0.05	0.30	0.15	0.17 ± 0.03	0.18	0.13	0.15 ± 0.03	0.16	2.67	2.90 ± 0.44	3.06	2.72	3.06 ± 0.44	3.25
30	0.28	0.31 ± 0.07	0.38	0.30	0.32 ± 0.06	0.36	0.17	0.20 ± 0.04	0.22	0.16	0.19 ± 0.04	0.21	3.18	3.36 ± 0.75	3.76	3.26	3.59 ± 0.71	4.05
32	0.39	0.46 ± 0.09	0.50	0.36	0.41 ± 0.08	0.46	0.24	0.27 ± 0.06	0.32	0.23	0.25 ± 0.06	0.30	4.25	4.93 ± 1.13	5.75	4.39	5.06 ± 1.14	5.85
34	0.48	0.51 ± 0.12	0.58	0.43	0.48 ± 0.10	0.56	0.28	0.31 ± 0.08	0.36	0.27	0.29 ± 0.07	0.32	5.72	6.25 ± 1.41	7.31	5.99	6.37 ± 1.44	7.12
36	0.53	0.60 ± 0.11	0.65	0.48	0.52 ± 0.10	0.58	0.34	0.39 ± 0.07	0.41	0.31	0.35 ± 0.06	0.39	6.90	7.68 ± 1.64	8.67	7.44	7.77 ± 1.71	8.63
38	0.56	0.61 ± 0.13	0.63	0.51	0.53 ± 0.12	0.56	0.36	0.44 ± 0.07	0.44	0.35	0.38 ± 0.06	0.40	7.75	9.47 ± 2.85	11.80	7.57	9.50 ± 3.03	12.04
40	0.67	0.76 ± 0.15	0.84	0.60	0.65 ± 0.13	0.76	0.42	0.47 ± 0.10	0.52	0.39	0.43 ± 0.09	0.48	11.24	12.53 ± 2.07	13.72	11.43	12.74 ± 2.09	14.14
42	0.74	0.80 ± 0.18	0.90	0.65	0.72 ± 0.13	0.79	0.48	0.51 ± 0.10	0.56	0.43	0.45 ± 0.09	0.51	12.92	14.36 ± 2.73	15.53	12.98	14.50 ± 2.94	15.86
44	0.74	0.80 ± 0.17	0.96	0.69	0.76 ± 0.14	0.86	0.45	0.51 ± 0.09	0.57	0.42	0.45 ± 0.09	0.53	13.03	15.34 ± 3.28	16.80	13.54	15.34 ± 3.34	17.05

Scan age(weeks)	Brainstem			Caudate nucleus r			Caudate nucleus l			Thalamus r			Thalamus l			Subthalamic nucleus r		
28	2.45	2.55 ± 0.44	2.77	0.50	0.55 ± 0.11	0.61	0.51	0.58 ± 0.11	0.62	1.48	1.66 ± 0.27	1.79	1.48	1.68 ± 0.27	1.76	0.10	0.12 ± 0.02	0.12
30	2.65	2.84 ± 0.53	3.31	0.60	0.71 ± 0.17	0.81	0.64	0.74 ± 0.17	0.85	1.72	1.94 ± 0.36	2.19	1.75	1.95 ± 0.35	2.22	0.12	0.13 ± 0.03	0.15
32	3.40	3.77 ± 0.68	4.29	0.89	1.06 ± 0.22	1.19	0.93	1.09 ± 0.20	1.21	2.39	2.60 ± 0.49	2.97	2.38	2.63 ± 0.50	2.92	0.16	0.17 ± 0.03	0.19
34	3.92	4.18 ± 0.85	4.70	1.05	1.23 ± 0.31	1.43	1.10	1.28 ± 0.31	1.47	2.79	3.03 ± 0.59	3.25	2.83	3.0 ± 0.59	3.25	0.18	0.19 ± 0.05	0.21
36	4.39	4.65 ± 0.82	5.14	1.32	1.44 ± 0.29	1.60	1.24	1.47 ± 0.32	1.59	3.12	3.41 ± 0.61	3.68	3.11	3.41 ± 0.59	3.71	0.20	0.22 ± 0.04	0.23
38	4.54	5.02 ± 0.99	5.48	1.44	1.58 ± 0.31	1.73	1.49	1.67 ± 0.34	1.80	3.32	3.83 ± 0.60	4.15	3.36	3.76 ± 0.59	4.09	0.22	0.23 ± 0.04	0.26
40	5.36	5.87 ± 0.95	6.30	1.58	1.77 ± 0.38	2.05	1.62	1.87 ± 0.38	2.04	4.08	4.40 ± 0.81	4.71	4.04	4.36 ± 0.81	4.77	0.23	0.26 ± 0.05	0.28
42	5.90	6.26 ± 0.99	6.55	1.71	1.94 ± 0.35	2.12	1.82	1.98 ± 0.37	2.21	4.61	4.82 ± 0.83	5.33	4.63	4.82 ± 0.82	5.32	0.26	0.28 ± 0.05	0.31
44	5.83	6.42 ± 1.24	7.01	1.77	2.02 ± 0.40	2.35	1.89	2.10 ± 0.40	2.35	4.57	5.14 ± 0.90	5.55	4.62	5.07 ± 0.89	5.52	0.26	0.29 ± 0.05	0.32

Scan age(weeks)	Subthalamic nucleus l			Lentiform Nucleus r			Lentiform Nucleus l			Corpus Callosum			Lateral Ventricle r			Lateral Ventricle l		
28	0.10	0.11 ± 0.02	0.12	1.04	1.16 ± 0.20	1.24	1.10	1.19 ± 0.20	1.27	0.62	0.74 ± 0.12	0.81	1.76	2.29 ± 0.82	2.57	2.05	2.45 ± 0.84	2.91
30	0.11	0.12 ± 0.03	0.14	1.20	1.32 ± 0.30	1.60	1.24	1.38 ± 0.29	1.67	0.84	0.93 ± 0.21	1.10	1.74	1.97 ± 1.01	2.55	2.24	2.49 ± 1.11	3.03
32	0.15	0.16 ± 0.03	0.18	1.67	1.87 ± 0.38	2.12	1.69	1.91 ± 0.36	2.16	1.14	1.34 ± 0.30	1.58	2.29	2.68 ± 1.18	4.11	2.61	3.43 ± 1.76	4.19
34	0.17	0.18 ± 0.04	0.19	1.94	2.14 ± 0.50	2.31	1.96	2.14 ± 0.48	2.39	1.44	1.60 ± 0.40	1.78	2.32	2.93 ± 0.95	3.53	2.75	3.19 ± 1.05	3.95
36	0.18	0.20 ± 0.04	0.22	2.24	2.45 ± 0.48	2.66	2.24	2.46 ± 0.48	2.75	1.73	1.97 ± 0.41	2.14	2.57	3.10 ± 1.68	3.85	2.67	3.49 ± 2.23	4.30
38	0.20	0.23 ± 0.04	0.23	2.61	2.77 ± 0.47	3.10	2.63	2.91 ± 0.44	3.0	1.87	2.06 ± 0.60	2.62	2.67	3.14 ± 3.78	6.27	2.70	3.65 ± 3.40	6.16
40	0.22	0.24 ± 0.05	0.27	2.82	3.20 ± 0.62	3.53	2.89	3.22 ± 0.64	3.57	2.35	2.64 ± 0.48	2.99	3.31	3.89 ± 1.39	4.86	3.57	4.52 ± 1.67	5.59
42	0.24	0.25 ± 0.05	0.28	3.19	3.40 ± 0.58	3.76	3.20	3.41 ± 0.59	3.73	2.60	2.90 ± 0.58	3.22	3.67	4.67 ± 1.51	5.49	4.03	5.38 ± 2.42	6.37
44	0.24	0.26 ± 0.05	0.28	3.31	3.71 ± 0.65	4.01	3.34	3.63 ± 0.67	3.87	2.81	3.14 ± 0.53	3.54	3.93	4.64 ± 1.69	6.4	4.02	5.44 ± 1.99	6.69

Scan age(weeks)	Frontal lobe r gm			Frontal lobe l gm			Parietal lobe r gm			Parietal lobe l gm			Occipital lobe r gm			Occipital lobe l gm		
28	4.16	4.40 ± 0.75	4.88	4.25	4.74 ± 0.83	5.09	2.77	3.14 ± 0.54	3.50	2.90	3.25 ± 0.57	3.62	1.93	2.06 ± 0.30	2.32	1.89	2.06 ± 0.33	2.31
30	4.83	5.43 ± 1.36	6.33	5.10	5.75 ± 1.43	7.10	3.47	3.86 ± 0.90	4.41	3.58	4.15 ± 0.93	4.69	2.28	2.52 ± 0.55	2.93	2.29	2.58 ± 0.54	2.97
32	6.76	8.11 ± 1.62	9.34	7.30	8.50 ± 1.70	9.81	4.71	5.66 ± 1.13	6.52	4.96	5.93 ± 1.18	6.80	2.93	3.48 ± 0.65	3.87	3.04	3.63 ± 0.70	4.03
34	9.27	9.82 ± 2.54	11.01	9.28	10.31 ± 2.45	11.52	6.55	6.93 ± 1.69	7.84	6.79	7.26 ± 1.62	8.08	3.93	4.31 ± 1.04	4.75	4.12	4.57 ± 1.07	5.22
36	10.79	12.66 ± 2.40	13.93	11.02	12.96 ± 2.34	14.34	7.63	8.99 ± 1.61	9.60	7.92	9.15 ± 1.62	9.82	4.49	5.61 ± 1.01	6.03	4.91	5.81 ± 1.04	6.27
38	13.05	15.35 ± 3.80	17.72	13.29	14.99 ± 3.59	18.11	9.10	10.42 ± 3.40	13.46	9.27	11.18 ± 3.0	14.26	5.78	6.39 ± 1.90	8.09	6.12	6.68 ± 1.78	8.52
40	17.28	19.87 ± 3.88	22.32	17.31	20.15 ± 3.79	22.68	12.33	14.15 ± 2.40	15.39	12.70	14.08 ± 2.42	15.68	7.78	8.70 ± 1.56	9.65	8.07	8.97 ± 1.64	10.07
42	20.38	22.90 ± 4.86	26.54	20.62	22.58 ± 4.66	26.42	14.27	15.82 ± 3.12	18.36	14.37	15.58 ± 3.14	18.48	8.80	9.81 ± 1.92	11.16	9.40	10.07 ± 1.91	11.27
44	21.26	23.23 ± 6.55	32.53	21.35	23.70 ± 6.26	30.89	15.03	16.29 ± 4.14	21.63	15.20	16.18 ± 4.15	20.93	9.03	10.17 ± 2.41	12.41	9.27	10.49 ± 2.39	13.09

Scan age(weeks)	Anterior temporal lobe M r gm			Anterior temporal lobe M l gm			Anterior temporal lobe L r gm			Anterior temporal lobe L l gm			Insula r gm			Insula l gm		
28	0.18	0.20 ± 0.04	0.23	0.15	0.16 ± 0.04	0.21	0.16	0.19 ± 0.05	0.22	0.17	0.18 ± 0.05	0.20	0.16	0.23 ± 0.11	0.33	0.15	0.19 ± 0.09	0.27
30	0.24	0.29 ± 0.08	0.32	0.20	0.24 ± 0.06	0.28	0.22	0.25 ± 0.07	0.30	0.22	0.25 ± 0.06	0.29	0.21	0.24 ± 0.15	0.34	0.18	0.25 ± 0.13	0.35
32	0.31	0.39 ± 0.09	0.45	0.27	0.34 ± 0.09	0.39	0.29	0.36 ± 0.09	0.42	0.30	0.34 ± 0.10	0.43	0.35	0.47 ± 0.21	0.66	0.30	0.45 ± 0.19	0.59
34	0.40	0.45 ± 0.12	0.54	0.36	0.40 ± 0.11	0.47	0.37	0.43 ± 0.11	0.53	0.40	0.47 ± 0.12	0.53	0.59	0.67 ± 0.32	0.87	0.52	0.58 ± 0.25	0.70
36	0.54	0.59 ± 0.12	0.70	0.42	0.52 ± 0.12	0.57	0.44	0.56 ± 0.12	0.63	0.48	0.55 ± 0.13	0.60	0.77	1.03 ± 0.27	1.11	0.74	0.91 ± 0.24	1.04
38	0.55	0.65 ± 0.19	0.74	0.50	0.55 ± 0.15	0.64	0.49	0.66 ± 0.15	0.69	0.51	0.58 ± 0.13	0.65	0.89	1.38 ± 0.45	1.63	0.79	1.34 ± 0.39	1.49
40	0.75	0.88 ± 0.20	1.0	0.66	0.74 ± 0.18	0.87	0.67	0.76 ± 0.21	0.89	0.68	0.80 ± 0.21	0.95	1.50	1.79 ± 0.45	2.13	1.37	1.64 ± 0.42	1.92
42	0.85	0.98 ± 0.24	1.18	0.71	0.87 ± 0.21	1.01	0.74	0.91 ± 0.23	1.05	0.79	0.94 ± 0.21	1.06	1.93	2.14 ± 0.51	2.55	1.68	1.98 ± 0.46	2.32
44	0.89	0.96 ± 0.27	1.14	0.78	0.85 ± 0.22	1.03	0.77	0.91 ± 0.23	1.08	0.82	0.93 ± 0.22	1.07	1.94	2.06 ± 0.84	2.83	1.73	1.94 ± 0.82	2.56

Scan age(weeks)	Cingulate g A r gm			Cingulate g A l gm			Cingulate g P r gm			Cingulate g P l gm			Superior temporal g middle r gm			Superior temporal g middle l gm		
28	0.33	0.35 ± 0.08	0.42	0.30	0.38 ± 0.07	0.41	0.36	0.42 ± 0.07	0.45	0.35	0.42 ± 0.07	0.45	0.35	0.39 ± 0.07	0.46	0.34	0.39 ± 0.08	0.45
30	0.35	0.43 ± 0.11	0.51	0.36	0.41 ± 0.12	0.51	0.43	0.49 ± 0.11	0.57	0.43	0.47 ± 0.11	0.57	0.40	0.47 ± 0.14	0.58	0.44	0.51 ± 0.13	0.64
32	0.50	0.61 ± 0.13	0.71	0.53	0.61 ± 0.14	0.71	0.53	0.65 ± 0.13	0.73	0.55	0.63 ± 0.13	0.75	0.57	0.73 ± 0.22	0.88	0.65	0.77 ± 0.20	0.92
34	0.63	0.70 ± 0.21	0.84	0.66	0.75 ± 0.16	0.85	0.64	0.75 ± 0.20	0.81	0.64	0.75 ± 0.17	0.81	0.91	1.01 ± 0.25	1.08	0.87	0.99 ± 0.27	1.10
36	0.73	0.88 ± 0.23	0.96	0.71	0.84 ± 0.18	0.93	0.74	0.83 ± 0.18	0.96	0.71	0.86 ± 0.17	0.91	1.08	1.25 ± 0.24	1.40	1.11	1.27 ± 0.22	1.39
38	0.83	1.10 ± 0.32	1.42	0.95	1.01 ± 0.25	1.26	0.89	1.10 ± 0.36	1.53	0.87	1.03 ± 0.35	1.43	1.32	1.64 ± 0.35	1.81	1.40	1.58 ± 0.38	2.04
40	1.08	1.27 ± 0.27	1.45	0.97	1.16 ± 0.25	1.34	1.12	1.28 ± 0.25	1.47	1.04	1.21 ± 0.24	1.36	1.66	1.96 ± 0.44	2.24	1.77	2.06 ± 0.41	2.20
42	1.21	1.40 ± 0.35	1.61	1.08	1.24 ± 0.31	1.49	1.22	1.44 ± 0.33	1.64	1.18	1.32 ± 0.31	1.50	2.0	2.22 ± 0.50	2.62	2.09	2.30 ± 0.50	2.70
44	1.23	1.39 ± 0.47	1.97	1.17	1.29 ± 0.33	1.69	1.21	1.31 ± 0.44	1.79	1.18	1.25 ± 0.40	1.76	2.05	2.29 ± 0.68	3.01	2.08	2.29 ± 0.68	3.14

Scan age(weeks)	Superior temporal g P r gm			Superior temporal g P l gm			Medial and inferior temporal g A r gm			Medial and inferior temporal g A l gm			Medial and inferior temporal g P r gm			Medial and inferior temporal g P l gm		
28	0.17	0.20 ± 0.06	0.27	0.18	0.21 ± 0.05	0.24	0.47	0.51 ± 0.11	0.62	0.43	0.47 ± 0.10	0.55	0.59	0.65 ± 0.09	0.72	0.56	0.58 ± 0.10	0.65
30	0.21	0.25 ± 0.08	0.34	0.20	0.26 ± 0.07	0.31	0.54	0.63 ± 0.15	0.72	0.52	0.58 ± 0.12	0.64	0.70	0.76 ± 0.18	0.85	0.63	0.75 ± 0.19	0.85
32	0.31	0.40 ± 0.09	0.46	0.30	0.36 ± 0.09	0.43	0.68	0.79 ± 0.16	0.91	0.65	0.76 ± 0.16	0.89	0.98	1.10 ± 0.22	1.28	0.89	1.07 ± 0.25	1.30
34	0.44	0.50 ± 0.13	0.58	0.36	0.43 ± 0.12	0.50	0.81	0.88 ± 0.21	1.01	0.83	0.91 ± 0.19	0.99	1.30	1.40 ± 0.31	1.61	1.27	1.40 ± 0.34	1.59
36	0.51	0.59 ± 0.14	0.69	0.49	0.56 ± 0.12	0.62	0.92	1.10 ± 0.23	1.26	0.92	1.08 ± 0.22	1.16	1.47	1.73 ± 0.36	1.97	1.52	1.72 ± 0.36	1.99
38	0.74	0.77 ± 0.22	1.01	0.63	0.80 ± 0.22	0.96	1.10	1.22 ± 0.37	1.49	1.16	1.24 ± 0.31	1.45	1.80	2.09 ± 0.71	3.02	1.95	2.18 ± 0.69	2.94
40	0.89	1.01 ± 0.18	1.11	0.79	0.94 ± 0.18	1.04	1.42	1.66 ± 0.37	1.92	1.41	1.63 ± 0.38	1.89	2.54	2.93 ± 0.51	3.25	2.53	2.92 ± 0.52	3.33
42	1.03	1.17 ± 0.24	1.32	0.96	1.10 ± 0.26	1.26	1.62	1.92 ± 0.44	2.25	1.62	1.79 ± 0.45	2.20	2.95	3.33 ± 0.64	3.76	3.04	3.38 ± 0.65	3.83
44	1.07	1.31 ± 0.34	1.48	0.91	1.18 ± 0.36	1.48	1.76	1.88 ± 0.51	2.45	1.76	1.92 ± 0.55	2.36	3.15	3.40 ± 0.81	4.55	3.28	3.64 ± 0.84	4.72

Scan age(weeks)	Gyri parahippocampalis A r gm			Gyri parahippocampalis A l gm			Gyri parahippocampalis P r gm			Gyri parahippocampalis P l gm			Fusiform g A r gm			Fusiform g A l gm		
28	0.22	0.29 ± 0.07	0.31	0.23	0.32 ± 0.08	0.35	0.12	0.14 ± 0.03	0.15	0.11	0.13 ± 0.03	0.14	0.12	0.16 ± 0.05	0.20	0.11	0.13 ± 0.02	0.14
30	0.29	0.32 ± 0.10	0.40	0.30	0.35 ± 0.11	0.42	0.15	0.18 ± 0.06	0.22	0.14	0.16 ± 0.06	0.20	0.15	0.20 ± 0.05	0.22	0.13	0.14 ± 0.05	0.17
32	0.39	0.46 ± 0.12	0.56	0.42	0.49 ± 0.13	0.57	0.22	0.28 ± 0.07	0.32	0.22	0.26 ± 0.07	0.31	0.20	0.25 ± 0.07	0.31	0.18	0.22 ± 0.07	0.29
34	0.45	0.55 ± 0.15	0.63	0.49	0.58 ± 0.17	0.64	0.29	0.35 ± 0.08	0.40	0.28	0.32 ± 0.08	0.36	0.28	0.34 ± 0.09	0.38	0.26	0.29 ± 0.08	0.35
36	0.60	0.66 ± 0.12	0.71	0.63	0.70 ± 0.12	0.76	0.35	0.40 ± 0.08	0.43	0.35	0.39 ± 0.06	0.41	0.35	0.41 ± 0.08	0.47	0.34	0.38 ± 0.08	0.44
38	0.78	0.84 ± 0.18	0.92	0.76	0.92 ± 0.18	0.95	0.42	0.49 ± 0.15	0.60	0.43	0.50 ± 0.11	0.52	0.42	0.45 ± 0.12	0.47	0.37	0.43 ± 0.06	0.44
40	0.78	0.88 ± 0.21	1.02	0.84	0.95 ± 0.21	1.05	0.54	0.62 ± 0.12	0.70	0.54	0.60 ± 0.11	0.67	0.49	0.55 ± 0.14	0.64	0.42	0.49 ± 0.14	0.59
42	0.88	1.03 ± 0.23	1.16	0.91	1.02 ± 0.25	1.19	0.63	0.72 ± 0.16	0.83	0.60	0.67 ± 0.16	0.80	0.56	0.64 ± 0.18	0.77	0.47	0.55 ± 0.14	0.66
44	0.89	0.95 ± 0.28	1.09	0.91	0.98 ± 0.29	1.15	0.67	0.72 ± 0.25	0.97	0.65	0.71 ± 0.22	0.92	0.57	0.61 ± 0.22	0.85	0.48	0.54 ± 0.20	0.73

Scan age(weeks)	Fusiform g P r gm			Fusiform g P l gm		
28	0.12	0.15 ± 0.04	0.17	0.13	0.16 ± 0.03	0.18
30	0.17	0.20 ± 0.05	0.24	0.18	0.19 ± 0.05	0.24
32	0.25	0.29 ± 0.07	0.34	0.24	0.28 ± 0.07	0.34
34	0.32	0.37 ± 0.10	0.42	0.32	0.36 ± 0.07	0.40
36	0.38	0.42 ± 0.10	0.46	0.36	0.41 ± 0.09	0.47
38	0.41	0.58 ± 0.17	0.59	0.38	0.49 ± 0.16	0.60
40	0.58	0.65 ± 0.13	0.74	0.54	0.64 ± 0.13	0.72
42	0.68	0.78 ± 0.18	0.88	0.64	0.76 ± 0.17	0.84
44	0.63	0.78 ± 0.23	0.92	0.68	0.73 ± 0.20	0.91

Scan age(weeks)	Frontal lobe r wm			Frontal lobe l wm			Parietal lobe r wm			Parietal lobe l wm			Occipital lobe r wm			Occipital lobe l wm		
28	11.85	13.54 ± 2.42	15.08	11.75	13.64 ± 2.33	14.70	6.72	7.91 ± 1.37	8.47	7.32	7.97 ± 1.43	8.56	3.40	3.80 ± 0.69	4.32	3.40	3.90 ± 0.73	4.38
30	13.56	15.55 ± 2.99	16.93	13.19	15.55 ± 2.94	16.94	7.80	9.19 ± 1.74	10.03	7.95	9.08 ± 1.73	10.20	3.80	4.35 ± 1.0	5.02	4.15	4.52 ± 0.93	5.06
32	17.14	20.40 ± 4.05	22.63	17.05	20.06 ± 3.95	22.50	9.91	11.51 ± 2.34	13.48	10.33	11.41 ± 2.30	13.53	4.72	5.34 ± 1.09	6.35	5.0	5.83 ± 1.08	6.59
34	20.72	22.97 ± 4.81	25.36	20.88	23.22 ± 4.93	25.37	12.49	13.38 ± 2.90	14.41	12.44	13.55 ± 2.97	14.64	5.92	6.54 ± 1.41	7.44	5.97	6.88 ± 1.58	7.40
36	22.75	26.92 ± 5.16	29.09	23.02	26.27 ± 5.35	28.81	13.70	15.74 ± 3.07	16.39	13.81	15.71 ± 3.21	16.28	6.34	7.56 ± 1.53	8.69	6.74	7.53 ± 1.63	8.50
38	23.19	27.35 ± 5.50	31.21	25.02	28.11 ± 5.85	32.02	14.89	16.14 ± 4.16	20.04	14.64	16.24 ± 3.60	20.44	6.86	7.79 ± 1.75	9.11	7.07	8.02 ± 1.86	9.51
40	28.42	32.62 ± 6.43	35.67	29.02	32.63 ± 6.32	36.33	17.88	19.81 ± 3.85	22.42	17.67	19.51 ± 3.94	22.32	8.36	9.58 ± 2.17	11.02	8.65	9.77 ± 2.28	11.46
42	30.25	33.45 ± 7.29	36.50	31.29	33.83 ± 7.36	36.95	18.85	20.92 ± 4.71	24.19	18.58	20.73 ± 4.57	23.44	8.94	9.81 ± 2.21	11.40	9.17	10.17 ± 2.37	11.86
44	31.18	33.50 ± 6.07	38.77	31.44	34.32 ± 6.37	38.57	20.28	21.63 ± 4.16	25.66	19.85	21.22 ± 4.31	25.74	9.21	10.18 ± 2.16	11.54	9.04	10.17 ± 2.18	11.58

Scan age(weeks)	Anterior temporal lobe M r wm			Anterior temporal lobe M l wm			Anterior temporal lobe L r wm			Anterior temporal lobe L l wm			Insula r wm			Insula l wm		
28	0.15	0.18 ± 0.09	0.28	0.12	0.14 ± 0.06	0.19	0.16	0.18 ± 0.06	0.22	0.17	0.21 ± 0.06	0.24	1.05	1.29 ± 0.23	1.38	0.93	1.14 ± 0.20	1.21
30	0.24	0.29 ± 0.09	0.37	0.18	0.19 ± 0.06	0.22	0.23	0.27 ± 0.10	0.35	0.25	0.29 ± 0.08	0.35	1.14	1.34 ± 0.35	1.69	1.09	1.24 ± 0.35	1.55
32	0.26	0.34 ± 0.12	0.45	0.21	0.25 ± 0.09	0.34	0.30	0.37 ± 0.10	0.43	0.30	0.37 ± 0.12	0.48	1.66	1.99 ± 0.39	2.14	1.53	1.87 ± 0.38	2.04
34	0.35	0.43 ± 0.17	0.59	0.28	0.36 ± 0.14	0.47	0.36	0.42 ± 0.11	0.49	0.39	0.51 ± 0.12	0.59	1.93	2.12 ± 0.45	2.47	1.84	2.05 ± 0.46	2.43
36	0.43	0.63 ± 0.18	0.72	0.35	0.44 ± 0.14	0.53	0.39	0.49 ± 0.14	0.58	0.45	0.57 ± 0.17	0.64	2.17	2.50 ± 0.55	2.69	1.99	2.39 ± 0.54	2.59
38	0.42	0.55 ± 0.19	0.63	0.36	0.41 ± 0.13	0.52	0.38	0.47 ± 0.11	0.52	0.44	0.53 ± 0.13	0.57	2.07	2.52 ± 0.73	2.69	2.06	2.39 ± 0.67	2.64
40	0.68	0.79 ± 0.24	0.93	0.55	0.64 ± 0.17	0.75	0.53	0.61 ± 0.20	0.75	0.65	0.72 ± 0.22	0.84	2.31	2.64 ± 0.64	2.97	2.19	2.50 ± 0.59	2.82
42	0.69	0.85 ± 0.25	1.02	0.60	0.70 ± 0.19	0.78	0.55	0.64 ± 0.21	0.78	0.69	0.81 ± 0.23	0.94	2.51	2.80 ± 0.61	3.13	2.32	2.63 ± 0.60	2.87
44	0.72	0.84 ± 0.23	1.08	0.63	0.74 ± 0.18	0.95	0.56	0.61 ± 0.20	0.78	0.65	0.80 ± 0.19	0.93	2.51	2.66 ± 0.65	3.01	2.27	2.46 ± 0.70	2.93

Scan age(weeks)	Cingulate g A r wm			Cingulate g A l wm			Cingulate g P r wm			Cingulate g P l wm			Superior temporal g middle r wm			Superior temporal g middle l wm		
28	0.35	0.46 ± 0.13	0.55	0.22	0.30 ± 0.12	0.43	0.35	0.47 ± 0.12	0.52	0.25	0.33 ± 0.09	0.37	1.06	1.26 ± 0.23	1.38	1.18	1.28 ± 0.21	1.48
30	0.50	0.58 ± 0.17	0.74	0.31	0.43 ± 0.17	0.61	0.51	0.56 ± 0.12	0.68	0.36	0.43 ± 0.12	0.53	1.29	1.40 ± 0.28	1.59	1.35	1.50 ± 0.29	1.65
32	0.76	0.89 ± 0.22	1.12	0.63	0.72 ± 0.19	0.89	0.72	0.83 ± 0.18	0.98	0.57	0.67 ± 0.16	0.78	1.60	1.82 ± 0.38	2.13	1.57	1.85 ± 0.36	2.14
34	0.99	1.13 ± 0.26	1.32	0.78	0.90 ± 0.27	1.05	0.86	0.98 ± 0.22	1.12	0.70	0.78 ± 0.22	0.90	1.86	2.0 ± 0.50	2.27	1.94	2.11 ± 0.50	2.48
36	1.21	1.37 ± 0.25	1.52	0.99	1.11 ± 0.30	1.30	1.02	1.19 ± 0.26	1.35	0.87	0.98 ± 0.21	1.14	2.19	2.37 ± 0.47	2.6	2.11	2.39 ± 0.49	2.66
38	1.33	1.50 ± 0.35	1.63	0.94	1.20 ± 0.38	1.45	1.07	1.33 ± 0.36	1.35	0.97	1.04 ± 0.34	1.15	1.87	2.41 ± 0.69	2.58	2.0	2.55 ± 0.64	2.72
40	1.48	1.66 ± 0.31	1.85	1.28	1.48 ± 0.35	1.65	1.44	1.61 ± 0.34	1.78	1.26	1.41 ± 0.30	1.59	2.58	2.92 ± 0.61	3.25	2.56	2.91 ± 0.61	3.31
42	1.49	1.68 ± 0.40	1.94	1.29	1.48 ± 0.35	1.68	1.58	1.74 ± 0.37	2.06	1.34	1.48 ± 0.35	1.72	2.74	3.16 ± 0.71	3.55	2.83	3.08 ± 0.64	3.50
44	1.49	1.73 ± 0.31	1.99	1.34	1.46 ± 0.29	1.64	1.68	1.83 ± 0.28	2.08	1.39	1.56 ± 0.29	1.86	2.93	3.17 ± 0.69	3.67	2.77	3.17 ± 0.68	3.64

Scan age(weeks)	Superior temporal g P r wm			Superior temporal g P l wm			Medial and inferior temporal g A r wm			Medial and inferior temporal g A l wm			Medial and inferior temporal g P r wm			Medial and inferior temporal g P l wm		
28	0.59	0.68 ± 0.13	0.77	0.51	0.57 ± 0.11	0.62	1.15	1.29 ± 0.20	1.42	1.25	1.34 ± 0.23	1.52	1.59	1.85 ± 0.33	1.98	1.65	1.87 ± 0.35	2.12
30	0.69	0.73 ± 0.19	0.91	0.62	0.66 ± 0.15	0.72	1.31	1.51 ± 0.28	1.63	1.43	1.59 ± 0.32	1.74	1.79	2.01 ± 0.39	2.23	1.84	2.13 ± 0.45	2.32
32	0.93	1.01 ± 0.25	1.21	0.77	0.88 ± 0.20	1.0	1.72	1.89 ± 0.42	2.20	1.77	2.03 ± 0.41	2.32	2.34	2.69 ± 0.50	3.04	2.39	2.84 ± 0.53	3.19
34	1.12	1.21 ± 0.32	1.37	0.92	1.05 ± 0.29	1.22	1.98	2.23 ± 0.46	2.43	2.17	2.33 ± 0.48	2.53	2.78	2.96 ± 0.64	3.15	2.94	3.18 ± 0.58	3.44
36	1.25	1.42 ± 0.29	1.60	0.99	1.09 ± 0.23	1.25	2.34	2.61 ± 0.54	2.78	2.29	2.63 ± 0.63	3.02	2.94	3.55 ± 0.70	3.89	3.08	3.52 ± 0.72	3.87
38	1.11	1.54 ± 0.48	1.99	0.99	1.17 ± 0.35	1.36	2.17	2.65 ± 0.61	3.08	2.32	2.59 ± 0.51	3.07	3.07	3.78 ± 1.20	5.04	3.34	3.70 ± 0.98	4.78
40	1.46	1.68 ± 0.37	1.89	1.16	1.33 ± 0.29	1.53	2.83	3.12 ± 0.75	3.59	2.93	3.22 ± 0.75	3.61	4.00	4.39 ± 0.87	4.92	4.06	4.47 ± 0.95	5.29
42	1.58	1.82 ± 0.43	1.97	1.22	1.38 ± 0.26	1.56	3.14	3.54 ± 0.78	4.04	3.11	3.60 ± 0.80	4.08	4.28	4.73 ± 1.09	5.50	4.35	4.93 ± 1.02	5.35
44	1.58	1.70 ± 0.37	2.05	1.22	1.37 ± 0.30	1.59	3.33	3.58 ± 0.72	4.14	3.46	3.77 ± 0.80	4.42	4.13	4.80 ± 0.97	5.41	4.41	5.0 ± 0.99	5.90

Scan age(weeks)	Gyri parahippocampalis A r wm			Gyri parahippocampalis A l wm			Gyri parahippocampalis P r wm			Gyri parahippocampalis P l wm			Fusiform g A r wm			Fusiform g A l wm		
28	0.18	0.22 ± 0.06	0.27	0.15	0.20 ± 0.05	0.23	0.19	0.21 ± 0.05	0.27	0.16	0.18 ± 0.05	0.23	0.31	0.37 ± 0.09	0.42	0.21	0.24 ± 0.07	0.31
30	0.23	0.26 ± 0.06	0.30	0.19	0.24 ± 0.08	0.29	0.27	0.31 ± 0.07	0.36	0.2	0.26 ± 0.06	0.31	0.36	0.43 ± 0.10	0.52	0.26	0.29 ± 0.08	0.33
32	0.29	0.38 ± 0.11	0.47	0.29	0.37 ± 0.12	0.44	0.36	0.41 ± 0.10	0.48	0.30	0.34 ± 0.08	0.40	0.44	0.56 ± 0.13	0.67	0.31	0.38 ± 0.11	0.47
34	0.37	0.46 ± 0.14	0.53	0.37	0.47 ± 0.16	0.51	0.42	0.49 ± 0.11	0.58	0.38	0.45 ± 0.12	0.50	0.53	0.66 ± 0.20	0.78	0.40	0.47 ± 0.15	0.57
36	0.44	0.54 ± 0.14	0.60	0.41	0.50 ± 0.15	0.52	0.51	0.58 ± 0.11	0.65	0.43	0.49 ± 0.12	0.58	0.65	0.80 ± 0.22	0.96	0.49	0.59 ± 0.19	0.77
38	0.30	0.49 ± 0.17	0.56	0.28	0.40 ± 0.20	0.50	0.46	0.61 ± 0.15	0.70	0.44	0.54 ± 0.15	0.62	0.83	0.85 ± 0.16	0.87	0.65	0.72 ± 0.17	0.79
40	0.54	0.65 ± 0.20	0.77	0.47	0.59 ± 0.19	0.71	0.62	0.76 ± 0.18	0.85	0.58	0.65 ± 0.16	0.75	0.93	1.08 ± 0.23	1.21	0.79	0.91 ± 0.19	1.01
42	0.57	0.69 ± 0.20	0.81	0.47	0.62 ± 0.18	0.73	0.68	0.79 ± 0.21	0.92	0.58	0.69 ± 0.16	0.77	1.04	1.16 ± 0.24	1.30	0.91	1.00 ± 0.23	1.16
44	0.56	0.64 ± 0.22	0.84	0.44	0.64 ± 0.24	0.80	0.72	0.76 ± 0.21	0.97	0.64	0.74 ± 0.18	0.84	1.06	1.19 ± 0.28	1.42	0.93	1.03 ± 0.26	1.22

Scan age(weeks)	Fusiform g P r wm			Fusiform g P l wm		
28	0.29	0.33 ± 0.07	0.39	0.24	0.27 ± 0.06	0.31
30	0.34	0.38 ± 0.10	0.46	0.27	0.34 ± 0.10	0.40
32	0.49	0.57 ± 0.17	0.74	0.41	0.49 ± 0.15	0.60
34	0.69	0.79 ± 0.20	0.89	0.58	0.70 ± 0.21	0.85
36	0.89	0.95 ± 0.22	1.11	0.76	0.89 ± 0.20	0.97
38	0.86	1.13 ± 0.24	1.27	0.87	0.99 ± 0.21	1.07
40	1.17	1.34 ± 0.30	1.53	1.03	1.20 ± 0.29	1.39
42	1.25	1.46 ± 0.31	1.65	1.14	1.37 ± 0.29	1.52
44	1.30	1.48 ± 0.31	1.79	1.12	1.34 ± 0.32	1.60

Table 7.15: Volume(mL) centiles of the 82 structures of the whole brain with increasing scan age. The left column for each region represents the 25% centile over the subjects in the database, the middle column the median value ± the standard deviation, and the right column the 75% centile.

7.4.5 Tables with surface results

SA		relative SA	
Frontal lobe r	**0.918***	**Frontal lobe r**	**-0.657***
Frontal lobe l	**0.919***	**Frontal lobe l**	**-0.584***
Parietal lobe r	**0.921***	**Parietal lobe r**	**0.754***
Parietal lobe l	**0.924***	**Parietal lobe l**	**0.639***
Occipital lobe r	**0.902***	**Occipital lobe r**	-0.044
Occipital lobe l	**0.894***	**Occipital lobe l**	-0.058
Anterior temporal lobe M r	**0.865***	**Anterior temporal lobe M r**	**-0.125**
Anterior temporal lobe M l	**0.870***	**Anterior temporal lobe M l**	0.033
Anterior temporal lobe L r	**0.831***	**Anterior temporal lobe L r**	**-0.412***
Anterior temporal lobe L l	**0.877***	**Anterior temporal lobe L l**	**-0.266***
Insula r	**0.910***	**Insula r**	**0.412***
Insula l	**0.898***	**Insula l**	**0.350***
Cingulate g A r	**0.858***	**Cingulate g A r**	**-0.536***
Cingulate g A l	**0.871***	**Cingulate g A l**	**-0.307***
Cingulate g P r	**0.901***	**Cingulate g P r**	**-0.373***
Cingulate g P l	**0.883***	**Cingulate g P l**	**-0.266***
Superior temporal g middle r	**0.887***	**Superior temporal g middle r**	0.025
Superior temporal g middle l	**0.910***	**Superior temporal g middle l**	**-0.155**
Superior temporal g P r	**0.906***	**Superior temporal g P r**	**0.663***
Superior temporal g P l	**0.905***	**Superior temporal g P l**	**0.488***
Medial & inferior temporal g A r	**0.866***	**Medial & inferior temporal g A r**	**-0.638***
Medial & inferior temporal g A l	**0.892***	**Medial & inferior temporal g A l**	**-0.665***
Medial and inferior temporal g P r	**0.904***	**Medial and inferior temporal g P r**	**0.519***
Medial and inferior temporal g P l	**0.927***	**Medial and inferior temporal g P l**	**0.673***
Gyri parahippocampalis A r	**0.784***	**Gyri parahippocampalis A r**	**-0.495***
Gyri parahippocampalis A l	**0.727***	**Gyri parahippocampalis A l**	**-0.515***
Gyri parahippocampalis P r	**0.875***	**Gyri parahippocampalis P r**	0.095
Gyri parahippocampalis P l	**0.863***	**Gyri parahippocampalis P l**	0.085
Fusiform g A r	**0.876***	**Fusiform g A r**	**-0.313***
Fusiform g A l	**0.898***	**Fusiform g A l**	0.026
Fusiform g P r	**0.921***	**Fusiform g P r**	**0.625***
Fusiform g P l	**0.913***	**Fusiform g P l**	**0.520***

Table 7.16: Correlations of regional surface area with age at scan (bold=significant at $p < 0.05$, *=significant after Bonferroni correction).

MLN_T	
Frontal lobe r	**0.890***
Frontal lobe l	**0.891***
Parietal lobe r	**0.852***
Parietal lobe l	**0.854***
Occipital lobe r	**0.891***
Occipital lobe l	**0.895***
Anterior temporal lobe M r	**0.705***
Anterior temporal lobe M l	**0.655***
Anterior temporal lobe L r	**0.741***
Anterior temporal lobe L l	**0.768***
Insula r	**0.619***
Insula l	**0.679***
Cingulate g A r	**0.762***
Cingulate g A l	**0.729***
Cingulate g P r	**0.854***
Cingulate g P l	**0.824***
Superior temporal g middle r	**0.773***
Superior temporal g middle l	**0.785***
Superior temporal g P r	**0.693***
Superior temporal g P l	**0.657***
Medial & inferior temporal g A r	**0.903***
Medial & inferior temporal g A l	**0.909***
Medial and inferior temporal g P r	**0.892***
Medial and inferior temporal g P l	**0.896***
Gyri parahippocampalis A r	**0.317***
Gyri parahippocampalis A l	**0.140**
Gyri parahippocampalis P r	**0.692***
Gyri parahippocampalis P l	**0.667***
Fusiform g A r	**0.799***
Fusiform g A l	**0.793***
Fusiform g P r	**0.840***
Fusiform g P l	**0.831***

GLN_T	
Frontal lobe r	**0.898***
Frontal lobe l	**0.896***
Parietal lobe r	**0.877***
Parietal lobe l	**0.874***
Occipital lobe r	**0.904***
Occipital lobe l	**0.903***
Anterior temporal lobe M r	**0.729***
Anterior temporal lobe M l	**0.703***
Anterior temporal lobe L r	**0.785***
Anterior temporal lobe L l	**0.802***
Insula r	**0.720***
Insula l	**0.732***
Cingulate g A r	**0.814***
Cingulate g A l	**0.799***
Cingulate g P r	**0.881***
Cingulate g P l	**0.863***
Superior temporal g middle r	**0.849***
Superior temporal g middle l	**0.856***
Superior temporal g P r	**0.835***
Superior temporal g P l	**0.785***
Medial & inferior temporal g A r	**0.924***
Medial & inferior temporal g A l	**0.926***
Medial and inferior temporal g P r	**0.908***
Medial and inferior temporal g P l	**0.904***
Gyri parahippocampalis A r	**0.694***
Gyri parahippocampalis A l	**0.628***
Gyri parahippocampalis P r	**0.804***
Gyri parahippocampalis P l	**0.776***
Fusiform g A r	**0.817***
Fusiform g A l	**0.781***
Fusiform g P r	**0.874***
Fusiform g P l	**0.852***

GC_T	
Frontal lobe r	**0.917***
Frontal lobe l	**0.917***
Parietal lobe r	**0.873***
Parietal lobe l	**0.873***
Occipital lobe r	**0.916***
Occipital lobe l	**0.917***
Anterior temporal lobe M r	**0.746***
Anterior temporal lobe M l	**0.708***
Anterior temporal lobe L r	**0.804***
Anterior temporal lobe L l	**0.845***
Insula r	**0.689***
Insula l	**0.716***
Cingulate g A r	**0.760***
Cingulate g A l	**0.713***
Cingulate g P r	**0.869***
Cingulate g P l	**0.837***
Superior temporal g middle r	**0.797***
Superior temporal g middle l	**0.825***
Superior temporal g P r	**0.706***
Superior temporal g P l	**0.643***
Medial & inferior temporal g A r	**0.934***
Medial & inferior temporal g A l	**0.938***
Medial and inferior temporal g P r	**0.901***
Medial and inferior temporal g P l	**0.901***
Gyri parahippocampalis A r	**0.329***
Gyri parahippocampalis A l	**0.132**
Gyri parahippocampalis P r	**0.720***
Gyri parahippocampalis P l	**0.665***
Fusiform g A r	**0.801***
Fusiform g A l	**0.773***
Fusiform g P r	**0.849***
Fusiform g P l	**0.832***

Table 7.17: Correlations of regional curvature measures with age at scan (bold=significant at $p < 0.05$, *=significant after Bonferroni correction).

SA		relative SA	
Frontal lobe r	$\downarrow^*$	**Frontal lobe r**	$\downarrow$
Frontal lobe l	$\downarrow^*$	**Frontal lobe l**	$\downarrow^*$
Parietal lobe r	$\downarrow$	**Parietal lobe r**	
Parietal lobe l	$\downarrow^*$	**Parietal lobe l**	$\downarrow^*$
Occipital lobe r	$\downarrow$	**Occipital lobe r**	
Occipital lobe l		**Occipital lobe l**	
Anterior temporal lobe M r	$\downarrow$	**Anterior temporal lobe M r**	
Anterior temporal lobe M l	$\downarrow^*$	**Anterior temporal lobe M l**	$\downarrow$
Anterior temporal lobe L r	$\downarrow^*$	**Anterior temporal lobe L r**	$\downarrow^*$
Anterior temporal lobe L l	$\downarrow^*$	**Anterior temporal lobe L l**	$\downarrow^*$
Insula r	$\downarrow$	**Insula r**	
Insula l	$\downarrow^*$	**Insula l**	
Cingulate g A r		**Cingulate g A r**	$\uparrow^*$
Cingulate g A l		**Cingulate g A l**	$\uparrow^*$
Cingulate g P r		**Cingulate g P r**	$\uparrow^*$
Cingulate g P l	$\downarrow$	**Cingulate g P l**	
Superior temporal g middle r	$\downarrow$	**Superior temporal g middle r**	
Superior temporal g middle l	$\downarrow$	**Superior temporal g middle l**	
Superior temporal g P r		**Superior temporal g P r**	$\uparrow^*$
Superior temporal g P l		**Superior temporal g P l**	
Medial & inferior temporal g A r	$\downarrow$	**Medial & inferior temporal g A r**	
Medial & inferior temporal g A l	$\downarrow$	**Medial & inferior temporal g A l**	
Medial and inferior temporal g P r		**Medial and inferior temporal g P r**	$\uparrow^*$
Medial and inferior temporal g P l	$\downarrow$	**Medial and inferior temporal g P l**	$\uparrow$
Gyri parahippocampalis A r	$\downarrow$	**Gyri parahippocampalis A r**	
Gyri parahippocampalis A l	$\downarrow^*$	**Gyri parahippocampalis A l**	$\downarrow$
Gyri parahippocampalis P r		**Gyri parahippocampalis P r**	$\uparrow$
Gyri parahippocampalis P l		**Gyri parahippocampalis P l**	
Fusiform g A r		**Fusiform g A r**	$\uparrow$
Fusiform g A l		**Fusiform g A l**	$\uparrow^*$
Fusiform g P r		**Fusiform g P r**	$\uparrow$
Fusiform g P l		**Fusiform g P l**	$\uparrow$

Table 7.18: Comparison of regional surface area between the group of early preterm infants and the term controls. Significant ($p < 0.05$) increases/decreases of the measures in the preterm subjects are annotated with $\uparrow/\downarrow$ (*=significantly different after Bonferroni correction).

MLN_T	
Frontal lobe r	↑
Frontal lobe l	↑
Parietal lobe r	↑*
Parietal lobe l	↑*
Occipital lobe r	↑
Occipital lobe l	↑
Anterior temporal lobe M r	↑
Anterior temporal lobe M l	↑
Anterior temporal lobe L r	
Anterior temporal lobe L l	
Insula r	
Insula l	
Cingulate g A r	↑*
Cingulate g A l	↑*
Cingulate g P r	↑
Cingulate g P l	↑
Superior temporal g middle r	
Superior temporal g middle l	
Superior temporal g P r	↑*
Superior temporal g P l	↑
Medial & inferior temporal g A r	↑
Medial & inferior temporal g A l	↑*
Medial and inferior temporal g P r	↑*
Medial and inferior temporal g P l	↑
Gyri parahippocampalis A r	↑*
Gyri parahippocampalis A l	↑*
Gyri parahippocampalis P r	↑
Gyri parahippocampalis P l	↑*
Fusiform g A r	↑
Fusiform g A l	
Fusiform g P r	↑
Fusiform g P l	↑

GLN_T	
Frontal lobe r	
Frontal lobe l	
Parietal lobe r	↑
Parietal lobe l	↑
Occipital lobe r	↑
Occipital lobe l	↑
Anterior temporal lobe M r	↑
Anterior temporal lobe M l	
Anterior temporal lobe L r	
Anterior temporal lobe L l	
Insula r	
Insula l	
Cingulate g A r	↑
Cingulate g A l	↑
Cingulate g P r	
Cingulate g P l	
Superior temporal g middle r	
Superior temporal g middle l	
Superior temporal g P r	↑*
Superior temporal g P l	
Medial & inferior temporal g A r	
Medial & inferior temporal g A l	↑
Medial and inferior temporal g P r	↑*
Medial and inferior temporal g P l	↑
Gyri parahippocampalis A r	↑
Gyri parahippocampalis A l	↑
Gyri parahippocampalis P r	
Gyri parahippocampalis P l	
Fusiform g A r	
Fusiform g A l	
Fusiform g P r	
Fusiform g P l	

GC_T	
Frontal lobe r	↑
Frontal lobe l	↑
Parietal lobe r	↑*
Parietal lobe l	↑*
Occipital lobe r	↑
Occipital lobe l	↑
Anterior temporal lobe M r	↑
Anterior temporal lobe M l	
Anterior temporal lobe L r	
Anterior temporal lobe L l	
Insula r	
Insula l	
Cingulate g A r	↑*
Cingulate g A l	↑*
Cingulate g P r	↑
Cingulate g P l	
Superior temporal g middle r	
Superior temporal g middle l	
Superior temporal g P r	↑*
Superior temporal g P l	
Medial & inferior temporal g A r	↑
Medial & inferior temporal g A l	↑*
Medial and inferior temporal g P r	↑*
Medial and inferior temporal g P l	↑*
Gyri parahippocampalis A r	↑*
Gyri parahippocampalis A l	↑
Gyri parahippocampalis P r	↑
Gyri parahippocampalis P l	↑
Fusiform g A r	
Fusiform g A l	
Fusiform g P r	↑
Fusiform g P l	↑

Table 7.19: Comparison of regional curvature measures between the group of early preterm infants and the term controls. Significant ($p < 0.05$) increases/decreases of the measures in the preterm subjects are annotated with ↑/↓ (*=significantly different after Bonferroni correction).

SA	
Frontal lobe r	**0.269***
Frontal lobe l	**0.258***
Parietal lobe r	**0.201***
Parietal lobe l	**0.234***
Occipital lobe r	**0.191***
Occipital lobe l	**0.184***
Anterior temporal lobe M r	**0.187***
Anterior temporal lobe M l	**0.165***
Anterior temporal lobe L r	**0.307***
Anterior temporal lobe L l	**0.257***
Insula r	**0.249***
Insula l	**0.304***
Cingulate g A r	**0.202***
Cingulate g A l	**0.208***
Cingulate g P r	**0.172***
Cingulate g P l	**0.200***
Superior temporal g middle r	**0.334***
Superior temporal g middle l	**0.281***
Superior temporal g P r	0.089
Superior temporal g P l	**0.172***
Medial & inferior temporal g A r	**0.262***
Medial & inferior temporal g A l	**0.283***
Medial and inferior temporal g P r	0.080
Medial and inferior temporal g P l	**0.123**
Gyri parahippocampalis A r	**0.224***
Gyri parahippocampalis A l	**0.310***
Gyri parahippocampalis P r	**0.249***
Gyri parahippocampalis P l	**0.235***
Fusiform g A r	**0.170***
Fusiform g A l	**0.153**
Fusiform g P r	**0.117**
Fusiform g P l	**0.116**

relative SA	
Frontal lobe r	0.029
Frontal lobe l	-0.037
Parietal lobe r	0.048
Parietal lobe l	0.094
Occipital lobe r	**-0.118**
Occipital lobe l	-0.085
Anterior temporal lobe M r	-0.061
Anterior temporal lobe M l	-0.067
Anterior temporal lobe L r	**0.112**
Anterior temporal lobe L l	0.039
Insula r	**0.140**
Insula l	**0.211***
Cingulate g A r	-0.091
Cingulate g A l	-0.042
Cingulate g P r	**-0.141**
Cingulate g P l	-0.067
Superior temporal g middle r	**0.330***
Superior temporal g middle l	**0.129**
Superior temporal g P r	0.003
Superior temporal g P l	0.063
Medial & inferior temporal g A r	-0.037
Medial & inferior temporal g A l	-0.093
Medial and inferior temporal g P r	**-0.259***
Medial and inferior temporal g P l	**-0.208***
Gyri parahippocampalis A r	0.042
Gyri parahippocampalis A l	**0.105**
Gyri parahippocampalis P r	**0.168***
Gyri parahippocampalis P l	**0.146**
Fusiform g A r	**-0.101**
Fusiform g A l	-0.101
Fusiform g P r	-0.096
Fusiform g P l	-0.042

Table 7.20: Correlations of regional surface area with age at birth correcting for the age at scan (bold=significant at $p < 0.05$, *=significant after Bonferroni correction).

MLN_T	
Frontal lobe r	-0.036
Frontal lobe l	-0.022
Parietal lobe r	-0.004
Parietal lobe l	-0.015
Occipital lobe r	0.000
Occipital lobe l	0.004
Anterior temporal lobe M r	**-0.274***
Anterior temporal lobe M l	**-0.230***
Anterior temporal lobe L r	**-0.227***
Anterior temporal lobe L l	**-0.235***
Insula r	-0.090
Insula l	**-0.121**
Cingulate g A r	-0.050
Cingulate g A l	-0.069
Cingulate g P r	**-0.109**
Cingulate g P l	-0.078
Superior temporal g middle r	**-0.140**
Superior temporal g middle l	-0.034
Superior temporal g P r	-0.072
Superior temporal g P l	-0.028
Medial & inferior temporal g A r	**-0.214***
Medial & inferior temporal g A l	**-0.109**
Medial and inferior temporal g P r	0.012
Medial and inferior temporal g P l	0.046
Gyri parahippocampalis A r	0.005
Gyri parahippocampalis A l	-0.031
Gyri parahippocampalis P r	**-0.161**
Gyri parahippocampalis P l	-0.036
Fusiform g A r	0.015
Fusiform g A l	**0.117**
Fusiform g P r	-0.080
Fusiform g P l	-0.015

GLN_T	
Frontal lobe r	-0.010
Frontal lobe l	0.002
Parietal lobe r	0.005
Parietal lobe l	0.008
Occipital lobe r	0.047
Occipital lobe l	0.027
Anterior temporal lobe M r	**-0.235***
Anterior temporal lobe M l	**-0.186***
Anterior temporal lobe L r	**-0.235***
Anterior temporal lobe L l	**-0.249***
Insula r	**-0.132**
Insula l	**-0.122**
Cingulate g A r	**-0.116**
Cingulate g A l	-0.061
Cingulate g P r	-0.054
Cingulate g P l	-0.000
Superior temporal g middle r	**-0.132**
Superior temporal g middle l	-0.089
Superior temporal g P r	-0.070
Superior temporal g P l	-0.026
Medial & inferior temporal g A r	**-0.103**
Medial & inferior temporal g A l	-0.005
Medial and inferior temporal g P r	0.082
Medial and inferior temporal g P l	**0.118**
Gyri parahippocampalis A r	-0.006
Gyri parahippocampalis A l	-0.081
Gyri parahippocampalis P r	**-0.112**
Gyri parahippocampalis P l	-0.036
Fusiform g A r	0.101
Fusiform g A l	**0.168***
Fusiform g P r	-0.033
Fusiform g P l	0.060

GC_T	
Frontal lobe r	0.101
Frontal lobe l	**0.117**
Parietal lobe r	**0.104**
Parietal lobe l	**0.105**
Occipital lobe r	**0.166***
Occipital lobe l	**0.156**
Anterior temporal lobe M r	**-0.266***
Anterior temporal lobe M l	**-0.231***
Anterior temporal lobe L r	**-0.195***
Anterior temporal lobe L l	**-0.233***
Insula r	-0.085
Insula l	**-0.107**
Cingulate g A r	-0.014
Cingulate g A l	-0.022
Cingulate g P r	-0.026
Cingulate g P l	-0.016
Superior temporal g middle r	-0.093
Superior temporal g middle l	-0.018
Superior temporal g P r	-0.037
Superior temporal g P l	0.006
Medial & inferior temporal g A r	-0.099
Medial & inferior temporal g A l	0.040
Medial and inferior temporal g P r	**0.154**
Medial and inferior temporal g P l	**0.193***
Gyri parahippocampalis A r	0.047
Gyri parahippocampalis A l	-0.024
Gyri parahippocampalis P r	**-0.120**
Gyri parahippocampalis P l	0.007
Fusiform g A r	**0.151**
Fusiform g A l	**0.226***
Fusiform g P r	0.009
Fusiform g P l	0.067

Table 7.21: Correlations of regional curvature measures with age at birth correcting for the age at scan (bold=significant at $p < 0.05$, *=significant after Bonferroni correction).

Scan age(weeks)	Frontal lobe r			Frontal lobe l			Parietal lobe r			Parietal lobe l			Occipital lobe r			Occipital lobe l		
28	26.32	29.79 ± 4.22	32.79	26.72	29.91 ± 4.20	32.28	13.89	16.56 ± 2.46	17.59	15.31	16.77 ± 2.45	18.25	10.51	11.36 ± 1.40	12.40	10.66	11.13 ± 1.65	12.78
30	30.47	35.34 ± 5.95	40.05	31.37	34.65 ± 5.97	39.12	17.70	20.18 ± 3.71	22.98	17.76	20.28 ± 3.94	23.63	11.75	13.54 ± 2.56	14.91	12.79	13.58 ± 2.45	15.44
32	42.18	47.97 ± 8.47	53.88	42.57	47.82 ± 8.49	53.93	25.14	28.41 ± 5.88	33.41	26.38	29.05 ± 5.56	33.64	15.97	18.03 ± 3.22	19.95	16.24	18.86 ± 3.38	21.18
34	54.28	57.71 ± 11.79	63.52	53.99	59.01 ± 11.35	63.30	35.11	37.62 ± 8.35	41.43	35.11	37.45 ± 8.18	42.25	21.94	23.64 ± 4.83	27.05	23.12	24.12 ± 5.74	25.97
36	62.25	72.56 ± 13.17	80.10	62.99	74.19 ± 12.82	79.24	41.73	48.40 ± 9.30	50.83	42.16	47.31 ± 9.06	49.49	24.93	29.83 ± 5.89	34.38	25.7	30.48 ± 6.28	33.65
38	72.08	76.90 ± 18.98	95.55	71.22	77.16 ± 19.63	95.42	44.68	57.88 ± 14.75	64.50	46.67	55.80 ± 12.80	68.88	28.89	33.21 ± 7.94	41.38	29.69	34.43 ± 7.83	41.68
40	93.92	102.76 ± 17.22	115.01	92.89	104.30 ± 16.70	115.25	65.48	71.71 ± 12.59	80.70	63.72	69.84 ± 11.72	77.60	38.12	43.22 ± 8.59	48.09	39.75	45.31 ± 8.87	49.46
42	106.21	115.24 ± 20.63	129.03	108.04	114.84 ± 21.23	130.30	74.88	80.28 ± 15.94	93.86	72.46	79.02 ± 14.79	89.48	42.72	46.56 ± 9.19	54.81	44.37	47.33 ± 10.08	55.22
44	113.72	123.49 ± 18.33	137.30	114.30	125.44 ± 19.79	142.36	78.92	82.72 ± 15.21	92.74	77.60	84.96 ± 14.21	94.48	45.22	49.00 ± 9.28	55.36	44.17	47.40 ± 9.40	53.81

Scan age(weeks)	Anterior temporal lobe M r			Anterior temporal lobe M l			Anterior temporal lobe L r			Anterior temporal lobe L l			Insula r			Insula l		
28	0.91	1.02 ± 0.22	1.18	0.65	0.80 ± 0.21	0.88	0.97	1.05 ± 0.26	1.26	1.02	1.19 ± 0.23	1.29	1.46	2.08 ± 0.68	2.40	1.30	1.61 ± 0.60	2.04
30	1.11	1.33 ± 0.31	1.55	0.84	1.00 ± 0.24	1.11	1.28	1.41 ± 0.39	1.77	1.30	1.46 ± 0.34	1.81	1.61	2.07 ± 0.88	2.62	1.59	2.19 ± 0.86	2.62
32	1.32	1.61 ± 0.42	1.92	1.11	1.28 ± 0.33	1.57	1.59	1.90 ± 0.42	2.17	1.59	1.89 ± 0.43	2.36	2.78	3.41 ± 1.08	4.49	2.57	3.50 ± 1.12	4.30
34	1.68	1.96 ± 0.55	2.32	1.37	1.66 ± 0.52	2.02	1.92	2.26 ± 0.49	2.54	2.08	2.55 ± 0.55	2.89	4.19	4.51 ± 1.37	5.31	3.86	4.32 ± 1.22	5.03
36	2.09	2.66 ± 0.57	3.09	1.75	2.07 ± 0.52	2.47	2.18	2.78 ± 0.63	3.14	2.44	2.97 ± 0.64	3.33	5.09	5.98 ± 1.21	6.83	5.13	5.77 ± 1.17	6.68
38	2.27	2.78 ± 0.87	3.09	1.91	2.26 ± 0.61	2.58	2.31	3.01 ± 0.71	3.57	2.55	3.18 ± 0.69	3.31	5.75	6.92 ± 1.82	7.46	5.30	7.07 ± 1.70	7.43
40	3.34	3.80 ± 0.82	4.14	2.75	3.06 ± 0.65	3.51	3.31	3.81 ± 0.87	4.36	3.73	4.22 ± 0.87	4.65	7.64	8.81 ± 1.71	9.69	7.46	8.38 ± 1.68	9.61
42	3.53	4.24 ± 1.03	4.95	3.02	3.59 ± 0.85	4.01	3.55	4.17 ± 1.04	4.94	4.03	4.74 ± 1.01	5.38	8.88	9.88 ± 1.72	11.23	8.27	9.32 ± 1.73	10.54
44	3.87	4.36 ± 1.01	5.23	3.35	3.59 ± 0.80	4.39	3.71	4.21 ± 0.98	5.30	4.38	4.71 ± 1.01	5.85	9.45	10.58 ± 1.81	11.40	9.03	9.65 ± 2.32	11.64

Scan age(weeks)	Cingulate g A r			Cingulate g A l			Cingulate g P r			Cingulate g P l			Superior temporal g middle r			Superior temporal g middle l		
28	1.61	1.95 ± 0.33	2.20	1.29	1.56 ± 0.36	1.70	1.54	1.86 ± 0.31	2.06	1.35	1.57 ± 0.30	1.77	2.22	2.61 ± 0.41	2.83	2.31	2.84 ± 0.48	3.25
30	1.93	2.20 ± 0.51	2.75	1.54	1.84 ± 0.47	2.19	1.95	2.23 ± 0.40	2.61	1.73	1.96 ± 0.41	2.34	2.79	2.97 ± 0.81	3.92	3.11	3.43 ± 0.68	3.89
32	2.71	3.17 ± 0.66	3.73	2.34	2.73 ± 0.62	3.30	2.76	3.21 ± 0.64	3.62	2.53	2.84 ± 0.55	3.13	4.0	4.73 ± 1.20	5.75	4.36	4.93 ± 1.05	5.71
34	3.56	3.84 ± 0.80	4.59	3.06	3.38 ± 0.75	3.74	3.51	3.75 ± 0.67	4.02	3.03	3.28 ± 0.72	3.77	5.44	5.96 ± 1.43	6.66	5.78	6.31 ± 1.41	7.03
36	3.92	4.77 ± 1.06	5.19	3.36	4.12 ± 0.91	4.64	4.11	4.59 ± 0.88	5.01	3.60	4.08 ± 0.85	4.58	7.10	7.89 ± 1.19	8.40	7.01	8.03 ± 1.25	8.54
38	4.70	5.50 ± 1.35	5.82	3.89	4.49 ± 1.54	6.37	4.41	5.52 ± 1.42	6.39	3.87	4.51 ± 1.54	5.38	6.88	8.19 ± 2.01	9.39	7.74	8.74 ± 1.94	10.74
40	5.60	6.47 ± 1.27	7.28	4.93	5.71 ± 1.10	6.35	5.93	6.62 ± 1.19	7.43	5.29	6.04 ± 1.08	6.77	9.58	10.61 ± 2.18	11.95	9.58	10.92 ± 1.99	12.0
42	6.07	6.77 ± 1.48	7.84	5.6	6.01 ± 1.32	6.77	6.66	7.42 ± 1.38	8.4	5.74	6.41 ± 1.49	7.33	10.83	11.59 ± 2.55	13.76	11.14	12.17 ± 2.18	13.42
44	5.75	6.42 ± 1.58	8.34	5.77	6.23 ± 0.75	6.74	6.58	7.52 ± 1.36	8.88	6.37	6.81 ± 1.21	7.50	10.83	11.63 ± 2.97	14.51	11.22	12.38 ± 2.17	13.12

Scan age(weeks)	Superior temporal g P r			Superior temporal g P l			Medial and inferior temporal g A r			Medial and inferior temporal g A l			Medial and inferior temporal g P r			Medial and inferior temporal g P l		
28	0.75	0.91 ± 0.22	1.10	0.80	0.96 ± 0.18	1.08	3.07	3.29 ± 0.35	3.48	3.08	3.28 ± 0.34	3.55	3.50	3.61 ± 0.47	4.01	3.31	3.56 ± 0.39	3.81
30	0.98	1.17 ± 0.43	1.67	0.98	1.13 ± 0.37	1.57	3.38	3.73 ± 0.48	4.05	3.38	3.60 ± 0.58	3.90	3.83	4.24 ± 0.72	4.76	3.71	4.13 ± 0.69	4.61
32	1.68	2.13 ± 0.56	2.53	1.55	1.97 ± 0.53	2.31	4.30	4.81 ± 0.86	5.47	4.31	4.85 ± 0.75	5.41	5.45	6.11 ± 1.14	6.99	5.21	5.86 ± 1.16	6.97
34	2.44	2.80 ± 0.76	3.21	2.11	2.46 ± 0.70	2.84	5.25	5.54 ± 1.17	6.16	5.33	5.71 ± 1.02	6.23	6.96	7.83 ± 1.83	8.35	7.03	7.72 ± 1.86	8.88
36	3.04	3.51 ± 0.79	3.75	2.68	2.95 ± 0.84	3.59	6.29	7.04 ± 1.22	7.80	6.19	6.92 ± 1.25	7.98	8.84	10.48 ± 2.08	11.46	8.87	9.52 ± 2.17	11.05
38	3.90	4.41 ± 1.42	5.58	3.08	3.70 ± 0.95	4.29	7.03	8.16 ± 1.85	9.56	7.22	7.33 ± 1.70	8.80	10.38	12.36 ± 4.23	16.73	9.67	11.58 ± 3.21	15.70
40	4.88	5.47 ± 1.10	6.21	4.12	4.73 ± 0.89	5.36	8.81	9.98 ± 2.16	11.10	8.65	9.83 ± 1.88	10.96	13.76	15.66 ± 2.81	17.41	14.05	15.52 ± 2.72	17.34
42	5.57	6.19 ± 1.46	7.42	4.81	5.37 ± 1.10	6.23	9.69	11.24 ± 2.50	12.63	9.85	10.73 ± 2.19	12.19	15.81	17.44 ± 3.82	20.49	15.89	17.64 ± 3.11	19.39
44	5.86	6.52 ± 1.34	8.05	5.02	6.03 ± 1.17	6.65	10.07	10.85 ± 2.47	12.75	10.26	12.13 ± 2.21	12.84	16.26	18.22 ± 3.61	21.35	17.27	19.48 ± 2.89	21.84

Scan age(weeks)	Gyri parahippocampalis A r			Gyri parahippocampalis A l			Gyri parahippocampalis P r			Gyri parahippocampalis P l			Fusiform g A r			Fusiform g A l		
28	0.74	0.93 ± 0.30	1.13	0.82	0.90 ± 0.26	1.11	0.66	0.73 ± 0.17	0.86	0.57	0.70 ± 0.17	0.86	0.94	1.10 ± 0.24	1.34	0.77	0.89 ± 0.15	1.01
30	0.90	1.11 ± 0.29	1.45	0.97	1.12 ± 0.35	1.44	0.87	1.02 ± 0.30	1.20	0.77	0.96 ± 0.27	1.11	1.10	1.20 ± 0.37	1.53	0.91	1.02 ± 0.24	1.15
32	1.38	1.68 ± 0.50	2.09	1.50	1.76 ± 0.55	2.23	1.34	1.65 ± 0.45	1.95	1.22	1.48 ± 0.48	1.92	1.39	1.66 ± 0.41	1.99	1.16	1.43 ± 0.34	1.67
34	1.69	2.00 ± 0.56	2.38	1.86	2.28 ± 0.62	2.53	1.91	2.13 ± 0.47	2.32	1.81	2.08 ± 0.46	2.26	1.87	2.02 ± 0.49	2.34	1.63	1.80 ± 0.43	2.03
36	2.23	2.56 ± 0.57	2.80	2.17	2.46 ± 0.61	2.69	2.26	2.56 ± 0.47	2.87	2.09	2.38 ± 0.49	2.63	2.20	2.54 ± 0.58	2.95	1.96	2.33 ± 0.55	2.81
38	2.03	2.33 ± 0.63	2.46	1.85	2.40 ± 0.85	2.56	2.19	2.76 ± 0.83	3.0	2.43	2.59 ± 0.70	2.88	2.85	3.05 ± 0.49	3.24	2.62	2.74 ± 0.48	3.04
40	2.59	3.13 ± 0.80	3.60	2.65	2.94 ± 0.76	3.50	3.06	3.64 ± 0.78	4.04	3.05	3.41 ± 0.73	3.90	3.33	3.68 ± 0.74	4.04	2.99	3.25 ± 0.65	3.74
42	2.76	3.26 ± 0.75	3.83	2.45	3.03 ± 0.78	3.72	3.59	3.99 ± 0.97	4.85	3.16	3.72 ± 0.88	4.21	3.61	4.05 ± 0.86	4.82	3.27	3.75 ± 0.73	4.41
44	2.84	3.10 ± 0.68	3.39	2.38	2.88 ± 0.93	3.63	3.79	4.11 ± 0.90	4.69	3.24	3.67 ± 0.85	4.34	3.68	4.00 ± 1.02	4.88	3.32	3.96 ± 0.72	4.19

Scan age(weeks)	Fusiform g P r			Fusiform g P l			Whole GM		
28	0.86	0.91 ± 0.14	0.98	0.76	0.93 ± 0.15	1.01	141.74	159.15 ± 20.74	172.24
30	1.02	1.08 ± 0.22	1.26	0.98	1.08 ± 0.21	1.29	165.34	188.03 ± 32.81	209.58
32	1.37	1.62 ± 0.35	1.88	1.30	1.48 ± 0.40	1.87	235.27	265.92 ± 48.09	302.29
34	1.87	2.17 ± 0.48	2.41	1.87	2.09 ± 0.50	2.47	308.82	333.40 ± 67.81	364.36
36	2.37	2.71 ± 0.52	3.20	2.38	2.81 ± 0.60	3.07	360.83	426.76 ± 75.49	458.46
38	2.90	3.18 ± 1.01	4.31	2.74	3.13 ± 0.80	3.88	418.26	458.49 ± 113.56	567.81
40	3.90	4.39 ± 0.75	5.04	3.66	4.09 ± 0.76	4.56	542.82	611.49 ± 100.17	659.74
42	4.37	4.98 ± 0.96	5.78	4.38	4.90 ± 0.95	5.47	616.75	662.69 ± 123.85	756.40
44	4.67	5.00 ± 0.97	6.19	4.20	4.92 ± 1.03	5.73	659.25	724.41 ± 109.11	776.65

Table 7.22: Surface area(cm^2) of the 32 structures of the whole brain with increasing scan age. The left column for each region represents the 25% centile over the subjects in the database, the middle column the median value ± the standard deviation, and the right column the 75% centile.

7.4.6 Tables with DTI results

FA	
Hippocampus	0.108
Amygdala	**0.418***
Cerebellum	**0.419***
Brainstem	**0.808***
Caudate nucleus	**0.493***
Thalamus	**0.655***
Subthalamic nucleus	**0.812***
Lentiform Nucleus	**0.678***
Corpus Callosum	**0.609***
Frontal lobe wm	**0.709***
Parietal lobe wm	**0.756***
Occipital lobe wm	**0.485***
Temporal lobe wm	**0.540***
Fusiform gyrus wm	**0.260***
Cingulate gyrus wm	0.090
Frontal lobe gm	**-0.675***
Parietal lobe gm	**-0.659***
Occipital lobe gm	**-0.752***
Temporal lobe gm	**-0.814***
Fusiform gyrus gm	**-0.594***
Cingulate gyrus gm	**-0.510***

ADC	
Hippocampus	**-0.651***
Amygdala	**-0.775***
Cerebellum	**-0.889***
Brainstem	**-0.674***
Caudate nucleus	**-0.825***
Thalamus	**-0.871***
Subthalamic nucleus	**-0.782***
Lentiform Nucleus	**-0.846***
Corpus Callosum	**-0.529***
Frontal lobe wm	**-0.693***
Parietal lobe wm	**-0.848***
Occipital lobe wm	**-0.841***
Temporal lobe wm	**-0.733***
Fusiform gyrus wm	**-0.679***
Cingulate gyrus wm	**-0.601***
Frontal lobe gm	**-0.616***
Parietal lobe gm	**-0.686***
Occipital lobe gm	**-0.732***
Temporal lobe gm	**-0.674***
Fusiform gyrus gm	**-0.755***
Cingulate gyrus gm	**-0.354***

AD	
Hippocampus	**-0.658***
Amygdala	**-0.727***
Cerebellum	**-0.872***
Brainstem	**-0.517***
Caudate nucleus	**-0.798***
Thalamus	**-0.852***
Subthalamic nucleus	**-0.677***
Lentiform Nucleus	**-0.819***
Corpus Callosum	**-0.247***
Frontal lobe wm	**-0.654***
Parietal lobe wm	**-0.831***
Occipital lobe wm	**-0.854***
Temporal lobe wm	**-0.726***
Fusiform gyrus wm	**-0.680***
Cingulate gyrus wm	**-0.632***
Frontal lobe gm	**-0.812***
Parietal lobe gm	**-0.842***
Occipital lobe gm	**-0.889***
Temporal lobe gm	**-0.871***
Fusiform gyrus gm	**-0.872***
Cingulate gyrus gm	**-0.630***

RD	
Hippocampus	**-0.633***
Amygdala	**-0.774***
Cerebellum	**-0.885***
Brainstem	**-0.724***
Caudate nucleus	**-0.825***
Thalamus	**-0.873***
Subthalamic nucleus	**-0.807***
Lentiform Nucleus	**-0.847***
Corpus Callosum	**-0.600***
Frontal lobe wm	**-0.704***
Parietal lobe wm	**-0.852***
Occipital lobe wm	**-0.828***
Temporal lobe wm	**-0.731***
Fusiform gyrus wm	**-0.670***
Cingulate gyrus wm	**-0.558***
Frontal lobe gm	**-0.402***
Parietal lobe gm	**-0.482***
Occipital lobe gm	**-0.496***
Temporal lobe gm	**-0.394***
Fusiform gyrus gm	**-0.619***
Cingulate gyrus gm	-0.120

Table 7.23: Correlations of DTI measures with age at scan (bold=significant at $p < 0.05$, *=significant after Bonferroni correction).

FA	
Hippocampus	
Amygdala	
Cerebellum	
Brainstem	
Caudate nucleus	$\uparrow$
Thalamus	$\downarrow^{*}$
Subthalamic nucleus	
Lentiform Nucleus	$\downarrow$
Corpus Callosum	$\downarrow^{*}$
Frontal lobe wm	$\downarrow$
Parietal lobe wm	$\downarrow$
Occipital lobe wm	
Temporal lobe wm	
Fusiform gyrus wm	$\downarrow$
Cingulate gyrus wm	
Frontal lobe gm	
Parietal lobe gm	
Occipital lobe gm	
Temporal lobe gm	
Fusiform gyrus gm	
Cingulate gyrus gm	

ADC	
Hippocampus	
Amygdala	
Cerebellum	
Brainstem	
Caudate nucleus	
Thalamus	
Subthalamic nucleus	
Lentiform Nucleus	
Corpus Callosum	$\uparrow^{*}$
Frontal lobe wm	
Parietal lobe wm	$\uparrow$
Occipital lobe wm	$\uparrow$
Temporal lobe wm	
Fusiform gyrus wm	
Cingulate gyrus wm	$\uparrow$
Frontal lobe gm	
Parietal lobe gm	
Occipital lobe gm	
Temporal lobe gm	
Fusiform gyrus gm	
Cingulate gyrus gm	$\uparrow$

AD	
Hippocampus	
Amygdala	
Cerebellum	
Brainstem	
Caudate nucleus	
Thalamus	
Subthalamic nucleus	
Lentiform Nucleus	
Corpus Callosum	
Frontal lobe wm	
Parietal lobe wm	$\uparrow$
Occipital lobe wm	
Temporal lobe wm	
Fusiform gyrus wm	
Cingulate gyrus wm	$\uparrow$
Frontal lobe gm	
Parietal lobe gm	
Occipital lobe gm	
Temporal lobe gm	
Fusiform gyrus gm	
Cingulate gyrus gm	$\uparrow^{*}$

RD	
Hippocampus	
Amygdala	
Cerebellum	
Brainstem	
Caudate nucleus	
Thalamus	
Subthalamic nucleus	
Lentiform Nucleus	
Corpus Callosum	$\uparrow^{*}$
Frontal lobe wm	$\uparrow$
Parietal lobe wm	$\uparrow$
Occipital lobe wm	$\uparrow$
Temporal lobe wm	
Fusiform gyrus wm	$\uparrow$
Cingulate gyrus wm	
Frontal lobe gm	
Parietal lobe gm	
Occipital lobe gm	
Temporal lobe gm	
Fusiform gyrus gm	
Cingulate gyrus gm	

Table 7.24: Comparison of regional DTI measures between the group of early preterm infants and the term controls. Significant ($p < 0.05$) increases/decreases of the measures in the preterm subjects are annotated with $\uparrow/\downarrow$ (*=significantly different after Bonferroni correction).

FA		ADC	
Hippocampus	0.025	**Hippocampus**	-0.064
Amygdala	0.003	**Amygdala**	-0.017
Cerebellum	-0.009	**Cerebellum**	**0.206**
Brainstem	0.063	**Brainstem**	0.076
Caudate nucleus	**-0.370***	**Caudate nucleus**	0.024
Thalamus	**0.214***	**Thalamus**	0.003
Subthalamic nucleus	**0.148**	**Subthalamic nucleus**	-0.005
Lentiform Nucleus	**-0.197**	**Lentiform Nucleus**	0.112
Corpus Callosum	**0.325***	**Corpus Callosum**	**-0.310***
Frontal lobe wm	**-0.187**	**Frontal lobe wm**	0.134
Parietal lobe wm	0.064	**Parietal lobe wm**	-0.005
Occipital lobe wm	0.038	**Occipital lobe wm**	0.058
Temporal lobe wm	-0.059	**Temporal lobe wm**	**0.195**
Fusiform gyrus wm	0.056	**Fusiform gyrus wm**	**0.191**
Cingulate gyrus wm	**-0.178**	**Cingulate gyrus wm**	0.114
Frontal lobe gm	**-0.229***	**Frontal lobe gm**	0.088
Parietal lobe gm	**-0.179**	**Parietal lobe gm**	0.040
Occipital lobe gm	**-0.174**	**Occipital lobe gm**	0.106
Temporal lobe gm	**-0.174**	**Temporal lobe gm**	0.051
Fusiform gyrus gm	**-0.167**	**Fusiform gyrus gm**	0.008
Cingulate gyrus gm	**-0.199**	**Cingulate gyrus gm**	0.040

AD		RD	
Hippocampus	-0.061	**Hippocampus**	-0.063
Amygdala	-0.008	**Amygdala**	-0.020
Cerebellum	**0.202**	**Cerebellum**	**0.194**
Brainstem	0.089	**Brainstem**	0.067
Caudate nucleus	-0.110	**Caudate nucleus**	0.097
Thalamus	0.079	**Thalamus**	-0.041
Subthalamic nucleus	0.062	**Subthalamic nucleus**	-0.041
Lentiform Nucleus	0.054	**Lentiform Nucleus**	**0.137**
Corpus Callosum	-0.135	**Corpus Callosum**	**-0.368***
Frontal lobe wm	0.102	**Frontal lobe wm**	**0.146**
Parietal lobe wm	0.009	**Parietal lobe wm**	-0.011
Occipital lobe wm	0.061	**Occipital lobe wm**	0.055
Temporal lobe wm	**0.202**	**Temporal lobe wm**	**0.189**
Fusiform gyrus wm	**0.223***	**Fusiform gyrus wm**	**0.170**
Cingulate gyrus wm	0.071	**Cingulate gyrus wm**	0.128
Frontal lobe gm	-0.023	**Frontal lobe gm**	0.135
Parietal lobe gm	-0.082	**Parietal lobe gm**	0.097
Occipital lobe gm	-0.022	**Occipital lobe gm**	**0.156**
Temporal lobe gm	-0.049	**Temporal lobe gm**	0.096
Fusiform gyrus gm	-0.097	**Fusiform gyrus gm**	0.054
Cingulate gyrus gm	-0.068	**Cingulate gyrus gm**	0.084

Table 7.25: Correlations of DTI measures with gestational age at birth correcting for the age at scan (bold=significant at $p < 0.05$, *=significant after Bonferroni correction).

7.5 Spatiotemporal structural atlas construction

Structural information of probabilistic brain atlases is constructed by averaging segmentations of different brains in the same coordinate space, in order to account for the anatomical variability in the brain. This section describes the construction of the first regional spatio-temporal structural atlas for the neonatal brain with a methodology similar to Kuklisova-Murgasova et al. (2011); Serag et al. (2012). As in Kuklisova-Murgasova et al. (2011); Serag et al. (2012), the segmentations are averaged with a non-parametric kernel regression according to the age at scan of the subjects.

The spatio-temporal template of Serag et al. (2012) is used as the coordinate space of the atlas. This template defines mean brain images for the ages of 28 to 44 weeks age at scan (with a week interval). The segmentations of the 420 T2 images described in Section 7.2 are warped to the space of the template according to the age at scan of each subject. In order to enforce consistency of the atlas in the time domain (different ages of the template), each segmentation is warped to the $[a-3, a+3]$ mean images, where a is the rounded age at scan of the subject. The transformations are calculated with non-rigid registration of the subject's T2 image to the corresponding mean images of the template. Having computed the transformations for all the subjects, the age-dependent probability map $P_{k,t}$ of each structure k at time t of the atlas can be computed as:

$$P_{k,t} = \frac{\sum_{s=1}^{S} w(t_s, t) M_{s,k} \circ T_{s,t}}{\sum_{s=1}^{S} w(t_s, t)} \tag{7.1}$$

where s denotes the different subjects ($S = 420$ in total). $M_{s,k}$ is the binary mask of structure k from the segmentation of subject s. $M_{s,k}$ is warped ($\circ$) under the transformation $T_{s,t}$ of s to the mean image of the template at age t. $w(t_s, t)$ is an age-dependent weight of subject s according to how closely the age t_s of the subject matches the age t of the atlas. The weight is defined according to a Gaussian kernel:

$$w(t_s, t) = \frac{1}{\sigma_w \sqrt{2\pi}} e^{\frac{-(t_s - t)^2}{2\sigma_w^2}} \tag{7.2}$$

where σ_w is set to 1 to introduce a large weight for subjects close to each age of the atlas and small weight for those that deviate from it. The

probabilistic atlas at each age t is then defined as the union of the probability maps at the corresponding age: $P_t = \{P_{k,t}\}$.

A maximum-probability atlas at time t is further constructed by assigning the structure with the maximum probability to each voxel at age t:

$$P_{max,t} = argmax_k \; P_{k,t} \tag{7.3}$$

The constructed probabilistic and maximum-probability structural atlases incorporate the 82 structures of the brain and the CSF, intra-cranial and extra-cranial background. Illustrations of the atlases are presented in Figures 7.9, 7.10. The atlases are publicly available from http://brain-development.org/.

7.6 Discussion and conclusions

Quantitative measurements of the developing neonatal brain are required to study normal brain growth and potentially aid the prognosis of neurological impairments. In this chapter the proposed automatic segmentation algorithm is employed to delineate 82 regions of the brain in an extensive database and derive a number of volumetric, cortical surface and DTI measurements. This is the first study to provide measurements on detailed regional structures of the neonatal brain.

Absolute and relative volumes of the brain tissues are provided from the early preterm period to term-equivalent age. Derived volumes are similar to tissue volumes reported in studies where the subjects have been manually annotated. Regional volumes are presented for the first time. Surface area and curvature measures of the whole cortex and regional cortical parts are estimated based on the segmentations. To further explore the tissue microstructure, DTI measurements are analysed over 21 regions of the brain. All the measures are significantly associated with brain maturation.

The volumetric, DTI, surface area and curvature measures are further used to characterize the effect of prematurity in the neonatal brain. Comparison of term controls with an age-matched group of early preterm infants is presented to investigate differences associated with prematurity. The effect of increasing prematurity is further quantified in a large cohort of preterm subjects. Prematurity is related to widespread reductions in the

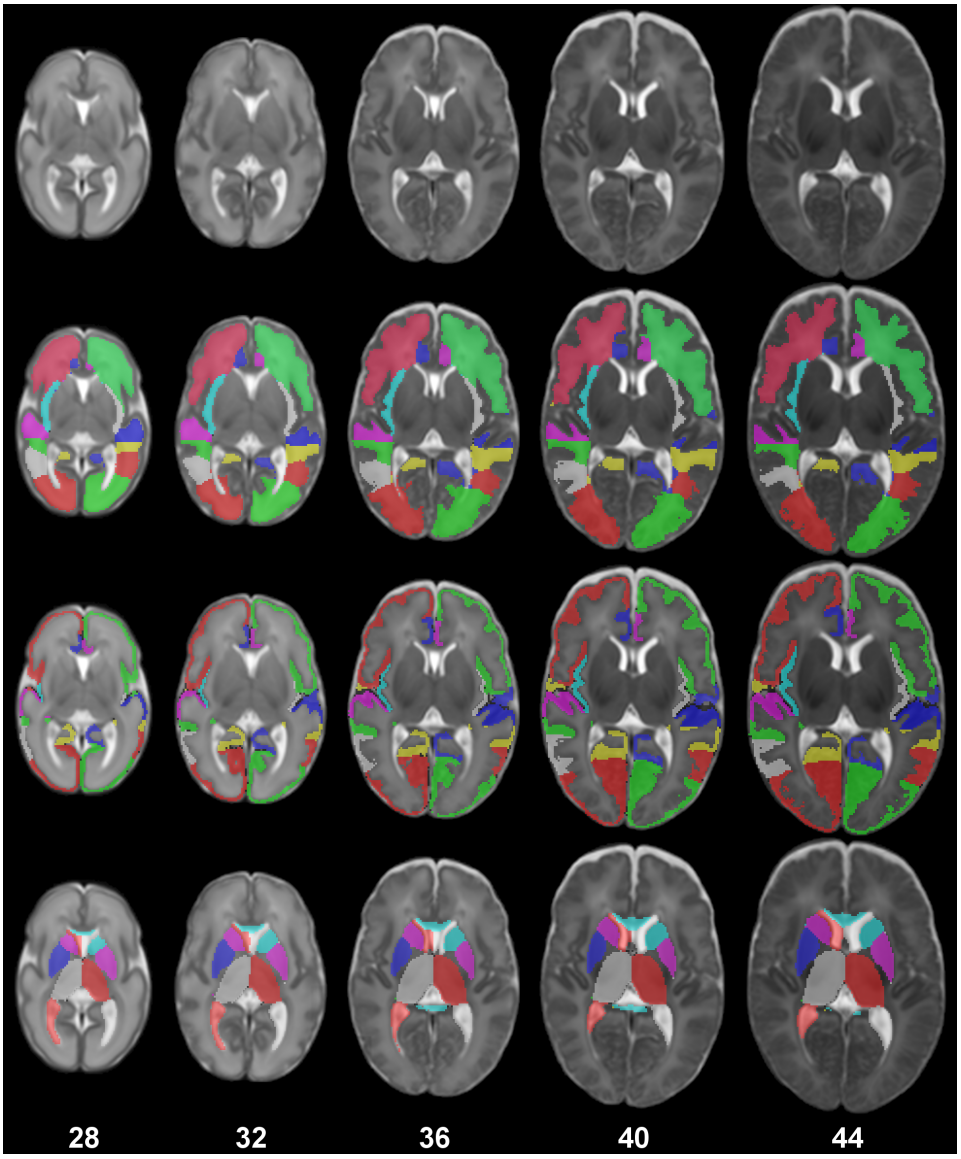

Figure 7.9: Different ages of the maximum probability structural atlas. The structures of the atlas (second row: WM structures, third row: CGM structures, fourth row: subcortical GM structures and ventricles) are defined in the coordinate space of the spatio-temporal template of Serag et al. (2012) (first row).

volume and surface area of the WM, CGM and subcortical structures, and increases in the relative CSF and ventricular volume. Cortical curvature is largely not associated with the age at birth of the infants. An exception is the anterior temporal lobe that presents a positive correlation with

increasing prematurity. Increased temporal lobe gyrification is consistent with a previous study in children born prematurily (Kesler et al., 2006). Here, these alterations are specifically localised in the anterior part of the temporal lobe. DTI measurements of the brain appear to be less affected in preterm infants. Notable exceptions are the regions of corpus callosum and thalamus that are known to be disrupted by prematurity (Anjari et al., 2007). Future studies with the inclusion of clinical variables and neurodevelopmental outcome will help to further elucidate the effect of prematurity in the neonatal brain.

Finally, a probabilistic and a maximum-probability structural atlas is constructed for different ages of the neonatal brain for all the segmented brain structures. The atlases define the structure probability and average segmentation respectively of each structure in the spatio-temporal space of Serag et al. (2012). These atlases can be used to derive regional brain measurements in subjects aligned to the common space of the atlas, or can be used in turn as spatial prior information for the segmentation of other subjects.

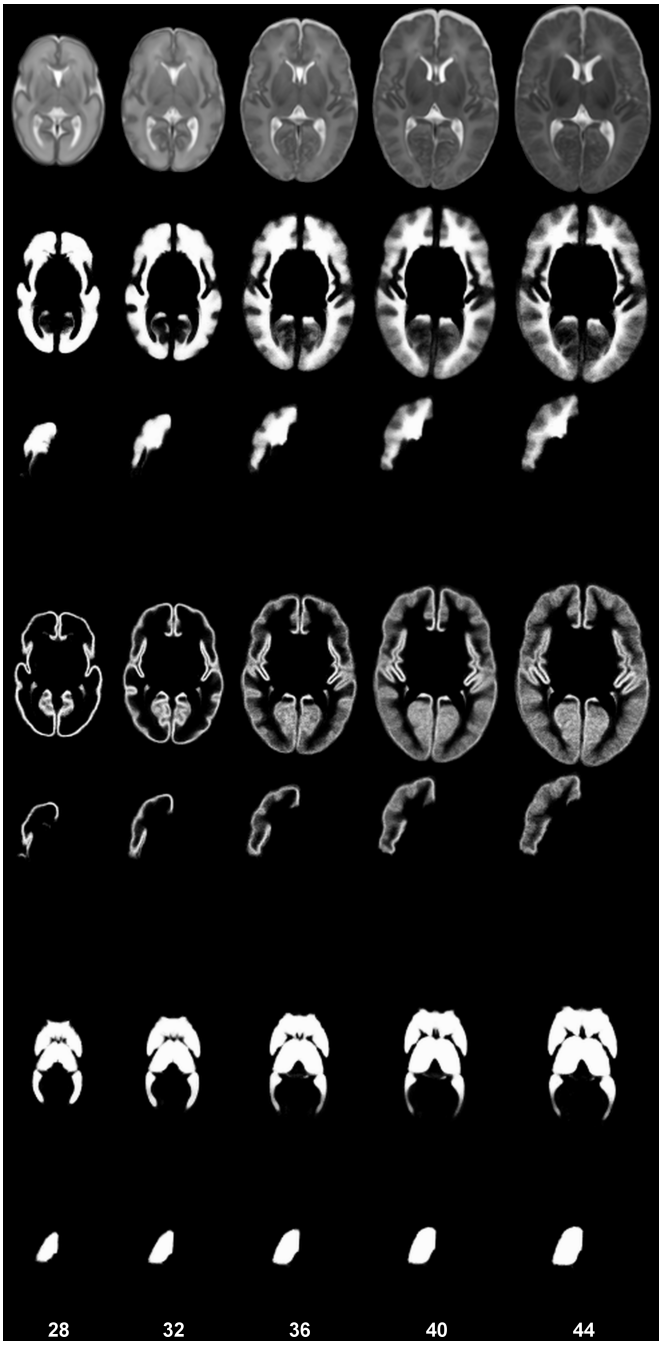

Figure 7.10: Different ages of the probabilistic structural atlas. The following probability maps are displayed (second-seventh row) : WM (sum of the probability maps of the WM structures), right frontal lobe WM, GM (sum of the probability maps of the GM structures), right frontal lobe GM, subcortical GM and ventricles (sum of the probability maps of the subcortical GM structures and the ventricles), right thalamus. The probabilistic structural atlas is defined in the coordinate space of the spatio-temporal template of Serag et al. (2012) (first row).

Chapter 8

Conclusion

This thesis has developed an automatic segmentation pipeline for the neonatal brain. Automated segmentation of infant MR imaging data is considerably more difficult than segmentation in adults or children. Neonatal brain development is accompanied by large changes in the shape and appearance of structures. In addition, partial volume effects and limited signal-to-noise ratio introduce challenges in the automatic techniques.

In Chapter 3, the problem of automatic delineation of the brain tissues was addressed. An adaptive algorithm was introduced that allows the segmentation of the neonatal brain in a wide range of gestational ages, from the early preterm to the term equivalent period. The algorithm extended the standard EM algorithm used for the segmentation of the adult brain to account for the specific challenges in the neonatal brain segmentation. Adaptivity to the large developmental changes was incorporated with a combination of atlas-driven and image-driven tissue priors and a prior relaxation scheme. Different components of the algorithm deal with image-related problems: the effect of noise and partial volume in the interface of the CSF-cortical grey matter are accounted for. The algorithm was tested on manually segmented data in a recent neonatal brain segmentation challege and produced state-of-the-art results.

Chapter 4 introduced a novel approach for the regional segmentation of the brain. Proposed adaptations of the segmentation model limit the influence of intensity in the delineation of structures with very similar intensity profiles. The modelling was performed with a structure hierarchy in the brain and a model averaging term. This method has allowed for the first

time to study the regional brain growth in an automatic and reproducible way. An extensive validation was performed to verify the robustness of the algorithm in different ages of the developing neonatal brain.

In Chapter 5 the segmentation of images was formulated in a group-wise manner. A cross-image term ensures the consistent labelling between corresponding regions of different images. Validation on term-equivalent brains demonstrated the advantage over the individual segmentation of images.

Chapter 6 proposed a methodology for the accurate cortical ribbon delineation. The problem of cortical grey matter oversegmentation was addressed with a novel partial volume correction for the boundary between white matter and cortical grey matter. A novel morphological correction was presented that delineates the cortical sulci, that cannot be detected with the intensity alone, according to local thickness information.

The segmentation method was used to analyse the neonatal brain for the first time in a detailed, regional scale. Regional measurements of volumes, DTI and cortical surface were used to explore different aspects of the growth of structures over the neonatal period and provided new insights on the consequences of prematurity. Finally, the segmented data were utilized for the construction of the first regional structural atlas of the developing brain, which is now freely available for the neonatal community.

8.1 Future research directions

There are a number of interesting directions to extend the work presented in this thesis, both in terms of methodology and clinical applications.

From a methodological point of view, the proposed segmentation algorithm could be extended for the multi-modal segmentation of the neonatal brain. Different imaging modalities provide complementary information of the brain development and could be integrated to potentially improve the segmentation. A straightforward extension would be the inclusion of T1, T2 and DTI data simultaneously for the brain parcellation similarly to Avants et al. (2011); Wang et al. (2012b). A multi-modality extension of the segmentation algorithm would further allow a more consistent labelling across different images of the same subject.

Chapter 4 demonstrated the advantage of combining different segmentation models. The proposed weighting of the models was based on the

intensity gradient of the images. Different weighting strategies could be explored. An example strategy would involve the automatic learning of regional weights for each model based on supervised classification techniques.

A limiting factor in the development of automatic segmentation techniques for the neonatal brain is the lack of manually segmented atlases. In this study 20 manually labelled atlases at term-equivalent brains were used to propagate the labelling information to neonatal brains at term but also the preterm period. Manually segmented atlases at the preterm age could potentially help to further improve the segmentation performance in the early brains. Additionally, the proposed technique should not be limited to the segmentation of the neonatal brain, but could be further utilised for the delineation of brain structures in the fetus. However, this would require additional atlases since the fetal brain presents large developmental differences from the newborn brain.

Chapter 7 analysed a number of different cortical surface measures calculated at the interior cortical surface. The interior cortical surface does not suffer from the problem of merging gyri and can thus be easily reconstructed. Nevertheless, the obtained surfaces may still include small topological defects. Topological correction of the surfaces was not addressed. Furthermore, the inner cortical surface could be deformed, e.g. according to forces defined from the Laplace's equation, in order to reconstruct the medial surface of the cortex. The middle cortical surface provides a more unbiased representation of the sulcal and gyral regions than the inner or outer cortical surfaces (Essen et al., 2006).

With respect to the clinical applications, Chapter 7 presented the analysis of a large cohort of newborn subjects to investigate the regional brain development and effect of prematurity. The data analysis was performed majorly in preterm subjects and a few term-equivalent datasets. Access to imaging data of more term controls would allow better characterisation of the normal development of the neonatal brain. Moreover, availiability of additional clinical variables would help to factor out the effect of other clinical conditions and localise even more the disturbances in prematurily born infants. The work in this thesis allows regional exploration of the aberrant effects of brain abnormalities and should not be therefore limited only to the effect of prematurity.

Bibliography

Adams, R. and Bischof, L. (1994). Seeded region growing. *IEEE Transactions on Pattern Analysis and Machine Intelligence*, 16(6):641–647.

Ajayi-Obe, M., Saeed, N., Cowan, F. M., Rutherford, M. A., and Edwards, A. D. (2000). Reduced development of cerebral cortex in extremely preterm infants. *Lancet*, 356(9236):1162–1163.

Al-Attas, R. and El-Zaart, A. (2007). Thresholding of medical images using minimum cross entropy. In Ibrahim, F., Osman, N. A. A., Usman, J., and Kadri, N. A., editors, *3rd Kuala Lumpur International Conference on Biomedical Engineering 2006*, number 15 in IFMBE Proceedings, pages 296–299. Springer Berlin Heidelberg.

Aljabar, P., Heckemann, R. A., Hammers, A., Hajnal, J. V., and Rueckert, D. (2009). Multi-atlas based segmentation of brain images: atlas selection and its effect on accuracy. *NeuroImage*, 46(3):726–738.

Anbeek, P., Vincken, K. L., Groenendaal, F., Koeman, A., van Osch, M. J. P., and van der Grond, J. (2008). Probabilistic brain tissue segmentation in neonatal magnetic resonance imaging. *Pediatric Research*, 63(2):158–163.

Anjari, M., Srinivasan, L., Allsop, J. M., Hajnal, J. V., Rutherford, M. A., Edwards, A. D., and Counsell, S. J. (2007). Diffusion tensor imaging with tract-based spatial statistics reveals local white matter abnormalities in preterm infants. *NeuroImage*, 35(3):1021–1027.

Artaechevarria, X., Munoz-Barrutia, A., and Ortiz-de Solorzano, C. (2009). Combination strategies in multi-atlas image segmentation: application to brain MR data. *IEEE Transactions on Medical Imaging*, 28(8):1266–1277.

Ashburner, J. and Friston, K. J. (2005). Unified segmentation. *NeuroImage*, 26(3):839–851.

Avants, B. B., Tustison, N. J., Wu, J., Cook, P. A., and Gee, J. C. (2011). An open source multivariate framework for n-tissue segmentation with evaluation on public data. *Neuroinformatics*, 9(4):381–400.

Babalola, K. O., Patenaude, B., Aljabar, P., Schnabel, J., Kennedy, D., Crum, W., Smith, S., Cootes, T., Jenkinson, M., and Rueckert, D. (2009). An evaluation of four automatic methods of segmenting the subcortical structures in the brain. *NeuroImage*, 47(4):1435–1447.

Ball, G., Boardman, J. P., Rueckert, D., Aljabar, P., Arichi, T., Merchant, N., Gousias, I. S., Edwards, A. D., and Counsell, S. J. (2012). The effect of preterm birth on thalamic and cortical development. *Cerebral Cortex*, 22(5):1016–1024.

Ball, G., Counsell, S. J., Anjari, M., Merchant, N., Arichi, T., Doria, V., Rutherford, M. A., Edwards, A. D., Rueckert, D., and Boardman, J. P. (2010). An optimised tract-based spatial statistics protocol for neonates: applications to prematurity and chronic lung disease. *NeuroImage*, 53(1):94–102.

Bankman, I. (2008). *Handbook of Medical Image Processing and Analysis*. Academic Press, 2 edition.

Beauchamp, M. H., Thompson, D. K., Howard, K., Doyle, L. W., Egan, G. F., Inder, T. E., and Anderson, P. J. (2008). Preterm infant hippocampal volumes correlate with later working memory deficits. *Brain*, 131(Pt 11):2986–2994.

Belaroussi, B., Milles, J., Carme, S., Zhu, Y. M., and Benoit-Cattin, H. (2006). Intensity non-uniformity correction in MRI: existing methods and their validation. *Medical Image Analysis*, 10(2):234–246.

Bezdek, J. C. (1981). *Pattern Recognition with Fuzzy Objective Function Algorithms*. Kluwer Academic Publishers, Norwell, MA, USA.

Bhatia, K. K., Aljabar, P., Boardman, J. P., Srinivasan, L., Murgasova, M., Counsell, S. J., Rutherford, M. A., Hajnal, J., Edwards, A. D., and

Rueckert, D. (2007). Groupwise combined segmentation and registration for atlas construction. *Medical Image Computing and Computer-assisted Intervention (MICCAI)*, 10(Pt 1):532–540.

Black, M., Sapiro, G., Marimont, D., and Heeger, D. (1998). Robust anisotropic diffusion. *IEEE Transactions on Image Processing*, 7(3):421–432.

Boardman, J. P., Counsell, S. J., Rueckert, D., Kapellou, O., Bhatia, K. K., Aljabar, P., Hajnal, J., Allsop, J. M., Rutherford, M. A., and Edwards, A. D. (2006). Abnormal deep grey matter development following preterm birth detected using deformation-based morphometry. *NeuroImage*, 32(1):70–78.

Boardman, J. P., Craven, C., Valappil, S., Counsell, S. J., Dyet, L. E., Rueckert, D., Aljabar, P., Rutherford, M. A., Chew, A. T. M., Allsop, J. M., Cowan, F., and Edwards, A. D. (2010). A common neonatal image phenotype predicts adverse neurodevelopmental outcome in children born preterm. *NeuroImage*, 52(2):409–414.

Cardoso, M. J., Melbourne, A., Kendall, G. S., Modat, M., Hagmann, C. F., Robertson, N. J., Marlow, N., and Ourselin, S. (2011). Adaptive neonate brain segmentation. *Medical Image Computing and Computer-assisted Intervention (MICCAI)*, 14(Pt 3):378–386.

Cardoso, M. J., Melbourne, A., Kendall, G. S., Modat, M., Robertson, N. J., Marlow, N., and Ourselin, S. (2013). AdaPT: an adaptive preterm segmentation algorithm for neonatal brain MRI. *NeuroImage*, 65:97–108.

Cardoso, M. J., Wolz, R., Modat, M., Fox, N. C., Rueckert, D., and Ourselin, S. (2012). Geodesic information flows. *Medical Image Computing and Computer-assisted Intervention (MICCAI)*, 15(Pt 2):262–270.

Cheong, J. L. Y., Thompson, D. K., Wang, H. X., Hunt, R. W., Anderson, P. J., Inder, T. E., and Doyle, L. W. (2009). Abnormal white matter signal on MR imaging is related to abnormal tissue microstructure. *American Journal of Neuroradiology*, 30(3):623–628.

Chiţă, S. M., Benders, M., Moeskops, P., Kersbergen, K. J., Viergever, M. A., and Išgum, I. (2013). Automatic segmentation of the preterm

neonatal brain with MRI using supervised classification. In *SPIE Medical Imaging. International Society for Optics and Photonics*, volume 8669, pages 86693X–86693X–6.

Christensen, G. E., Rabbitt, R. D., and Miller, M. I. (1994). 3D brain mapping using a deformable neuroanatomy. *Physics in Medicine and Biology*, 39(3):609–618.

Collins, D. L., Holmes, C. J., Peters, T. M., and Evans, A. C. (1995). Automatic 3-d model-based neuroanatomical segmentation. *Human Brain Mapping*, 3(3):190–208.

Collins, D. L., Neelin, P., Peters, T. M., and Evans, A. C. (1994). Automatic 3D intersubject registration of MR volumetric data in standardized talairach space. *Journal of Computer Assisted Tomography*, 18(2):192–205.

Cootes, T. F., Edwards, G. J., and Taylor, C. J. (1998). Active appearance models. *IEEE Transactions on Pattern Analysis and Machine Intelligence*, pages 484–498.

Cootes, T. F., Taylor, C. J., Cooper, D. H., and Graham, J. (1995). Active shape models-their training and application. *Computer Vision and Image Understanding*, 61(1):38–59.

Counsell, S. J., Edwards, A. D., Chew, A. T. M., Anjari, M., Dyet, L. E., Srinivasan, L., Boardman, J. P., Allsop, J. M., Hajnal, J. V., Rutherford, M. A., and Cowan, F. M. (2008). Specific relations between neurodevelopmental abilities and white matter microstructure in children born preterm. *Brain*, 131(Pt 12):3201–3208.

Counsell, S. J. and Rutherford, M. A. (2002). Magnetic resonance imaging of the newborn brain. *Current Paediatrics*, 12(5):401–413.

Counsell, S. J., Shen, Y., Boardman, J. P., Larkman, D. J., Kapellou, O., Ward, P., Allsop, J. M., Cowan, F. M., Hajnal, J. V., Edwards, A. D., and Rutherford, M. A. (2006). Axial and radial diffusivity in preterm infants who have diffuse white matter changes on magnetic resonance imaging at term-equivalent age. *Pediatrics*, 117(2):376–386.

Coupé, P., Manjón, J. V., Fonov, V., Pruessner, J., Robles, M., and Collins, D. L. (2011). Patch-based segmentation using expert priors: application to hippocampus and ventricle segmentation. *NeuroImage*, 54(2):940–954.

Criminisi, A., Shotton, J., and Konukoglu, E. (2012). Decision forests: A unified framework for classification, regression, density estimation, manifold learning and semi-supervised learning. *Foundations and Trends in Computer Graphics and Vision*, 7:81–227.

Delobel-Ayoub, M., Arnaud, C., White-Koning, M., Casper, C., Pierrat, V., Garel, M., Burguet, A., Roze, J.-C., Matis, J., Picaud, J.-C., Kaminski, M., and Larroque, B. (2009). Behavioral problems and cognitive performance at 5 years of age after very preterm birth: The EPIPAGE study. *Pediatrics*, 123(6):1485–1492.

Dempster, A. P., Laird, N. M., and Rubin, D. B. (1977). Maximum likelihood from incomplete data via the EM algorithm. *Journal of the Royal Statistical Society*, 39(1):1–38.

Dice, L. R. (1945). Measures of the amount of ecologic association between species. *Ecology*, 26(3):297–302.

Dittrich, E., Riklin-Raviv, T., Kasprian, G., Brugger, P., Prayer, D., and Langs, G. (2011). Learning a spatio-temporal latent atlas for fetal brain segmentation. In *MICCAI Workshop on Image Analysis of Human Brain Development*, pages 9–16.

Donner, R., Reiter, M., Langs, G., Peloschek, P., and Bischof, H. (2006). Fast active appearance model search using canonical correlation analysis. *IEEE Transactions on Pattern Analysis and Machine Intelligence*, 28(10):1690–1694.

Dubois, J., Benders, M., Borradori-Tolsa, C., Cachia, A., Lazeyras, F., Ha-Vinh Leuchter, R., Sizonenko, S. V., Warfield, S. K., Mangin, J. F., and Hüppi, P. S. (2008a). Primary cortical folding in the human newborn: an early marker of later functional development. *Brain*, 131(Pt 8):2028–2041.

Dubois, J., Benders, M., Cachia, A., Lazeyras, F., Ha-Vinh Leuchter, R., Sizonenko, S. V., Borradori-Tolsa, C., Mangin, J. F., and Hüppi, P. S.

(2008b). Mapping the early cortical folding process in the preterm newborn brain. *Cerebral Cortex*, 18(6):1444–1454.

Essen, D. C. V., Dierker, D., Snyder, A. Z., Raichle, M. E., Reiss, A. L., and Korenberg, J. (2006). Symmetry of cortical folding abnormalities in williams syndrome revealed by surface-based analyses. *The Journal of Neuroscience*, 26(20):5470–5483.

Evans, A., Collins, D., Mills, S. R., Brown, E. D., Kelly, R. L., and Peters, T. (1993). 3D statistical neuroanatomical models from 305 MRI volumes. In *Nuclear Science Symposium and Medical Imaging Conference, 1993., 1993 IEEE Conference Record.*, pages 1813–1817 vol.3.

Fischl, B., Salat, D. H., Busa, E., Albert, M., Dieterich, M., Haselgrove, C., van der Kouwe, A., Killiany, R., Kennedy, D., Klaveness, S., Montillo, A., Makris, N., Rosen, B., and Dale, A. M. (2002). Whole brain segmentation: automated labeling of neuroanatomical structures in the human brain. *Neuron*, 33(3):341–355.

Gilmore, J. H., Lin, W., Prastawa, M. W., Looney, C. B., Vetsa, Y. S. K., Knickmeyer, R. C., Evans, D. D., Smith, J. K., Hamer, R. M., Lieberman, J. A., and Gerig, G. (2007). Regional gray matter growth, sexual dimorphism, and cerebral asymmetry in the neonatal brain. *The Journal of Neuroscience*, 27(6):1255–1260.

Giménez, M., Miranda, M. J., Born, A. P., Nagy, Z., Rostrup, E., and Jernigan, T. L. (2008). Accelerated cerebral white matter development in preterm infants: a voxel-based morphometry study with diffusion tensor MR imaging. *NeuroImage*, 41(3):728–734.

Gousias, I. S., Edwards, A. D., Rutherford, M. A., Counsell, S. J., Hajnal, J. V., Rueckert, D., and Hammers, A. (2012). Magnetic resonance imaging of the newborn brain: Manual segmentation of labelled atlases in term-born and preterm infants. *NeuroImage*, 62(3):1499–1509.

Gousias, I. S., Hammers, A., Counsell, S. J., Srinivasan, L., Rutherford, M. A., Heckemann, R. A., Hajnal, J. V., Rueckert, D., and Edwards, A. D. (2013). Magnetic resonance imaging of the newborn brain: Automatic segmentation of brain images into 50 anatomical regions. *PLoS ONE*, 8(4):e59990.

Gui, L., Lisowski, R., Faundez, T., Hüppi, P. S., Lazeyras, F., and Kocher, M. (2012a). Morphology-based segmentation of newborn brain MR images. In *MICCAI Grand Challenge on Neonatal Brain Segmentation 2012 (NeoBrainS12)*, pages 1–8.

Gui, L., Lisowski, R., Faundez, T., Hüppi, P. S., Lazeyras, F., and Kocher, M. (2012b). Morphology-driven automatic segmentation of MR images of the neonatal brain. *Medical Image Analysis*, 16(8):1565–1579.

Hack, M. and Fanaroff, A. A. (2000). Outcomes of children of extremely low birthweight and gestational age in the 1990s. *Seminars in Neonatology*, 5(2):89–106.

Hammers, A., Allom, R., Koepp, M. J., Free, S. L., Myers, R., Lemieux, L., Mitchell, T. N., Brooks, D. J., and Duncan, J. S. (2003). Three-dimensional maximum probability atlas of the human brain, with particular reference to the temporal lobe. *Human Brain Mapping*, 19(4):224–247.

Han, X., Pham, D. L., Tosun, D., Rettmann, M. E., Xu, C., and Prince, J. L. (2004). CRUISE: cortical reconstruction using implicit surface evolution. *NeuroImage*, 23(3):997–1012.

Heckemann, R. A., Hajnal, J. V., Aljabar, P., Rueckert, D., and Hammers, A. (2006). Automatic anatomical brain MRI segmentation combining label propagation and decision fusion. *NeuroImage*, 33(1):115–126.

Herrmann, L. R. (1976). Laplacian-isoparametric grid generation scheme. *Journal of the Engineering Mechanics Division*, 102(5):749–907.

Hüppi, P. S., Maier, S. E., Peled, S., Zientara, G. P., Barnes, P. D., Jolesz, F. A., and Volpe, J. J. (1998a). Microstructural development of human newborn cerebral white matter assessed in vivo by diffusion tensor magnetic resonance imaging. *Pediatric Research*, 44(4):584–590.

Hüppi, P. S., Warfield, S., Kikinis, R., Barnes, P. D., Zientara, G. P., Jolesz, F. A., Tsuji, M. K., and Volpe, J. J. (1998b). Quantitative magnetic resonance imaging of brain development in premature and mature newborns. *Annals of Neurology*, 43(2):224–235.

Inder, T. E., Warfield, S. K., Wang, H., Hüppi, P. S., and Volpe, J. J. (2005). Abnormal cerebral structure is present at term in premature infants. *Pediatrics*, 115(2):286–294.

Jezzard, P. and Balaban, R. S. (1995). Correction for geometric distortion in echo planar images from b0 field variations. *Magnetic Resonance in Medicine*, 34(1):65–73.

Jezzard, P., Barnett, A. S., and Pierpaoli, C. (1998). Characterization of and correction for eddy current artifacts in echo planar diffusion imaging. *Magnetic Resonance in Medicine*, 39(5):801–812.

Jia, H., Yap, P.-T., and Shen, D. (2012). Iterative multi-atlas-based multi-image segmentation with tree-based registration. *NeuroImage*, 59(1):422–430.

Jiao, F., Li, S., Shum, H.-Y., and Schuurmans, D. (2003). Face alignment using statistical models and wavelet features. In *Computer Vision and Pattern Recognition*, volume 1, pages 321–327.

Jones, S. E., Buchbinder, B. R., and Aharon, I. (2000). Three-dimensional mapping of cortical thickness using laplace's equation. *Human Brain Mapping*, 11(1):12–32.

Justice, R. and Stokely, E. (1996). 3-d segmentation of MR brain images using seeded region growing. In *IEEE Engineering in Medicine and Biology Society*, volume 3, pages 1083–1084 vol.3.

Kapellou, O., Counsell, S. J., Kennea, N., Dyet, L., Saeed, N., Stark, J., Maalouf, E., Duggan, P., Ajayi-Obe, M., Hajnal, J., Allsop, J. M., Boardman, J., Rutherford, M. A., Cowan, F., and Edwards, A. D. (2006a). Abnormal cortical development after premature birth shown by altered allometric scaling of brain growth. *PLoS Medicine*, 3(8):e265.

Kapellou, O., Counsell, S. J., Kennea, N., Dyet, L., Saeed, N., Stark, J., Maalouf, E., Duggan, P., Ajayi-Obe, M., Hajnal, J., Allsop, J. M., Boardman, J., Rutherford, M. A., Cowan, F., and Edwards, A. D. (2006b). Abnormal cortical development after premature birth shown by altered allometric scaling of brain growth. *PLoS Medicine*, 3(8):e265.

Kass, M., Witkin, A., and Terzopoulos, D. (1988). Snakes: Active contour models. *International Journal of Computer Vision*, 1(4):321–331.

Kesler, S. R., Vohr, B., Schneider, K. C., Katz, K. H., Makuch, R. W., Reiss, A. L., and Ment, L. R. (2006). Increased temporal lobe gyrification in preterm children. *Neuropsychologia*, 44(3):445–453.

Kuklisova-Murgasova, M., Aljabar, P., Srinivasan, L., Counsell, S. J., Doria, V., Serag, A., Gousias, I. S., Boardman, J. P., Rutherford, M. A., Edwards, A. D., Hajnal, J. V., and Rueckert, D. (2011). A dynamic 4D probabilistic atlas of the developing brain. *NeuroImage*, 54(4):2750–2763.

Kullback, S. and Leibler, R. A. (1951). On information and sufficiency. *The Annals of Mathematical Statistics*, 22(1):79–86.

Langs, G., Peloschek, P., Donner, R., Reiter, M., and Bischof, H. (2006). Active feature models. In *International Conference on Pattern Recognition (ICPR)*, volume 1, pages 417–420.

Ledig, C., Wolz, R., Aljabar, P., Lotjonen, J., Heckemann, R., Hammers, A., and Rueckert, D. (2012). Multi-class brain segmentation using atlas propagation and EM-based refinement. In *IEEE International Symposium on Biomedical Imaging (ISBI)*, pages 896 –899.

Limperopoulos, C., Soul, J. S., Gauvreau, K., Huppi, P. S., Warfield, S. K., Bassan, H., Robertson, R. L., Volpe, J. J., and du Plessis, A. J. (2005). Late gestation cerebellar growth is rapid and impeded by premature birth. *Pediatrics*, 115(3):688–695.

Lind, A., Haataja, L., Rautava, L., Väliaho, A., Lehtonen, L., Lapinleimu, H., Parkkola, R., Korkman, M., and PIPARI Study Group (2010). Relations between brain volumes, neuropsychological assessment and parental questionnaire in prematurely born children. *European child & adolescent psychiatry*, 19(5):407–417.

Lind, A., Parkkola, R., Lehtonen, L., Munck, P., Maunu, J., Lapinleimu, H., Haataja, L., and PIPARI Study Group (2011). Associations between regional brain volumes at term-equivalent age and development at 2 years of age in preterm children. *Pediatric Radiology*, 41(8):953–961.

Lodygensky, G. A., Seghier, M. L., Warfield, S. K., Tolsa, C. B., Sizonenko, S., Lazeyras, F., and Hüppi, P. S. (2008). Intrauterine growth restriction affects the preterm infant's hippocampus. *Pediatric Research*, 63(4):438–443.

Lorensen, W. E. and Cline, H. E. (1987). Marching cubes: A high resolution 3D surface construction algorithm. In *Proceedings of the 14th Annual Conference on Computer Graphics and Interactive Techniques*, SIGGRAPH '87, pages 163–169, New York, NY, USA. ACM.

Lötjönen, J. M., Wolz, R., Koikkalainen, J. R., Thurfjell, L., Waldemar, G., Soininen, H., and Rueckert, D. (2010). Fast and robust multi-atlas segmentation of brain magnetic resonance images. *NeuroImage*, 49(3):2352–2365.

Macqueen, J. (1967). Some methods of classification and analysis of multivariate observations. In *Proceedings of the Fifth Berkeley Symposium on Mathematical Statistics and Probability*, pages 281–297.

Makropoulos, A., Gousias, I., Ledig, C., Aljabar, P., Serag, A., Hajnal, J. V., Edwards, A. D., Counsell, S. J., and Rueckert, D. (2012a). Automatic multi-label segmentation of the preterm brain with the use of adaptive atlases. In *International Society for Magnetic Resonance in Medicine (ISMRM)*.

Makropoulos, A., Gousias, I. S., Ledig, C., Aljabar, P., Serag, A., Hajnal, J., Edwards, A. D., Counsell, S., and Rueckert, D. (2014). Automatic whole brain MRI segmentation of the developing neonatal brain. *IEEE Transactions on Medical Imaging*.

Makropoulos, A., Ledig, C., Aljabar, P., Serag, A., Hajnal, J. V., Edwards, A. D., Counsell, S. J., and Rueckert, D. (2012b). Automatic tissue and structural segmentation of neonatal brain MRI using expectation-maximization. In *MICCAI Grand Challenge on Neonatal Brain Segmentation 2012 (NeoBrainS12)*, pages 9–15.

Malladi, R., Sethian, J., and Vemuri, B. (1995). Shape modeling with front propagation: a level set approach. *IEEE Transactions on Pattern Analysis and Machine Intelligence*, 17(2):158–175.

Mangin, J.-F., Frouin, V., Bloch, I., Régis, J., and López-Krahe, J. (1995). From 3D magnetic resonance images to structural representations of the cortex topography using topology preserving deformations. *Journal of Mathematical Imaging and Vision*, 5(4):297–318.

Marlow, N., Wolke, D., Bracewell, M. A., and Samara, M. (2005). Neurologic and developmental disability at six years of age after extremely preterm birth. *New England Journal of Medicine*, 352(1):9–19.

Matthews, I. and Baker, S. (2004). Active appearance models revisited. *International Journal of Computer Vision*, 60(2):135–164.

Mazziotta, J. C., Toga, A. W., Evans, A., Fox, P., and Lancaster, J. (1995a). A probabilistic atlas of the human brain: theory and rationale for its development. the international consortium for brain mapping (ICBM). *NeuroImage*, 2(2):89–101.

Mazziotta, J. C., Toga, A. W., Evans, A. C., Fox, P. T., and Lancaster, J. L. (1995b). Digital brain atlases. *Trends in Neurosciences*, 18(5):210–211.

Melbourne, A., Cardoso, M. J., Kendall, J. S., Robertson, N. J., Marlow, N., and Ourselin, S. (2012). NeoBrainS12 challenge: Adaptive neonatal MRI brain segmentation with myelinated white matter class and automated extraction of ventricles i-IV. In *MICCAI Grand Challenge on Neonatal Brain Segmentation 2012 (NeoBrainS12)*, pages 16–21.

Mewes, A. U. J., Hüppi, P. S., Als, H., Rybicki, F. J., Inder, T. E., McAnulty, G. B., Mulkern, R. V., Robertson, R. L., Rivkin, M. J., and Warfield, S. K. (2006). Regional brain development in serial magnetic resonance imaging of low-risk preterm infants. *Pediatrics*, 118(1):23–33.

Miller, S. P., Vigneron, D. B., Henry, R. G., Bohland, M. A., Ceppi-Cozzio, C., Hoffman, C., Newton, N., Partridge, J. C., Ferriero, D. M., and Barkovich, A. J. (2002). Serial quantitative diffusion tensor MRI of the premature brain: development in newborns with and without injury. *Journal of Magnetic Resonance Imaging*, 16(6):621–632.

Moeskops, P., Benders, M. J. N. L., Pearlman, P. C., Kersbergen, K. J., Leemans, A., Viergever, M. A., and Išgum, I. (2013). Assessment of quantitative cortical biomarkers in the developing brain of preterm infants. In

SPIE Medical Imaging. Computer-Aided Diagnosis, volume 8670, pages 867011–867011–7.

Murphy, B. P., Inder, T. E., Huppi, P. S., Warfield, S., Zientara, G. P., Kikinis, R., Jolesz, F. A., and Volpe, J. J. (2001). Impaired cerebral cortical gray matter growth after treatment with dexamethasone for neonatal chronic lung disease. *Pediatrics*, 107(2):217–221.

NeoBrainS12 (2012). *MICCAI Grand Challenge on Neonatal Brain Segmentation 2012, http://neobrains12.isi.uu.nl*.

Nishida, M., Makris, N., Kennedy, D. N., Vangel, M., Fischl, B., Krishnamoorthy, K. S., Caviness, V. S., and Grant, P. E. (2006). Detailed semiautomated MRI based morphometry of the neonatal brain: preliminary results. *NeuroImage*, 32(3):1041–1049.

Osher, S. and Sethian, J. A. (1988). Fronts propagating with curvature-dependent speed: Algorithms based on hamilton-jacobi formulations. *Journal of Computational Physics*, 79(1):12–49.

Partridge, S. C., Mukherjee, P., Henry, R. G., Miller, S. P., Berman, J. I., Jin, H., Lu, Y., Glenn, O. A., Ferriero, D. M., Barkovich, A. J., and Vigneron, D. B. (2004). Diffusion tensor imaging: serial quantitation of white matter tract maturity in premature newborns. *NeuroImage*, 22(3):1302–1314.

Patenaude, B., Smith, S. M., Kennedy, D. N., and Jenkinson, M. (2011). A bayesian model of shape and appearance for subcortical brain segmentation. *NeuroImage*, 56(3):907–922.

Pereira, S., Festa, J., Mariz, J. A., Sousa, N., and Silva, C. A. (2013). Automatic brain tissue segmentation of multi-sequence MR images using random decision forests. In *MICCAI Grand Challenge on MR Brain Image Segmentation (MRBrainS13)*.

Peterson, B. S., Anderson, A. W., Ehrenkranz, R., Staib, L. H., Tageldin, M., Colson, E., Gore, J. C., Duncan, C. C., Makuch, R., and Ment, L. R. (2003). Regional brain volumes and their later neurodevelopmental correlates in term and preterm infants. *Pediatrics*, 111(5 Pt 1):939–948.

Peterson, B. S., Vohr, B., Staib, L. H., Cannistraci, C. J., Dolberg, A., Schneider, K. C., Katz, K. H., Westerveld, M., Sparrow, S., Anderson, A. W., Duncan, C. C., Makuch, R. W., Gore, J. C., and Ment, L. R. (2000). Regional brain volume abnormalities and long-term cognitive outcome in preterm infants. *Journal of the American Medical Association*, 284(15):1939–1947.

Pham, D. (2002). Fuzzy clustering with spatial constraints. In *Proceedings of the International Conference on Image Processing*, volume 2, pages 65–68.

Pham, D. L. and Prince, J. L. (1999). Adaptive fuzzy segmentation of magnetic resonance images. *IEEE Transactions on Medical Imaging*, 18(9):737–752.

Pienaar, R., Fischl, B., Caviness, V., Makris, N., and Grant, P. E. (2008). A methodology for analyzing curvature in the developing brain from preterm to adult. *International Journal of Imaging Systems and Technology*, 18(1):42–68.

Pitas, I. (2000). *Digital Image Processing Algorithms and Applications*. Wiley-Blackwell, New York.

Pohl, K. M., Bouix, S., Kikinis, R., and Grimson, W. E. L. (2004). Anatomical guided segmentation with non-stationary tissue class distributions in an expectation-maximization framework. In *IEEE International Symposium on Biomedical Imaging (ISBI)*, pages 81–84.

Prastawa, M., Gilmore, J. H., Lin, W., and Gerig, G. (2005). Automatic segmentation of MR images of the developing newborn brain. *Medical Image Analysis*, 9(5):457–466.

Pratt, W. K. (2007). *Digital Image Processing: PIKS Scientific Inside*. Wiley-Interscience, 4 edition.

Rathbone, R., Counsell, S. J., Kapellou, O., Dyet, L., Kennea, N., Hajnal, J., Allsop, J. M., Cowan, F., and Edwards, A. D. (2011). Perinatal cortical growth and childhood neurocognitive abilities. *Neurology*, 77(16):1510–1517.

Riklin-Raviv, T., Van Leemput, K., Menze, B. H., Wells, 3rd, W. M., and Golland, P. (2010). Segmentation of image ensembles via latent atlases. *Medical Image Analysis*, 14(5):654–665.

Rodriguez-Carranza, C. E., Mukherjee, P., Vigneron, D., Barkovich, J., and Studholme, C. (2008). A framework for in vivo quantification of regional brain folding in premature neonates. *NeuroImage*, 41(2):462–478.

Rohlfing, T., Brandt, R., Menzel, R., and Maurer, Jr, C. R. (2004). Evaluation of atlas selection strategies for atlas-based image segmentation with application to confocal microscopy images of bee brains. *NeuroImage*, 21(4):1428–1442.

Rousseau, F., Habas, P., and Studholme, C. (2011). A supervised patch-based approach for human brain labeling. *IEEE Transactions on Medical Imaging*, 30(10):1852 –1862.

Rubinstein, M., Liu, C., and Freeman, W. T. (2012). Annotation propagation in large image databases via dense image correspondence. In Fitzgibbon, A., Lazebnik, S., Perona, P., Sato, Y., and Schmid, C., editors, *Computer Vision - ECCV 2012*, number 7574 in Lecture Notes in Computer Science, pages 85–99. Springer Berlin Heidelberg.

Rueckert, D., Sonoda, L. I., Hayes, C., Hill, D. L., Leach, M. O., and Hawkes, D. J. (1999). Nonrigid registration using free-form deformations: application to breast MR images. *IEEE Transactions on Medical Imaging*, 18(8):712–721.

Rutherford, M. A. (2002). *MRI of the Neonatal Brain*. W.B. Saunders.

Schwartz, R. M., Luby, A. M., Scanlon, J. W., and Kellogg, R. J. (1994). Effect of surfactant on morbidity, mortality, and resource use in newborn infants weighing 500 to 1500 g. *New England Journal of Medicine*, 330(21):1476–1480.

Serag, A., Aljabar, P., Ball, G., Counsell, S. J., Boardman, J. P., Rutherford, M. A., Edwards, A. D., Hajnal, J. V., and Rueckert, D. (2012). Construction of a consistent high-definition spatio-temporal atlas of the developing brain using adaptive kernel regression. *NeuroImage*, 59(3):2255–2265.

Shattuck, D. W., Mirza, M., Adisetiyo, V., Hojatkashani, C., Salamon, G., Narr, K. L., Poldrack, R. A., Bilder, R. M., and Toga, A. W. (2008). Construction of a 3D probabilistic atlas of human cortical structures. *NeuroImage*, 39(3):1064–1080.

Shi, F., Fan, Y., Tang, S., Gilmore, J. H., Lin, W., and Shen, D. (2010). Neonatal brain image segmentation in longitudinal MRI studies. *NeuroImage*, 49(1):391–400.

Shi, F., Shen, D., Yap, P.-T., Fan, Y., Cheng, J.-Z., An, H., Wald, L. L., Gerig, G., Gilmore, J. H., and Lin, W. (2011). CENTS: cortical enhanced neonatal tissue segmentation. *Human Brain Mapping*, 32(3):382–396.

Shi, F., Wang, L., Wu, G., Li, G., Gilmore, J. H., Lin, W., and Shen, D. (2014). Neonatal atlas construction using sparse representation. *Human Brain Mapping*.

Shiee, N., Bazin, P.-L., Cuzzocreo, J. L., Blitz, A., and Pham, D. L. (2011). Segmentation of brain images using adaptive atlases with application to ventriculomegaly. In *Proceedings of the Information Processing in Medical Imaging*, volume 22, pages 1–12.

Sijbers, J., Scheunders, P., Verhoye, M., van der Linden, A., van Dyck, D., and Raman, E. (1997). Watershed-based segmentation of 3D MR data for volume quantization. *Magnetic Resonance Imaging*, 15(6):679–688.

Smith, S. M. (2002). Fast robust automated brain extraction. *Human Brain Mapping*, 17(3):143–155.

Song, S.-K., Sun, S.-W., Ramsbottom, M. J., Chang, C., Russell, J., and Cross, A. H. (2002). Dysmyelination revealed through MRI as increased radial (but unchanged axial) diffusion of water. *NeuroImage*, 17(3):1429–1436.

Song, Z., Awate, S. P., Licht, D. J., and Gee, J. C. (2007). Clinical neonatal brain MRI segmentation using adaptive nonparametric data models and intensity-based markov priors. *Medical Image Computing and Computer-assisted Intervention (MICCAI)*, 10(Pt 1):883–890.

Song, Z., Tustison, N., Avants, B., and Gee, J. C. (2006). Integrated graph cuts for brain MRI segmentation. *Medical Image Computing and Computer-assisted Intervention (MICCAI)*, 9(Pt 2):831–838.

Sotiras, A., Komodakis, N., Langs, G., and Paragios, N. (2009). Atlas-based deformable mutual population segmentation. In *IEEE International Symposium on Biomedical Imaging (ISBI)*, pages 5–8.

Srhoj-Egekher, V., Benders, M. J., Kersbergen, K. J., Viergever, M. A., and Isgum, I. (2012). Automatic segmentation of neonatal brain MRI using atlas based segmentation and machine learning approach. In *MICCAI Grand Challenge on Neonatal Brain Segmentation 2012 (NeoBrainS12)*, pages 22–27.

Srinivasan, L., Allsop, J., Counsell, S. J., Boardman, J. P., Edwards, A. D., and Rutherford, M. (2006). Smaller cerebellar volumes in very preterm infants at term-equivalent age are associated with the presence of supratentorial lesions. *American Journal of Neuroradiology*, 27(3):573–579.

Srinivasan, L., Dutta, R., Counsell, S. J., Allsop, J. M., Boardman, J. P., Rutherford, M. A., and Edwards, A. D. (2007). Quantification of deep gray matter in preterm infants at term-equivalent age using manual volumetry of 3-tesla magnetic resonance images. *Pediatrics*, 119(4):759–765.

Stejskal, E. and Tanner, J. (1965). Spin diffusion measurements: Spin echoes in the presence of a time-dependent field gradient. *The Journal of Chemical Physics*, 42(1):288–292.

Studholme, C., Hill, D., and Hawkes, D. (1999). An overlap invariant entropy measure of 3D medical image alignment. *Pattern Recognition*, 32(1):71–86.

Talairach, J., David, M., Tournoux, P., Corredor, H., and Kvasina, T. (1957). *Atlas d'anatomie stereotaxique; reperage radiologique indirect des noyaux gris centraux des regions mesencephalo-sous-optique et hypothalamique de l'homme.* Masson, Paris.

Talairach, J. and Tournoux, P. (1988). *Co-Planar Stereotaxic Atlas of the Human Brain: 3-D Proportional System: An Approach to Cerebral Imaging.* Thieme.

Tang, H., Wu, E. X., Ma, Q. Y., Gallagher, D., Perera, G. M., and Zhuang, T. (2000). MRI brain image segmentation by multi-resolution edge detection and region selection. *Computerized Medical Imaging and Graphics*, 24(6):349–357.

Terzopoulos, D. and Fleischer, K. (1988). Deformable models. *The Visual Computer*, 4(6):306–331.

Thompson, D. K., Warfield, S. K., Carlin, J. B., Pavlovic, M., Wang, H. X., Bear, M., Kean, M. J., Doyle, L. W., Egan, G. F., and Inder, T. E. (2007). Perinatal risk factors altering regional brain structure in the preterm infant. *Brain*, 130(Pt 3):667–677.

Thompson, D. K., Wood, S. J., Doyle, L. W., Warfield, S. K., Lodygensky, G. A., Anderson, P. J., Egan, G. F., and Inder, T. E. (2008). Neonate hippocampal volumes: prematurity, perinatal predictors, and 2-year outcome. *Annals of Neurology*, 63(5):642–651.

Tofts, P. (2003). *Quantitative MRI of the Brain: Measuring Changes Caused by Disease*. Wiley.

Tustison, N. J., Avants, B. B., Cook, P. A., Zheng, Y., Egan, A., Yushkevich, P. A., and Gee, J. C. (2010). N4ITK: improved n3 bias correction. *IEEE Transactions on Medical Imaging*, 29(6):1310–1320.

van der Lijn, F., den Heijer, T., Breteler, M. M. B., and Niessen, W. J. (2008). Hippocampus segmentation in MR images using atlas registration, voxel classification, and graph cuts. *NeuroImage*, 43(4):708–720.

Van Ginneken, B., Frangi, A., Staal, J., ter Haar Romeny, B., and Viergever, M. (2002). Active shape model segmentation with optimal features. *IEEE Transactions on Medical Imaging*, 21(8):924–933.

van Kooij, B. J. M., de Vries, L. S., Ball, G., van Haastert, I. C., Benders, M. J. N. L., Groenendaal, F., and Counsell, S. J. (2012). Neonatal tract-based spatial statistics findings and outcome in preterm infants. *American Journal of Neuroradiology*, 33(1):188–194.

Van Leemput, K., Bakkour, A., Benner, T., Wiggins, G., Wald, L. L., Augustinack, J., Dickerson, B. C., Golland, P., and Fischl, B. (2009). Auto-

mated segmentation of hippocampal subfields from ultra-high resolution in vivo MRI. *Hippocampus*, 19(6):549–557.

Van Leemput, K., Maes, F., Vandermeulen, D., and Suetens, P. (1999). Automated model-based tissue classification of MR images of the brain. *IEEE Transactions on Medical Imaging*, 18(10):897–908.

Van Leemput, K., Maes, F., Vandermeulen, D., and Suetens, P. (2003). A unifying framework for partial volume segmentation of brain MR images. *IEEE Transactions on Medical Imaging*, 22(1):105–119.

Wang, H., Das, S., Pluta, J., Craige, C., Altinay, M., Avants, B., Weiner, M., Mueller, S., and Yushkevich, P. (2010). Standing on the shoulders of giants: improving medical image segmentation via bias correction. *Medical Image Computing and Computer-assisted Intervention (MICCAI)*, 13(Pt 3):105–112.

Wang, H., Suh, J. W., Das, S. R., Pluta, J., Craige, C., and Yushkevich, P. A. (2012a). Multi-atlas segmentation with joint label fusion. *IEEE Transactions on Pattern Analysis and Machine Intelligence*.

Wang, H. and Yushkevich, P. A. (2013). Multi-atlas segmentation with joint label fusion and corrective learning-an open source implementation. *Frontiers in Neuroinformatics*, 7:27.

Wang, L., Shi, F., Lin, W., Gilmore, J. H., and Shen, D. (2011). Automatic segmentation of neonatal images using convex optimization and coupled level sets. *NeuroImage*, 58(3):805–817.

Wang, L., Shi, F., Yap, P.-T., Gilmore, J. H., Lin, W., and Shen, D. (2012b). 4D multi-modality tissue segmentation of serial infant images. *PloS ONE*, 7(9):e44596.

Wang, L., Shi, F., Yap, P.-T., Lin, W., Gilmore, J. H., and Shen, D. (2013). Longitudinally guided level sets for consistent tissue segmentation of neonates. *Human Brain Mapping*, 34(4):956–972.

Wang, S., Kuklisova-Murgasova, M., and Schnabel, J. A. (2012c). An atlas-based method for neonatal MR brain tissue segmentation. In *MICCAI Grand Challenge on Neonatal Brain Segmentation 2012 (NeoBrainS12)*, pages 28–35.

Wang, S., Wu, E. X., Cai, K., Lau, H.-F., Cheung, P.-T., and Khong, P.-L. (2009). Mild hypoxic-ischemic injury in the neonatal rat brain: longitudinal evaluation of white matter using diffusion tensor MR imaging. *American Journal of Neuroradiology*, 30(10):1907–1913.

Wang, Z., Bovik, A., Sheikh, H., and Simoncelli, E. (2004). Image quality assessment: from error visibility to structural similarity. *IEEE Transactions on Image Processing*, 13(4):600–612.

Warfield, S. K., Zou, K. H., and Wells, W. M. (2004). Simultaneous truth and performance level estimation (STAPLE): an algorithm for the validation of image segmentation. *IEEE Transactions on Medical Imaging*, 23(7):903–921.

Weisenfeld, N. I. and Warfield, S. K. (2009). Automatic segmentation of newborn brain MRI. *NeuroImage*, 47(2):564–572.

Weishaupt, D., Froehlich, J. M., Nanz, D., Köchli, V. D., Pruessmann, K. P., and Marincek, B. (2008). *How does MRI work?: An Introduction to the Physics and Function of Magnetic Resonance Imaging*. Springer.

Wells, W. M., Grimson, W. L., Kikinis, R., and Jolesz, F. A. (1996). Adaptive segmentation of MRI data. *IEEE Transactions on Medical Imaging*, 15(4):429–442.

Wilson-Costello, D., Friedman, H., Minich, N., Fanaroff, A. A., and Hack, M. (2005). Improved survival rates with increased neurodevelopmental disability for extremely low birth weight infants in the 1990s. *Pediatrics*, 115(4):997–1003.

Wolz, R., Aljabar, P., Hajnal, J. V., Hammers, A., and Rueckert, D. (2010). LEAP: learning embeddings for atlas propagation. *NeuroImage*, 49(2):1316–1325.

Woodward, L. J., Edgin, J. O., Thompson, D., and Inder, T. E. (2005). Object working memory deficits predicted by early brain injury and development in the preterm infant. *Brain*, 128(Pt 11):2578–2587.

Wu, J. and Avants, B. (2012). Automatic registration-based segmentation for neonatal brains using ANTs and atropos. In *MICCAI Grand Challenge on Neonatal Brain Segmentation 2012 (NeoBrainS12)*, pages 36–47.

Xue, H., Srinivasan, L., Jiang, S., Rutherford, M., Edwards, A. D., Rueckert, D., and Hajnal, J. V. (2007). Automatic segmentation and reconstruction of the cortex from neonatal MRI. *NeuroImage*, 38(3):461–477.

Yu, X., Zhang, Y., Lasky, R. E., Datta, S., Parikh, N. A., and Narayana, P. A. (2010). Comprehensive brain MRI segmentation in high risk preterm newborns. *PloS ONE*, 5(11):e13874.

Yu-qian, Z., Wei-hua, G., Zhen-cheng, C., Jing-tian, T., and Ling-yun, L. (2005). Medical images edge detection based on mathematical morphology. In *IEEE Engineering in Medicine and Biology Society*, pages 6492–6495.

Zacharia, A., Zimine, S., Lovblad, K. O., Warfield, S., Thoeny, H., Ozdoba, C., Bossi, E., Kreis, R., Boesch, C., Schroth, G., and Hüppi, P. S. (2006). Early assessment of brain maturation by MR imaging segmentation in neonates and premature infants. *American Journal of Neuroradiology*, 27(5):972–977.

Zeng, X., Staib, L. H., Schultz, R. T., and Duncan, J. S. (1999). Segmentation and measurement of the cortex from 3-d MR images using coupled-surfaces propagation. *IEEE Transactions on Medical Imaging*, 18(10):927–937.